Design and Development of Surface Plasmon Resonance Imaging Microfluidic Assays

Jennifer Olivia Foley

A dissertation submitted in partial fulfillment of the requirements for the degree of

Doctor of Philosophy

University of Washington

2007

Program Authorized to Offer Degree: Department of Bioengineering

INFORMATION TO USERS

The quality of this reproduction is dependent upon the quality of the copy submitted. Broken or indistinct print, colored or poor quality illustrations and photographs, print bleed-through, substandard margins, and improper alignment can adversely affect reproduction.

In the unlikely event that the author did not send a complete manuscript and there are missing pages, these will be noted. Also, if unauthorized copyright material had to be removed, a note will indicate the deletion.

ProQuest Information and Learning Company
300 North Zeeb Road
P.O. Box 1346
Ann Arbor, MI 48106-1346

University of Washington
Graduate School

This is to certify that I have examined this copy of a doctoral dissertation by

Jennifer Olivia Foley

and have found that it is complete and satisfactory in all respects, and that any and all revisions required by the final examining committee have been made.

Chair of the Supervisory Committee:

Paul Yager

Reading Committee:

Paul Yager

Bruce Finlayson

Clement Furlong

Date: 5/31/07

In presenting this dissertation in partial fulfillment of the requirements for the Doctoral degree at the University of Washington, I agree that the Library shall make its copies freely available for inspection. I further agree that extensive copying of the dissertation is allowable only for scholarly purposes, consistent with "fair use" as prescribed in the U.S. Copyright Law. Requests for copying or reproduction of this dissertation may be referred to ProQuest Information and Learning, 300 North Zeeb Road, Ann Arbor, MI 48106-1346, 1-800-521-0600, to whom the author has granted "the right to reproduce and sell (a) copies of the manuscript in microform and/or (b) printed copies of the manuscript made from microform."

Signature Jennifer Olivia Bley

Date 5/31/07

University of Washington

Abstract

Design and Development of Surface Plasmon Resonance Imaging Microfluidic Assays

Jennifer Olivia Foley

Chairperson of the Supervisory Committee:
Professor Paul Yager
Department of Bioengineering

This dissertation focuses on the design and development of SPR-imaging microfluidic assays to quantify nanomolar concentrations of small molecules (cortisol and phenytoin) in saliva for a point-of-care medical diagnostic. Microcontact printing, as a method to immobilize proteins on gold surfaces, was characterized with SPR-imaging, XPS, and XPS-imaging. Computational models of a standard microfluidic flow assay, an indirect immunoassay, and the concentration gradient immunoassay were developed to achieve a deeper understanding of the mass transport of analytes within a microchannel as well as to explore methods to improve the sensitivity of a microfluidic flow assay. The models showed strong qualitative agreement with experimental results. A microfluidic mixer – the herringbone channel – was incorporated in a microfluidic assay. The surface binding profile of a protein was significantly altered with this geometry. The surface binding profile was confirmed with SPR-imaging experiments. The model did not indicate an increase in the rate of binding of the protein to the surface of the herringbone microchannel when compared to a straight microchannel. Experimentally, at distances further downstream than that explored by the computational model, there was a modest increase in the rate of binding of the protein to the surface, suggesting that the herringbone geometry requires longer distances to significantly increase the rate of binding of a protein to a surface.

Table of Contents

Page

List of Equations

List of Figures

List of Tables

Acknowledgements

All work completed at the University of Washington has been supervised by Prof. Paul Yager. Prof. Clement Furlong, Prof. Bruce Finlayson, Prof. Dave Castner and Prof. Mark Cooper served on the advisory committee. Prof. Bruce Finlayson advised the work on the computational modeling of assays. Afshin-Moshadi-Hossein assisted with many of the computational models and also was central in the development of an optimization routine for the models. Prof. Dave Castner and Bronwyn Wickes gave helpful advice with regard to surface analysis techniques and microcontact printing. The oxygen plasma activation was completed using equipment provided by Prof. Folch's group. Prof. Castner and Dr. Lara Gamble from NESAC-BIO gave advice for the XPS and XPS imaging experiments. All XPS data was be collected by Dr. Lara Gamble at NESAC-BIO at the University of Washington. Dr. Elain Fu built the SPRM and with Dr. Tim Chinowsky developed the image processing protocols. Dr. Kjell Nelson developed the concentration gradient immunoassay and the indirect immunoassay and also provided experimental results for the assays. Dr. Kjell Nelson and Neil Geisler developed and perfected the wicking technique to pattern thiols on gold surfaces. Dr. Roya Sabeti assisted with the microfabrication of the two layer SU8 molds. Elena Garcia gave helpful advice with regard to the two layer SU8 microfabrication as well as computational modeling. Dr. Ken Hawkins gave helpful advice on all topics particularly the kinetic parameters of antibodies. Other Yager lab group members past and present including Dr. Mark Blaylock, Hugh Chang, Dr. Anson Hatch, Melissa Hasenback, Dr. Andy Kamholz, Jason Li, Kristen Lloyd, Dr. Matt Munson, and Dr. Chris Neils are gratefully acknowledged for their advice and support.

The research at IBM Research Labs in Switzerland was carried out under the supervision of Dr. Emmanuel Delamarche and in collaboration with Dr. Heinz Schmidt and Richard Stutz. Dr. David Juncker, Tobias Kraus, Dr. Heiko Wolf, Dr. Laurent Malaquin and Martin Zimmerman gave extremely helpful advice and suggestions. Dr. Walter Reiss and Dr. Paul Seidler are gratefully acknowledged for their support. The State Secretariat for

Education and Research (SER) in the framework of the EC project NaPa (contract no. NMP4-CT-2003-500120) funded this research.

The majority of this work was completed under the full support of a NIH training grant (1 T32 GM065098-01A1) and the NIDCR (Grant No. 1UO1 DE14971-01).

Dedication

To my parents, John and Lauretta Foley, and grandparents, John and Marie Tucker and Jack and Mary Foley, for their support and guidance.

Chapter 1: Introduction

Microfluidic technologies have the potential to change the medical diagnostic paradigm by serving as an enabling technology in the development of point-of-care (POC) diagnostics. Typically, patients must travel to hospitals where large centralized laboratories carry out medical tests that may take several hours to several days to complete. POC diagnostics bring the test to the patient, thereby increasing the availability and frequency of the tests and in turn improving the quality of health care the patient receives.

Microfluidic assays have several advantages over conventional large scale methods, making this technology suitable for POC diagnostics. These advantages include a reduction in sample and reagent volumes, the potential to reduce the size of the instrumentation in order to develop portable diagnostic equipment, the potential to use affordable and disposable polymeric devices, and a reduction in the amount of waste generated. Immunoassays represent versatile platform technologies capable of detecting and quantifying a wide variety of analytes and therefore represent an ideal assay format for a POC diagnostic.

The primary focus of the entire research project, funded by the National Institute of Dental and Craniofacial Research (NIDCR), was the development of a point-of-care microfluidic diagnostic to quantify nanomolar concentrations of a hormone, cortisol, and an epileptic drug, phenytoin, in saliva. Surface plasmon resonance (SPR) imaging, the detection method chosen for the salivary POC diagnostic, requires relatively simple optical components, and a portable and affordable SPR system is commercially available (Spreeta – Texas Instruments). Not only is the development of an affordable and portable SPR instrument feasible, but quantitative microfluidic assays using SPR have been widely reported in the literature.[1-11] Initial research for this dissertation aided in the development of a home-built SPR instrument.[12, 13]

A typical format for an SPR microfluidic assay is shown in Figure 1. An analyte, the molecule to be quantified, binds to a capture molecule immobilized to a gold surface in a microchannel. SPR monitors in real time the binding of the analyte to the gold surface.[14]

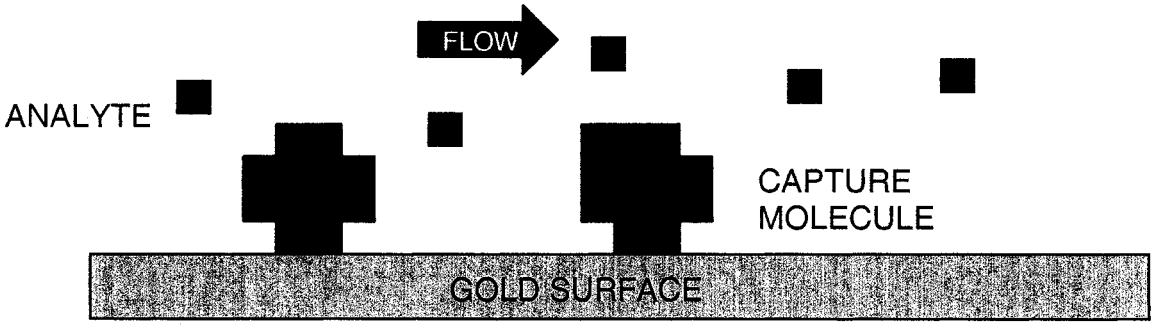

Figure 1. Microfluidic flow assay. A capture molecule immobilized to a surface of a microfluidic device binds to analytes in solution.

Producing well-defined and uniform patterns of capture molecules on a gold surface is a critical step in the development of sensitive microfluidic SPR-imaging assays. The immobilized capture molecules should be resistant to non-specific fouling and have a high surface density. Ideally, multiple capture molecules should be immobilized to the gold surface to allow several analytes to be quantified simultaneously. In Chapter 3, the characterization of proteins immobilized onto a gold surface using the surface patterning method – microcontact printing – was conducted using SPR-imaging, XPS, and XPS-imaging. In Chapter 4, the ability to pattern proteins inside three-dimensional microstructures using microcontact printing was also explored.

Computational models of several microfluidic assay formats were developed to achieve a more thorough understanding of the mass transport of the analyte within the microchannel as well as the binding profile of the analyte to the immobilized capture molecule. The models served as an efficient method to quickly explore a range of assay parameters, including flow rates, device dimensions, and analyte concentrations. The model results complemented the primary experimental method – SPR-imaging – in that the models gave insight not only into the binding of the analyte to the surface, but also into the concentration profile of the analyte in the microchannel. Chapter 5 describes the development of a computational model of a generic assay format – the binding of a

protein, streptavidin, to its immobilized ligand, biotin. Experiments were completed to assess the validity of the model. A computational model of an indirect immunoassay is detailed in Chapter 6. Chapter 7 details the computational model for a novel immunoassay developed by Dr. Kjell Nelson, the CGIA.[15]

In Chapter 8, a herringbone microchannel – a microfluidic geometry proven to mix solutions in the bulk of the microchannel[16] – was incorporated in a microfluidic flow assay to assess whether the geometry would improve the performance of a generic microfluidic assay format. Experiments and computational simulations were completed. All relevant background information for this research can be found in Chapter 2.

Chapter 2: Background and significance

2.1 Microfluidics

Significance and potential

A microfluidic device has channels with at least one dimension greater or equal to one micron but less than one millimeter. Microfluidic technology has been applied in the research and development of a number of fields including single cell studies,[17] cell and protein patterning,[17-19] tissue engineering,[20, 21] chemical and medical diagnostics,[8, 9, 22-27] and chemical synthesis[28, 29] to name a few. Some advantages[30] associated with using microfluidic devices over traditional laboratory equipment include a reduction in the sample and reagent volumes required to carry out a particular process, a reduction in the size of the equipment, and a reduction in the amount of waste generated.

Given these advantages, a major goal in microfluidics is to develop a lab-on-a-chip (LOC) in which several laboratory operations are integrated onto a single microfluidic device. The LOC concept has been promoted particularly in the area of medical diagnostics.[31] Large centralized hospital labs typically carry out these assays which may require several milliliters of blood, urine, or another biological sample. Often, several types of laboratory equipment are required to complete the tests, and it may be many days before the patient and doctors receive the test results.

Microfluidic technologies have the potential to change the medical diagnostic paradigm by bringing the test to the patient in what is termed a point-of-care (POC) diagnostic. The motivation of this work is to develop portable, rapid, easy-to-use, affordable assays capable of monitoring more than one analyte. Microfluidic technology fits into the vision of POC diagnostics by reducing the volume of the sample required from the patient, reducing the size of the analytical instrumentation equipment, and integrating several processes onto a single device. Microfluidic devices, particularly those made from

plastic, could potentially be mass-produced resulting in affordable and disposable products.

The concept of POC diagnostics is not new. Portable home glucose monitors are readily available to diabetics[32] and illustrate how POC diagnostics can greatly improve health care. The unique aspects of the POC diagnostic for which the majority of work in this proposal was completed are that it analyzes saliva from patients and will simultaneously quantify multiple analytes. By multiplexing the assay and using a minimally invasive sample, this technology would represent a significant advancement in the development of POC medical diagnostics.

Microfluidic Assays

One area of microfluidic medical diagnostic research focuses on the development of microfluidic immunoassays. Immunoassays are tests that use antibodies to identify and quantify molecules (analytes) of interest known as analytes. Antibodies, 150 kDa proteins produced by the immune system, specifically bind to an antigen (Figure 2). Antibodies recognize a variety of antigens including proteins, peptides, and small organic molecules.[33, 34] The ability of an antibody to recognize a range of molecules coupled with the commercial mass-production of antibodies has enabled immunoassays to become a platform diagnostic technology with an important role in medicine as well as for detection of agents of chemical and biological warfare. In traditional assay formats, such as the ELISA,[35, 36] antibodies are an integral part of the assay. ELISAs typically take several hours to overnight to perform, and the assay is conducted at pseudo-equilibrium time points. By carrying out immunoassays in a microfluidic format, all of the aforementioned benefits associated with the smaller size scale are gained.

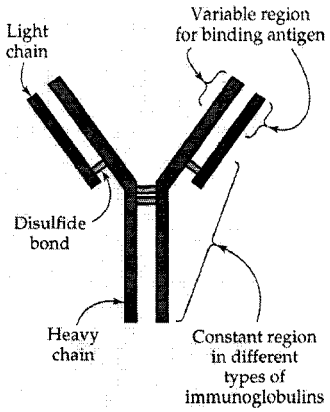

Figure 2. Structure of an antibody.[34] An antibody contains two antigen binding sites and is composed of heavy and light chains. The antigen-binding sites are located at the variable regions (Fab portion of the molecule). The ability to specifically recognize antigen molecules has made antibodies an essential tool in diagnostics. Image reproduced from the cited reference.

Another protein molecule often incorporated in microfluidic assays is streptavidin (Figure 3). Streptavidin has one of the highest measured affinities (~1.8×10^{13} M^{-1})[37] for its ligand, the small molecule biotin.[38, 39] Streptavidin is a 60 kDa tetrameric protein and has four binding sites for biotin. Given the strength of the streptavidin-biotin affinity, these molecules are frequently used in a number of life science applications which include purification, labeling, and diagnostics.[40-43] For the purpose of this thesis, the streptavidin-biotin system will serve as proof of principle for a new assay format.

A

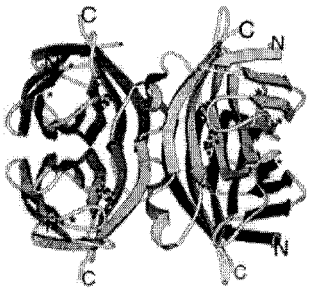

B

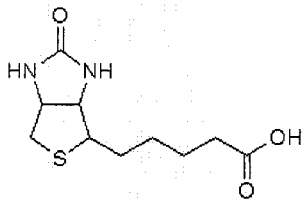

Figure 3. Structures of (A) streptavidin[44] and (B) biotin. (A) Cartoon of streptavidin with biotin binding sites. (A) is reproduced from the cited reference. Streptavidin is a 60 kDa tetrameric protein which has four binding pockets for the small molecule biotin. The affinity between SA/biotin is one of the highest affinity protein-ligand interactions known.

Microfluidic Flow Assays

A common microfluidic immunoassay format is shown in (Figure 1) and for the purpose of this dissertation is termed "the flow assay." In this assay format, the surface of a microchannel is functionalized with a capture molecule that will bind to a molecule (analyte) from a solution. Flow assays can be qualitative or quantitative and may be coupled to a variety of detection methods including fluorescence and colorimetric methods.[26, 45, 46] Because molecules bind to a surface, this assay format is also particularly conducive to surface sensitive detection methods and will be the primary assay format explored in this research.

Diffusion Immunoassay

The T-sensor device (Figure 3),[47-49] patented by the Yager group[50] and used in the development of a patented immunoassay,[51] takes advantage of the fluid flow properties that often characterize microfluidic devices.

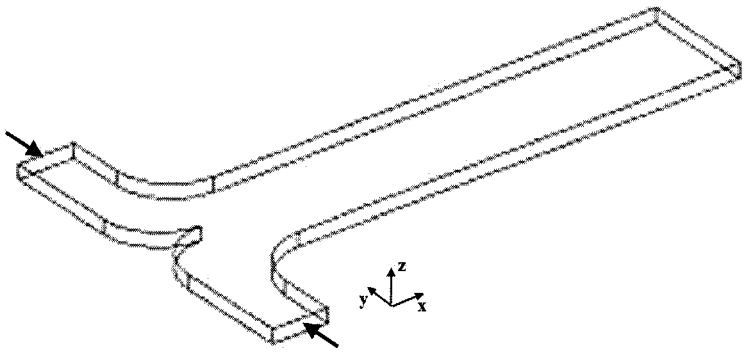

Figure 4. T-sensor. Microfluidic device to which two fluid streams are introduced (indicated by the arrows) and exit the device with one outlet.

The Reynolds number (Equation 1) is a non-dimensional parameter describing the influence of viscous forces versus inertial forces.[52, 53]

$$\mathrm{Re} = \frac{\rho u x_s}{\mu} \qquad \text{Equation 1}$$

where μ represents the viscosity of the fluid, ρ represents the density of the fluid, u_s represents the characteristic velocity, and x_s represents the characteristic dimension.

Given the small characteristic dimensions of microfluidic devices and relatively low flow rates, the Reynolds number is often <1 indicating that viscous rather than inertial forces dominate. Under these flow conditions – termed "laminar flow" – the fluid moves as if it were a series of layers – or laminae – that do not cross.[52, 53] In this flow regime, a well-characterized velocity profile – a parabolic velocity profile – for fluids in a rectangular duct (Figure 5) exists.

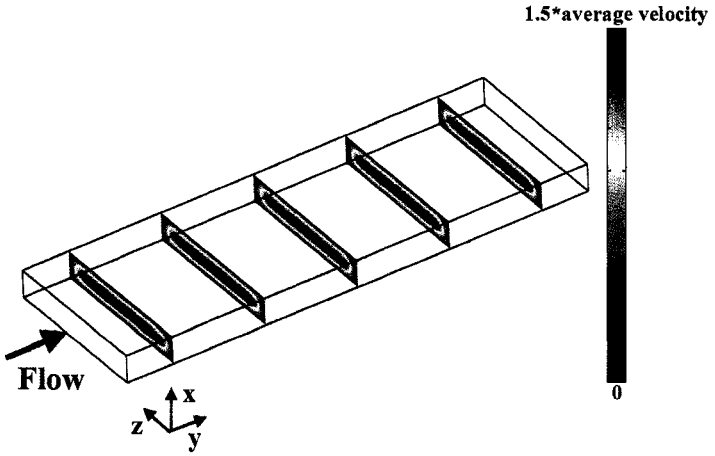

Figure 5. Velocity profile under laminar flow conditions for a rectangular duct microchannel. The computational model results illustrate the parabolic velocity profile. The velocity ranges from zero to 1.5×(average velocity).

The velocity at the walls is zero and the maximal velocity occurs at the center of the device. Because the fluid streamlines do not cross, mixing between fluid streams occurs solely due to diffusion. Given the properties of laminar flow, when two fluid streams are introduced to the T-sensor, mixing occurs at the fluid/fluid interface.

The Yager group developed a microfluidic immunoassay, the diffusion immunoassay (DIA), which takes advantage of the predictable mixing properties in low Reynolds number flows.[54] In one stream of the device, a sample with an analyte of interest is introduced. In the other stream, an antibody recognizing that antigen is introduced (Figure 6A). If no antibody is present in the adjacent stream, the antigen freely diffuses into the next channel (Figure 6B) as the solutions stream flow down the length of the device. When antibody is present, the antibody will bind to the antigen. The antibody-

antigen complex has a smaller diffusion coefficient than the free antigen and therefore the antigen bound to the antibody will be more concentrated at the fluid/fluid interface than the free antigen (Figure 6B). Depending on the concentration of the antigen in solution relative to the concentration of antibody, the amount of antibody-antigen complex will vary.

A *B*

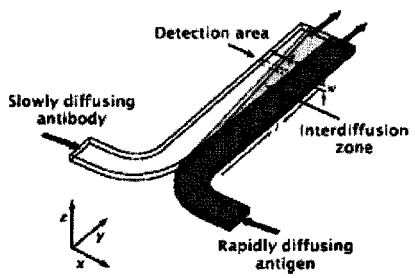

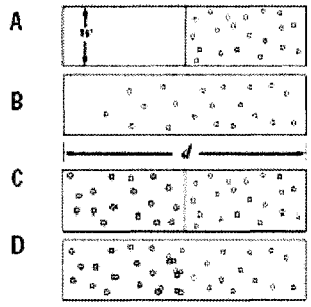

C

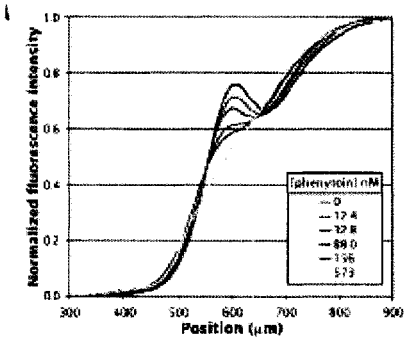

Figure 6. DIA[54] (A) Solutions of antibody and antigen (sample analyte and fluorescently labeled analyte spiked into the sample) are introduced to a T-sensor. Under conditions of laminar flow, the antigen and antibody mix and react in the microchannel. The concentration profile (x dimension) of the fluorescently labeled analyte is taken at the detection zone. (B) Cross-sectional cartoon of the distribution of analyte at the inlet and the detection zone (*A* and *B*) and the distribution of the analyte in the microchannel when antibody is presented in the adjacent stream (*C* and *D*). (C) The concentration profile across the width of the channel (x dimension) of the fluorescently labeled analyte at the detection zone. This profile quantitatively relates to the amount of sample analyte (unlabeled analyte) in the stream. The images were reproduced from the cited reference.

To create an assay capable of measuring the amount of antigen in the sample solution, a known quantity of fluorescently labeled antigen is introduced to the sample stream. This fluorescently labeled antigen competes with the unlabeled antigen in the sample to bind to the antibody. At very high concentrations of antigen in the sample (unlabeled antigen),

most of the antibody binds to the unlabeled antigen enabling the unbound labeled antigen to freely diffuse into the adjacent stream. At low concentrations of antigen in the sample (unlabeled antigen), most of the antibody binds to the labeled antigen thereby concentrating it at the fluid/fluid interface (Figure 6C). By analyzing the concentration profiles of the fluorescently labeled antigen across the width of the channel ("x" dimension), the amount of antigen in the sample can be quantified.

An important design parameter in this assay is the diffusion coefficient of the analyte relative to the diffusion coefficient of the antibody. The concentration profile of the labeled antigen is most significantly modulated when there is large difference between the diffusion coefficient for the antigen and the diffusion coefficient for the antibody-antigen complex. Dr. Ken Hawkins has been exploring the utility of the DIA to measure high molecular weight analytes such as proteins. The work has shown that the ability to measure slow diffusing analytes is a challenge. Therefore, the DIA is better suited to quantify fast-diffusing analytes.

Concentration Gradient Immunoassay

A modified version of the DIA, the concentration gradient immunoassay (CGIA), was invented by Dr. Kjell Nelson.[15, 55] As in the DIA, two fluid streams are introduced to the device – one contains the sample with a fast diffusing analyte and the second contains an antibody to the analyte (Figure 7).

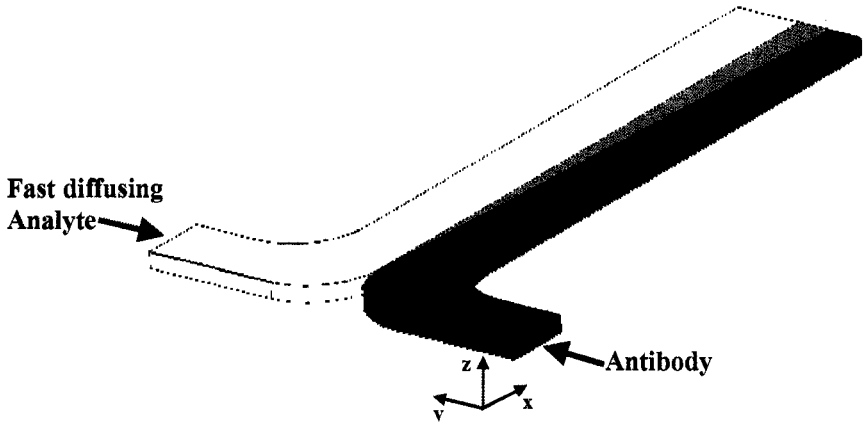

Figure 7. DIA. A solution of antibody and a sample containing a fast-diffusing analyte are introduced to a T-sensor. Due to the laminar flow conditions, the solutions mix by diffusion at the interface of the streams. As they travel downstream and mix, the analyte and antibody bind giving rise to complex (green). The complex formation is biased to the side of the channel the antibody was introduced due to the relative difference in the diffusion coefficients for the analyte and antibody.

In solution, the antibody and antigen bind at the interface of the fluid streams. The amount of complex generated for a given concentration of antibody depends on the concentration of antigen in the sample. At a region several millimeters downstream of the channel inlet (~22 mm), a surface of the device is functionalized with immobilized antigen. This surface binds the free antibody in solution. The signal for this assay is generated by the change in the mass at the surface of the binding region (Figure 8) due to the binding of the free antibody.

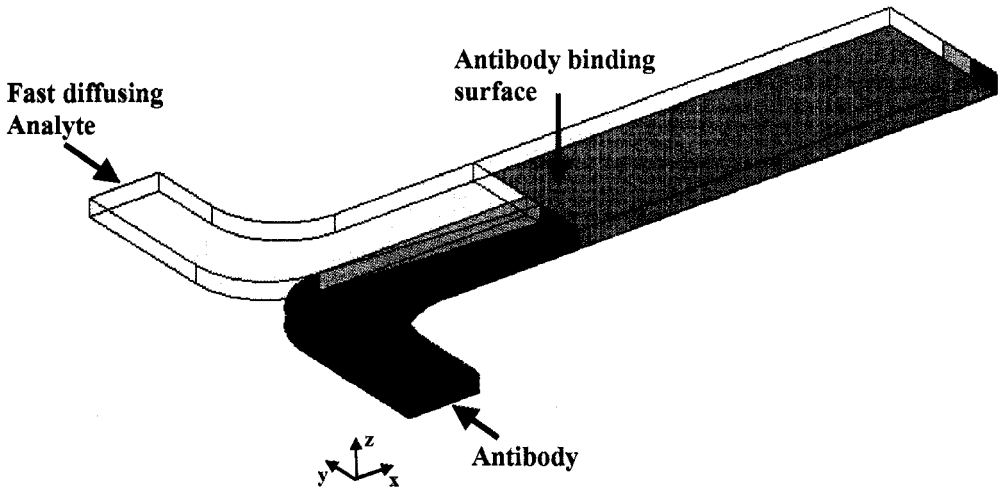

Figure 8. Diagram of the CGIA. This assay extends the DIA (Figure 6) by incorporating a surface with immobilized antigen. Antibody that is not bound to an analyte could bind to the surface. The amount of antibody bound to the surface inversely relates to the amount of analyte in solution.

Because the amount of free antibody depends on the amount of antigen in the sample, the total amount of antibody bound as well as the surface profile of the binding could potentially be used to quantify the amount of antigen. This has been proven experimentally and explored with a computational model in Chapter 7.

Microfluidic Mixers

The fluid flow properties in microfluidic devices generally fall within the laminar flow regime. Although the T-sensor described above takes advantage of the properties of laminar flow, many lab-on-a-chip applications require that the fluid streams are mixed. However, at low Reynolds number, mixing occurs due to diffusion which depending on the geometry of the device could be a slow process. To reduce the time scale required to mix fluid streams, several different device geometries have been explored.[16, 56, 57] Often, the purpose of these geometries is to either impose a secondary flow to increase mixing, divide and recombine the fluid streams into thin strips to reduce the diffusion length, or generate fluid flow patterns in which inertial effects become more significant than if the channel geometry were a rectangular duct.

Staggered Herringbone Microfluidic Mixer

One microfluidic mixer geometry, the staggered herringbone microfluidic mixer (Figure 9) first presented by Whitesides et al.,[16] was designed to impose a secondary flow that would circulate the flow perpendicular to the overall flow trajectory. When oblique rectangular structures are place on a straight microchannel the pressure fields on the fluid are altered generating a slowly rotating velocity field (Figure 9A) In the staggered herringbone geometry (Figure 9B) two spiraling flows (clockwise and counter-clockwise) on either side of the herringbone point are created. By imposing two circulating streams, it was shown that the total time to achieve full mixing was significantly reduced (Figure 9B and C).

A

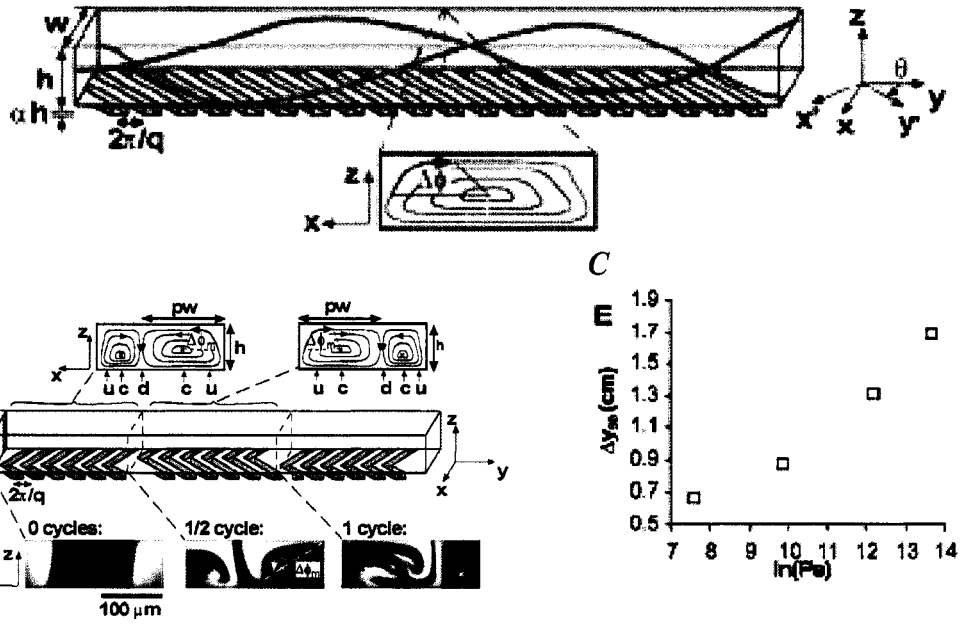

Figure 9. Staggered herringbone mixer.[16] (A) Influence of oblique microstructures above a microchannel on the velocity profile. (B) Diagram of a staggered herringbone microchannel. The grooves induce two circulations transverse to flow which serves to mix solutions in the bulk. A confocal fluorescence image of a fluorescein solution introduced to the device illustrates the mixing process. (C) Plot relating the position in the microchannel (y dimension) at which the fluorescein solutions were ninety percent mixed as a function of the log of the Peclet number. The Peclet numbers ranged from ~1000 to ~ 20,000. The images were reproduced from the cited reference.

In Chapter 8, the influence of the chevron mixer microchannel in a microfluidic assay will be explored to determine its impact on the performance of a microfluidic flow assay.

Microfluidic Device Fabrication

Numerous types of materials – glass, silicon wafers, and elastomers – and fabrication techniques – laser ablation, photolithography, electrodeposition and embossing – to name a few are used to fabricate microfluidic geometries.[58-63] In this research, two materials were used (1) the elastomer polydimethylsiloxane (PDMS) and (2) the plastic laminate – mylar (polyethylene terephthalate).

PDMS is an optically transparent, hydrophobic, elastomer permeable to oxygen which is often used in microfluidic research (Figure 10A and B).[60, 64] A process known as photolithography – a method in which light is exposed to a light-sensitive chemical, termed a photoresist – is often used in the fabrication process of PDMS microfluidics. Photoresists either polymerize (negative resist) upon exposure to light or are dissolved (positive resist) by the light. By exposing the photoresist through a mask some areas of the photoresist are exposed to light while others areas are not thereby allowing a pattern of resist to be generated on a substrate that can serve as a mold for a PDMS device.[64] In this research, the negative photoresist, SU8 (Microchem, Newton, MA), is spun on a

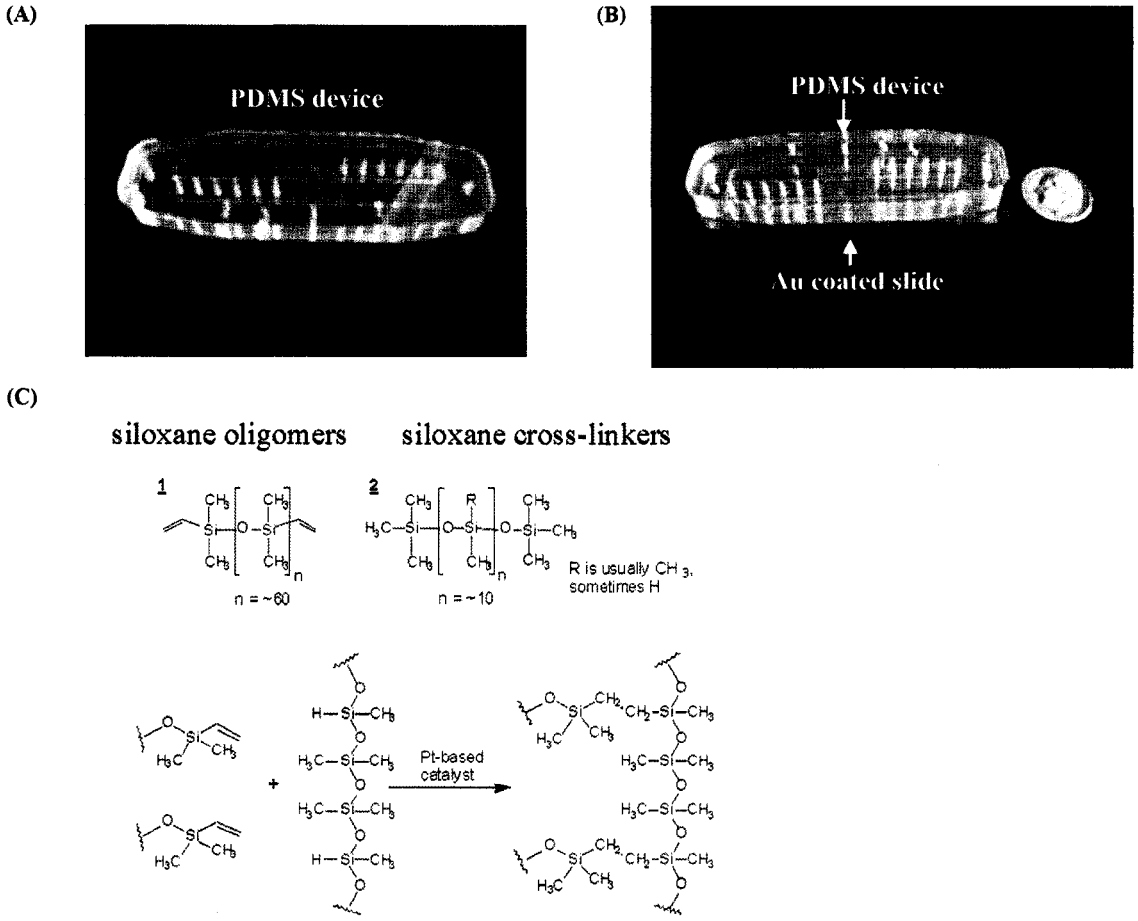

Figure 10. PDMS device. (A) PDMS microfluidic device fabrication using soft lithography. (B) PDMS/Au slide microfluidic device assembled. (C) PDMS chemical structure and reaction.[65] The image was reproduced from the cited reference. The devices depicted in (A) and (B) were constructed by Dr. Mark Blaylock.

wafer and exposed to UV light under a photomask to create mold onto which a solution of siloxane oligomers are poured (Figure 10C). The oligomers are then cross-linked as described by the reaction in Figure 10C. A benefit of using photolithography is that from one SU8 master, numerous PDMS microfluidic devices can be cast.

Other popular materials in microfluidic research are polymeric laminates – thin sheets of plastics.[66, 67] Advantages associated with using plastics are that they are affordable to manufacture and can be mass-produced; thereby making it a feasible possibility that disposable microfluidic devices can be produced in an affordable manner. The polymeric

laminates used in this research, mylar, are ablated with a carbon dioxide laser to create channels within the laminate (Figure 11B and C). Mylar coated with adhesive on both sides is commercially available (Fralock, CA). Once the laminates are cut they are stacked together and adhere to each other with the adhesives (Figure 11A).

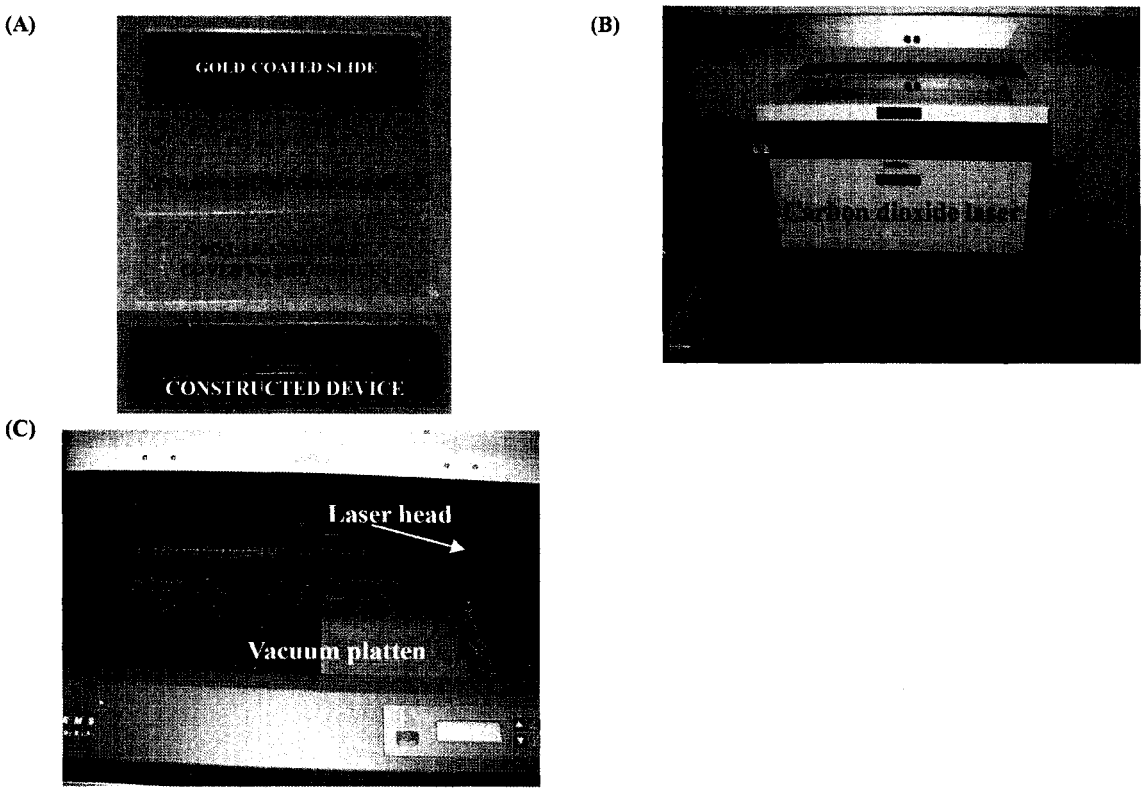

Figure 11. Mylar device fabrication. (A) Mylar polymeric laminates. The mylar with the microchannel has adhesive on both sides to adhere it to the other laminate and the gold-coated glass slide. (B)-(C) Carbon dioxide laser to manufacture device.

Computational modeling of microfluidic systems

An important tool in the development and design of microfluidic assays is computational modeling. Computational models assist in the rational design of a device and aid in the understanding of the physical processes which occur inside the microchannel. They also serve as an efficient tool to optimize and improve the sensitivity of an assay. In this dissertation, the primary experimental method, SPR imaging, only monitors the microchannel very near the surface. On the other hand, the computational models give insight into the physical processes occurring throughout the microchannel.

The Finite Element Method

A commercially-available finite element method software, COMSOL®, (Comsol, Inc. Uppsala, Sweden) was used to model microfluidic assays. The exact details of the COMSOL operating protocols are not available due to proprietary concerns. However, the finite element method is well-documented and developed computational method and often a weighted residual method – such as the Galerkin method – is used to solve finite element problems.[68]

Briefly, when the finite element method is employed, the geometry of the model system is drawn and then divided into discrete elements in a process known as meshing. Approximate solutions to the partial differential equations governing each element are determined. The coefficients to approximate the solution can be determined with the Galerkin method. The approximate solution to a problem could be defined as: [68]

$$\theta(x) = \theta_0 + \sum_{i=0}^{N} c_i \alpha_i(x) \qquad \text{Equation 2}$$

where c_j and α_j represent undetermined coefficients and trial functions respectively. A linear operator such that the exact solution is zero is applied to the approximate solution yielding the residual R. The $c_j s$ can be determined using the following equation: [68]

$$\int W_k R(x) dx = 0 \qquad \text{Equation 3}$$

where W_k is a set of weighted functions.

Governing equations of microfluidic systems

The following equations were employed to model microfluidic assays. The equations were derived from chemical engineering textbooks[52, 53] and modified for the particular application based on discussions with Prof. Bruce Finlayson.

The Navier-Stokes Equation

The Navier-Stokes equation expresses the conservation of momentum. Solving this equation in COMSOL® yields the fluid flow properties in the microfluidic device such as the velocity profile in the microchannel and the fluid streamlines.

When the influence of gravity is negligible as is the case with the models explored in this proposal, the equation reduces to:

$$\rho\frac{\partial \mathbf{u}}{\partial t}+\rho\mathbf{u}\bullet\nabla\mathbf{u}=-\nabla p+\mu\nabla^2\mathbf{u} \qquad \text{Equation 4}$$

where $\boldsymbol{u}$ is the fluid velocity, p is the pressure, ρ is the density of the fluid, μ is the viscosity of the fluid, and t is time.

Conservation of Mass

The Navier-Stokes equation and the conservation of mass are typically solved simultaneously. In this proposal, we will only study incompressible fluids in which, ρ, the density of the fluid, is constant. The expression of the conservation of mass for an incompressible fluid is below.

$$\nabla\bullet\mathbf{u}=0 \qquad \text{Equation 5}$$

The Convection-Diffusion Equations

The convection-diffusion equation describes the conservation of chemical species in a system. When the solution to the Navier-Stokes equation is coupled to this equation in

COMSOL®, the concentration profiles of reacting and non-reacting species in a microchannel with fluid flow can be determined.

$$\frac{\partial c}{\partial t} + \nabla \bullet (-D\nabla c + c\mathbf{u}) = R \qquad \text{Equation 6}$$

where **u** is the fluid velocity, c is the concentration of the chemical species, D is the diffusion coefficient of the chemical species, R is the rate of production of the chemical species, and t is time.

2.2 Surface Plasmon Resonance

Significance and potential

Surface plasmon resonance (SPR) is an optical detection method that measures changes in refractive index near a surface.[14] This surface sensitive detection method is conducive to the microfluidic flow assay format described in 2.1, and quantitative SPR microfluidic assays have been reported in the literature.[1-11] With SPR, measurements can be collected in real-time and have been shown to yield kinetic information on the binding of biological species.

SPR has several advantages over other optical detection methods – in particular fluorescence. It does not require any components of the system to be labeled, and the instrumentation is relatively simple and inexpensive. Given these advantages as well as the potential to develop quantitative microfluidic assays, there have been increased efforts – including the work in this dissertation – to develop affordable point-of-care SPR instruments.

Surface plasmon resonance

In SPR, polarized light reaches a metal surface under conditions of total internal reflection creating an evanescent electric field at the interface of the metal and a dielectric. The evanescent field can interact with the free electron clouds in the metal generating plasmons – charge oscillations. When the energy from the incident field is

transferred to the plasmons in the metal thereby reducing the intensity of the light reflected off the metal surface, resonant conditions have been achieved.[14, 69-71] For the plasmons to be excited, energy and momentum must be conserved. Therefore, not only the energy of the incident light but also the incident angle at which it strikes the gold surface, determine if plasmons can be excited. Based on the principles of the conservation of energy and momentum, instruments can be designed to either keep the incident angle constant and alter the wavelength of light or keep the wavelength of light constant and alter the incident angle.

The condition at which resonance occurs depends on several factors including the dielectric constant of the media at and near the gold surface. The dielectric constant relates to the square root of the refractive index of the media. If the refractive index changes at the surface of the metal, the resonance conditions are altered. This change in refractive index at a surface correlates with a change in mass at the surface. By monitoring the light reflected off the metal substrate, it can be determined whether the refractive index (i.e. amount of mass at the surface) has been altered at or very near the surface of the metal (Figure 12).[14, 69-72]

Due to the evanescent nature of the electric field, the contribution to the signal is strongest at the metal surface and exponentially falls as the distance from the surface increases. The surface-sensitivity of this detection method makes it conducive to microfluidic flow immunoassays described in Section 2.1 in which molecules from solution bind to capture molecules immobilized to a surface, thereby altering the resonance conditions. SPR immunoassays have been reported in the literature and have been shown to quantitatively measure analytes. Numerous research groups have built SPR instruments. Several commercially available SPR instruments are also available from Biacore (Uppsala, Sweden) and Texas Instruments (Spreeta).

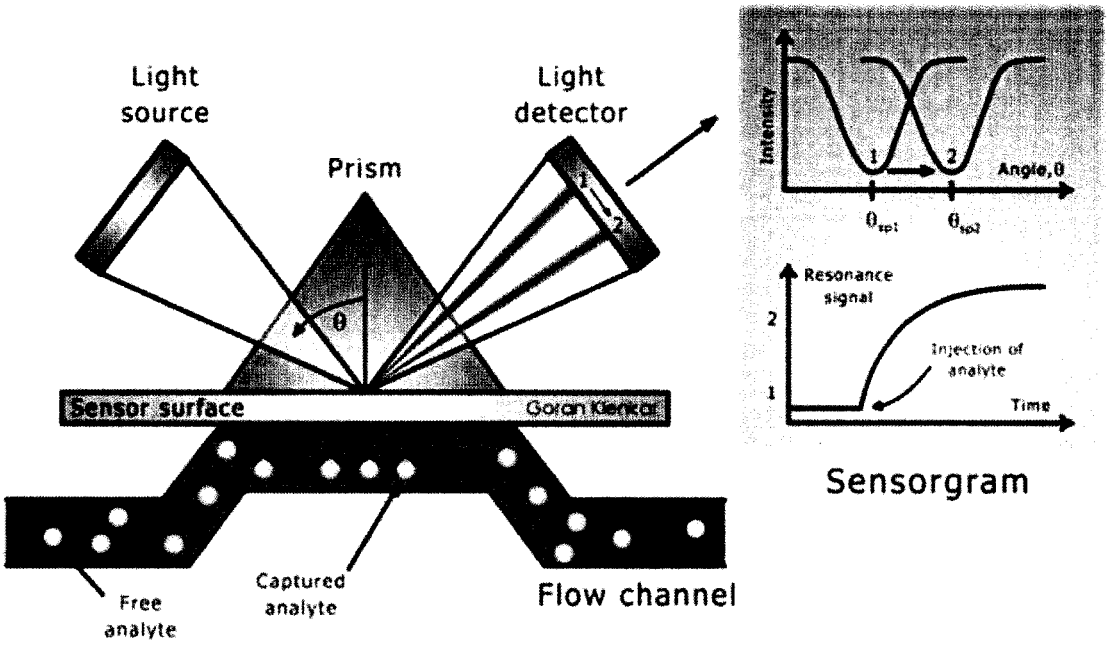

Figure 12. Principles of a surface plasmon resonance immunoassay in an angle dependent system. Polarized light is incident on a prism and a gold surface. On the gold surface, an antibody is immobilized to which the analyte will bind. The incident light is reflected from the sensor surface and collected by a spectrophotometer. As analyte is flowed across the sensor surface and binds to the antibody, the local refractive index changes at the surface and shifts the angle at which resonance occurs from theta 1 to theta 2 (upper inset). This shift can be monitored over time (lower inset) and may be used to quantify the amount of analyte in a sample. The image was copied from http://www.ifm.liu.se/applphys/sensor/bilder/SPR_schem2.jpg

Surface plasmon resonance microscopy

In traditional SPR, the signal represents the average refractive index over an entire area as a function of wavelength or the incident angle (Figure 12). In surface plamson resonance microscopy (SPRM), also referred to as SPR-imaging, the output is a grey-scale image in which the local refractive index (Figure 13) can be determined by the intensity of the signal in different regions of the image. Unlike traditional SPR with only a single output, multiple regions can be monitored simultaneously with SPR microscope. SPR imaging assays can detect and quantify multiple analytes, assuming the surface is functionalized with multiple capture molecules.

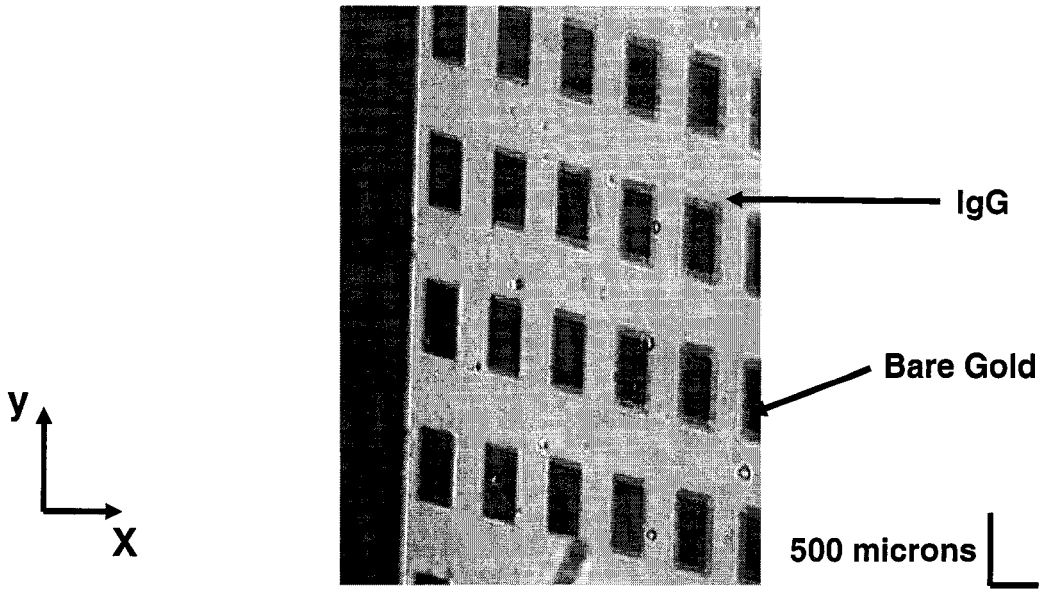

Figure 13. SPR Image. An image of protein printed on a gold surface. The different intensities of light indicate different local refractive indexes at the gold surface. The background solution is a PBS buffer.

Given the ability to multiplex assays, a number of research teams[1, 3, 73-75] including the Yager group have built SPR imaging systems. Since 2001, Dr. Elain Fu built and characterized this instrument.[13] A major portion of my initial work on this project contributed to the characterization of the SPR imaging system and two articles have been published on its development.

1. Fu, E., Foley, J., and Yager, P. (2003). "Wavelength-tunable surface plasmon resonance microscope." *Review of Scientific Instruments*. **74**: 3182.

2. Fu, E., Chinowsky, T., Foley, J., Weinstein, J. and Yager, P. (2004). "Characterization of a wavelength -tunable surface plasmon resonance microscope." *Review of Scientific Instruments*. **75**: 2300.

The instrument shown in Figure 14 was designed to scan wavelengths of light while keeping the incident angle constant. The instrument was constructed in the Kretschmann geometry. The source is a halogen lamp. An interference filter selects the incident wavelength. As the interference filter is tilted from the normal to the incident light, the

light is blue shifted (Figure 15) thereby enabling a range of wavelengths to be quickly scanned. The advantage of this design over angle-scanning instruments which require bulky mechanical parts to alter the angle of incidence is that it is a relatively compact design that is amenable to the development of a portable device. For improved sensitivity, the incident wavelengths chosen are in the near infrared.[76] (Interference filters for 880 nm and 905 nm have been used). The substrates are gold-coated glass microscope slides, and a CCD camera collects the light reflected from the prism. (Note: For a detailed description of the instrument please refer to Chapter 3.4)

A

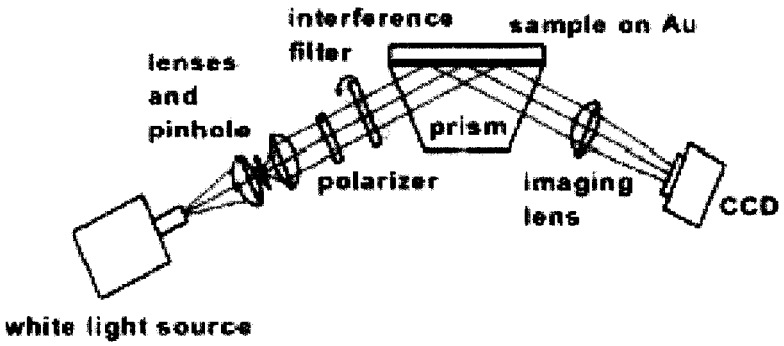

B

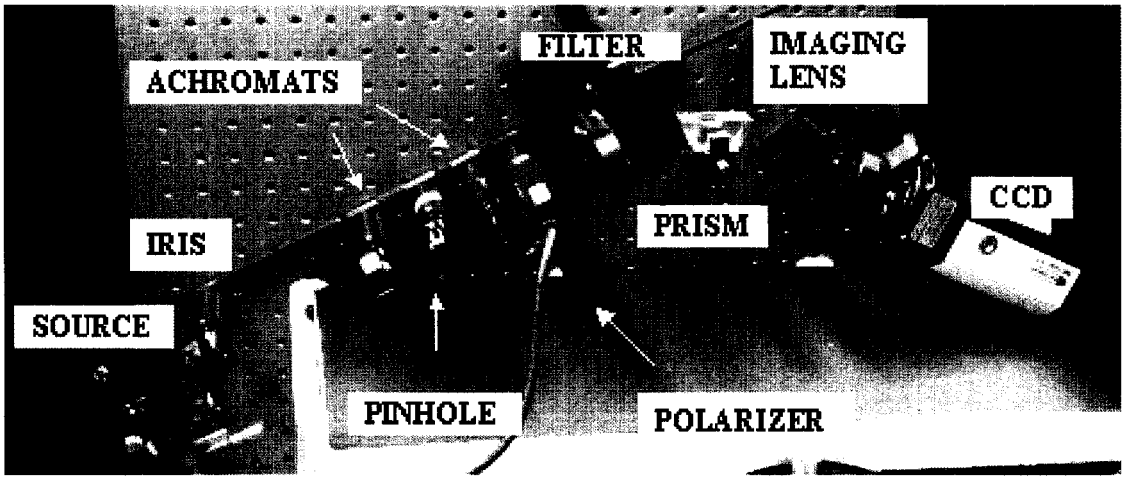

Figure 14. SPR microscope[13] (A) Diagram of the wave-length tunable SPRM. The interference filter positioned immediately before the prism when tilted blue-shifts the light.[13] The images were reproduced from Fu et al. (2003). (B) Photograph of the SPRM courtesy of Dr. Elain Fu.

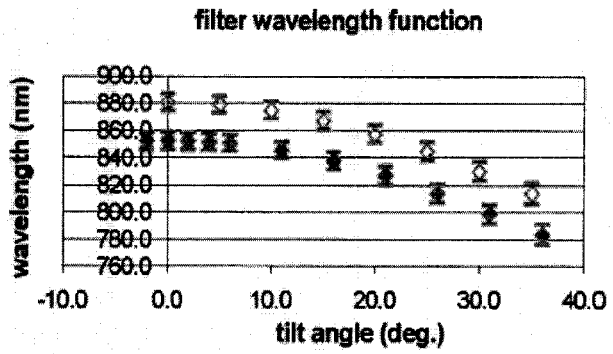

Figure 15. Wavelength tunability of an interference filter. [13] Wavelength of light selected to pass through an interference filter as a function of tilt angle. The data for an 850 nm and an 880 nm interference filter are presented. The tilt angle represents the angle the filter is positioned from normal incidence with the light source. The image was reproduced from the cited reference.

2.3 Surface Patterning

Significance

Producing well-defined and uniform patterns of molecules on surfaces – in particular antibodies or antigens – is an essential component of the microfluidic flow assays presented in this dissertation. Patterning surfaces with molecules is also important in a variety of other research areas including tissue engineering, DNA microarrays, chemical sensors, and cell assays to name a few. Due to this interest, a large body of research has explored methods to pattern surfaces with molecules from DNA to proteins to lipids to alkanethiols. For the purpose of this research, we will focus on methods to pattern two types of molecules – self-assembled monolayers and proteins.

Self-Assembled Monolayers

Self-assembled monolayers (SAMs) (Figure 16) are "ordered molecular assemblies formed by the adsorption of an active surfactant on a solid surface."[77] Chemical interaction of the head group and the surface as well as inter-molecular interactions drive the formation of SAMs. SAM formation is relatively simple and typically requires the

incubation of a substrate in a dilute solution of the surfactant. The highly-ordered crystalline nature of SAMs enables the study of precise surface chemistries. The introduction of different tail groups to the SAMs permits the exploration of a variety of surface properties.[77-79]

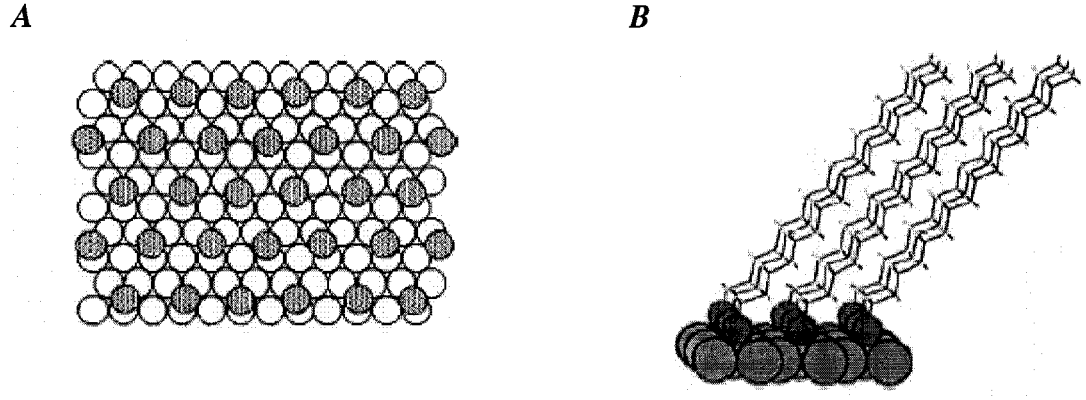

Figure 16. Structure and order of self-assembled monolayers on gold.[77] (A) A cross-sectional view of the chemical structure of hexadecanethiol monolayers on Au(111) determined by a computational model. (B) A top-down view of the orientation of the sulfur atoms (shaded) on Au (111) (open circles). The images were reproduced from the cited reference.

Many thiol-terminated molecules have been shown to form SAMs on gold. Alkanethiols in particular have been studied extensively. The alkanethiol monolayers typically have thicknesses on the order of nanometers. Although the exact nature of the thiol-gold interaction is unknown and under investigation,[80-82] research indicates that the longer the alkane chain, the more stable and well-ordered the monolayer. It is hypothesized that this stability arises from increased inter-molecular van der Waals interactions. The need for increased van der Waals interactions also has been suggested to induce a tilt from normal to the surface in the SAMs structure.[77, 83, 84] Several different terminal groups have been introduced to alkanethiols to explore different engineered surfaces. These chemistries include carboxyls, hydroxyls, ethylene glycols, and biotins.[85-89] Generally, the introduction of a terminal group has been associated with a reduction in the order and stability of the SAM and careful attention must be given to characterize these SAM systems.[79, 83, 84, 86, 87, 90-93]

Given the ease of assembly and well-characterized behavior, SAMs – in particular polyethylene glycol terminated thiols (HS-PEG) – have been used extensively in sensor technologies which require the functionalization of a gold surface such as SPR. Ethylene glycol is neutral and hydrophilic moiety. Research suggests that the water of hydration at a HS-PEG surface serve to "shield" it from proteins thereby significantly reducing non-specific adsorption.[85, 94-100] Resistance to non-specific adsorption would reduce the background and improve the sensitivity of an assay.

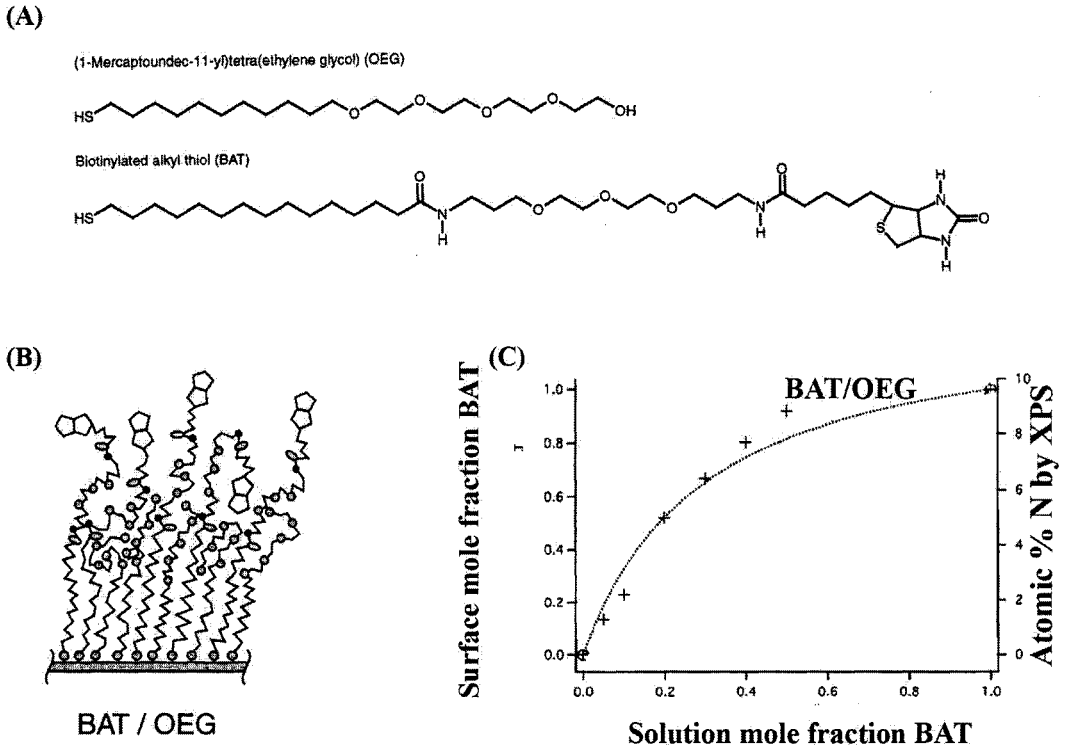

Figure 17. Mixed biotinylated alkyl thiol (BAT)/ oligoethylene glycol (OEG) thiol.[88] (A) Chemical structures of the thiol molecules. (B) Cartoon depicting structure of mixed thiol layer on a gold surface. (C) Graph relating solution mole fraction of BAT and surface mole fraction BAT based on XPS measurements assessing atomic percentage of nitrogen in the sample. The optimal binding profile was determined to be a solution with a 0.1mole fraction of BAT for a solution with a total of 0.1 mM thiols in ethanol. The images were modified from the cited reference.

Thiol systems have also been developed to immobilize biotin molecules to the surface (Figure 17B and Figure 18A) and bind the protein streptavidin from solution.[88, 89, 101] The mixed thiol system developed and characterized by Jung et al.[88] and Nelson et al.[101] used in this research incorporates a thiol with a biotin group at the terminus (Figure 17A) and an OEG (oligoethylene glycol) thiol (Figure 17A) to reduce non-specific adsorption of

protein to the surface. The amount of BAT thiol in solution during the deposition of the thiol onto the surface did not relate linearly to the amount bound to the surface (Figure 17C). The research by Nelson et al.[101] indicated that a surface concentration of BAT at ~20% bound the highest concentration of streptavidin to the surface from solution (Figure 18B).

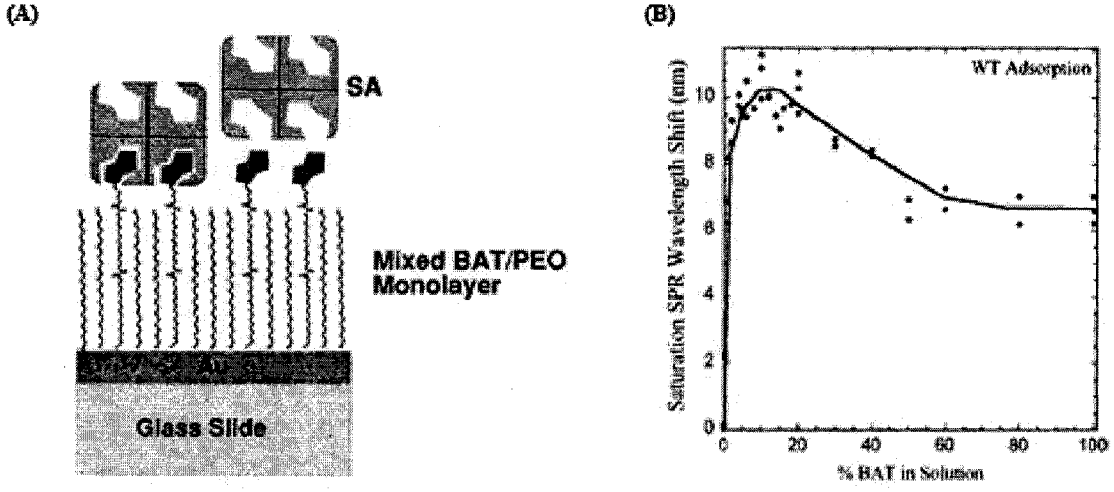

Figure 18. Streptavidin binding properties of mixed biotinylated alkyl thiol (BAT)/ polyethylene oxide (PEO) thiol layers on gold.[101] (A) Cartoon of streptavidin (SA) binding to mixed BAT/PEO thiols on a gold-coated slide. (B) SPR binding profile of SA to mixed thiols on gold for wildtype (WT) SA as a function of BAT percentage of total thiol in solution where the total thiol concentration is 0.1 mM. The images were reproduced from the cited reference.

Current patterning techniques

A number of methods to pattern surfaces with molecules – in particular SAMs and proteins – have been developed. Physical adsorption of proteins and SAMs onto surfaces is the most conventional method. For proteins, the exact nature of the binding interaction is non-specific and the interactions vary from protein to protein and surface to surface. Proteins have been deposited from microfluidic channels onto surfaces to generate micron-scale patterns (Figure 19). By introducing a different protein to each microchannel, multiple proteins may be patterned simultaneously on a surface.[64, 102, 103] Proteins may also be covalently linked to an activated surface via amines, thiols and carboxyls present on proteins.[104] Proteins immobilized to surfaces in this way could also be patterned by introducing them to a substrate in a microfluidic device. When using ultra-violet light (UV) activated chemistries, the surfaces may also be patterned using

photolithographic techniques in which a mask covers the substrates and selectively exposes it to UV thereby generating a pattern of immobilized proteins. Thiols and proteins have been patterned onto surfaces with UV methods.[105, 106] Unlike physical adsorption methods in which the proteins over time may release from the surface due to the non-specific interactions with the surface, covalent linkages ensure to a greater extent that the proteins will not be removed.

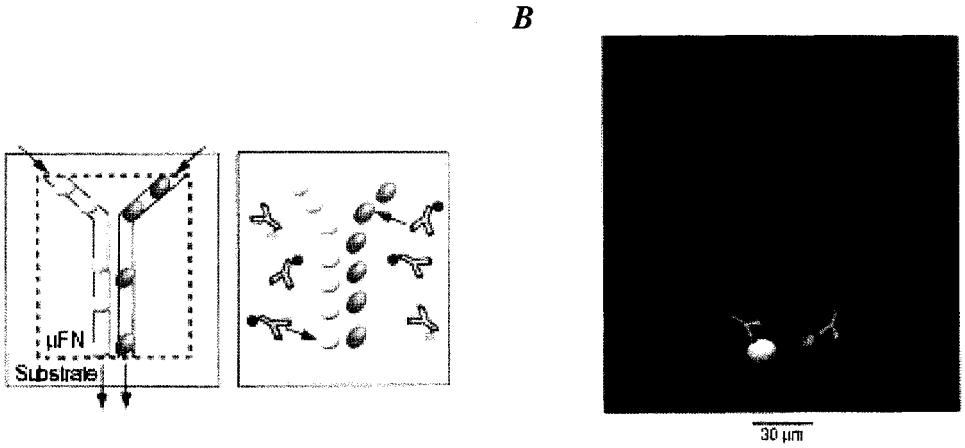

Figure 19. Patterning of proteins onto surfaces using multiple microchannels.[103] (A) Protein antigens are introduced to a microfluidic device and physically adsorb to a glass surface. (B) Fluorescently labeled antibodies recognize the immobilized antigens indicating the location of the proteins as well as the fact that the proteins retain some if not all of their structure. The images were reproduced from the cited references.

Dip pen nanolithography (DPN), pioneered by the Mirkin group (Figure 20), uses one or several cantilevers to pattern nanoscale features on planar surfaces. Molecules are transported and deposited onto the substrate via the water meniscus present at the cantilever tip. DPN can pattern a variety of molecules including proteins and SAMs. When multiple cantilevers and solutions are introduced, DPN may pattern multiple molecules onto a surface. However, this method has limited throughput (i.e., "writing" large areas of molecules takes time), depends on the relative humidity of the chamber, and requires expensive instrumentation. Ink-jet printing and pin-spotting methods create droplets with volumes on the order of tens of picoliters and deposit them onto a surface.[107-109] Inkjet technologies have been shown to print proteins and alkanethiols onto surfaces (Figure 21). The major concerns with these methods of patterning are the

uniformity of the spots due to drying effects, the wettability of the surface, and the thickness of the deposited films.[110, 111]

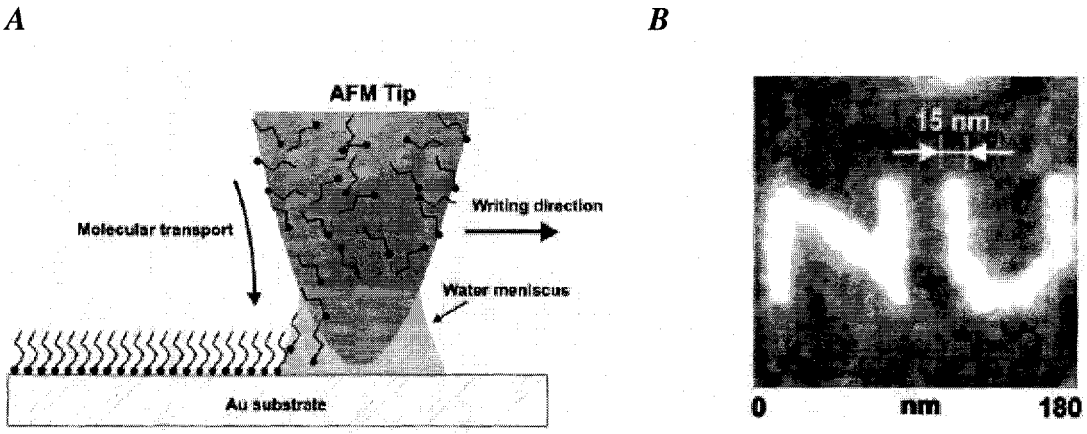

Figure 20. Dip pen nanolithography. (A) An AFM tip inked with an alkanethiol is drawn across a surface generating nanometer-sized patterns.[109] (B) AFM image of hexadecanethiol written onto a gold surface with DPN.[107] The images were reproduced from the cited references.

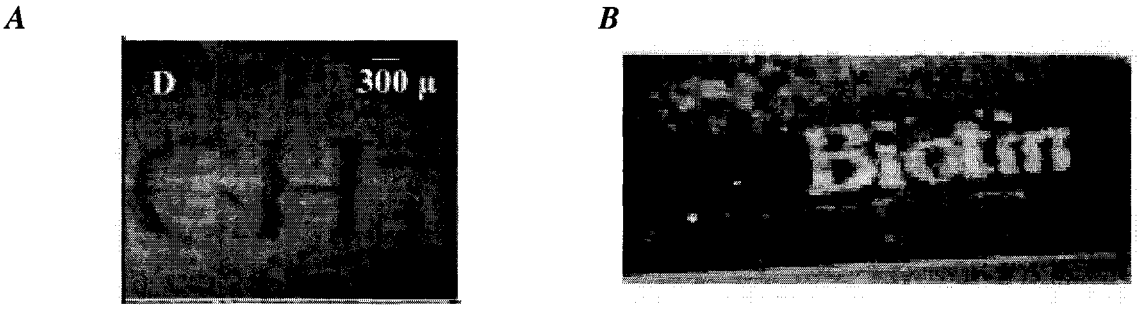

Figure 21. Inkjet printed molecules. (A) Condensation photograph of hexadecanethiol printed onto a gold surface and backfilled with mercaptohexadecanoic acid.[110] (B) Photographic image of BSA printed onto a glass surface.[111] The images were reproduced from the cited references.

Microcontact printing

Microcontact printing (μCP) will be the primary method to pattern surfaces with SAMs and proteins explored in this dissertation. In μCP, a concentrated solution of a thiol or protein is introduced to a poly(dimethylsiloxane) (PDMS)[65] stamp. The molecules non-specifically adsorb to the stamp. The stamp is rinsed, dried, and placed onto the substrate.[112-115] A monolayer of protein or thiols transfers from the stamp to the substrate. Homogeneous, sub-micron-sized patterns of proteins can be produced (Figure 22). The

patterned features have sharp edges and are uniform.[116, 117] The microcontact-printed proteins retain some of their activity in solution.[118] Multiple proteins may be patterned onto a surface by inking a flat PDMS stamp with several microfluidic channels.[113]

A

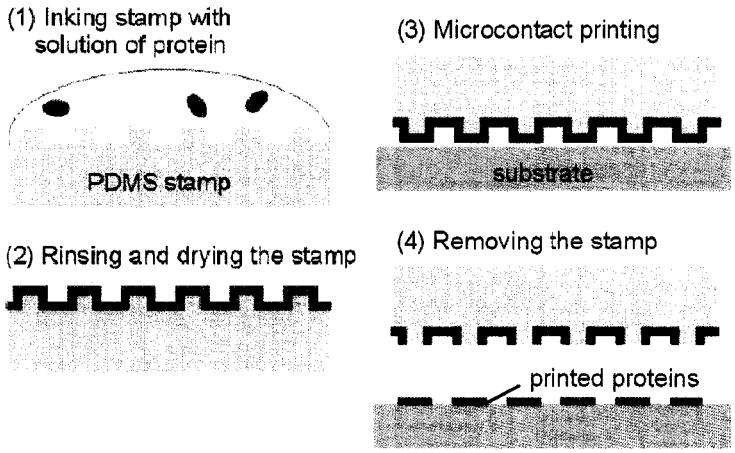

B

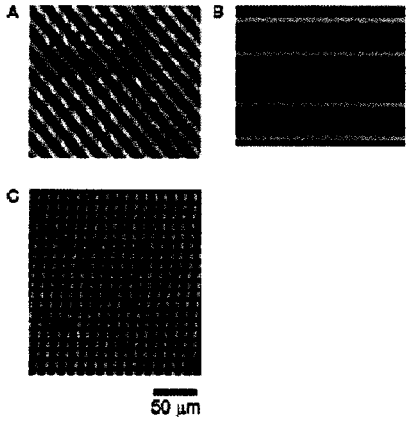

Figure 22. Microcontact printing proteins onto surfaces. (A) Procedure to microcontact print proteins on a surface.[115] (B) Fluorescently labeled protein printed on a glass slide.[119] The images were reproduced from the cited references.

Microcontact printing has several disadvantages. PDMS is a silicone polymer. Short oligomers are present in the PDMS stamp and have been shown to contaminate the substrate.[120-127] The oligomers may serve to reduce and/or interrupt the function of the printed protein. Several methods including solvent extraction,[120] UV/ozone treatment,[121] exposure to oxygen plasma,[124] and polymerizing the PDMS at an elevated temperature[125] have been shown to reduce the oligomer contamination, but no method completely

eliminates all oligomers from the substrate surface. There has also been shown to be a dependence on the type of ink as well as the pre-treatment of the PDMS stamp on the amount of silicone oligomers transferred to the substrate.[125, 128] The precise placement of the stamp onto a substrate is also difficult. In most protocols, the stamp is placed onto the surface with tweezers allowing for large error and the imprecise registration of the pattern on the substrate.

The physical process by which a protein, thiol, or cell transfers from the PDMS stamp to a surface is not completely understood. There are several mechanisms by which the molecules may transfer from the stamp to the surface – including vapor deposition, wicking from the recessed regions of a patterned stamp, and direct contact.[114] Some research suggests that it is the free energy of the surface versus the free energy of the stamp that determines if the molecule will transfer. Chen et al. microcontact printed proteins on a variety of self-assembled thiols on gold.[122] This work suggested that the more hydrophilic the substrate the more protein transferred. The authors suggest that increasing the wettability of a substrate and in turn increasing the free energy of the surface improves the transfer of proteins. It was demonstrated that PDMS stamps exposed to oxygen plasma and modified with hydrophilic groups transfer less protein than the native hydrophobic PDMS surface.[122]

Experimental Analysis Techniques

SPR and X-ray photoelectron spectroscopy (XPS)[129] characterized the molecules patterned with microcontact printing. XPS (Figure 23) provides quantitative information on the elemental surface composition of a sample. Monochromatic X-rays strike a surface and interact with orbital electrons. Photoelectrons are released. The kinetic energy of the released electron yields information on the identity of the elements present at the surface. Conventional XPS measures the average elemental composition of a substrate. Imaging XPS provides local information about the elements present on a sample.[130] Both of these techniques were employed to characterize patterns of molecules on gold.

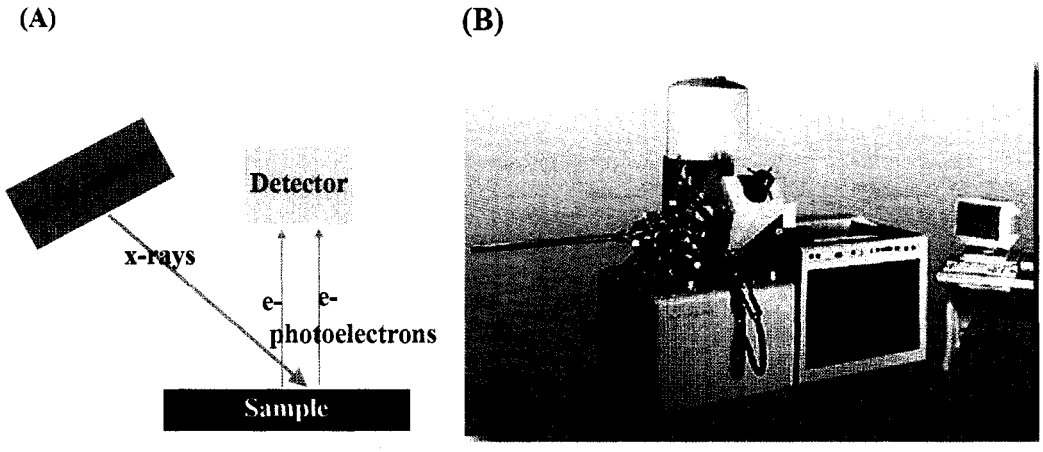

Figure 23. Schematic of X-ray photoelectron spectroscopy (XPS). (A) Diagram of the principles of XPS. X-rays are directed towards the sample. Photoelectrons are released from the surface to a detector which by measuring the kinetic energy of the photoelectron can chemically identify the element it was released from. (B) The XPS instrument used for this research was the Kratos Axis Ultra. The image was copied from the following website (http://www.kratos.com/Axis/).

Chapter 3: Surface patterning: Microcontact printing molecules on gold surfaces

3.1 Objectives

1) Microcontact print alkyl thiols on a gold surface.

2) Microcontact print proteins on a gold surface.

3) Characterize the density of microcontact printed proteins and the amount of non-specific and specific binding to the patterned protein.

3.2 Background

A critical component in the design of microfluidic flow assays is the immobilized capture molecule to which analytes from solution bind. As mentioned in Chapter 2, microcontact printing is one method of patterning a surface with molecules. This method of patterning has been used extensively in immunoassays and microfluidic cell studies.[118, 126, 131-144] It is well-established and unlike other patterning methods, such as ink jet printing, does not require expensive capital equipment.

Given the popularity of microcontact printing as a patterning technique, the literature is filled with extensive studies of microcontact printed thiols.[112, 117, 120, 127, 144-150] Initial work for this dissertation focused on the patterning of thiols onto gold surfaces to assist with the characterization and development of the SPR microscope.[13] However, the primary focus of this Chapter is the microcontact printing of a protein on a gold surface. Most of the Chapter is devoted to the characterization of the ability of an antibody from solution to bind to the patterned protein (antigen), the non-specific adsorption of a protein (BSA) from solution to the microcontact printed protein, and the uniformity of the patterned protein. Two controls were studied: (1) a gold surface to which a protein was physically adsorbed and (2) a gold surface stamped with a PDMS stamp inked with a solution of buffer.

In the literature, proteins and PDMS stamps inked with solvent (i.e., no protein) have been patterned on a variety of surfaces and substrates including gold,[120, 122, 151-157] self-

assembled monolayers,[122, 153] lipid bilayers on glass substrates,[123] immobilized bovine serum albumin (BSA),[158] GaAs,[159] polymers (PMMA,[124, 160] PET,[161] PTFE[125]), InTiO,[162] and glass.[118, 142, 163, 164] The protein may be non-covalently adsorbed to the substrate[118, 155, 164] or the protein may be introduced to a substrate with reactive groups which will covalently link the protein to the surface.[151, 153, 165] The studies have employed numerous analytical techniques to characterize the patterned protein. These techniques include atomic force microscopy (AFM),[116, 123, 128, 131, 154, 159, 163, 165-169] contact angle measurements,[122, 154, 165] XPS,[120, 121, 123-125, 128, 154, 159, 165] scanning electron microscopy (SEM),[124, 163] secondary X-ray induced electron imaging (SXI),[128] secondary electron emission,[170] ellipsometry,[165, 171] Fourier transform infrared reflection absorption spectroscopy (FT-IRRAS),[128, 154, 159, 165] time-of-flight secondary ion mass spectroscopy (TOF-SIMS),[120, 121, 125, 161] fluorescence microscopy,[116, 118, 122, 123, 131, 142, 163-166, 171-173] and SPR.[151, 152, 157]

Research indicates that a monolayer of protein transfers to the substrate during microcontact printing.[164] Studies suggest that the microcontact printed proteins retain their structure (i.e. they are recognized by antibodies or other ligands from solution).[131, 151, 155, 164] In the case of a microcontact printed IgG on a glass substrate, it has been shown to retain its ability to bind to antigen from in solution. However, the microcontact printed antibody bound ~80% of the amount of antigen as the physically adsorbed IgG.[118] An enzyme, alkaline phosphatase, has also shown that in the microcontact printed form it retains its ability to catalyze reactions.[166]

As described in the Background, the exact mechanism of the transfer of the protein to the surface is not well-understood at the molecular level. Attempts to explore methods of transfer were completed by Workman et al.[114] in which they assert the ink may transfer to the substrate through vapor deposition, wicking from the recessed regions of a patterned stamp, and direct contact.

In this dissertation, two surface analysis techniques were used to characterize a microcontact printed protein on a gold surface – SPR-imaging, XPS, and XPS imaging.

This research represents the first known attempt to (1) quantify the uniformity of the pattern of microcontact printed protein versus another protein immobilization method (physical adsorption) using SPR-imaging, (2) assess the uniformity of the specific and non-specific binding of proteins to microcontact printed proteins as well as microcontact printed buffer using SPR-imaging, and (3) characterize microcontact printed proteins on gold using XPS-imaging. The advantage of characterizing the microcontact printed protein using SPR-imaging versus other imaging techniques – such as fluorescence – is that it detects changes in refractive index near a surface – whether it is a result of PDMS stamp contamination or the patterned protein. Fluorescence, on the other hand, only detects the fluorescently labeled molecule – typically a protein – and therefore does not give a sense of the amount and distribution of PDMS contamination.

Other research has been published in the literature which has characterized microcontact printed proteins using SPR-imaging. Wilkop et al.[151] patterned bacterial toxins on a gold surface and assessed the binding of an antibody to the patterned protein. However, Wilkop et al.[151] did not have any controls such as physically adsorbed bacterial toxins to compare the uniformity of the patterned protein or the specific or non-specific binding of proteins from solution to the patterned protein. Nor did they explore the contamination of the silicone oligomer with SPR-imaging. The protein was also patterned onto a SAM with a reactive N-hydroxysuccinimide (NHS) group to covalently link the protein to the surface. Park et al.[152] used SPR-imaging to characterize pattern of gold-binding protein (GBP) – fusion proteins. They also did not have any controls nor did they attempt any rigorous quantification of the binding of a molecule to the patterned protein or the uniformity of the patterned protein. Therefore, this work represents the first attempt to quantitatively characterize microcontact printed proteins using SPR-imaging with proper control groups.

XPS has been used extensively to study microcontact printing. This technique has often been used to assess the amount of silicone oligomer contamination transferred from the PDMS stamp to the substrate. These studies have suggested several methods to reduce

the amount of silicone oligomer contamination. Glasmastar et al.[121] evaluated the silicone contamination transferred to gold coated substrates from PDMS stamps inked with water. The authors indicate that exposing the stamp to UV/ozone for 10 minutes significantly reduced the amount of silicone oligomers transferred to the surface. . The authors suggest that during the UV/ozone treatment the surface of the PDMS became glassy (SiO_x) and brittle thereby reducing the amount of silicone oligomers transferred to the surface. Graham et al.[120] used stamps extracted in hexanes over the course of a week and explored silicone contamination on gold substrates using dodecanethiol as the ink. Their work suggests that hexanes extraction reduced the silicone oligomer contamination on the substrate. Sharpe et al.[128] patterned a gold surface using microcontact printing with two different thiols as an ink and indicated that the type of ink can impact the extent of silicone oligomer contamination. Langowski et al. [124] assessed the silicone oligomer transfer from a PDMS stamp inked with water to a PMMA substrate and reported that exposure of the stamp to oxygen plasma served to reduce the amount of silicone oligomer. The authors also hypothesize that during the oxygen plasma treatment the surface of the PDMS becomes glassy (SiO_x) thereby reducing the amount of silicone oligomers transferred to the surface.

Several studies in the literature have used XPS to characterize microcontact printed substrates where the ink was not simply a thiol or a solvent (i.e. water or PBS). The purpose of the XPS studies presented in this dissertation was to quantify the amount of each element on a substrate microcontact printed with a protein and to the extent of silicone oligomer contamination. However, the majority of the XPS studies completed on microcontact printed proteins did not aim to quantify the atomic concentrations of all of the elements present on the substrate nor did most studies examine silicone oligomer contamination.

Cho et al.[154] microcontact printed the TAT peptide (a peptide found in HIV) on a gold substrate. The authors did not use the XPS data to calculate the atomic percent of each element on the surface. Instead, they used the location and shape of the C(1s) and N(1s)

peaks to obtain structural information about the immobilized peptide and confirm the presence of amide bonds. The authors did not indicate if Si was present on the surface. In 2006, Cho et al.[159] again immobilized the TAT peptide onto a substrate – GaAs – and used high resolution XPS spectra to obtain structural information about the microcontact printed peptide. No silicone oligomer contamination was reported. Rozkiewicz at al. [165] microcontact printed proteins onto aldehyde terminated SAMs on gold and a silicon wafer. The proteins were covalently attached to the surface. The authors did not report the atomic percent of each element on the surface – only the ratio carbon to nitrogen. Nor did the authors mention the presence of silicone oligomers on the substrate.

The only known XPS study widely available in the literature which used XPS to analyze the amount of silicone oligomer contamination on a surface microcontact printed with a protein was completed by Ross et al.[123] In this study, BSA was microcontact printed on dried poly(bis-SorbPC) planar support lipid bilayers. The authors collected XPS spectra which indicated that Si was present on the substrate contacted with an untreated PDMS stamps. The PDMS stamp was exposed to oxygen plasma. The Si(2p) peak on the lipid substrate was greatly reduced indicating that less silicone oligomer was transferred to the substrate. However, the authors did not report an atomic composition of the surface. The authors indicated that oxidizing the stamp reduced the amount of silicone oligomer contamination, but it also reduced the efficient transfer of the protein from the stamp to the substrate. The authors suggest the reduction in the transfer of the protein from the stamp to the substrate can be attributed to the increased wettability of the stamp which in research completed by Tan et al.[122] and described in the Background is a major factor in the proper transfer of a protein to a substrate. Ross et al.[123] also indicated that the presence of the silicone oligomer increased the non-specific binding to the substrate.

A major controversy in the literature of microcontact printed substrates is the distribution of the silicone oligomer contamination. Numerous studies using fluorescence and AFM clearly indicate that protein is transferred in region of contact of the stamp and the substrate. Proteins are large molecules and are slow to diffuse or vaporize. Therefore, the

indirect methods to noncovalently transfer a protein to a surface suggested by Workman et al.[114] are less likely for a large molecule like a protein. However, silicone oligomers, depending on the extent of cross-linking, can vary in size and could be rather small. Hale et al.[125] completed TOF-SIMS imaging of a poly(tetrafluoroethylene) (PTFE) substrate brought into contact with an oxygen plasma treated PDMS stamp that was not inked with any solution. The results indicated that silicone fragments were everywhere – in the regions of direct contact with the stamp where most of the fragments were located as well as in the regions where the stamp did not contact the surface. The authors suggest that volatile silicone oligomer fragments from the PDMS stamp transferred to the substrate during contact. On the other hand, a TOF-SIMs imaging study completed by Yang et al. [161] indicated that silicone oligomers were located only in the regions the stamp contacted the substrate. In this study, an oxygen plasma treated PDMS stamp transferred a biotin derivative to a poly(ethylene terephalate) (PET) substrate. Glasmastar et al.[121] completed XPS analysis (spectroscopy not imaging mode) on gold surface brought into contact with a patterned (i.e. not a flat PDMS stamp) PDMS stamp inked with a solution of deionized water. The results indicated that the patterned PDMS stamps transferred more Si to the surface (10% +/-1.2%) than the flat PDMS stamps (6.2% +/-1.6%). To determine if silicone fragments were transferred through the vapor phase to regions of the substrate not in contact with the stamp, a gold substrate was exposed to a flat piece of PDMS position 13 microns from the surface. No Si peaks were detected suggesting that transfer from the vapor phase to the surface is unlikely for the silicone oligomers, and thereby bringing into question the hypothesis proposed for oligomer transfer by Hale et al.[125] TOF-SIMs images were completed which indicated that the majority of the silicone oligomer transfer occurred in areas where the stamp contacted the surface with a greatly reduced signal in the regions the stamp did not contact the surface. For stamps treated with UV/ozone, however, TOF-SIMs images indicated that the majority of the oligomer transfer occurred in regions the stamp did not contact the surface. The authors suggest that a potential route for transfer of more silicone oligomers from the patterned stamp versus the unpatterned stamp may be a result of the escape of material down the walls of the PDMS features (due to capillary forces perhaps), and that

the UV/ozone treated stamps are more brittle and more likely to crack at the wall structures thereby releasing silicone oligomers that travel from the features of the stamp to the surface. This result suggests that the geometry of the stamp may have a significant influence on the transfer mechanism of silicone oligomers to a substrate. However, UV/ozone treated stamps have not been examined in this dissertation and that route of silicone transfer has not been extensively explored.

An important point which the authors did not note was that the methods they used to study the substrates, XPS and TOF-SIMs, required an ultra high vacuum. Under these conditions, the vacuum may have spread the silicone oligomer across the surface during pump down. Therefore, this research which used SPR-imaging to explore the pattern of a gold substrate microcontact printed with a PDMS stamp inked with buffer and patterned and imaged under ambient conditions serves to reveal the silicone oligomer pattern before it has been exposed to an ultra-high vacuum.

A major limitation of the literature characterizing microcontact printed patterns is that the protocols, inks, and substrates vary substantially. Because surfaces are highly reactive and prone to contamination, subtle variations in a protocol may have a huge influence on the properties of a patterned protein. Therefore, it is difficult to directly compare the results of one study with another. Several potential variations in protocols and materials are listed below.

(1) Method of curing the PDMS. The PDMS could be cured at room temperature or at an elevated temperature in an oven. The method of curing will affect the cross-linking reaction. Therefore, the temperature and the age of the PDMS will affect the amount of oligomer in the stamp. Work by Hale et al.[125] has suggested that curing the stamp at an elevated temperature reduces the amount of silicone contamination.

(2) Ratio of elastomer base to curing agent. Typically the PDMS is measured and mixed manually. Therefore, user error could either increase or decrease cross-linking thereby altering the amount of small silicone oligomers in the stamp.

(3) Solvent for the ink. Sharpe et al.[128] and Hale et al.[125] have shown that silicone contamination can depend on the type of ink employed.

(4) PDMS Stamp preparation. The type of master to create the stamp, the type of solution to clean the stamp, and whether the stamp underwent UV/ozone treatment,[121] oxygen plasma treatment,[124, 162] hexanes extraction,[120] or was modified with another functional group on the surface of the PDMS[122] will each affect the surface properties of the stamp and in turn the properties of the patterned molecules.

(5) Concentration of the ink. The concentration of the ink varies widely – particularly for proteins – ranging from several micrograms/milliliter[151] to hundreds of micrograms/milliliter.[155] Wilkop et al.[151] and Graber et al.[118] have shown that there is a concentration dependence on the uniformity of the pattern of a protein on a gold surface.

(6) Incubation time of the ink on the PDMS stamp. The incubation time in the literature has ranged from five minutes[151] to an hour.[122]

(7) Substrate. As previously mentioned, numerous types of substrates have been patterned with microcontact printed proteins. Given the fact that the molecular mechanism of the transfer of the protein is not yet completely understood and that Tan et al.[122] have shown that the relative wettabilities of the stamp and the substrate significantly influence the ability to generate clean patterns with microcontact printing, the type of substrate examined will significantly affect the patterning procedure.

(8) Functionalization of the substrate. Some substrates have been functionalized with other molecules including SAMs,[122, 153] lipids,[123] and immobilized BSA.[158]

(9) Manual dexterity. This technique requires the user to gently place the stamp on the substrate and remove it without smudging the pattern. Therefore, this is a learning curve required to achieve reproducible patterns.

Given the number of variations in the protocols and materials used to microcontact print molecules onto a substrate as well as the wide range of techniques used to evaluate the patterned molecules, it is difficult to find a study in the literature to directly compare the results presented in this dissertation. As mentioned previously, there are some significant differences between the SPR-imaging experiments completed by Wilkop et al. [151] and Park et al.[152] and the work completed in this dissertation. Therefore, only qualitative comparisons can be made. However, the XPS analysis presented by Glasmastar et al.[121] that analyzed silicone oligomer contamination on gold surfaces contacted with PDMS stamps inked with deionized water can be compared to the XPS data presented in this dissertation. The major difference between the work presented in this dissertation and the work completed by Glasmastar et al.[121] are the contact time of the solution with the PDMS stamp (45 minutes for this dissertation and 3 minutes for referenced work) and the ink (PBS for this dissertation and deionized water for the referenced work). For the XPS analysis of the microcontact printed proteins, once again, there are substantial differences in the protocols and materials analyzed. The XPS analysis which shows the strongest similarity to the data presented in this dissertation was completed by Ross et al.[123] In this article, BSA molecules were microcontact printed onto lipid bilayers immobilized on glass. The authors did not present any quantification of the atomic percents of each element on the surface, but by analyzing the shape of the peak, they confirmed that silicone oligomers were transferred with the protein to the substrate and that treatment of the PDMS stamp with oxygen plasma will reduce the amount of contamination. Therefore, this work can again be used for qualitatively comparison of the data presented in this dissertation.

3.3 Initial Design Considerations

An important experimental design parameter for the microcontact printing experiments was the size of the patterned features. The SPRM had a lower spatial resolution than the XPS instrument. Patterned features had to be on the order of 100 microns to be resolved by the SPRM. For XPS-imaging experiments, the imaging spot size was on the order of 400 micron × 400 micron.[174] To ensure that the regions that were contacted by the PDMS stamp and the regions that were not contacted by the stamp were imaged simultaneously, the patterned features were approximately 200 micron × 200 micron in dimension. Given the difficulty in locating a particular region within the XPS field of view, it was important to pattern the entire gold-coated slide.

3.4 Materials and Methods

Chemicals and reagents

Bovine serum albumin (BSA) and all antibodies were purchased from Sigma (St. Louis, MO). The proteins were diluted in phosphate-buffered saline (PBS) (Sigma, St. Louis, MO). Deionized water (still from Barnstead International, Dubuque, Iowa at the University of Washington) was used throughout the work. Hexadecanethiol (HDT, Fluka, St. Louis, MO) and ethylene glycol thiol (HSC11-EG4, TH 003-1, Prochimia, Sopot, Poland) were diluted in absolute ethanol.

Fabrication of the SU8 masters for the PDMS stamps

SU8 masters for PDMS stamps were fabricated using established soft photolithography methods[64, 175] at the Washington Technology Center (WTC). First, custom black and white transparency masks were created (Publication Services, University of Washington, Seattle, WA). Next, a layer of SU8 (MicroChem, Newton, MA) was spun (Solitec Spinner, Milpitas, CA) onto a clean, three-inch silicon test wafer (Silicon Sense, Nashua, NH) and the wafer was pre-baked to densify the SU8 film. Then, the wafer was exposed to ultraviolet light using a four-inch infrared contact aligner (AB-M, San Jose, CA),

thereby polymerizing the exposed regions of the SU8. The wafer was incubated in a solution of SU8 developer (MicroChem, Newton, MA), which removed any unpolymerized SU8. The wafer was baked a final time to harden the SU8. The depth of the SU8 features were measured with the P15 surface profilometer (Tencor, San Jose, CA) located in the WTC.

Fabrication of the PDMS stamps

PDMS stamps were prepared by dispensing Sylgard 184 prepolymers (Dow Corning, Midland, MI) at a 10:1 ratio of polymer to curing agent onto SU8 masters. Unpolymerized Sylgard 184 was dispensed into planar Petri dishes (Falcon 1001 and 1013, Becton Dickinson Labware, NJ) to produce flat PDMS stamps. PDMS was cured at 60° C for at least 24 hours and the stamps had a thickness of 3-5 mm. Prior to being used, the PDMS stamps were sonicated in a 1:1 solution of isopropanol:deionized water or ethanol:deionized water for 10-15 minutes, rinsed with deionized water, and blown dry under N_2. Some stamps underwent a hexanes extraction procedure in which the stamps were soaked for ~24 hours in a solution of hexanes and sonicated three times for 5 minutes in a 1:1 solution of ethanol:deionized water. This procedure was repeated three times. Other stamps underwent oxygen plasma deposition (Barrel Etcher, Branson, WTC) at a power of 300 Watts for three minutes. These stamps were used immediately after plasma treatment to ensure that the hydrophilic layer of the PDMS was maintained.

Preparation of gold substrates

For the substrates that were microcontact printed with thiols, a 1 nm adhesion layer of chromium and a 45 nm layer of gold were electron beam-deposited (CHA 600, CHA Industries, Fremont, CA) onto a clean glass microscope slide (Fischer Scientific, Pittsburgh, PA). All gold depositions were completed at the Washington Technology Center (WTC). The gold-coated slides were cleaned in a 5:1:1 solution of deionized water:ammonium hydroxide:30% hydrogen peroxide for ~15 minutes at an elevated temperature or for ~ 45 minutes at room temperature. The slides were rinsed with deionized water and ethanol and then dried under a stream of N_2.

For all other substrates, electron-beam gold-deposited slides were purchased from Platypus Technologies (Madison, WI) with an adhesion layer of titanium and a 50 nm layer of gold. These gold-coated slides were cleaned under UV/ozone for 30 minutes.

The gold substrates used in the XPS experiments must be smaller than the traditional microscope slide used in the SPR imaging experiments to allow for the simultaneous analysis of multiple samples. The slides were diced with a diamond-tipped pen into 1 cm × 1 cm pieces.

Preparation of flow cells

Sheets of adhesive and Mylar® (Fralock, Canoga Park, CA) were ablated with a carbon dioxide laser (M25, Universal Laser System, Inc., Scottsdale, AZ) to form the channel and capping layers of the flowcell. These layers were then assembled on top of the gold-coated glass substrate and pressed to create a simple flow cell (Figure 24).

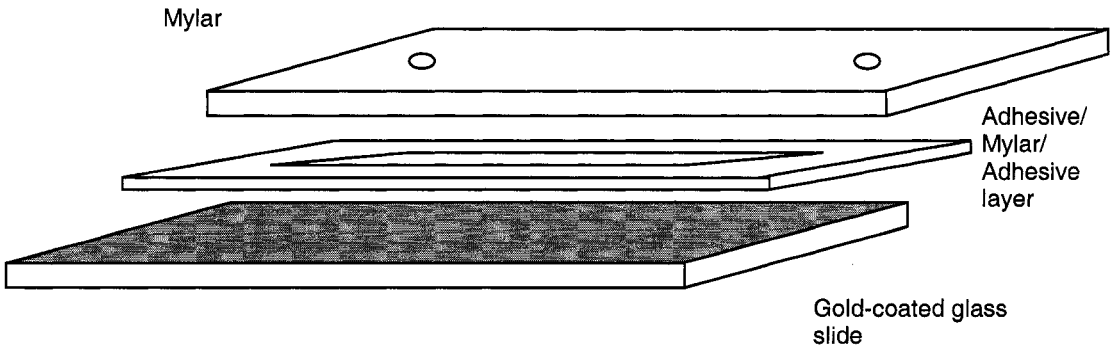

Figure 24. Laminate and glass microfluidic device for SPRM experiments. Two Mylar® sheets with inlets, outlets, and the microchannel were fabricated using a carbon dioxide laser and adhered to a gold-coated glass slide.

Microcontact printing of alkanethiols onto gold surfaces

Clean hexanes-treated PDMS stamps that contained 500 micron × 500 micron recessed square features were inked with a 10 mM solution of hexadecanethiol in absolute ethanol for 30-40 minutes at room temperature. The stamps were rinsed with ethanol and blown dry under a stream of N_2. The stamps were placed onto the gold-coated slide for 30-60 seconds and then removed.

Microcontact printing of proteins onto surfaces

Clean PDMS stamps were inked with a solution of IgG (200-500 microliters at 0.5 mg mL^{-1} in PBS) for 30-40 minutes at room temperature. The stamps were rinsed with solutions of PBS, PBS with 0.05% Tween 20, and deionized water, and blown dry under a stream of N_2. The stamps were placed onto the gold-coated slide for 30-60 seconds and then removed. This substrate is referred to as the μCP protein substrate in the text and MCP protein in all graphs. The control pattern (the μCP buffer substrate in the text and MCP buffer in all graphs) followed the same experimental protocol except that the PDMS stamps were inked with a solution of PBS rather than IgG in PBS.

Surface plasmon resonance imaging

The SPRM instrument (Figure 14) built by Dr. Elain Fu and described in the Background (Chapter 2) was used for the SPR imaging experiments. The experimental set-up is described in detail elsewhere.[13] Briefly, a 150 watt quartz halogen lamp (Dolan-Jenner, Lawrence, MA) served as the source and was coupled to a multi-fiber light pipe (Edmund Industrial Optics, Barrington, NJ). An achromatic lens (Edmund Industrial Optics, Barrington, NJ) collected and focused the light on a 100 micron pinhole (Edmund Industrial Optics, Barrington, NJ). Another achromatic lens (Edmund Industrial Optics, Barrington, NJ) collected and collimated the light from the pinhole. The beam of light passed through a polarizer (Edmund Industrial Optics, Barrington, NJ) and an interference filter (Edmund Industrial Optics, Barrington, NJ). The interference filter was mounted on a stage (Newport Corporation, Irvine, CA) which enabled rotation of the filter face with respect to the beam of incident light. As the filter was tilted off-axis, the light blue-shifted enabling the tuning of the wavelength of light (see Figure 13) that passed through the filter. The light traveled to a custom-ground BK7 prism (Matthew's Optical, Poulsbo, WA), which had an incident angle of 64.8° from the gold-coated substrate. The light reflected from the substrate was focused with an imaging lens (Edmund Industrial Optics, Barrington, NJ) onto a CCD camera (Retiga EX, Qimaging, Burnaby, Canada). Labview programs (National Instruments, Austin, TX), written by Dr.

Elain Fu, automated the collection of images taken by the CCD camera and the rotation of the interference filter and polarizer.

A manifold, built by Dr. Mark Blaylock (Figure 25), interfaced the gold-coated glass substrate with the prism and fluidic tubing. Before placing the manifold on the prism, one to two drops of refractive index matching fluid (Cargille Laboratories, Cedar Grove, NJ) were deposited on the prism. Two PDMS gaskets connected and sealed the polyetheretherketone (PEEK) tubing (0.33" diameter, Upchurch Scientific, Oak Harbor, WA) to the Mylar® device. Syringe pumps (Kloehn, Las Vegas, NV) generated pressure-driven flow.

Figure 25. Manifold that interfaced the microfluidic device with the SPRM and fluidic tubing. The PDMS gaskets connected the ports of the microfluidic device with fluidic tubing to the pump. The microfluidic device was secured between the two layers of the manifold using set screws. The manifold rested on the prism of the SPRM, thereby interfacing the gold-coated slide with the prism. Image of the manifold before assembly.

Two interference filters were used for the work in this dissertation. Initial studies of printed alkyl thiols used a filter with a peak emission of 880 nm. In later work, an interference filter with a peak emission of 905 nm was adopted. Typical integration times for the SPRM images were 0.2-1 second. TM, TE, and dark images were collected. A series of TM and TE correction images were also collected. For a thorough explanation

of image processing, the calculation of the percent change in reflectivity, and calibration of the instrument, see Appendix C. Labview programs (National Instruments, Austin, TX) written by Dr. Elain Fu automated the image processing.

SPR-imaging of microcontact printed protein (μCP protein)

To quantify the surface density of the microcontact printed protein, the non-specific binding of BSA, and the specific binding of an IgG to a microcontact printed protein, SPR-imaging experiments were conducted. The PDMS stamps used to microcontact print the protein onto the gold-coated slide had 500 micron × 500 micron recessed square features. SPR images of the μCP protein substrate were collected with PBS as the background solution. Then, the μCP protein substrate was exposed to a concentrated (0.3 mg/mL) solution of BSA for forty five minutes, rinsed with PBS, and imaged. Finally, a 0.1 mg/mL solution of an IgG that recognized the microcontact printed protein was incubated in the device for twenty minutes, rinsed with PBS, and imaged.

The control groups for the SPR-imaging experiments were (1) the μCP buffer substrate – a gold-coated slide printed with a PDMS stamp inked with PBS for forty five minutes and (2) the physically adsorbed protein substrate – a gold-coated slide to which IgG was physically adsorbed by incubating the slide in a 0.5 mg/mL solution of IgG for 45 minutes. The same experimental protocol was followed for the experimental and the control groups.

SPR images were collected over a range of imaging wavelengths (approximately 905 nm to 825 nm) corresponding to a thirty-eight degree shift of the 905 nm interference filter. The imaging wavelength was approximated using the following filter function for a similar interference filter (880 nm filter from Edmund Optics): $w=905-(0.17905* \theta)-(0.05019* \theta * \theta)$ where w=imaging wavelength and θ =degree shift of the 905 nm interference filter from normal incidence.

The SPR images were processed using the methods described in Appendix C. To assess the homogeneity of the substrates, histograms were generated relating the reflectivity from a given surface or the change in reflectivity (upon the binding of an IgG molecule to the substrate or the non-specific adsorption of a BSA molecule to the substrate) as a function of number of pixels which had the corresponding reflectivity or the change in reflectivity. The full width at the half maximum (FWHM) of each histogram was determined manually. For each type of substrate, three experiments were completed (n=3). The calculated FWHM for each substrate is the mean of the manually determined FWHM. The error bars represent the standard deviation of the mean FWHM.

To quantify the change in reflectivity upon the binding of an IgG molecule to a substrate or the non-specific adsorption of a BSA molecule to a substrate, the difference of the mean reflectivity (calculated by the analysis software) was calculated for each selected region. Once again for each type of substrate, three experiments were completed (n=3). The calculated change in reflectivity is the average of the mean change in reflectivity for each replicate (over the region of interest). The error bars represent the standard deviation of the average of the mean change in reflectivity for the three replicates.

The entire region of the μCP protein substrate and the μCP buffer substrate that contacted the PDMS stamp were selected for analysis. A region comparable in size to the regions selected for the μCP protein substrate and the μCP buffer substrate was selected for the physically adsorbed substrate. The areas of the selected regions for the SPR-imaging analysis ranged from approximately 3.1 mm^2 to 8.2 mm^2.

An important data analysis parameter was the imaging wavelength selected for each data set. In order to select the appropriate imaging conditions, SPR curves relating the reflectivity versus wavelength (as described in Appendix C, the wavelength in the system is determined by the tilt of the interference filter) were generated. The wavelength that gave rise to the largest change in reflectivity for the binding of a molecule to the surface was selected for the analysis of the change in reflectivity. For the analysis of the

homogeneity of the initial pattern of molecules on the surface, the wavelength that was the most sensitive to small changes in refractive index (i.e., the linear portion of the steeper side of the SPR curve) was selected for the analysis.

XPS experiments

All XPS and XPS-imaging data were collected at NESAC-BIO at the University of Washington by Dr. Lara Gamble using the Kratos Axis Ultra-DLD spectrometer (Shimadzu, Kyoto, Japan). The instrument had a monochromatized Al Kalpha X-ray and a low energy electron flood gun for charge neutralization. The pressure in the chamber during data acquisition was less than 5×10^{-9} torr. The analyzer was located normal to the surface of the substrate yielding a 10 nm sampling depth. The pass energy for survey spectra was 150 eV. The pass energy for high resolution spectra was 20 eV. All substrates were approximately 1 cm × 1 cm. Commercial software, Kratos Vision2, analyzed the data and calculated elemental compositions. The atomic concentrations of Si, N, O, C, and Au were quantified using the Si(2s), N(1s), O(1s), C(1s), and Au(4f) peaks with the peaks corresponding to binding energies of 153 eV, 400 eV, 532 eV, 285 eV, and 84 eV. No other chemicals contributed significantly to the XPS spectra. All unprocessed XPS data are presented in Appendix I.

Non-imaging XPS

The experimental group was the μCP protein substrate – a gold-coated slide microcontact printed with an IgG. The control groups were 1) a gold-coated slide, 2) the μCP buffer substrate – a gold-coated slide microcontact printed with a PDMS stamp inked with PBS for forty five minutes, and (3) the physically adsorbed protein substrate – a gold-coated slide to which IgG was physically adsorbed by incubating the slide in a 0.5 mg/mL solution of IgG for 45 minutes. The PDMS stamps were not patterned (i.e., they were flat), ensuring the entire surface of the PDMS contacted the substrate. The X-ray spot size for these acquisitions was on the order of 300 micron × 700 micron. No high resolution scans were completed.

Two substrates were analyzed for the experimental group and each control group. Three spots were analyzed on each sample for a total of six XPS spectra for the experimental group and each control group. General survey scans were analyzed to determine the atomic concentration of C, N, O, Si, and Au at the surface. The error bars represent the replicate standard deviation of the mean.

Imaging XPS

The XPS-image interrogated approximately 400 micron × 400 micron areas on the substrate. The PDMS stamps had 200 micron × 200 micron recessed square features. The experimental group was the μCP protein substrate. The control group was the μCP buffer substrate. Given the strength of the Au(4f) signal for regions of the surface not contacted with the PDMS stamp, the Au(4f) signal was used to focus the analyzer on the patterned substrate. Two spots were imaged on the μCP protein substrate. The majority of the data analysis was completed by Dr. Lara Gamble.

Initial studies indicated that it was difficult to image elements other than Au(4f) due to noise considerations and the fact that it was difficult to select an appropriate background signal to subtract. The noise and high background signal may be a result of inelastically scattered electrons from the gold surface.

An XPS-image of Au(4f) was collected on the μCP protein substrate in order to locate the bare gold regions of the substrate. Then, region of interest scans (ROI) (55 micron diameter circle of the surface) were completed in regions of the surface contacted and not contacted by the PDMS stamp. High resolution scans of Si(2s), N(1s), O(1s), and C(1s) were used to calculate the local atomic concentrations. The error bars represent the standard deviation of the mean.

For the control surface (the μCP buffer substrate), there was no detectable variation in the Au(4f) signal across the surface, suggesting that the surface was relatively uniform in atomic composition. Therefore, the instrument had difficulty focusing on the patterned

substrate, and it was not possible to collect an XPS-image for this substrate. One hypothesis for this difficulty is that PDMS oligomers, which had transferred in a pattern to the gold-coated slide under ambient conditions, spread across the entire surface under the high vacuum conditions that are required to collect XPS data.

3.4 Results and Discussion

There are several considerations that should be applied when assessing the quality of a pattern of molecules on a surface. The patterned molecules should be homogeneous and have a high surface density. The printed molecule, if a protein, should retain its structure and binding specificity. There should be limited non-specific binding to the patterned molecule. The patterning method should be reproducible. The patterns produced with μCP were judged by several or all of these criteria.

For the analysis of surfaces microcontact printed with protein, several substrates were studied with SPR-imaging, XPS, and XPS-imaging.

1) μCP protein substrate (or MCP protein on all graphs).
This substrate was a gold-coated slide microcontact printed with a protein – an IgG molecule.

2) μCP buffer substrate (or MCP buffer on all graphs).
This substrate was a gold-coated slide microcontact printed with a PDMS stamp inked with a solution of PBS – not a solution of protein in PBS. This substrate was not only an important control group for the μCP protein substrate; it also provided relevant information for another method of patterning a substrate with multiple proteins using μCP. In this method, a flat PDMS stamp patterned with multiple proteins via ink jet printing or an open ended series of microchannels was brought into contact with the substrate. Some regions of the PDMS stamp were not functionalized with protein, and therefore bare PDMS contacted the surface in this case also.

3) Physically adsorbed protein substrate

This substrate was a gold-coated slide to which a protein – an IgG molecule – had physically adsorbed across the entire surface. As previously mentioned in Chapter 2, physical adsorption is a common method to immobilize a protein onto a surface. Therefore, this control group served to compare the μCP protein substrate with another standard method of immobilizing a protein on a surface.

4) Bare gold surface

This control group was only studied with XPS and XPS-imaging and served as a control necessary to assess the density of the patterned or adsorbed protein on the surface.

SPR Images of patterned gold surfaces.

Alkanethiol microcontact printed on gold

Hexadecanethiol was microcontact printed onto a gold-coated slide with a PDMS stamp that had 500 micron × 500 micron recessed square features. The substrate was imaged with the SPRM (Figure 26). Due to the optics of the SPRM (see Appendix C for further explanation), the image was foreshortened in the horizontal direction (x-dimension) by a factor 0.42. The pattern was relatively homogeneous and had well-defined edges. This method of patterning has been shown to be reproducible and robust. Figure 26 also demonstrates the effect of imaging wavelength on image contrast in SPRM. As the wavelength was shifted away from the optimal imaging conditions (Figure 26), the patterned region became indistinguishable from the background. By introducing another thiol that would adsorb to the bare gold regions of the substrate, it is also possible with this technique to pattern two thiols onto a surface. A stamp inked with an alkyl thiol also may repeatedly pattern the surface without the need for re-inking (data not shown) due to the absorption of the hydrophobic alkane thiols into the bulk of the hydrophobic PDMS stamp.

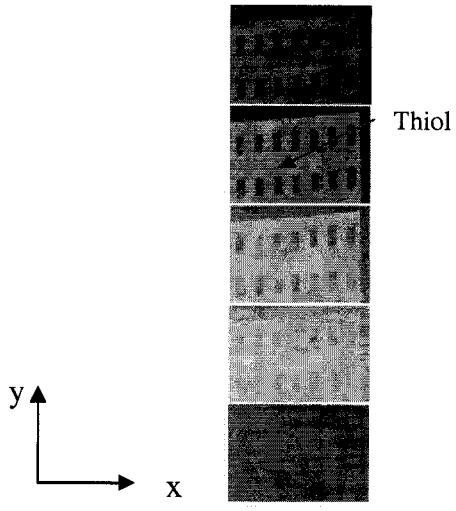

Figure 26. Microcontact printed alkanethiols on gold. SPRM images of hexadecanethiol (HDT) printed on a gold slide with a solution of water as the background. [13] The thiols appear lighter in this series of images. The interference filter angle shifts fifteen degrees which correlates to approximately 40 nm wavelength shift. The dimension of the recessed rectangular pattern is 500 microns × 500 microns. The image was reproduced from cited reference.

μCP protein substrate

An IgG molecule was microcontact printed onto a gold-coated glass slide with a PDMS stamp that had 500 micron × 500 micron recessed square features (Figure 27). SPR images of the patterned surface were collected over a range of imaging wavelengths (Figure 27). The data indicate that microcontact printing generated a pattern of protein on the surface with well-defined edges. The patterned protein was not homogeneous across the entire gold surface (Figure 27B and C). In some locations on the gold-coated surface, it appeared that very little to no protein was transferred from the stamp to the surface. These results are comparable to the patterns of proteins assessed with SPR-imaging in other studies.[151, 152] The uniformity of the patterned protein will be quantified in later sections of this chapter.

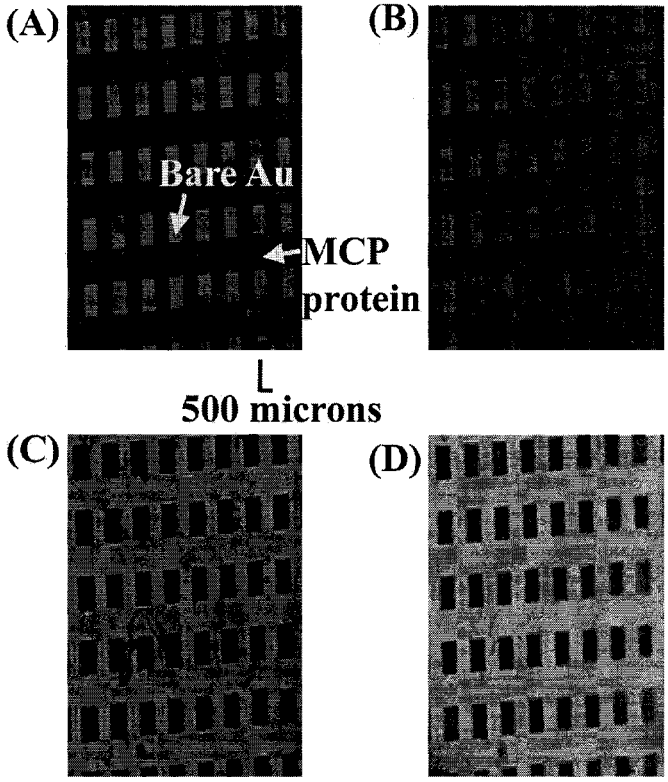

Figure 27. SPR images of microcontact printed protein on a gold surface over a range of wavelengths (λ). The PDMS stamp had 500 micron × 500 micron recessed square features. The 500 micron × 500 micron square regions were bare gold. (A) λ =905 nm. (B) λ =898 nm. (C) λ =881 nm. (D) λ =854 nm. PBS was the background solution. The contrast in the image has been enhanced for viewing purposes. The images are uncorrected TM images.

μCP buffer substrate

The μCP buffer substrate was imaged over a range of imaging wavelengths (Figure 28). The data indicate that the PDMS stamp deposited a residue of silicone oligomer that could be detected with the SPRM. This result corroborates previous findings in the literature.[121, 124-127] The pattern was extremely inhomogeneous (particularly in Figure 28C), with some regions of the surface modified with a thick layer of silicone oligomer (upper right portion of the surface) and other regions of the surface unmodified by the oligomer. When compared to the μCP protein substrate, the pattern of the silicone oligomer does not have well-defined edges. Less material was transferred to the surface, as is evident in the low contrast in the SPR signal between the patterned and unpatterned

regions of the surface. Furthermore, the PDMS appears to be located only in regions the PDMS stamp contacted the surface. Since this experiment was performed under ambient conditions, it suggests that the silicone oligomers remain in the regions the stamp contacted the gold substrate. The ultra high vacuum TOF-SIMs analysis of similar substrates presented by Glasmastar et al.[121] indicated that silicone oligomer was present over the entire surface, but the majority of the silicone oligomer was located in the regions the PDMS stamp contacted the surface. A possible explanation for the low levels of silicone oligomer in the regions not contacted with the PDMS stamp in the TOF-SIMs image given that the SPR-imaging data does not suggest that silicone oligomers are present in the areas not contacted with the stamp is that under the ultra-high vacuum some of the oligomer spread across the entire surface. The uniformity of the SPR-imaging pattern will be assessed later in this chapter.

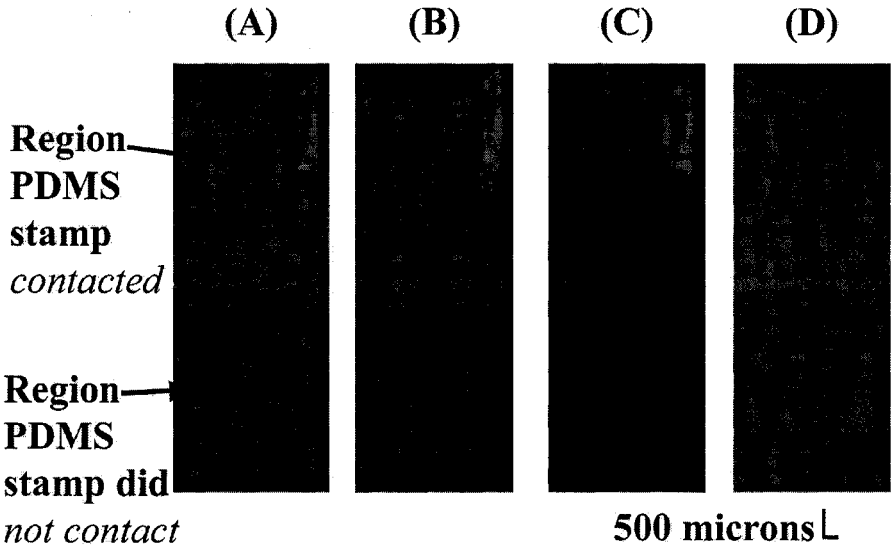

Figure 28. SPR images of the μCP buffer substrate – a gold surface microcontact printed with a PDMS stamp inked with PBS buffer. Each image was collected with a different imaging wavelength. The PDMS stamp had 500 micron × 500 micron recessed square features. In the images, the stamp did not come into contact with the gold surface in the location of the 500 micron × 500 micron square features. (A) λ ~905 nm. (B) λ ~898 nm. (C) λ ~881 nm. (D) λ =854 nm. PBS was the background solution. The contrast in the image has been enhanced for viewing purposes. The images are uncorrected TM images.

Uniformity of the patterned surfaces for the μCP protein and the μCP buffer substrates

An important characterization of a patterned substrate is the uniformity of the pattern across the surface. As evident in Figure 27 and Figure 28, microcontact printing did not

generate perfectly homogeneous patterns of protein or silicone oligomer on the surface. To achieve a quantitative measure of the uniformity of a patterned surface, histograms relating the reflectivity (a value ranging from 0 to 1) versus the number of pixels that had the respective reflectivity value were generated. Histograms for the physically adsorbed protein substrate (Figure 29), the μCP protein substrate (Figure 30), the μCP buffer substrate (Figure 31), and a clean gold surface – termed the buffer substrate (Figure 32) – were generated. A major advantage of using histograms to achieve a greater quantitative understanding of the uniformity of the surface rather than the mean reflectivities and the standard variations is that the histograms will indicate if two or more distinct populations are present on the surface as opposed to a large value for the standard variation which would occur if only mean reflectivities were analyzed. Therefore, if only the mean reflectivity and the respective variances were used to assess the homogeneity (as completed by Wilkop et al.[151]), this information would remain uncovered.

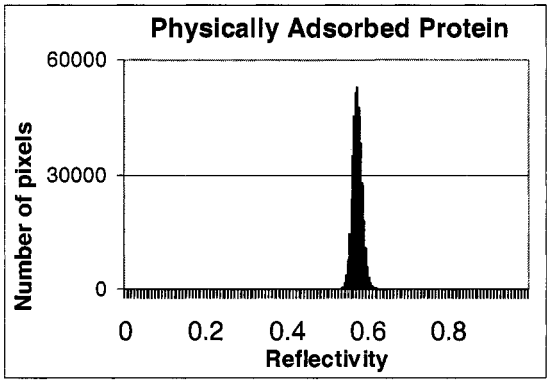

Figure 29. Physically adsorbed protein histogram. A histogram of the reflectivity as a function of pixel number for a gold substrate to which a protein (an IgG) was physically adsorbed. SPR-imaging results. The imaging wavelength was approximately 893 nm. The background solution was PBS buffer.

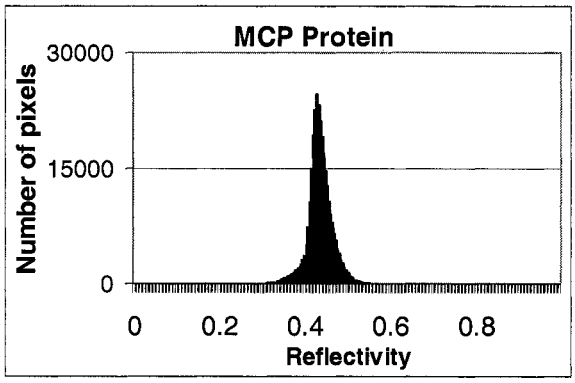

Figure 30. MCP protein histogram. A histogram of the reflectivity as a function of pixel number for the μCP protein substrate. SPR-imaging results. The imaging wavelength was approximately 889 nm. The background solution was PBS buffer.

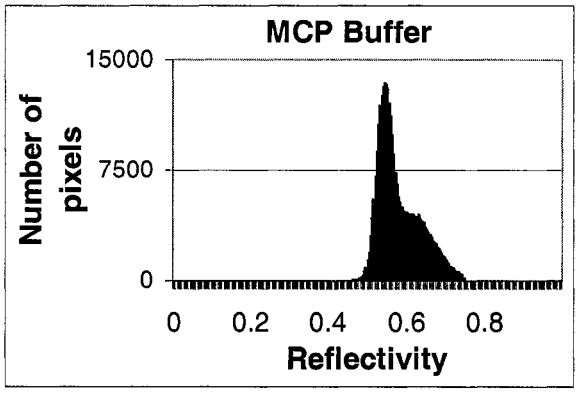

Figure 31. MCP buffer histogram. A histogram of the reflectivity as a function of pixel number for the μCP buffer substrate. SPR-imaging results. The imaging wavelength was approximately 861 nm. The background solution was PBS buffer.

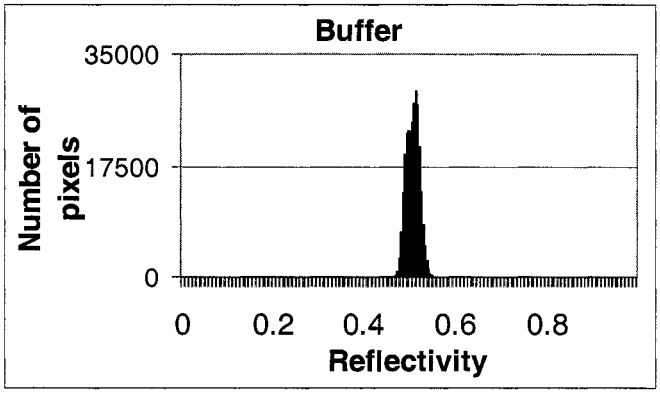

Figure 32. Buffer histogram. A histogram of the reflectivity as a function of pixel number for an unmodified gold substrate. SPR-imaging results. The imaging wavelength was approximately 866 nm. The background solution was a solution of PBS buffer.

The histograms indicate that there were relatively unimodal distributions of reflectivities for the physically adsorbed protein substrate (Figure 29), the μCP protein substrate (Figure 30), and the buffer substrate (Figure 32). On the other hand, there was a bimodal distribution of reflectivities for the μCP buffer substrate (Figure 31), which indicates the surface pattern was inhomogeneous. This result is expected since the SPR image (Figure 28) of the substrate indicated the pattern of the silicone oligomer on the surface was extremely inhomogeneous. The populations of the reflectivities on the μCP buffer substrate can be attributed to the regions of the surface modified by the silicone oligomer and the regions that were not modified by the silicone oligomer (i.e., a bare gold surface).

The full-width of the half maximum (FWHM) of each histogram was determined manually (Figure 33). (Please note that Figure 33 assesses the FWHM of the % reflectivity, which equals 100 × reflectivity value in the histogram.) This value yields a quantitative measure of the uniformity of the pattern on the surface. Ideally, every pixel would have the same reflectivity value. Therefore, the larger the FWHM, the less uniform the pattern. The buffer substrate served as a control for this experiment since it yields information about the uniformity of the gold surface to which all molecules adsorb. Therefore, it should ideally have the lowest FWHM. The results (Figure 33) indicate that the FWHM for the μCP protein substrate (~5%) was larger than the FWHM for the physically adsorbed protein substrate and the buffer substrate (~3%). This indicates that the μCP protein substrate had a less homogeneous surface than the physically adsorbed protein. This result is not surprising since it is likely that not only protein but silicone oligomer was transferred to the gold-coated slide. The buffer substrate and the physically adsorbed substrate had very similar values of FWHM, suggesting that the surface of the physically adsorbed substrate was extremely homogeneous. Given the bimodal nature of the histogram for the μCP buffer substrate, it was not possible to calculate a FWHM using the simple manual procedure. However, the difference in the reflectivity for the maximum reflectivity value for each population was consistent (~0.09 +/-0.001; n=3).

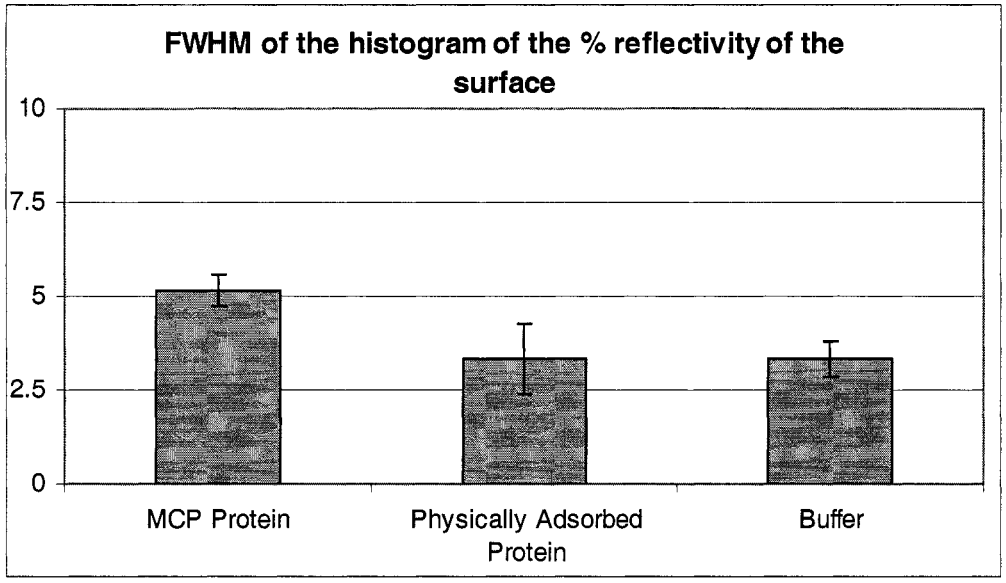

Figure 33. Full-width half max (FWHM) of the histogram relating the percent reflectivity for several substrates versus pixel number from the SPR-imaging results. The error bars represent the replicate standard deviation of the mean FWHM. (n=3)

Characterization of the binding of the protein physically adsorbed to a gold-coated slide

To assess the amount of the protein that physically adsorbed to the gold-coated slide and to quantify how uniform the surface was, SPR images were collected. The initial SPR image of a clean gold surface was subtracted from the SPR image after incubation with a solution of protein (an IgG) to quantify the change in reflectivity due to the adsorption of the protein to the surface. There was an approximately 44% (+/-1%; n=3) change in reflectivity when IgG was physically adsorbed to the gold-coated glass slide. This percent change in reflectivity is relatively high compared to other SPR-imaging studies completed in the lab in which a layer of streptavidin (SA) is expected to yield ~20% change in reflectivity. However, a different gold substrate (different type of glass and a titanium not a chromium adhesion layer) was used in this study, and a larger protein (an IgG ~150 kDa versus SA ~60 kDa) was immobilized onto the surface. The SPRM instrument has been shown to have linear response up to approximately a twenty percent change in reflectivity under similar but not identical imaging conditions.[12] Therefore, the measured change in reflectivity was well outside the linear range, and it is not possible to quantify the total amount of protein with this calibration curve.

The histogram of the change in reflectivity (due to the physical adsorption of protein onto the gold surface) as a function of pixel number (Figure 34) was unimodal, symmetric, and narrow in width. This result indicates that the change in reflectivity was uniform across the entire surface. The FWHM of the percent change in reflectivity was ~1.8% (+/-0.3%) (n=3), which further illustrates that there was not very much variation in the change of reflectivity due to the binding of an IgG molecule to the surface. These results indicate that the surface of the physically adsorbed protein substrate was homogeneous.

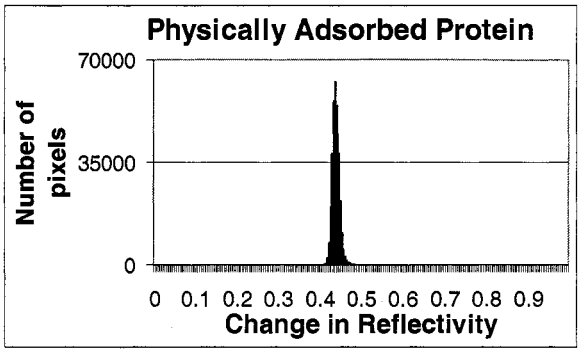

Figure 34. Histogram of the change in reflectivity when a protein adsorbed to a gold surface. SPR-imaging results. The imaging wavelength was approximately 877 nm. The background solution was PBS. The adsorbed protein was an IgG molecule.

Characterization of the non-specific binding of BSA to the surface

Each substrate was incubated in a solution of BSA to assess the non-specific binding of a protein to the surface. Ideally, in a microfluidic flow assay there should be little to no non-specific binding of protein to the surface immobilized protein. The initial SPR image (before BSA incubation) was subtracted from the SPR image after incubation with BSA to quantify the change in reflectivity due to the adsorption of BSA on the surface (Figure 35). The μCP protein substrate and the physically adsorbed protein substrate had very little non-specific adsorption of BSA to the patterned surface (2% and -0.8% change in reflectivity where the negative change in reflectivity suggests material was removed from the surface. However, the noise for this instrument is typically +/-1% thereby making it impossible to assess whether material was removed.) This corroborates findings by

Wilkop et al.[151] in which very little non-specific binding to a microcontact printed protein antigen was reported. There was an approximately 22% change in reflectivity for the μCP buffer substrate, indicating that a substantial amount of BSA adsorbed to the surface. Since μCP of proteins relies upon the non-specific adsorption of a protein to a PDMS stamp, it is expected that BSA would non-specifically adsorb to a gold surface modified with silicone oligomers from a PDMS stamp.

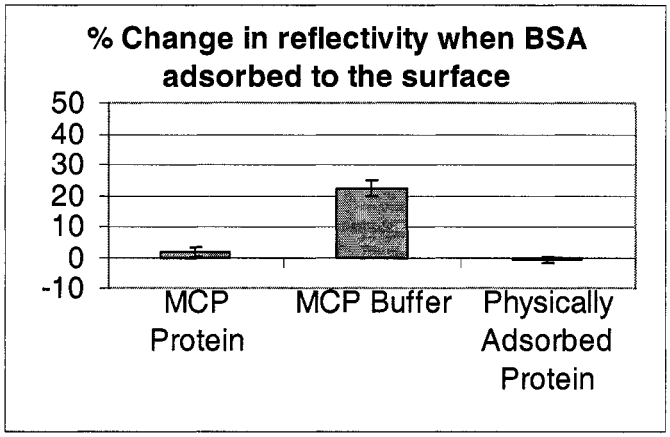

Figure 35. The percent change in reflectivity when BSA non-specifically adsorbed to the surface. SPR-imaging results. The error bars represent the replicate standard deviation of the mean change in reflectivity. (n=3)

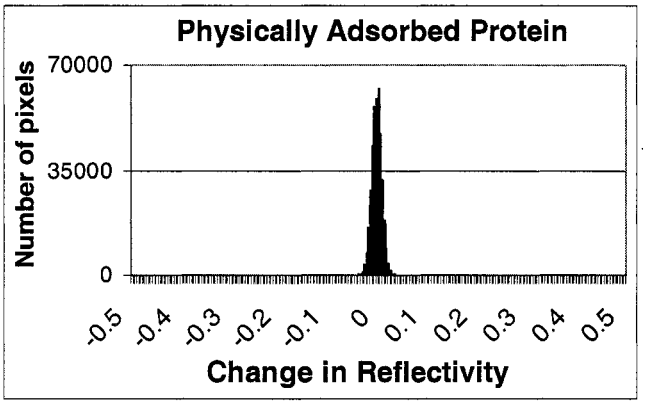

Figure 36. Histogram of the change in reflectivity versus the number of pixels when BSA non-specifically adsorbed to a gold surface to which a protein has been physically adsorbed. SPR-imaging results. The imaging wavelength was ~ 889 nm. The background solution was PBS. The physically adsorbed protein was an IgG molecule.

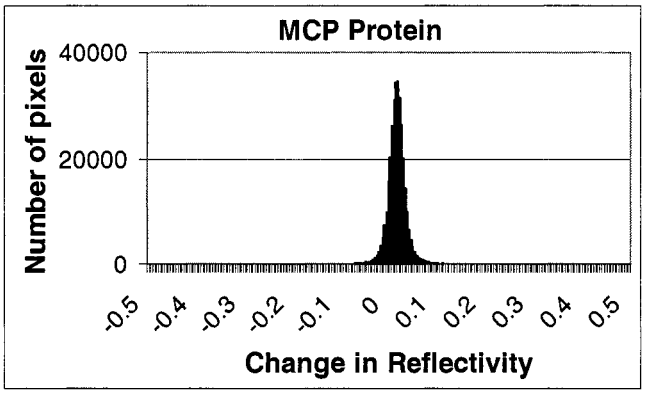

Figure 37. Histogram of the change in reflectivity versus number of pixels when BSA non-specifically adsorbed to the μCP protein substrate. SPR-imaging results. The imaging wavelength was ~ 866 nm. The background solution was a PBS. The microcontact printed protein was an IgG molecule.

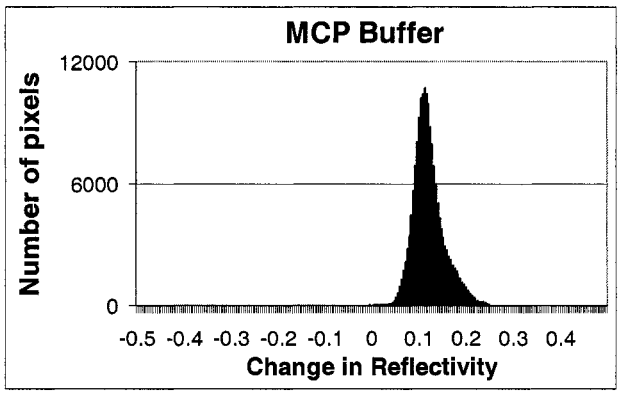

Figure 38. Histogram of the change in reflectivity versus the number of pixels when BSA non-specifically adsorbed to the μCP buffer substrate. SPR-imaging results. The imaging wavelength was ~ 877 nm. The background solution was PBS.

Histograms relating the change in reflectivity due to the adsorption of BSA to the surface versus the number of pixels were generated for each substrate (Figure 36–Figure 38). The histogram for each substrate had an unimodal and symmetric distribution, suggesting that the surfaces were relatively homogeneous. The width of the histogram is much larger for the μCP buffer substrate (Figure 38) than for the μCP protein substrate (Figure 37) or the physically adsorbed protein substrate (Figure 36). Since the histogram of the initial reflectivity for the μCP buffer substrate (Figure 32) was bimodal (suggesting that some regions of the surface were modified with silicone oligomers and other regions were not modified with the oligomers), it is interesting that the histogram has relatively normal distribution (granted the distribution is skewed with a long tail at higher changes in

reflectivity). This result suggests that similar amounts of BSA non-specifically adsorbed to the silicone oligomers on the surface as well as to the bare gold surface.

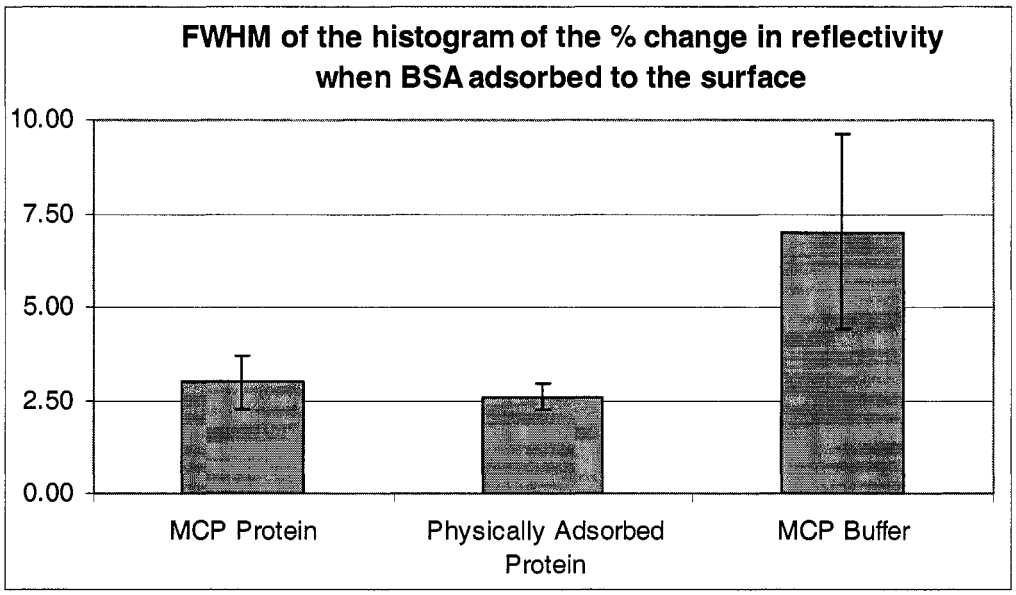

Figure 39. The full-width half max (FWHM) of the histogram relating the percent change in reflectivity when BSA adsorbed to the surface versus the number of pixels. SPR-imaging results. The error bars represent the replicate standard deviation of the FWHM. (n=3)

The FWHM of the percent change in reflectivity was again calculated to determine if the non-specific binding of BSA was uniform across the surface (Figure 39). The μCP protein substrate and the physically adsorbed protein substrate had comparable FWHM (~2.5%) suggesting the change in reflectivity due to the adsorption of BSA was relatively homogeneous over the entire surface. The μCP buffer substrate had a much higher FWHM (~7%) and a large replicate standard deviation. This suggests not only that the adsorption of BSA to the surface was inhomogeneous for a given sample, but also that it varied substantially from sample to sample.

Characterization of the specific binding of an IgG molecule to the surface

After incubation with BSA, each substrate was incubated in a solution of IgG that recognized the surface immobilized protein (i.e., the immobilized protein was the antigen of the IgG in solution). The SPR image of the substrate after incubation in a solution of

BSA was subtracted from the SPR image of the substrate after incubation in a solution of the IgG to quantify the percent change in reflectivity due to the adsorption of IgG to the surface.

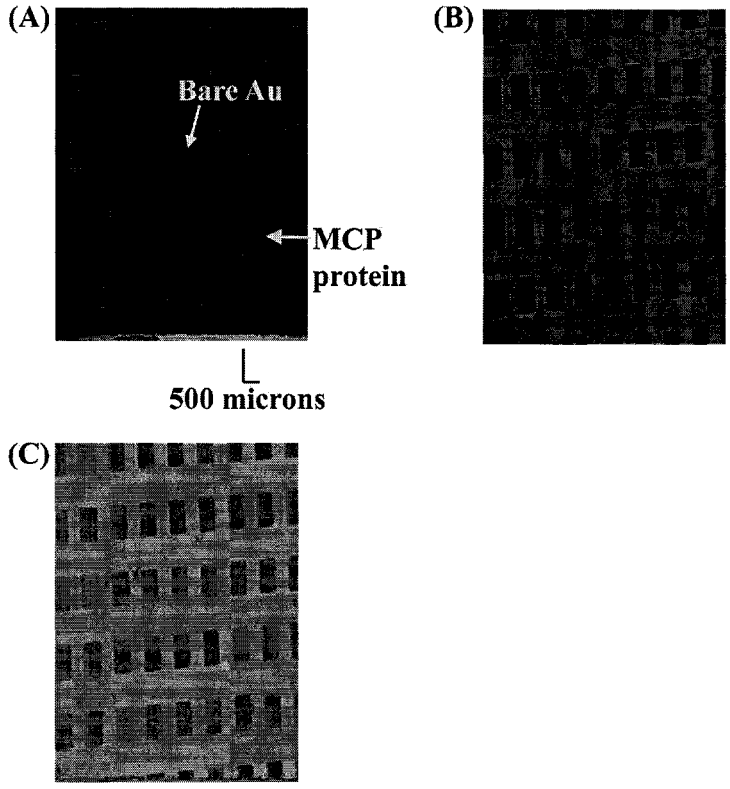

Figure 40. SPR images of the surface binding of an IgG molecule to the μCP protein substrate. The PDMS stamp had 500 micron × 500 micron recessed square features. Bare gold was located in the 500 micron × 500 micron square regions. (A) SPR image of the surface with microcontact printed antigen on the surface after incubation in a solution of BSA. (B) SPR image of the surface shown in (A) after incubation in a solution of an IgG molecule that recognized the microcontact printed antigen molecule. (C) SPR difference image. (B)-(A). The image in (C) indicates the local change in refractive index when the IgG molecule bound to the patterned protein. PBS buffer was the background solution for each image. The wavelength of light was ~904 nm. The selected wavelength yielded the greatest change in reflectivity in the microcontact printed protein regions on the surface. The contrast in the images has been enhanced for viewing purposes. The images in (A) and (B) are uncorrected TM images.

The SPR difference image (Figure 40C) indicates that the binding of the IgG to the μCP protein substrate was relatively uniform over the entire surface and resulted in a pattern of bound IgG that was similar to the initial pattern of protein in that it had well-defined features.

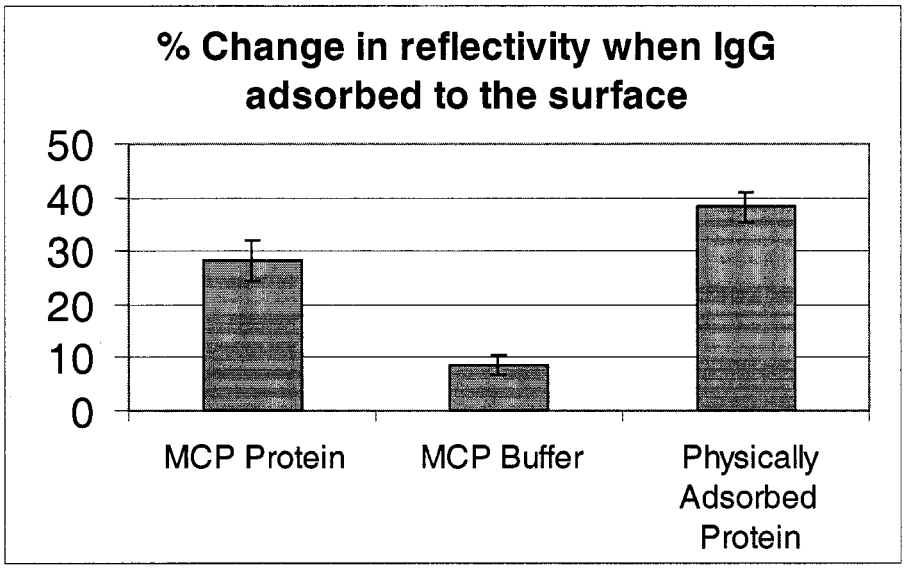

Figure 41. The percent change in reflectivity when IgG adsorbed to each substrate. SPR-imaging results. The error bars represent the replicate standard deviation of the mean change in reflectivity. (n=3)

There was a larger change in reflectivity due to the adsorption of IgG to the surface for the physically adsorbed protein substrate (~38%) versus the μCP protein substrate (~28%). Once again, the SPRM instrument has a linear relationship between the change in refractive index at the surface and the percent change in reflectivity up to a ~20% change in reflectivity.[12] Therefore, the measured changes in reflectivity for the physically adsorbed protein substrate and the μCP protein substrate are well outside this linear range, so the values should not be compared directly. The results clearly indicate that more IgG adsorbed to the physically adsorbed substrate than to the μCP protein substrate. There are several potential reasons for this large difference. Any or all of these hypotheses may be responsible for the difference in the amount of IgG that bound to the surface:

(1) More antigen was immobilized to the physically adsorbed substrate versus the μCP protein substrate.
(2) The antigen immobilized to the physically adsorbed substrate retained more of its structure than the antigen immobilized to the μCP protein substrate.

(3) Silicone oligomers transferred to the μCP protein substrate during the printing process covered the patterned antigen (protein) thereby blocking the IgG in solution from binding to the patterned antigen.

With the current SPR data, it is not possible to identify the specific cause(s) for the discrepancy in the total amount of IgG bound to the substrates. However, given the fact that very little BSA non-specifically bound to the μCP protein substrate and the physically adsorbed protein substrate, and a significant amount of IgG bound to each substrate, the results suggest that the IgG molecules bound specifically to both the μCP protein substrate and the physically adsorbed protein substrate.

The μCP buffer substrate also non-specifically bound IgG (~9% change in reflectivity). This result suggests that the adsorption of BSA did not completely block the μCP buffer substrate.

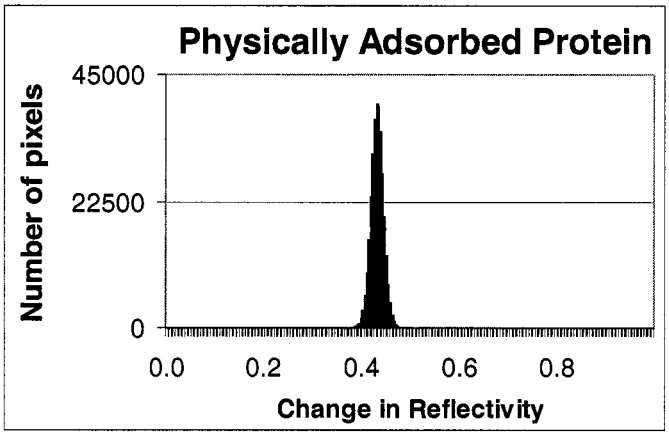

Figure 42. A histogram of the change in reflectivity when an IgG molecule bound to an antigen physically adsorbed to a gold surface versus the number of pixels. SPR-imaging results. The imaging wavelength was approximately 904 nm. The background solution was PBS. The physically adsorbed protein was an IgG molecule.

The histogram of the physically adsorbed substrate (Figure 42) had an unimodal and symmetric distribution and was relatively narrow in width. This result indicates that the binding of the IgG to the immobilized antigen was relatively uniform across the entire surface.

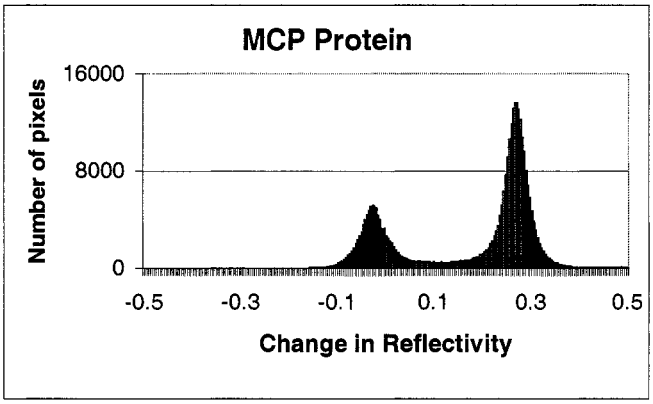

Figure 43. A histogram of the change in reflectivity for the μCP protein substrate when an IgG molecule specifically bound to an antigen immobilized to the surface with microcontact printing. SPR-imaging results. The imaging wavelength was approximately 904 nm. The background solution was PBS. The microcontact printed protein (antigen) was an IgG molecule.

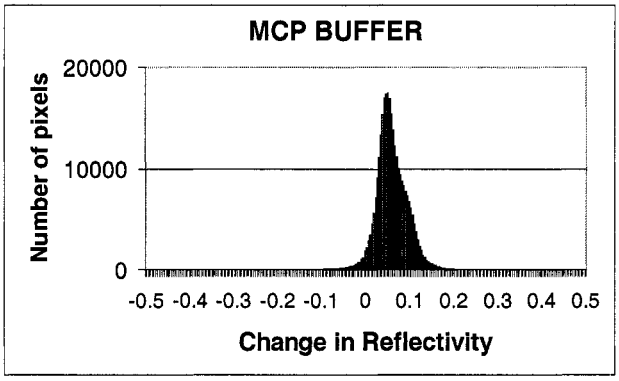

Figure 44. A histogram of the change in reflectivity when an IgG molecule non-specifically adsorbed to the μCP buffer substrate. SPR-imaging results. The imaging wavelength was approximately 881 nm. The background solution was PBS.

The histogram for the μCP protein substrate (Figure 43) had two distinct populations, each with an unimodal and symmetric distribution as a function of the change in reflectivity, indicating that some regions of the surface bound a significant amount of IgG (~30% change in reflectivity) and other regions did not bind any IgG. Of the three samples of the μCP protein substrate for which the binding of IgG to the surface was monitored, two exhibited this behavior, suggesting that the antigen was not transferred from the stamp to the surface in some regions of the μCP protein substrate. This corroborates the results for the SPR difference image (Figure 40), in which it appeared that some regions of the patterned surface did not bind any IgG.

Unlike the μCP protein substrate, the histogram for the μCP buffer substrate (Figure 44) did not indicate that there were two distinct populations on the surface. The histogram for the μCP buffer substrate was much wider than the histogram for the physically adsorbed protein. The histogram (Figure 44) also did not have as unimodal a distribution of changes in reflectivity when compared to the physically adsorbed protein substrate. This result indicates that the binding of IgG to the μCP buffer surface was not as homogeneous across the entire surface as the binding of the IgG to the physically adsorbed protein substrate.

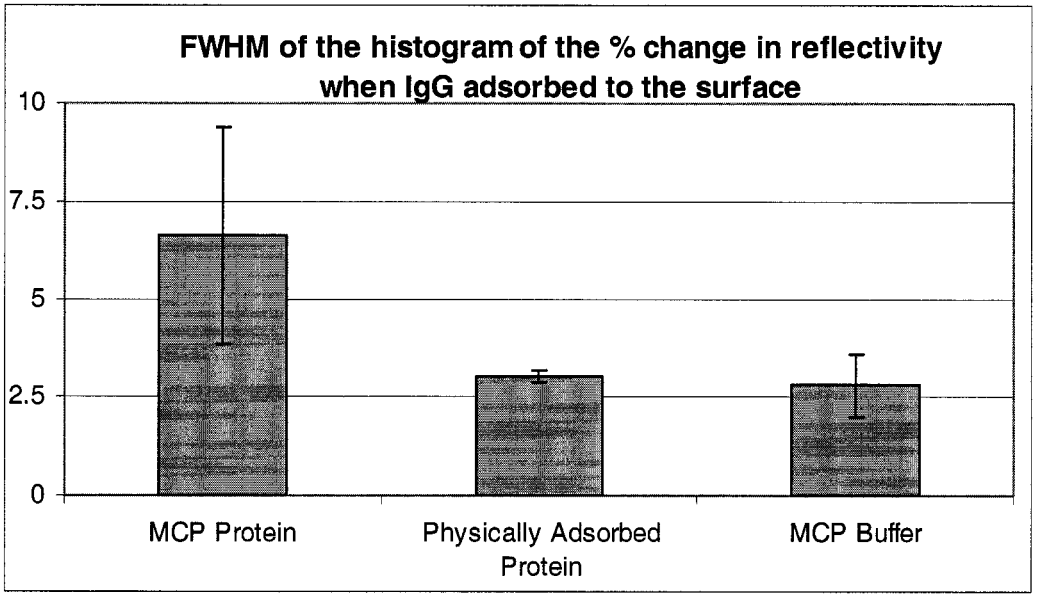

Figure 45. The full-width half max (FWHM) of the histogram of the percent change in reflectivity when an IgG adsorbed to the surface. SPR-imaging results. The error bars represent the replicate standard deviation of the mean FWHM. (n=3) For the μCP protein substrates that were bimodal (n=2), the FWHM was calculated for the largest change in reflectivity for the bimodal systems (i.e., for the pixels for which there was a change in reflectivity).

The FWHM was again calculated to assess the homogeneity of the binding of the IgG to the surface (Figure 45). The μCP protein substrate had the largest FWHM (~ 6%) and a large standard deviation indicating that the binding of IgG to the surface was inhomogeneous and also varied substantially from sample to sample. On the other hand, the FWHM for the μCP protein substrate had a comparable FWHM (~3%) to the physically adsorbed protein substrate and a small standard of deviation. This suggests

that the binding of IgG to the surface is relatively homogeneous across the entire surface and reproducible from sample to sample.

For an ideal microfluidic flow assay, the binding of the IgG to a surface immobilized antigen should be relatively homogeneous across the entire surface and reproducible. Therefore, these results suggest that a surface to which the antigen was physically adsorbed would be more robust for a microfluidic flow assay than a surface to which the antigen was microcontact printed.

XPS and XPS-Imaging

XPS and XPS-imaging experiments were completed to determine the chemical composition at the surface of a substrate microcontact printed with a protein.

XPS

The atomic concentrations of silicon, nitrogen, gold, oxygen and carbon were measured with XPS. The μCP protein and the μCP buffer substrates were contacted with a flat PDMS stamp. The atomic concentration of gold at the surface yields information about the density of the microcontact printed or adsorbed protein. A high atomic concentration of gold would indicate that a significant portion of the gold surface is exposed. This would suggest that the protein has a low surface density. The atomic concentration of nitrogen yields information about the amount of protein present on the substrate as protein is the only molecule that contains nitrogen (barring an outside source of contamination). Microcontact printing work in the literature indicates that when the stamp contacts the surface, silicone oligomers contaminate the surface.[113, 119, 123] The atomic concentration of silicon on the surface can be used to assess the extent of this contamination by silicone oligomers. Protein, organic contaminants, and silicone oligomers would all give rise to the presence of oxygen and carbon on the surface. Therefore, the atomic concentrations of oxygen and carbon cannot be attributed to a single source on the surface of the substrate.

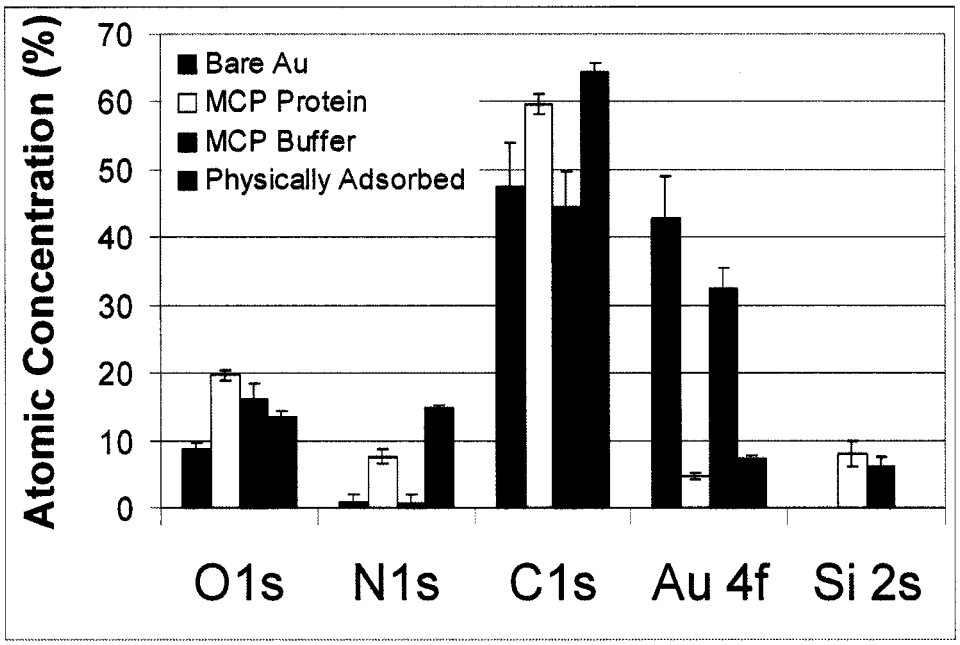

Figure 46. XPS data. (1) Bare gold slide. (2) Microcontact printed protein (μCP protein) on a gold-coated slide. (3) Microcontact printed buffer (μCP buffer) on a gold-coated slide. (4) Physically adsorbed protein. Two samples with 3 spots per sample were analyzed. The error bars represent the standard deviation of the measurements.

Figure 46 presents the atomic concentration of O, N, C, Au, and Si for the experimental group and the control groups.

1) Bare gold. (black in Figure 46). Bare gold becomes contaminated with hydrocarbons upon exposure to the atmosphere. The XPS data indicated that as expected the surface was contaminated with organics (C, O). This substrate also had the largest atomic concentration of gold (~43%), which also is expected as no molecules were intentionally adsorbed to the surface. No silicon was present. There was a small amount of nitrogen contamination on the surface (~1%), which may be due to background nitrogen contamination in the lab environment.

2) μCP protein substrate (white in Figure 46). The atomic concentration of nitrogen (~8%) indicates that protein was transferred to the surface. The surface concentration of gold was significantly reduced compared to the bare gold surface (~43% for the bare gold substrate versus ~5% for the μCP protein substrate), suggesting that the protein had

covered a significant amount of the gold surface. The μCP protein substrate also had some silicon (~6%) on the surface that can be attributed to the silicon found in the PDMS stamp, suggesting that there was transfer not only of protein but also silicone oligomers from the stamp to the surface. The silicone oligomers as well as the protein contributed to the atomic concentrations of oxygen and carbon, which makes it difficult to verify the source of these elements. The presence of silicone oligomers on the surface corroborates the qualitative findings of Ross et al.[123] which detected with XPS the transfer of silicone oligomers to a substrate patterned with microcontact printed BSA.

3) μCP buffer substrate (red in Figure 46). A high atomic concentration of silicon was detected on this surface (~8%), which can be attributed to the silicon found in the PDMS stamp. This corroborates the results of Glastmastar et al.[121] that detected 6.2% (+/-1.6%) of Si on a similar gold substrate. Given the error bars, the data cannot distinguish between the amounts of silicone oligomers transferred to the μCP protein substrate versus the μCP buffer substrate. This sample had a relatively high atomic concentration of gold (~33%), suggesting that the entire surface was not covered with the silicone oligomers. This corroborates the SPR-imaging data (Figure 28 and Figure 31) in which the pattern of silicone oligomer on the surface was very inhomogeneous. Once again, there was a small amount of nitrogen contamination on the surface (~1%), which may be due to background nitrogen contamination in the lab environment. The silicone oligomer also contributed to the atomic concentration of oxygen and carbon, but once again, it is difficult to verify the source of these elements.

4) Physically adsorbed protein substrate (blue in Figure 46). The atomic concentration of nitrogen for this sample (~12.5%) was higher than the amount present on the μCP protein substrate (~8%). This result suggests that more protein adsorbed to the physically adsorbed substrate than to the μCP protein substrate. The atomic concentration of gold was also reduced (~7%), indicating that most of the gold surface had been covered with protein. However, the atomic concentration of gold (~8%) was slightly higher than the

atomic concentration of gold for the μCP protein substrate (~5%), suggesting that more of the gold surface was exposed. No silicon signal was present.

XPS-imaging

As mentioned in the Materials and Methods section, several technical difficulties were encountered during the XPS-imaging experiments. It was not possible to collect an XPS-image for the μCP buffer substrate as it appeared to be uniform in atomic composition across the entire surface. It also was not possible to image an element other than gold for the μCP protein substrate. It is likely that inelastically scattered gold electrons created a very large background signal that made it difficult to isolate the signal from the other elements (N, C, Si, and O). To overcome these limitations, the substrate was imaged for Au(4f) (Figure 47). The XPS image of Au(4f) yielded the expected results for a PDMS stamp with recessed 200 micron x 200 micron square features spaced 200 microns apart – namely a high Au(4f) signal in the square feature regions that did not contact the stamp.

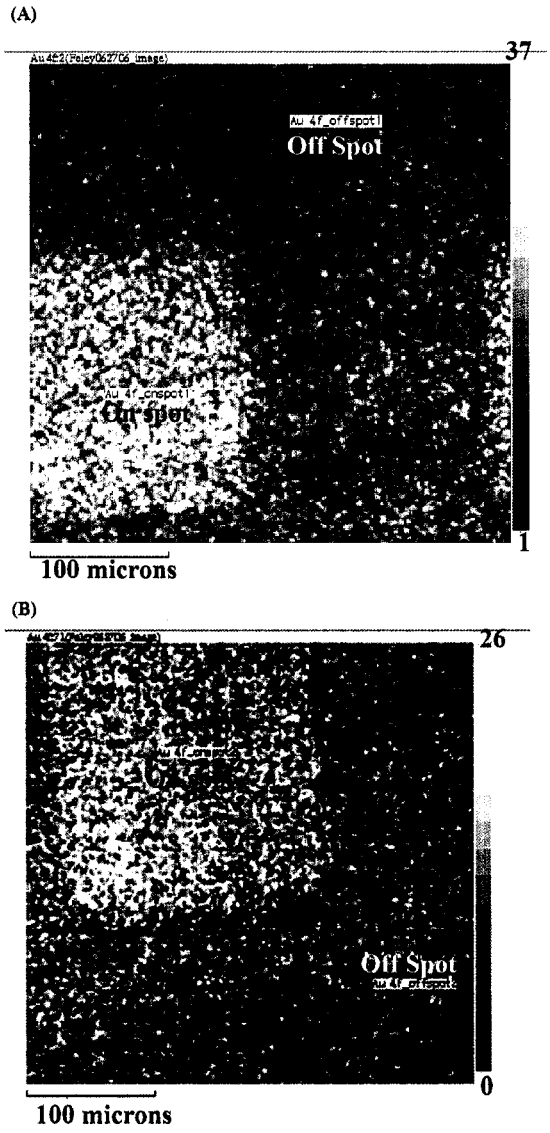

Figure 47. XPS-images of Au (4f). The larger the gold signal, the higher the surface atomic concentration of gold. The locations *"on spot"* refer to areas where the protein-functionalized patterned PDMS stamp *did not contact* the gold surface. The locations *"off spot"* refer to areas where the protein-functionalized patterned PDMS stamp *did contact* the gold surface.

Based on the locations of the high and low atomic concentration of gold, local regions of interest (ROI) XPS survey scans (Figure 48) for N(1s), C(1s), Si(2s), O(1s), and Au(4f) were completed in the regions unmodified (ROI unpatterned – high atomic concentration of gold) and modified (ROI patterned – low atomic concentration of gold) by contact with the protein-functionalized PDMS stamp. Nitrogen (Figure 48) was present only in

the region where the PDMS stamp contacted the surface. This suggests that protein was transferred only through direct contact of the stamp with the surface. The atomic concentration of gold for the ROI patterned surface was lower. This would be expected since the transferred protein layer would cover the gold surface.

Silicon was detected across the entire surface, with an atomic concentration ranging from ~7-10%. Given the error bars and sample size (n=2), it is difficult to distinguish between the amount of silicon present on the ROI patterned and unpatterned surfaces. However, it is not entirely intuitive that the unpatterned region may have slightly more Si present on the surface (~10% which is comparable to the atomic percentage that Glasmastar et al. [121] detected with XPS (non-imaging) for gold substrates contacted with PDMS stamps that were *not* inked with protein in buffer but water). Ignoring the SPR-imaging data (Figure 27), the fact that slightly more Si was present on the ROI unpatterned substrate (where the stamp did not contact the surface) suggests that the hypothesis presented by Glasmastar et al. [121] that suggested that the patterned stamp introduced more silicone oligomers to the surface due to the transport of the oligomers down the sidewalls of the featured stamp to the substrate possibly due to capillary forces may be correct. However, given the SPR-imaging data (Figure 27), the presence of silicon across the entire surface may more likely be an artifact of the ultra high vacuum required to conduct XPS as the SPR-image (Figure 27) which was collect under ambient conditions clearly indicated that the PDMS oligomers were transferred in a pattern during the printing process and in the locations the stamp directly contacted the substrate. However, the silicone oligomers may spread across the entire surface when exposed to the ultra high vacuum. Another ultra high vacuum technique, TOF-SIMs, that analyzed a gold substrate patterned with a stamp inked only with buffer (no protein) also saw the presence of silicone oligomer over the entire surface[121] further giving support to this hypothesis.

Nitrogen was not located in the unpatterned regions (ROI unpatterned). This suggests that even though the protein was transferred to the surface with silicone oligomers by the

PDMS stamp once the protein adsorbs to the gold, unlike the silicone oligomers, it does not spread across the entire substrate once exposed to ultra-high vacuum conditions.

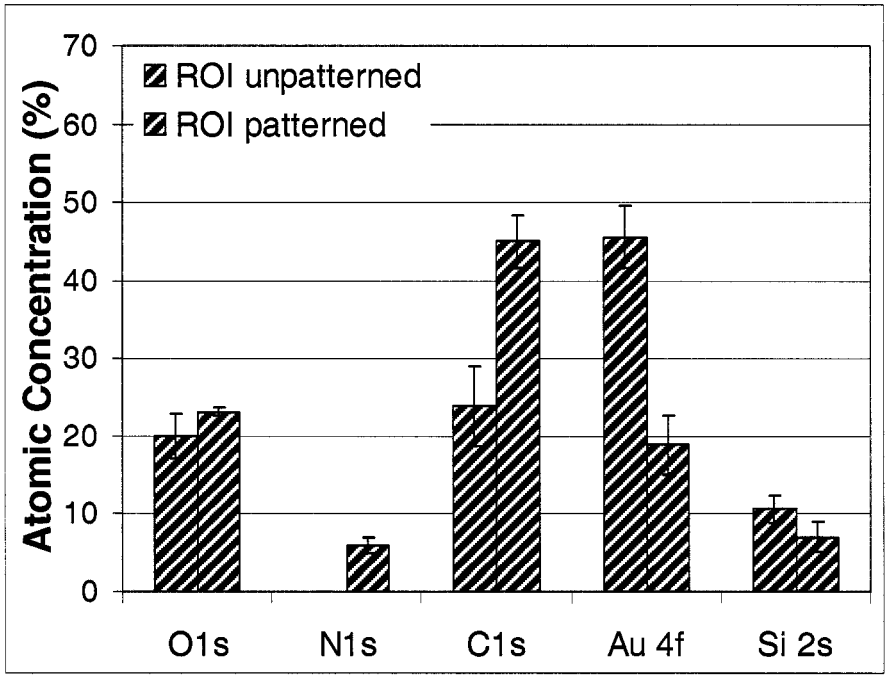

Figure 48. XPS region of interest (ROI) scans of gold slides microcontact printed with an IgG. Two regions were analyzed: (1) *Unpatterned* – the area where *the PDMS stamp did not contact* the surface and (2) *Patterned* – the area in which *the PDMS stamp did contact* the surface and protein should have been transferred to the gold surface. The error bars represent the standard deviation in the measurement (n=2).

Comparisons of the spectroscopy data, in which a flat PMDS stamp transferred protein to a gold surface (the μCP protein substrate), and the XPS-imaging data (ROI patterned and unpatterned), in which a patterned PDMS stamp transferred protein to a gold surface (Figure 49), indicate that there are some discrepancies between the data sets. The discrepancies could be a result of the redistribution of the silicone oligomer from the patterned to the unpatterned regions on the substrate under the ultra-high vacuum.

Ideally, the atomic composition of the ROI unpatterned surface (region of the surface where the PDMS stamp *did not contact* the surface) should correlate with the atomic composition of the bare gold substrate. The atomic composition of the ROI patterned surface (region of the surface where the PDMS stamp *did contact* the surface) should also correlate with the atomic composition of the μCP protein substrate.

The ROI patterned surface and the μCP protein substrate had similar atomic concentrations of silicon, oxygen, and nitrogen. However, the atomic concentration of gold was much higher for the ROI patterned surface (~18% atomic concentration of gold versus ~4% atomic concentration of gold for the μCP protein substrate). The atomic concentration of carbon was lower for the ROI patterned surface (~45% of the atomic concentration was carbon versus ~59% of the atomic concentration was carbon for the μCP protein substrate). The higher atomic concentration of gold and the lower atomic concentration of carbon for the ROI patterned surface may also be an artifact of the exposure of the substrate to an ultra high vacuum. The silicone oligomers transferred with the protein to the surface may have spread across the entire surface, thereby exposing bare gold in regions that contacted the PDMS stamp and reducing the amount of carbon present in those locations due to the loss of the silicone oligomer.

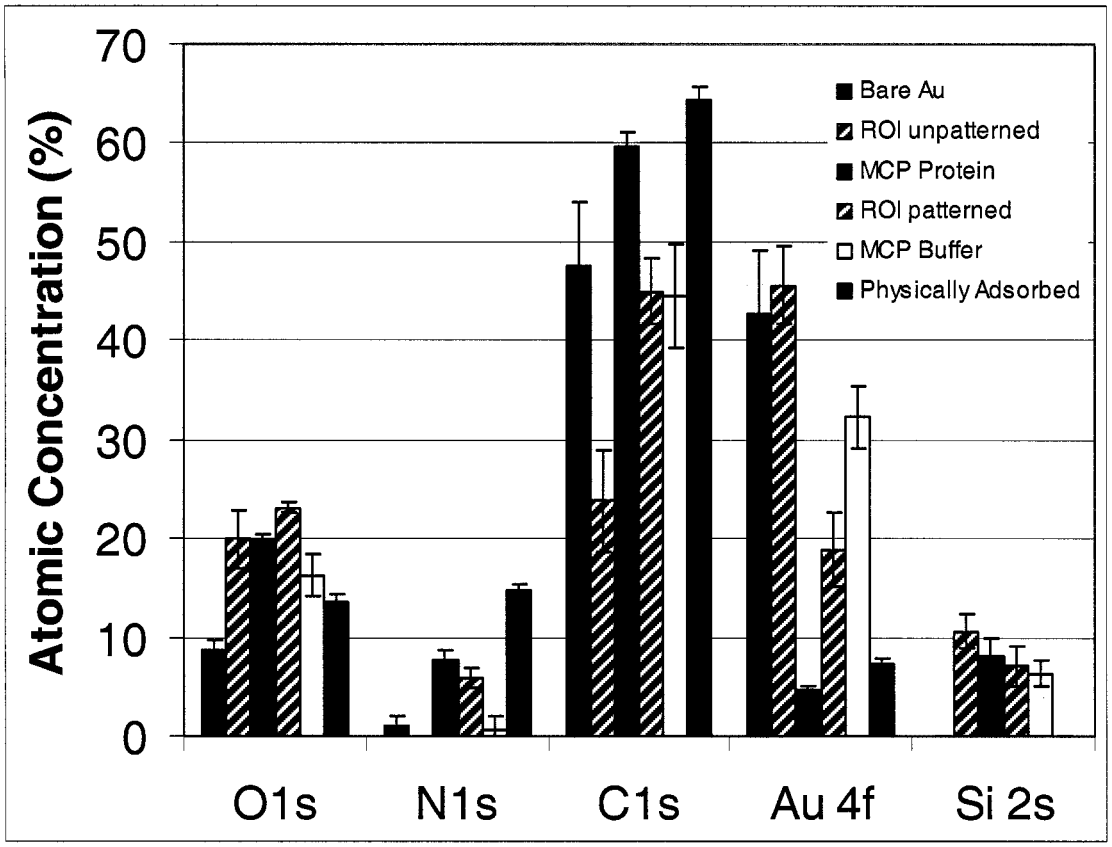

Figure 49. Comparison of XPS data – imaging and spectroscopy. Four data sets (Bare Au, μCP buffer, μCP Protein, and Physically Adsorbed Protein - see Figure 46) are spectroscopy data on modified gold-coated slide surfaces in which flat PDMS stamps were used for the μCP protein substrate and the μCP buffer substrate. The ROI patterned regions (where a PDMS stamp functionalized with a protein touched the surface) and unpatterned (regions where a PDMS stamp did not touch the surface – see Figure 48) are XPS imaging data sets in which a stamp with 200 micron × 200 micron recessed features and inked with a solution of protein contacted a gold-coated slide.

The ROI unpatterned surface (region where the PDMS stamp *did not contact* the surface) had higher atomic concentrations of silicon and oxygen than the bare gold substrate. This data once again suggest that silicone oligomer spread across the entire surface when the substrate was exposed to ultra-high vacuum. The atomic concentration of carbon for the ROI unpatterned was lower than the atomic concentration of carbon for the bare gold substrate (~24% versus ~48%). This may possibly be due to a reduction in the amount of organic contaminants on the ROI unpatterned surface as compared to on the bare gold substrate. However, as stated previously, it is difficult to determine the source of the

carbon on the surface since it may be the result of organic contaminants and/or silicone oligomers. A similar atomic concentration of gold was present in the ROI unpatterned surface and the bare gold substrate (~45% versus ~42%), suggesting that a similar percentage of the surface was covered by organic contaminants (bare gold) or silicone oligomer and/or organic contaminants (ROI unpatterned).

3.5. Conclusions

Protein and thiols were microcontact printed on gold. SPR-imaging experiments indicated that the alkyl thiol patterns were uniform and had well-defined micron-scale features. The microcontact printed protein pattern – the μCP protein substrate – also had well-defined micron-scale features. However, the patterned protein was not as homogeneous as a surface to which the protein was physically adsorbed. There was limited non-specific adsorption of BSA to the μCP protein substrate (~3% change in reflectivity). The non-specific adsorption of BSA to the μCP protein substrate was also relatively uniform across the entire surface when compared to the physically adsorbed protein substrate. An IgG from solution bound to its antigen – the microcontact printed protein. Less IgG bound to the microcontact printed antigen than a physically adsorbed antigen. The binding of IgG to the microcontact printed antigen was not homogeneous. Some regions bound no IgG, and other regions bound a significant amount of IgG. XPS data of the microcontact printed protein indicate that (1) silicone oligomer transferred to the surface along with the protein, (2) the gold surface was densely covered with the layer of protein/silicone oligomer, and (3) less protein was transferred to the gold surface for the microcontact printed substrate versus the substrate to which protein was physically adsorbed.

Chapter 4: Microcontact printing proteins inside of microstructures

4.1 Objective

1) Explore the ability to microcontact print proteins inside three-dimensional microstructures.
2) Determine if the patterned protein retains its structure.

4.2 Related Publications

Work for this aim was completed at IBM Research Labs in Rueschlikon, Switzerland. The work was completed under the supervision of Dr. Emmanuel Delamarche. Richard Stutz was responsible for the microfabrication. Dr. Heinz Schmid assisted with the development of a pressure sensor as well as fluorescence measurements. A research article has been published on this work:

Foley, J.; Schmid, H.; Stutz, R.; Delamarche, E. (2005). "Microcontact Printing of Proteins Inside Microstructures." Langmuir. 21:11296.

4.3 Materials and Methods

Chemicals and reagents

All antibodies were purchased from Sigma. The proteins were diluted in phosphate-buffered saline (PBS) (Sigma, St. Louis, MO). Deionized water (produced by the Simplicity 185 System, Millipore at the IBM Research Labs) was used throughout the work.

Fabrication of the molds for the PDMS stamps

Molds in silicon wafers (Siltronix, Geneva, Switzerland) were microfabricated using photolithography and a deep reactive ion etcher (STS ICP, Surface Technology Systems plc, Newport, U.K.). A thin layer (~40 nm) of Teflon was sputtered onto the silicon

master to improve the release of PDMS from the mold. The silicon molds had 3-μm-deep etched features. These molds created stamps with 2-μm-diameter posts positioned 12 μm apart and 5-μm-wide lines spaced 10 μm apart were used in this work.

Fabrication of the PDMS stamps

PDMS stamps were prepared by dispensing Sylgard 184 prepolymers (Dow Corning, Midland, MI) at a 10:1 ratio of polymer to curing agent onto the silicon. An automatic mixer (DOPAG Micro-ix E, Cham, Switzerland) dispensed the PDMS. In all cases (planar and patterned stamps), PDMS was cured at 60 °C for at least 24 h and the stamps had a thickness of ~3-5 mm. Prior to being used, the PDMS stamps were sonicated in a 1:1 solution of isopropanol:deionized water or ethanol: deionized water for 10-15 min, rinsed with deionized water, and blown dry under N_2.

Gold coated microfluidic networks (MFNs)[27, 176] (Figure 50) were fabricated in silicon wafers using photolithography and a deep reactive ion etcher (STS ICP, Surface Technology Systems plc, Newport, U.K.).

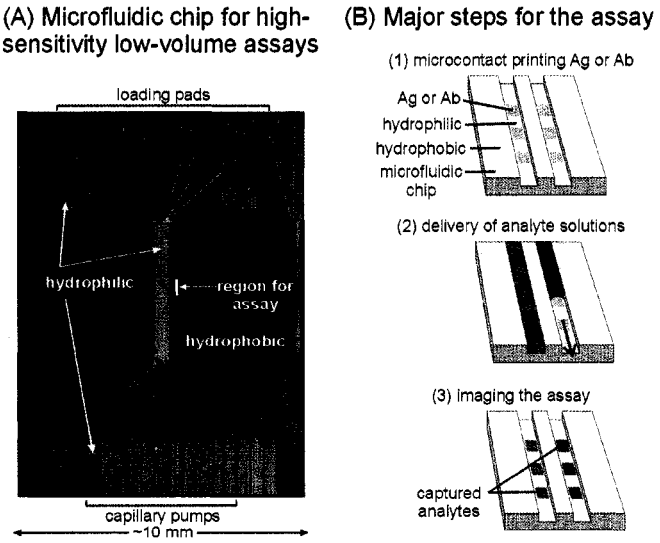

Figure 50. Microfluidic Network (MFN). A MFN fabricated in silicon and coated with gold.

Three depths of MFNs were studied: 2, 5, and 15 μm. Some MFNs were sputtered with Ti and Au (LA440S, VonArdenne Anlagetechnik GmbH, Dresden, Germany). 5 nm of Ti

(adhesion layer) and 40 nm of Au were deposited on the 2-μm and 5-μm-deep MFNs. In the case of the 15-μm-deep MFNs, 5 nm of Ti and 150 nm of Au were deposited. The MFNs were diced and separated (Dicing Saw 8003 from ESEC). Before each use, the MFNs were treated with ozone (UV-Ozone Photoreactor PR -100, Ultra-Violet Products, Upland, CA) for 30-40 min to remove contaminants from their surface. Some of the MFNs were modified with alkanethiols to control the wetting and protein-repellency of the various parts of the MFNs. A clean flat PDMS stamp inked with a solution of hexadecane thiol (HDT) was placed onto the MFN and removed. The MFN was covered with a solution of the hydrophilic HS-PEG for ~1 min, rinsed with ethanol, and dried under a stream of N_2.

Microcontact printing of proteins onto planar surfaces

Clean stamps with micron-sized features were inked with protein solutions (~200-500 microliters at 0.5 mg mL^{-1} in PBS) for 30-40 min at room temperature. The stamps were rinsed with solutions of PBS, PBS with 0.05% Tween 20, and deionized water, and blown dry under a stream of N_2. The stamp inked with proteins was placed onto the substrate for ~30-60 seconds and then removed.

Microcontact printing of proteins into three dimensional devices

To print proteins into microstructures, a controlled pressure was applied to the back of the stamp inked with protein. The pressure was directed toward the microstructures by placing a small PDMS piece (~4 mm^2 in area) on top of the stamp. This PDMS piece was centered over the microstructures of the MFN targeted for printing. The substrate, the protein-coated PDMS stamp, and the small PDMS piece were slowly raised with a micrometer-controlled stage and pressed against an optically transparent piece of plastic. As the MFN and stamp were raised, the collapse of the stamp into the microstructures was observed optically with a binocular (Nikon). A strain gauge measured the force applied to the stamp. To print into the 2-, 5-, and 15-μm-deep structures, pressures of ~0.2, ~4.2, and ~7.0 MPa were applied, respectively. Once the stamp contacted the

bottom of the microstructure, the stamp remained in that position for ~1 min and was then removed.

Fluorescence imaging

The fluorescent images were collected with a microscope (Labophot-2, Nikon) equipped with optical filters and captured by a cooled, low-noise CCD camera (ST-8, SBIG, Santa Barbara, CA). The images were not background or flat field corrected. The fluorescence images had an exposure time of 1 s.

Assays

Clean MFNs with 5-μm-deep features were modified with alkanethiols to generate hydrophobic and hydrophilic regions on the MFNs. Anti-guinea-pig IgG developed in rabbit (Sigma) was microcontact-printed onto the MFN with a PDMS stamp having patterned lines. Pressure was applied to the stamp to print in the recessed surfaces of the MFN. A solution of BSA in PBS at 1% w/w covered the MFN for 30 min at room temperature. The MFN was rinsed with solutions of PBS, PBS with 0.05% Tween 20, and deionized water, and dried under a stream of N_2. A 0.05 mg mL^{-1} solution of tetramethylrhodamine isothiocyanate (TRITC, red, $\square_{FE}$ = 570 nm) labeled anti-rabbit IgG developed in goat was used to cover the entire MFN for 30 min. The MFN was rinsed with solutions of PBS, PBS with 0.05% Tween 20, and deionized water, dried under a stream of nitrogen, and imaged with the fluorescence microscope using an exposure time of 1 s.

4.4 Results and Discussion

All of the results and figures presented in this portion of the proposal have been published. Captions as well images were directly copied from the publication.[173]

Microcontact printing has successfully patterned proteins on planar sensing surfaces. However, many microfluidic devices fabricated in silicon or glass are non-planar and cannot be patterned with conventional μCP. This is the first reported attempt to

functionalize the recessed regions of microstructures with a protein using μCP. To pattern recessed regions of microstructures, a force is applied to the back of the elastomeric PDMS stamp (Figure 51A) enabling the stamp to deform, contact the bottom of the microstructures and pattern the recessed surfaces. For this work, fluorescently labeled antibodies were patterned onto a gold microfluidic network (MFN) which was used for immunoassays. A fluorescence microscope imaged the patterns of proteins.

The aspect ratio of the microstructure for this printing method was found to be significant. The higher the aspect ratio, the more pressure was required to pattern the microstructure. A PDMS stamp with 3-μm-high lines printed fluorescently-labeled Abs into two types of 15-μm-deep features on a bare gold substrate. A well-defined pattern of protein was printed in a large microstructure (Figure 51 B and C) with a low aspect ratio (~1:100) and required only ~0.2 MPa of pressure. Higher aspect ratios (1:2) proved difficult to pattern (Figure 51D) and required ~ 7 MPa for the stamp to contact the bottom of the microstructure. The pattern was distorted indicating the high pressures needed deformed the stamp. At these high pressures, the protein patterns were not uniform. The regions where the stamp was subject to high pressure often did not have as much protein present and streaks of proteins leading toward the edge of the stamp (data not shown) were observed. This data suggest that when subjected to high pressures the protein behaved as a lubricant. Residue – possibly PDMS – also deposited on the surface, and was visible to the naked eye.

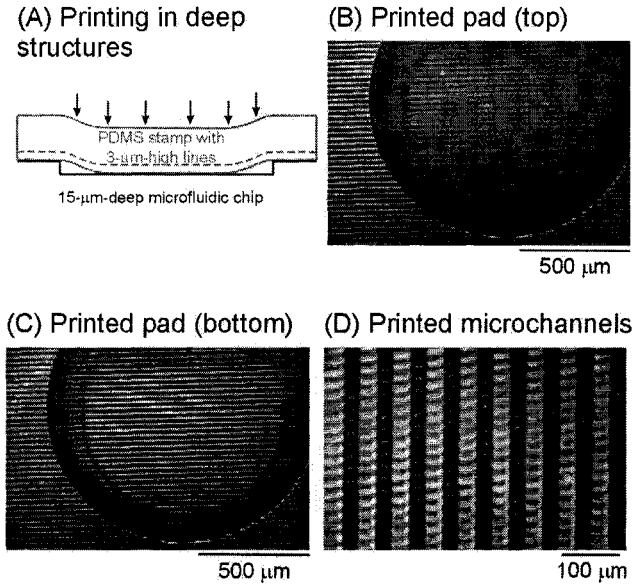

Figure 51. (A) Microcontact printing of proteins into 15-μm-deep microstructures using a PDMS stamp having 3-μm-high lines. (B)-(D) Fluorescence microscope images of TRITC-labeled antibody microcontact-printed around the loading pad of an Au-coated MFN (B), inside the loading pad (C), and across a 30-μm-wide microchannel (D) using the method shown in (A). A pressure of ~0.2 MPa was used to print the loading pad whereas ~7 MPa were needed to produce contact between the stamp and the recessed regions of the microchannels.

Well-defined protein patterns in the recessed region of a 5 μm-deep microchannel were produced with a stamp having 3-μm-high and 5-μm-wide lines (Figure 52 B-D). The reduction in the aspect ratio (1:6) improved the quality of the pattern and reduced the amount of pressure required to ~4.7 MPa. The fluorescent images of the PDMS stamp after printing indicated where protein was transferred from the stamp to the gold surface. (Figure 52 E and F) These images indicated that the recessed regions of the stamp collapsed on the mesas, thereby transferring protein to those regions.

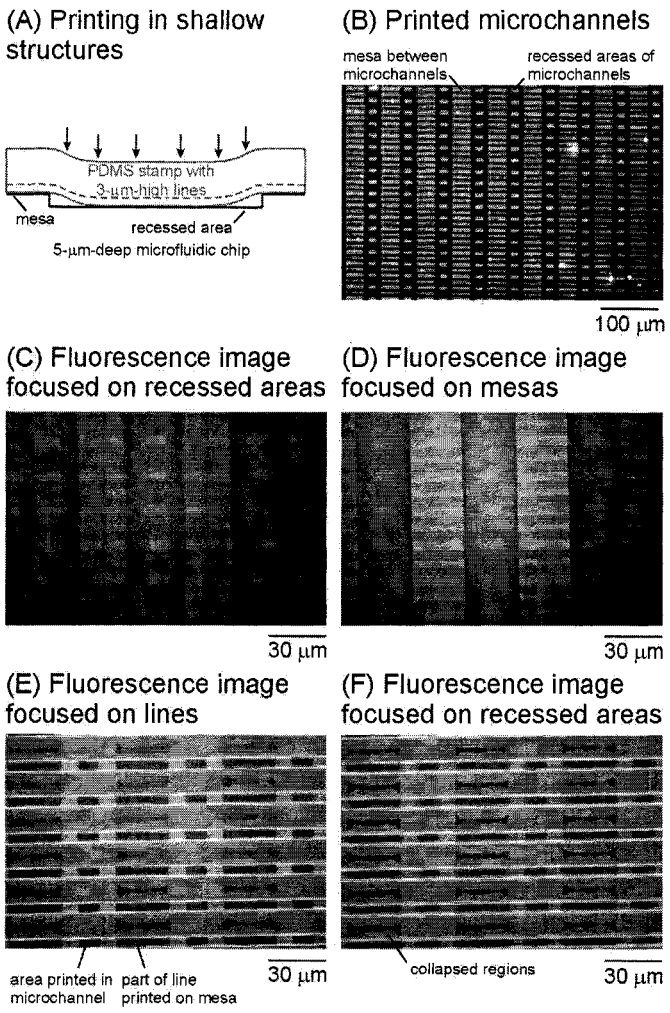

Figure 52. (A) Microcontact printing of proteins into 5-μm-deep microstructures using a PDMS stamp having 3-μm-high lines. (B)-(D) Fluorescence microscope images of TRITC-labeled Abs microcontact-printed into Au-coated microstructures using the method shown in (A). (B) Abs microcontact-printed into 30-μm-wide microchannels. (C) and (D) Higher-magnification images of the microcontact-printed antibody, focused on the bottom of the microchannels (C) and on the mesas (D). (E) and (F) Fluorescence microscope images of the PDMS stamp after printing reveal the areas from which antibody transferred from the stamp to the substrate. In (E), the focus is on the raised lines of the PDMS stamp, whereas in (F) it is on the recessed regions of the PDMS stamp. Under the pressure required to print in the 5-μm-deep microstructures, the recessed regions of the stamp collapsed and contacted the mesas of the MFN, thereby transferring proteins to the substrate.

Small discrete features – 2-μm-wide posts – were printed into a 5 μm-deep microchannel creating uniform and well-defined patterns (Figure 53). The small posts reached the bottom of the microchannel generating small discrete features, but the posts collapsed onto the mesas and patterned the entire surface.

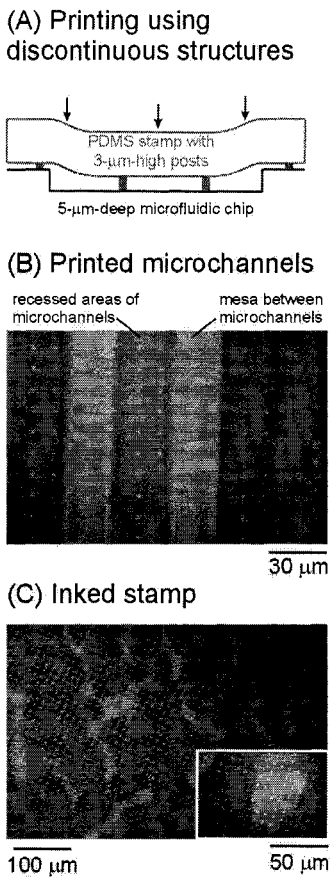

Figure 53. (A) Microcontact printing of proteins into 5-μm-deep structures using a PDMS stamp having 2-μm-diameter and 3-μm-high post features. (B) Fluorescence image of TRITC-labeled antibody printed into 30-μm-wide, Au-coated microchannels. (C) Fluorescence image of the PDMS stamp before it was used to print the antibody, illustrating the peculiar wetting characteristics of the stamp.

To determine if the proteins printed inside the microstructures retained some if any of their structural integrity, an immunoassay was completed in which unlabeled protein printed into the microchannel was exposed to a fluorescently labeled antibody. The printed protein was recognized by a fluorescently-labeled antibody (Figure 54) suggesting some of the structure of the protein remained. Further experiments are required to verify that the activity of a protein, such as an enzyme, is not reduced when printed with this method.

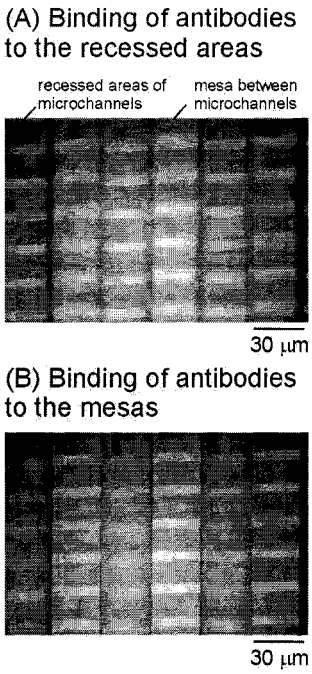

Figure 54. Fluorescence immunoassay in which Abs from solution bind to their specific antigen, which were microcontact-printed into 5-μm-deep microstructures using the method shown in Figure 51. (A) and (B) Fluorescence microscope images of TRITC-labeled Abs, which bound to the antigens in the 5-μm-deep microchannels and on the mesas separating the microchannels. The microchannels and mesas of this Au-coated MFN were derivatized with HS-PEG and HDT, respectively.

4.5 Conclusions

A novel method of patterning proteins inside recessed microstructures using microcontact printing has been demonstrated. Pressure applied to the back of an elastomer PDMS stamp inked with protein serves to contact the stamp to the surface. Protein transferred to the recessed surface. An immunoassay was conducted in which protein patterned with this method was recognized by an antibody. This result indicates that this patterning method does not significantly alter the structure of the protein as an antibody is still capable of recognizing its antigen.

Chapter 5: Computational model and experiments of streptavidin-biotin microfluidic assays

5.1 Objectives

1) Computationally model a standard microfluidic flow assay of streptavidin binding to a biotin-functionalized surface.
2) Verify the model results with SPR imaging experiments.
3) Explore the assay parameters that can influence the performance of an assay.

The purpose of this research is to develop computational models to aid in the understanding of microfluidic surface binding assays and confirm the validity of the model with SPR imaging experiments. The streptavidin/biotinylated alkyl thiol surface binding system developed by Nelson et al.[88, 101] and described in the Background (Chapter 2) was chosen as the model assay format due to the availability of experimentally determined kinetic and surface parameters. This model system is also widely used in the Yager group. The basic principles of surface binding microfluidic assays explored with this model format will serve as a basis of understanding of other microfluidic surface binding assay formats. Although some discussion of methods of quantification will be briefly described in this chapter, the next chapter (Chapter 6) will focus heavily on methods to quantify the amount of analyte for another assay format, the indirect microfluidic immunoassay.

The focus of this chapter is the surface binding pattern of streptavidin in a straight microchannel and the distribution of protein within the bulk of the microchannel as well as the influence of flow rate and the diffusion coefficient of the binding species on the surface binding profile. From this information, some guiding principles in SPR imaging assay design will be introduced. The model, confirmed experimentally, in future will serve as a tool to rapidly optimize and explore other designs (completed in Chapters 6-8). The results presented in this chapter are also frequently referred to in Chapter 8. The aim of the grant for which this research was completed was to develop a rapid microfluidic

assay. Therefore, model results have focused on the first five to ten minutes of the assay. Furthermore, quantification of nanomolar concentrations of small molecules – cortisol and phenytoin – in saliva was the focus of this research and hence the range of concentrations explored with the model.

5.2 Initial Design Considerations

Due to computer memory constraints and solution oscillations, the computational modeling is limited. These computational constraints limit the ability of the model to simulate the larger Peclet numbers.

5.3 Materials and Methods

Computational Simulations

All computational simulations were completed with the commercially-available finite element method software, COMSOL® (Version 3.3, Comsol, Inc., Burlington, MA). For a detailed description of the governing equations of each model as well as a detailed explanation of the modeling protocol, see Appendices A and B, respectively. The modeling protocols are described briefly below.

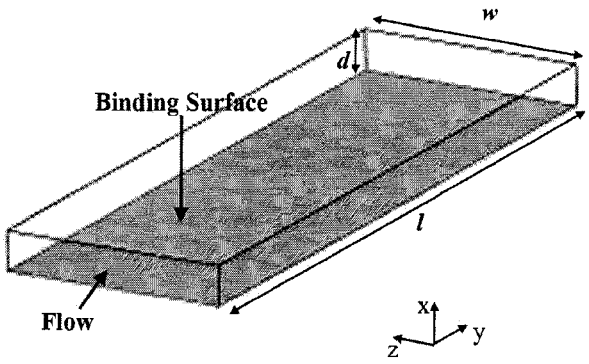

Figure 55. Straight microchannel geometry. For the simulated microchannel, d=90 microns, w=500 microns, and l=1.5 mm. For the experimental microchannel, d=82 microns and w=500 microns. The biotinylated surface to which streptavidin will bind is indicated.

Streptavidin assay

In the three-dimensional geometry of the assay (Figure 55), a portion of the surface of the channel is functionalized with biotinylated alkyl thiol to which streptavidin can bind. This system has been well-characterized by Nelson et al.[101] and gives experimentally measured kinetic and surface density parameters that can be used in the COMSOL® model. In the model, fully developed flow is imposed at the inlet of the device by solving the Poisson equation in two dimensions, yielding a fully developed parabolic flow profile. This velocity profile is mapped to the inlet of the three-dimensional model to impose a fully-developed flow profile at the inlet. COMSOL® then solves the steady-state Navier-Stokes equation. Next, the transient convection-diffusion mode and weak boundary mode are solved simultaneously using the fluid flow profile solved by the Navier-Stokes mode. The modeled flow rates are listed in Table 2. The dimensions of the experimental microchannel were slightly different than the dimensions of the modeled microchannel (see Figure 55) due to the destruction of an SU8 mold during experiments. The important fluid mechanic and mass transport parameters were calculated for the model, and the experimental systems are listed in Table 2 and Table 3 respectively. When solving the Navier-Stokes mode, the mesh consisted of 10,259 elements and 91,461 degrees

of freedomen. When solving the convection-diffusion and surface binding modes, the mesh consisted of 14,085 elements and 381,197 degrees of freedom. The governing equations for the surface binding reaction are:

$$c_{SA} + \theta \underset{kdes}{\overset{kads}{\rightleftarrows}} c_s \qquad \text{Equation 7}$$

$$\frac{dc_s}{dt} = k_{ads} c_{SA}(\theta_0 - c_s) - k_{des} c_s \qquad \text{Equation 8}$$

where c_{SA} is the streptavidin concentration in the bulk of the microchannel, c_s is the surface concentration of bound streptavidin, θ_0 is the initial surface concentration of antibody binding sites, θ is the surface concentration of antibody binding sites, and k_{ads} and k_{des} are the adsorption and desorption kinetic parameters.

Table 1. Surface binding parameters for the modeled system.[101] Binding parameters and density were calculated from the cited reference.

θ_0 (moles m^{-2}) Initial streptavidin binding sites on the surface, calculated based on experimental findings for a similar experimental situation.	3.9867×10^{-8}
c_0 (nM) initial concentration of streptavidin	20
ρ (kg m^{-3})	1000
μ (kg m^{-1} s^{-1})	1×10^{-3}
Base microchannel depth (m)	90×10^{-6}
Microchannel width (m)	500×10^{-6}
D_{SA}(m^2 s^{-1}) diffusion coeffient of streptavidin	7.4×10^{-11}
k_{ads} (m^3 $moles^{-1}$ s^{-1})	4000
k_{des} (s^{-1})	3×10^{-6}

Table 2. Velocities, Reynolds numbers, and Peclet numbers for the modeled straight microchannels.

	Average velocity (m/s)	Maximum velocity (m/s)	Re	Pe
5 nL/s	1.11E-04	1.67E-04	1.00E-02	1.35E+02
25 nL/s	5.56E-06	8.33E-06	5.00E-02	6.76E+00
50 nL/s	1.11E-03	1.67E-03	1.00E-01	1.35E+03

Experimental methods

Chemicals and reagents

Streptavidin (US Biologics, MA, USA) was diluted in phosphate-buffered saline (PBS, pH 7.4) (Sigma, St. Louis, MO). Deionized water (generated with a Barnstead

International still, Dubuque, Iowa) was used throughout the work. Biotinylated alkyl thiol (BAT) (Iris BioTECH GmbH, Germany – custom synthesis) and ethylene glycol (Prochimia, Sopot, Poland) were diluted in absolute ethanol.

Microfluidic device fabrication

The straight microchannel was constructed in PDMS (see Figure 55 for channel dimensions). Once again, molds for PDMS microfluidic channels were fabricated using established soft photolithography methods.[64, 175] The upstream portion of a PDMS chevron device (before the chevron microstructures) served as the straight microchannel for the experiments. The chevron microchannel required two layers of SU8, which must be precisely aligned to ensure that device geometry is accurate. A protocol for two-layer SU8 fabrication was adopted from Dr. Elena Garcia. The design of a photolithography mask was completed using AutoCAD 98 (Microsoft, Redmond, WA) and Adobe Illustrator 10 (Adobe Systems Inc., San Jose, CA). The first mask generated the rectangular base of the microchannel. The second mask outlined the chevrons that sit on top of the rectangular duct. When designing the mask, special attention was paid to the placement and geometry of the alignment marks. After several iterations it was determined that the optimal alignment marks were crosses located on either side of the microchannel along the same axis. Upon exposure to UV light, the first mask generated a small cross. After spinning the second layer of SU8 onto the wafer, the small cross could be visualized. The second mask had a large cross in which the smaller cross on the wafer was centered.

To create the photolithography mask, black and white transparencies were printed (Publication Services, University of Washington, Seattle, WA). At the Washington Technology Center (WTC), the first layer of SU8 (MicroChem, Newton, MA) was spun (Solitec Spinner, Milpitas, CA) onto a clean, three-inch silicon test wafer (Silicon Sense, Nashua, NH). The wafer was pre-baked to densify the SU8 film. A four-inch infrared contact aligner (AB-M, San Jose, CA) exposed the wafer to ultraviolet light, thereby polymerizing the exposed regions of the SU8. Given the viscous and adhesive properties

of the SU8, the WTC required that the wafer be placed onto the back of a clean, four-inch test wafer to ensure that SU8 did not contaminate the four-inch infrared contact aligner. After the first exposure, a second layer of SU8 was spun onto the wafer. The wafer was soft-baked, post-baked, and then incubated in a solution of SU8 developer (MicroChem, Newton, MA), which removed any unpolymerized SU8. The wafer was once again baked to harden the SU8. The depth of the SU8 features were measured with the P15 surface profilometer (Tencor, San Jose, CA) located in the WTC.

The PDMS microchannels were prepared by dispensing Sylgard 184 prepolymers (Dow Corning, Midland, MI) at a 10:1 ratio of polymer to curing agent onto the SU8 molds. To create inlets and outlets to the microchannel, silicone tubing (Cole Parmer, Vernon Hills, IL) was glued to the inlet and outlet with DuCo Cement (Devcon, Riviera Beach, FL) and allowed to dry. Then, Sylgard 184 prepolymers (Dow Corning, Midland, MI) at a 10:1 ratio of polymer to curing agent were dispensed onto the SU8 mold to create the PDMS microchannel. Upon drying the PDMS microchannel was removed with a razor blade. In initial studies the PDMS was placed onto the slide substrate, but bubbles tended to form. In order to overcome this difficulty, the PDMS device was activated in oxygen plasma to create a more hydrophilic surface (oxygen pressure 30 psi for 1 minute at 600 Watts Plasma Preen II 973, Plasmatic System, Inc., North Brunswick, NJ). The PDMS was masked such that only the microchannel itself was exposed to the oxygen plasma.

Gold-coated slide preparation

A one nm adhesion layer of chromium and a 45 nm layer of gold were electron beam (CHA 600, CHA Industries, Fremont, CA) deposited onto clean glass microscope slides (Fischer Scientific, Pittsburgh, PA) at the Washington Technology Center (WTC). Gold-coated (45 nM Au, 1 nM Cr for adhesion) glass substrates were cleaned under oxygen plasma (oxygen pressure 30 psi) for one minute (Plasma Preen II 973, Plasmatic System, Inc., North Brunswick, NJ) at 600 watts. Due to leaks at the PDMS/gold interface, gold was deposited on the gold-coated slide only in regions where the microchannel existed. Stainless steel masks (Precision Image Corporation, Bothell, WA) were placed onto clean

gold slides in the electron beam evaporator during the gold deposition. The oxygen plasma-cleaned slide was patterned with thiols using the "wicking method," a technique developed and optimized by Dr. Kjell Nelson and Neil Geisler. Briefly, a 10 mil sheet of mylar (Fralock, Canoga Park, CA, USA) was cut using a carbon dioxide laser (M25, Universal Laser System, Inc., Scottsdale, AZ) to serve as a wicking mask. In the mask, a 1 mm diameter hole was cut. The mask was placed onto the slide using an alignment jig. A 0.5 mM solution of BAT/PEG (10% BAT, 90% HS-PEG) was introduced to the hole cut in the mylar mask. Capillary forces wicked the solution underneath the mask. The thiol solution evaporated. A 0.5 mM solution of HS-PEG was pipetted onto the exposed regions of gold outside of the masked region and allowed to evaporate. The mylar mask was removed. The slide was thoroughly rinsed in ethanol for one minute to remove any excess thiols and then dried with nitrogen gas. The oxygen plasma-activated PDMS microchannel was then aligned and placed on top of the gold substrate.

SPR imaging experiments

SPR images were collected over time as a solution of streptavidin (US Biologics, Swampscott, MA) in PBS (Sigma, St. Louis MO) was introduced to a microfluidic device (Microflow system, Micronics, Redmond, WA). In the initial images, buffer filled the microchannel. A six-port injection valve (#V451 Upchurch Scientific, Oak Harbor, WA) introduced the solution of streptavidin from the 2 mL sample loop to the microchannel. The 905 nm bandpass filter was tilted 22 degrees from normal as the SPR curve indicated that wavelength was the most sensitive (data not shown). The integration time was on the order of 0.5 seconds. Images were collected at a frequency of every 15 or 30 seconds.

Table 3. Velocities, Reynolds numbers, and Peclet numbers for the experimental straight microchannel.

	Average velocity (m/s)	Maximum velocity (m/s)	Re	Pe
50 nL/s	1.22E-03	1.83E-03	1.10E-01	1.48E+03
100 nL/s	2.44E-03	3.66E-03	2.20E-01	2.96E+03

Data analysis

All SPR data were collected and analyzed using Labview software (National Instruments Corp., Austin, TX) developed by Dr. Elain Fu. All changes in reflectivity were dark and TE corrected (See Appendix C for further information).

5.4 Results and Discussion

Computational modeling of a microfluidic flow immunoassay

Numerous articles in the literature model microfluidic flow assays with protein analytes using the finite element method, the finite difference method, or fractals.[49, 177-196] Understanding mass transport and surface reaction within SPR biosensors for the quantitative measurement of binding and dissociation kinetics of biomolecules has been a major impetus in this field.[179, 180, 184, 185, 187, 189, 193, 195, 197] Many models of microfluidic flow assays are two-dimensional, do not incorporate Taylor dispersion (i.e., the concentration of analyte in the solution does not equal zero at time=0), and often assume that plug flow exists at the inlet.[182, 183, 186, 191, 197, 198] The assumptions limit the validity of these models. Furthermore, most of the models are completed using custom-coded software that is not accessible or necessarily easy to use.

The models completed in this research are a more accurate representation of the physical phenomena that occur in a microfluidic assay. The models are three-dimensional, include Taylor dispersion (i.e., the streptavidin concentration in the microchannel is zero at time = 0), and impose a fully developed flow profile at the inlet. By using COMSOL®, these models open up to the research community a precedent for modeling microfluidic assays with commercially available and relatively easy to use software (Please note that Gervais et al.[191] have also used COMSOL® to model in two-dimensions an immunoassay.). Furthermore, since microfluidic surface binding assays are often completed under non-equilibrium or steady-state conditions, a working computational model will yield

important insights into the physical processes occurring in the assay and will serve as a tool for further optimization and exploration into novel assay designs.

The geometry drawn in COMSOL® to model a microfluidic assay (Figure 55) is a rectangular duct with a surface functionalized with biotinylated alkyl thiol, to which streptavidin may bind. The most significant difference between the experiment and model is the distance that the streptavidin solution must travel before it reaches the binding surface. In the experiment, there are ~40 microliters of dead volume between the check valve and the binding surface (on-card valves were not available). In the model, the binding surface begins immediately. Given the computational constraints, it is not feasible to model the upstream 40 microliters. As a result, even though the model at time=0 has no protein solution inside the microchannel (only buffer is present), the influence of dispersion (see Appendix H for a more thorough qualitative description) will be markedly different for the model and experimental systems.

Given the computational constraints and numerical artifacts induced at high flow rates (50 nL/s versus 5 nL/s), most of the model results presented are for a flow rate of 5 nL/s. The numerical solution did converge with a flow rate of 50 nL/s but the quality of the numerical solution was low (some of the results are presented). Therefore, the model results for the 5 nL/s flow rate will be used throughout this dissertation. However, given the amount of dead volume in the device, to run the experiment with a flow rate of 5 nL/s would take an extensive period of time (350 minutes/experiment). Therefore, during the experiment, a flow rate of 50 nL/s was used (35 minutes/experiment).

The model results also used a streptavidin concentration of 20 nM versus the 40 nM concentration used in experiments. Due to the incorporation of dispersion in the model, the model that incorporated the 40 nM concentration of streptavidin had difficulty converging. However, the general principles of protein binding to a surface in a microchannel can still be achieved with this model.

Some numerical noise is present in the model results given the complex nature of the model. In particular, some of the results indicate that slightly negative concentrations of species (0.2% of the magnitude of the maximum concentration) are present in the microchannel. This non-physical result occurs in a relatively small portion of the model (<<2%). The noise and the negative concentrations can be attributed to several factors including (1) a mesh that is not dense enough and (2) discontinuities in the concentration profile arising from the initial conditions (i.e. surface concentrations and solution concentrations that are zero at time = 0). Higher flow rates also increase the noise in the solution due to the increased stiffness of the problem. Given the nature of the assay and the computational limitations, it is likely that if these models were conducted with a more computationally adequate computer the numerical artifacts could be eliminated.

Fluid mechanics

The solution to the Navier-Stokes equation provides the fluid flow field for the device. The model results yield the expected parabolic velocity profile occurring in the laminar flow regime in which the velocity ranges from zero at the walls and increases to 1.5* average velocity in the center of the channel (Figure 56). Furthermore, by imposing a fully developed profile at the inlet of the device, there is no need to incorporate a channel length upstream of the binding patch needed for this fluid flow profile to develop.

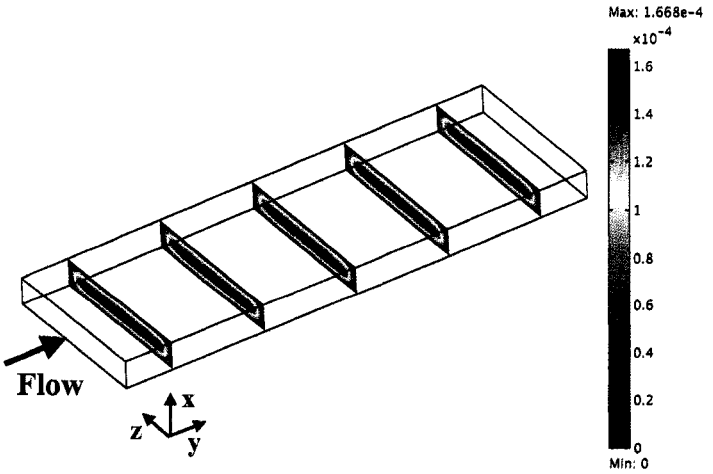

Figure 56. Velocity profile (m/s). Model results. Straight microchannel. The flow rate is 5 nL/s. Reynolds number = 0.01. Q=5 nL/s.

Bulk concentration profile of streptavidin in the straight microchannel

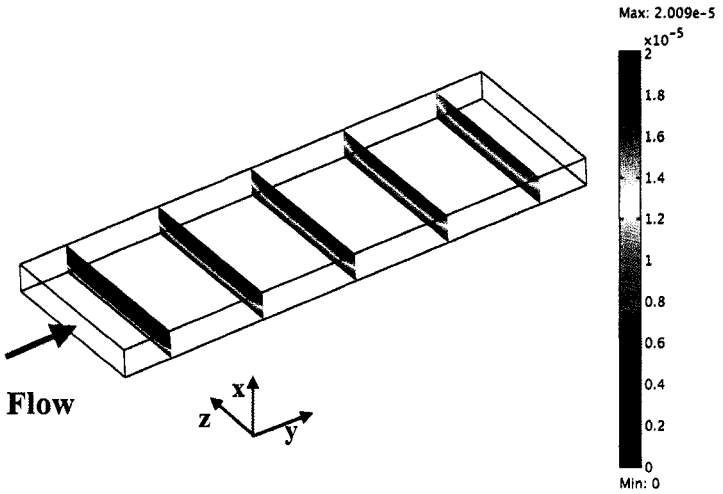

Figure 57. Concentration profile of streptavidin (moles/m^3) in straight microchannel. Model results. Streptavidin inlet concentration = 20 nM = 2×10^{-5} moles/m.^{3} Time = 350 seconds. Re= 0.01. Pe=135.1. Q=5 nL/s.

As the streptavidin flows over the binding area (Figure 57), the model results indicate that the concentration of the protein in the regions immediately above the surface is significantly reduced. The streptavidin molecules in this region – termed the "depletion zone" – must diffuse down a concentration gradient toward the surface while being convected down the length of the channel in order to bind to the immobilized biotinylated thiol. As a result, the capture efficiency of the analyte in regions of the binding surface further downstream of the inlet is greatly reduced (Figure 58) with a significant reduction in the total amount of protein binding downstream. The generation of a depletion zone gives rise to a surface binding profile that shows a steep reduction in surface concentration from the start of the binding surface to the end of the binding surface. For the modeled system, the depletion zone has a profound influence on binding, as the majority of the surface binding of the analyte occurs in the first ~300 microns of the surface nearest the inlet in the first ~5.5 minutes of the assay. This binding profile often indicates the assay system is operating within a mass transport limited regime.

When the binding of the protein to the surface is not transport-limited, a spatial variation in the surface binding profile would not exist. This assumes that the number of binding sites does not exceed the number of binding species in solution and that the entire channel is depleted of the binding species. In other words, it can be imagined that a spatial variation in the binding profile may exist if all of the binding species have bound but there are not enough to fill all of the available binding sites. Under these assay conditions, there will be a region without any bound species downstream of the inlet.

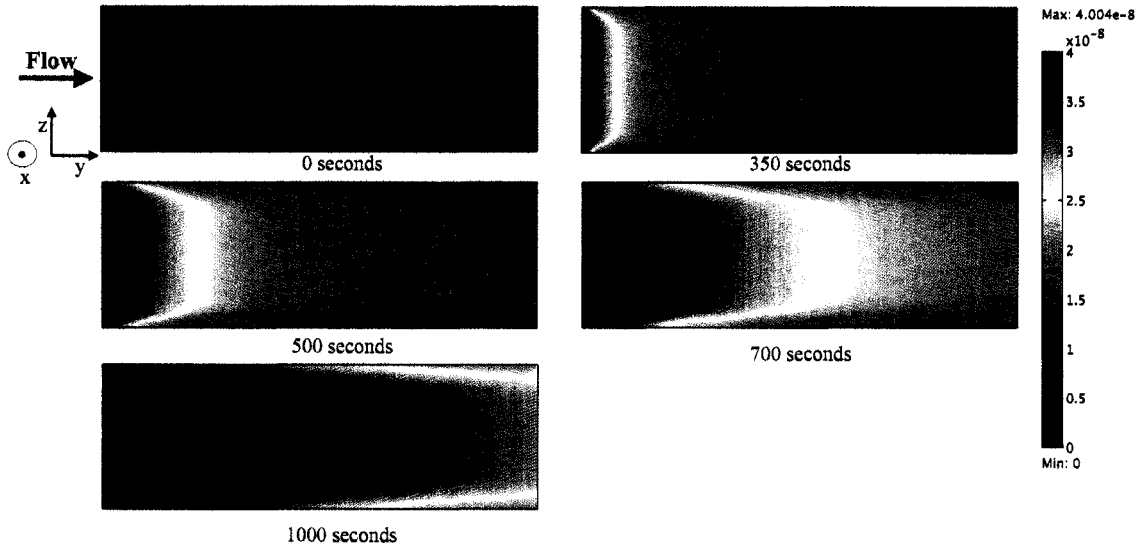

Figure 58. Surface concentration profile of bound streptavidin (moles/m^2). Model results. Streptavidin inlet concentration = 20 nM = 2×10^{-5} moles/m^3. Re= 0.01. Pe=135.1. Q=5 nL/s. The theoretical maximum SA surface binding concentration is 3.99×10^{-8} moles/m^2.

Whether the assay (A) will operate within a mass-transport limited regime and (B) will rapidly reach surface saturation of the binding protein primarily depend on the following factors:

(1) Diffusion coefficient of the binding species. A faster diffusing species is less transport-limited as the species more rapidly diffuses down the concentration gradient near the binding surface (Fick's law). There is more efficient capture of the binding species from the bulk of the microchannel with a rapidly diffusing species. As a result, the surface will more quickly reach saturation.

(2) Concentration of the binding species. The higher the concentration of binding species, the steeper the concentration gradient near the surface (which at time=0

has a surface concentration of protein of zero). When the concentration of binding species is high, more of the binding species is introduced to the microchannel. Given these considerations, at higher concentrations the surface reaches saturation more quickly.

(3) Surface binding kinetics. The more rapid the binding kinetics relative to the diffusional transport, the more transport-limited the assay. The Damkohler number (a ratio between the characteristic time of fluid motion and the characteristic reaction time) may be used to determine in what regime the assay is performed, with Da>>1 indicative of a very fast reaction rate and a transport-limited assay. The Damkohler number ($(k_{ads}*theta_0*h)/D_{SA}$) for this system is 193.15, indicating it falls in the mass transport-limited regime.

(4) Flow rate. The faster the flow rate, the less transport-limited the assay, as more of the binding species is introduced to the device and convective—rather than diffusive—transport dominates.

(5) Density of surface binding sites. The higher the density of the surface of binding sites, the longer it will take to saturate the surface.

The influence of flow rate, the diffusion coefficient, and concentration on the binding profile will be explored with the model and/or experiment later in the chapter. The binding kinetics and density of binding sites were not explored as this research focuses on two assay systems – streptavidin-biotin and antibody-antigen – each of which have fast binding kinetics and comparable surface densities. Therefore, these variables would not be explored experimentally and consequently are not a high priority to model.

Over time, the surface binding profile of streptavidin changes as the front of the binding surface reaches saturation (Figure 58). The profile also indicates that more streptavidin binds in the center of the channel than near the walls of the device. Comparison of the velocity profile parallel to the binding surface at x=30 microns (Figure 59B - blue) and surface binding profile (Figure 59B - pink) indicates that the variation in the surface binding profile relates to the parabolic nature of the velocity profile. At the walls, the

velocity is zero. Near the sidewall of the microchannel, the velocity is zero or near zero over the entire depth of the microchannel (x-dimension). In these regions, the surface binding is more transport-limited as the streptavidin must reach the surface by diffusion. Also, the concentration of streptavidin must be replenished via diffusion not convection. As a result, near the sidewalls the depletion zone is larger (Figure 57) and less streptavidin binds to the surface (Figure 58). Toward the center of the microchannel the velocity of the fluid might be zero at the binding surface, but the solution immediately above it is not zero (x-dimension) and in the middle of the device (x=45 microns) the velocity is maximal. A steep velocity gradient exists near the surface. In these regions, the solution is replenished through convection. Therefore, more protein binds to the surface.

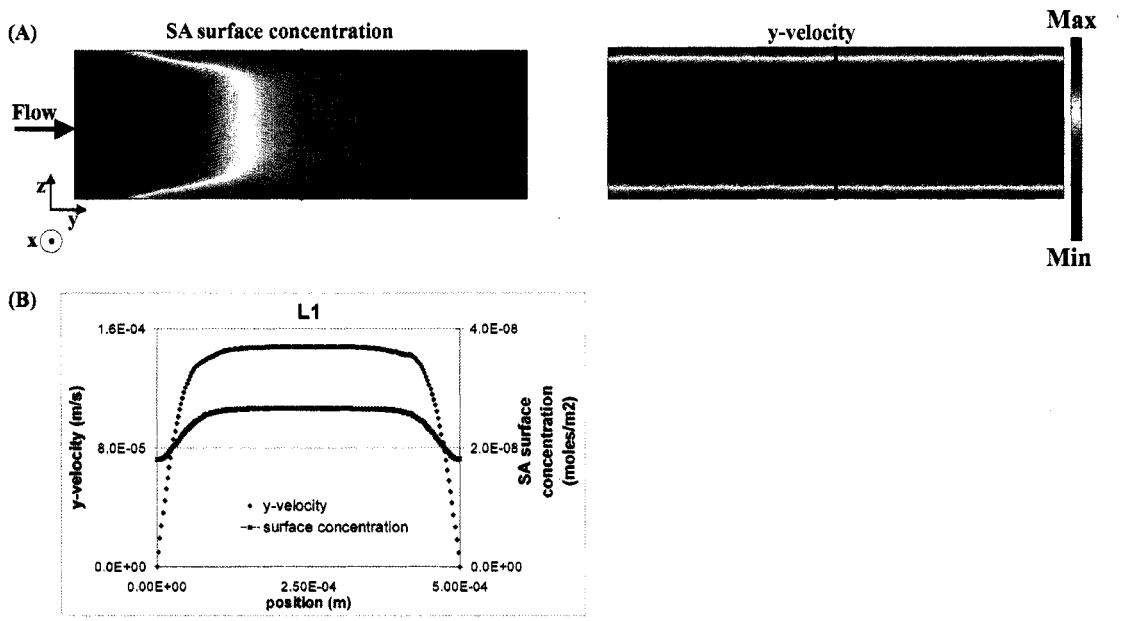

Figure 59. Comparison of the y-velocity profile and the SA binding profile in the straight microchannel. Model results. (A) Surface concentration profile of bound streptavidin (moles/m^2). Velocity profile (m/s) in the y-dimension at x=30 microns. The maximum surface concentration is 3.99 $\times 10^{-8}$ moles/m^2. The minimum surface concentration is 0 moles/m^2. The theoretical maximum surface binding concentration is 3.99 $\times 10^{-8}$ moles/m^2. (B) Line profile comparing surface concentration profile and velocity in the y-dimension. The location of the line profile is indicated in (A) and occurs at y=750 microns and z[0 to 500 microns]. Streptavidin inlet concentration = 20 nM = 2×10^{-5} moles/m^3. Time = 700 seconds. Re= 0.01. Pe=135.1. Q=5 nL/s. The maximum velocity is 1.526×10^{-4} m/s, and the minimum velocity is -4.089 $\times 10^{-19}$ m/s.

Experiments were completed to compare to the model results (Figure 60). The binding profile over time shows strong agreement with the modeled binding profile in which there is a steep decrease in the amount of streptavidin bound to the surface traveling downstream (y-dimension) and less binding near the sidewalls of the microchannel. Also as previously noted, the experimental velocity is higher than the modeled velocity but the concentration of streptavidin is reduced to enter a regime in which the binding profile is transport-limited. Therefore, the model cannot be directly compared to the experiment, but the general principles of the SA binding profile in a flow assay can still be drawn from the experimental and model data.

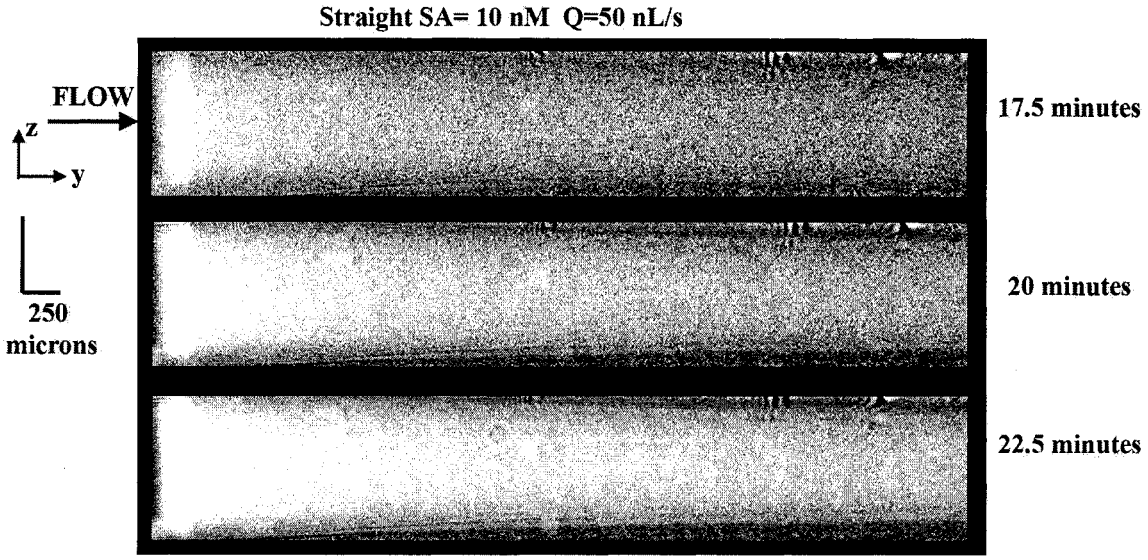

Figure 60. Surface concentration profile of bound streptavidin over time in a straight microchannel. Experimental results. SPRM difference images subtracted from initial image. Each image has been contrast enhanced for viewing purposes to demonstrate the variation of surface concentration of streptavidin within each image. Streptavidin inlet concentration = 10 nM. Re= 0.11. Pe=1480. Q=50 nL/s.

Line profiles of the experimentally measured change in surface concentration of bound streptavidin over time (Figure 61) show some qualitative agreement with the model results (Figure 59), suggesting that the model has captured the relevant parameters. The line profile down the length of the channel (Figure 61B y-dimension) indicates most of the binding occurs at the start of the binding patch and is greatly reduced downstream of the inlet. Downstream of the inlet, the amount of bound streptavidin never reaches the amount bound at the front of the binding surface. This may be an artifact related to the

surface patterning method, in which it appears that more BAT/PEG thiol is deposited at the front of the patterning mask due to the "coffee ring effect," a capillary flow induced by the evaporation of liquid at the edge of a drop which serves to deposit more material at the edge of the drop.[199, 200] With a higher BAT/PEG thiol density at the front of the binding surface, it may be capable of increased binding of the streptavidin.

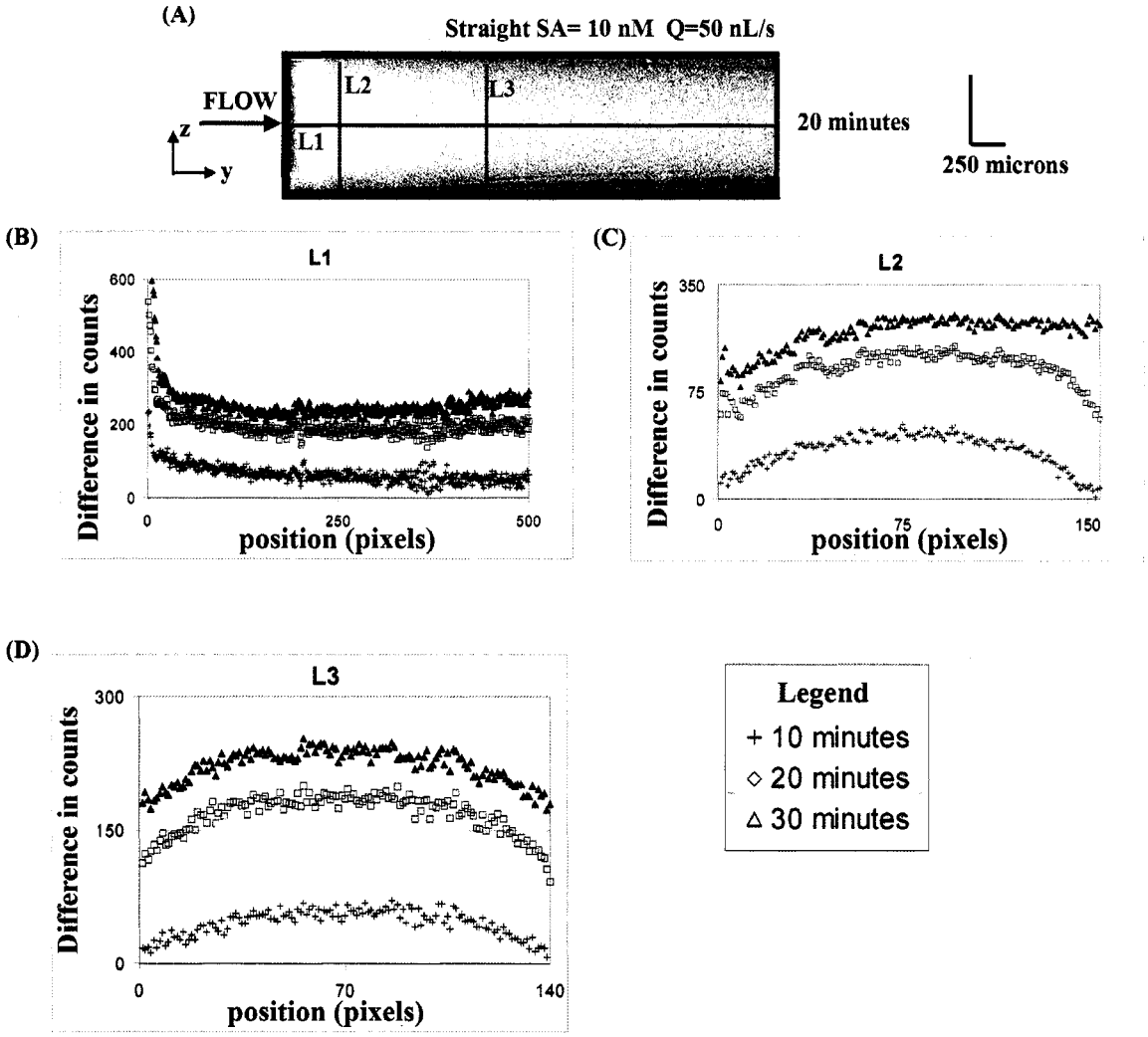

Figure 61. Difference in line profiles of the surface concentration profile of bound streptavidin. Experimental results. (A) SPRM difference image subtracted from the initial image. The image has been contrast enhanced for viewing purposes to demonstrate the variation of surface concentration of streptavidin. (B)-(D) Line profiles of the surface concentration of streptavidin over time. The location of the line profiles are indicated in (A). The line profiles were calculated from raw TM images. The line profile at time=0 was subtracted from each line profile at the indicated time point. The line profile L1 is five pixels (~17.5 microns) in width, and L2 and L3 are 10 pixels (~70 microns) in width. The difference in pixel:distance ratio on the substrate is due to image foreshortening discussed in Appendix C. Streptavidin inlet concentration = 10 nM. Re= 0.11. Pe=1480. Q=50 nL/s.

The two line profiles transverse to flow (L2 and L3 Figure 61) exhibit a strong similarity to the binding profile in Figure 59B. Early on, the binding profiles are parabolic. Over time, as the surface becomes saturated, the amount of protein increases but the line profiles lose their parabolic nature and the surface becomes saturated. The difference in time points for the experimental and model system is the result of the difference in the upstream distance the fluid must travel in the experimental system before it reaches the binding area.

Total amount of streptavidin bound to the surface over time.

By integrating the total amount of bound streptavidin on the surface as a function of time, the binding profile of streptavidin can be calculated (Figure 62). The model results indicate that the binding profile is sigmoidal. At early time points and/or low flow rates, there is a linear relationship between the amount of streptavidin bound to the surface and time. As the surface nears saturation, the curve becomes more sigmoidal in nature. The binding profiles also indicate that the efficiency of binding does not linearly correlate with the flow rate. For example, increasing the flow rate from 25 nL/s to 50 nL/s does not double the total amount of streptavidin bound to the surface at a given time point. When the binding profile does not change with increased flow rate, it indicates the surface binding of streptavidin is no longer mass transport-limited.

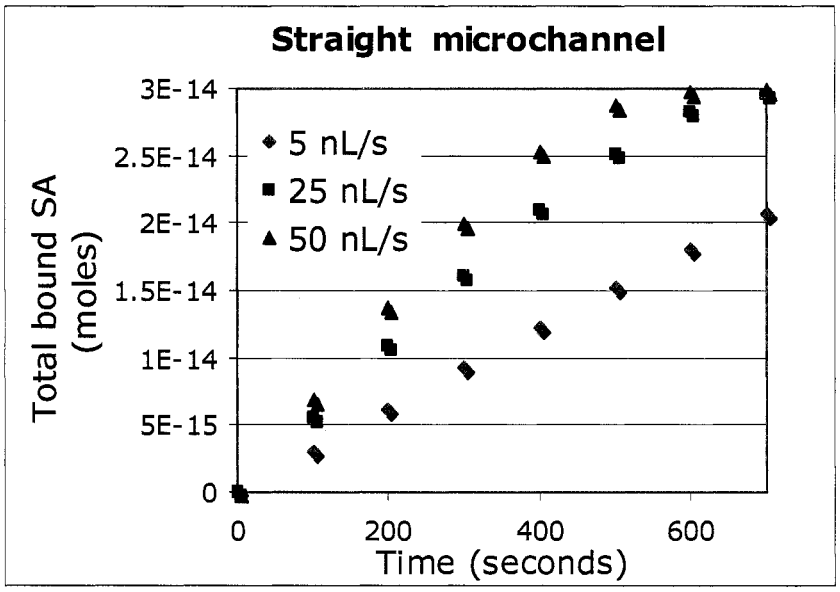

Figure 62. Total streptavidin bound to the surface for the straight microchannel as a function of flow rate. Model results. The streptavidin concentration introduced to the microchannel is 20 nM. The theoretical maximum for binding on the patch is 3×10^{-14} moles.

Experimental measurements of the binding profile (Figure 63 Q=50 nL/s) confirm the sigmoidal nature of the binding profile. The areas are three consecutive discrete regions on the binding surface that are ~1.8 mm in the y-dimension (downstream distance) with area 1 located at the start of the binding surface. The average change in reflectivity for that region is plotted over time. For reference, the modeled microchannel was only 1.5 mm in the y-dimension. Therefore, the experimental data explore an area that is ~3.6 times larger than the model system. The experimental results clearly indicate there is a delay in the binding as a function of distance down the channel. This confirms the spatial variation in the binding profile, with most binding occurring at the front of the binding surface.

Once again, the variation in the experimental and model time is due to the influence of dispersion and the dead volume in the experimental microchannel. The more significant difference in timing between the binding profiles of area 1 and area 2 may be due to the fact that area 1 contains the start of the binding surface, in which the thiol patterning method (wicking method) tends to deposit more material at the start of the binding

surface. Therefore, area 1 would bind more streptavidin than the other areas, thereby delaying the binding profile of area 2.

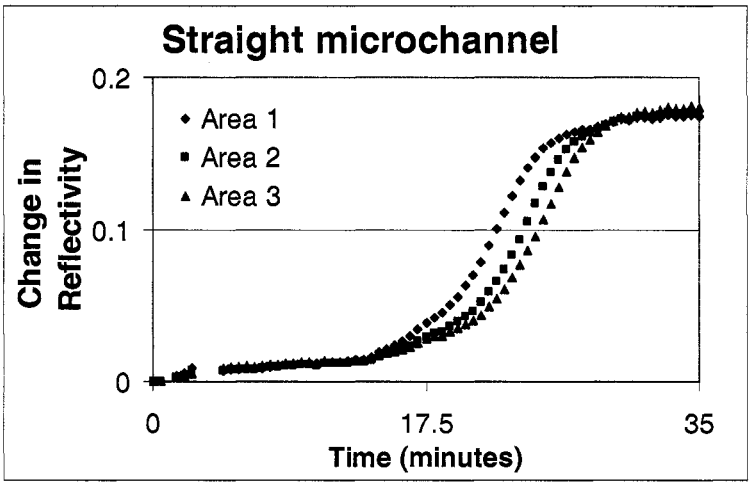

Figure 63. Change in reflectivity over time in three areas as a function of distance from the inlet for the straight microchannel. Experimental results – SPR Imaging. Area 1 is the closest to the inlet. Each area is 300 pixels in the y-dimension. Streptavidin inlet concentration = 40 nM. Re= 0.11. Pe=1480. Q=50 nL/s. The missing data points at early time points can be attributed to an air bubble introduced to the device.

To create an assay, a linear relationship between the total amount of streptavidin bound and time would be ideal. The amount of streptavidin bound or the rate of binding could then be used to quantify the amount of streptavidin in the solution (assay quantification methods will be further explored for an example immunoassay in Chapter 6). Therefore, the assay measurements should be collected when the surface is far from saturation. As a result, the highest density of binding sites is favorable and measurements should be collected at early time points.

Concentration slices of unbound streptavidin within the microchannel.

The depth of the depletion zone (x-dimension) varies with the distance downstream of the front of the binding surface. Figure 64 illustrates slices of the streptavidin concentration profile parallel to the SPR-imaging surface for several distances from the surface. The SPR interrogation depth is very close to the surface (~300 nm). At a one micron distance from the surface (Figure 64), the concentration of streptavidin near the surface is high near the start of the binding surface, due to the fact that the binding surface has become saturated at that time point (Figure 58, time=350 seconds). Therefore, some of the SPR

of streptavidin. Due to the binding of streptavidin to the surface and the transport limitations of the protein binding to the surface, the concentration of streptavidin dramatically drops further downstream of the front of the binding surface. In those regions, the bulk contribution from the streptavidin solution to the SPR signal will be negligible. At increasing distances from the binding surface, the concentration of streptavidin increases (x=15, 30, 60 and 80 microns). However, the general binding profile, in which the solution is most concentrated towards the inlet and is reduced further downstream, holds. Over time, the front of the binding surface becomes saturated with streptavidin, and the position of this depletion zone moves further downstream. Therefore, the location of the bulk contribution of the streptavidin solution to the SPR signal will vary over time. Given the exponential nature of the SPR signal, the importance of the bulk concentration on the SPR signal may remain negligible even at the front of the binding surface. However, it is a subtle point, necessary to understand the physical processes occurring in the assay.

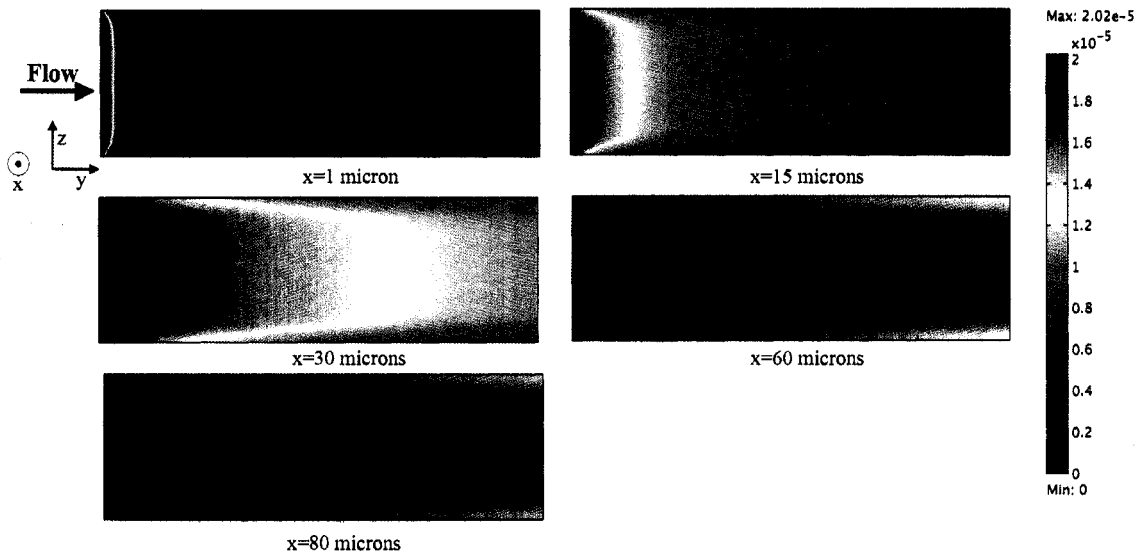

Figure 64. Concentration profile of streptavidin in the channel (moles/m^3) as a function of distance from the binding surface (x-dimension). Model results. Streptavidin inlet concentration = 20 nM = 2×10^{-5} moles/m^3. Time = 350 seconds. Re= 0.01. Pe=135.1. Q=5 nL/s.

Influence of increased flow rate on the bulk concentration profile and the surface binding profile.

The depth of the depletion zone relies heavily upon the flow rate. The faster the flow rate, the narrower the depletion zone (Figure 65A versus Figure 57) since convection rather than diffusion dominates the mass transport. At higher flow rates, more streptavidin is introduced into the device at a given time. The result is that more protein binds to the surface over a given period of time (Figure 65B versus Figure 58 time=350 seconds).

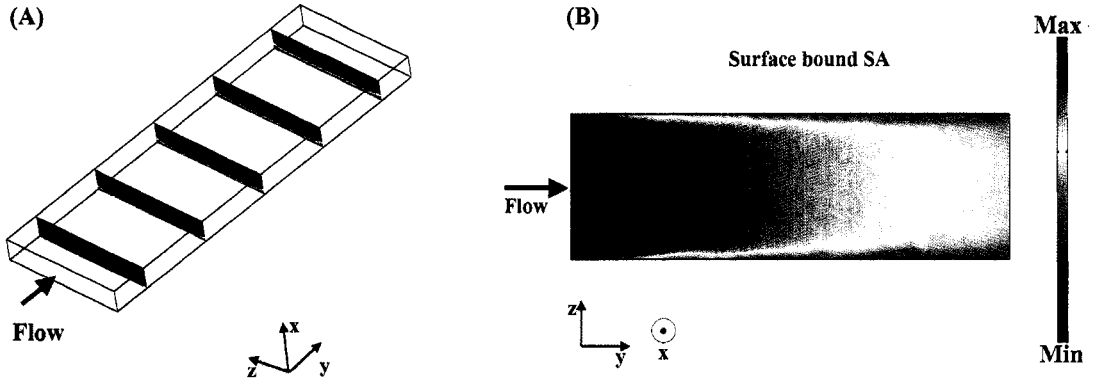

Figure 65. Increased flow rate (50 nL/s) on SA binding in straight microchannel. Model Results. (A) Concentration of streptavidin in the microchannel (moles/m^3). The maximum concentration is 2.02 $\times 10^{-5}$ moles/m^3. The minimum concentration is 0 moles/m^3. (B) Binding profile of streptavidin to biotinylated surface (moles/m^2). The maximum surface concentration is 3.99 $\times 10^{-8}$ moles/m^2. The minimum surface concentration is 0 moles/m^2. The theoretical maximum surface binding concentration is 3.99 $\times 10^{-8}$ moles/m^2. The streptavidin concentration introduced to the microchannel is 20 nM = 2×10^{-5} moles/m^3. Time = 350 seconds. Re= 0.1. Pe=1351 Q=50nL/s

Influence of increased concentration on binding profile.

The concentration of the streptavidin also significantly affects the binding profile. At higher concentrations of streptavidin, a steeper concentration gradient exists at the binding surface, and the surface reaches saturation much more rapidly as more streptavidin is introduced to the device for a given time point. Comparison of the experimental results of the surface binding profile at 40 nM (Figure 66) versus 10 nM (Figure 60) confirms that, as expected, the binding profile reaches saturation much more rapidly for the more concentrated streptavidin solution.

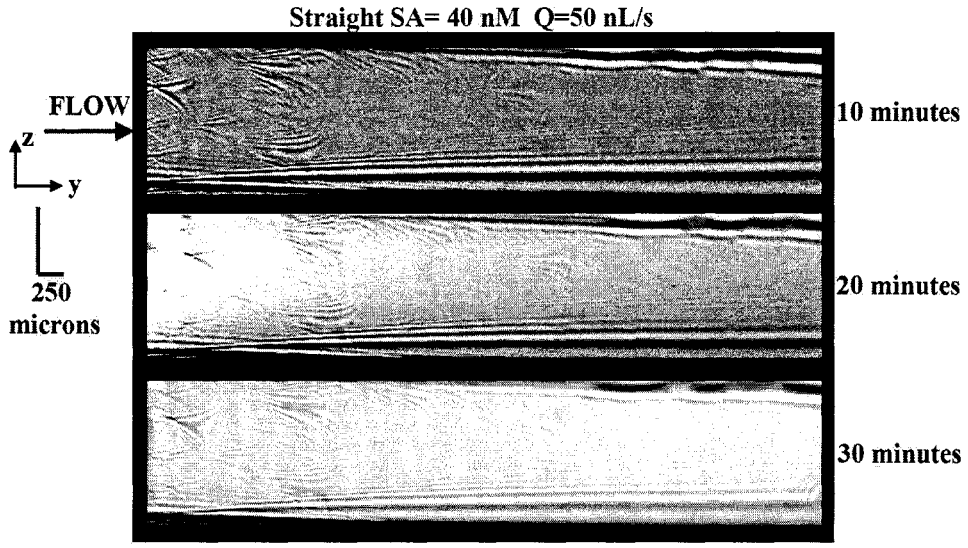

Figure 66. Surface concentration profile of surface-bound streptavidin over time in a straight microchannel. Experimental results. SPRM difference images subtracted from initial image. Each image has been contrast enhanced for viewing purposes to demonstrate the variation of surface concentration of streptavidin within each image. Streptavidin inlet concentration = 40 nM. Re= 0.11. Pe=1480. Q=50 nL/s.

The line profiles of the change in the SPR signal due to the binding streptavidin (Figure 61 [SA]=10 nM versus Figure 66 ([SA]=40 nM)) indicate that higher streptavidin concentrations result in a surface that more rapidly reaches saturation. As previously mentioned, this is expected as more streptavidin has been introduced to the microchannel. The line profiles downstream (Figure 66 L1 and L2) indicate that there is some spatial variation in the binding profile with more binding occurring at the upstream edge of the binding surface (time=20 minutes). However, unlike the 10 nM profile (L1), at the thirty minute time point, the binding profile has become saturated and largely uniform downstream. The transverse line profiles (Figure 66 L3 and L4) are less parabolic at the higher concentration of streptavidin. The increased binding at the sidewalls is a result of a steeper velocity gradient at the sidewalls. Therefore, the influence of convective transport to replenish the streptavidin concentration in those regions increases and results in increased binding at the sidewalls. The difference in absolute change in SPR counts over time between Figure 61 and Figure 66 arises from different integration times.

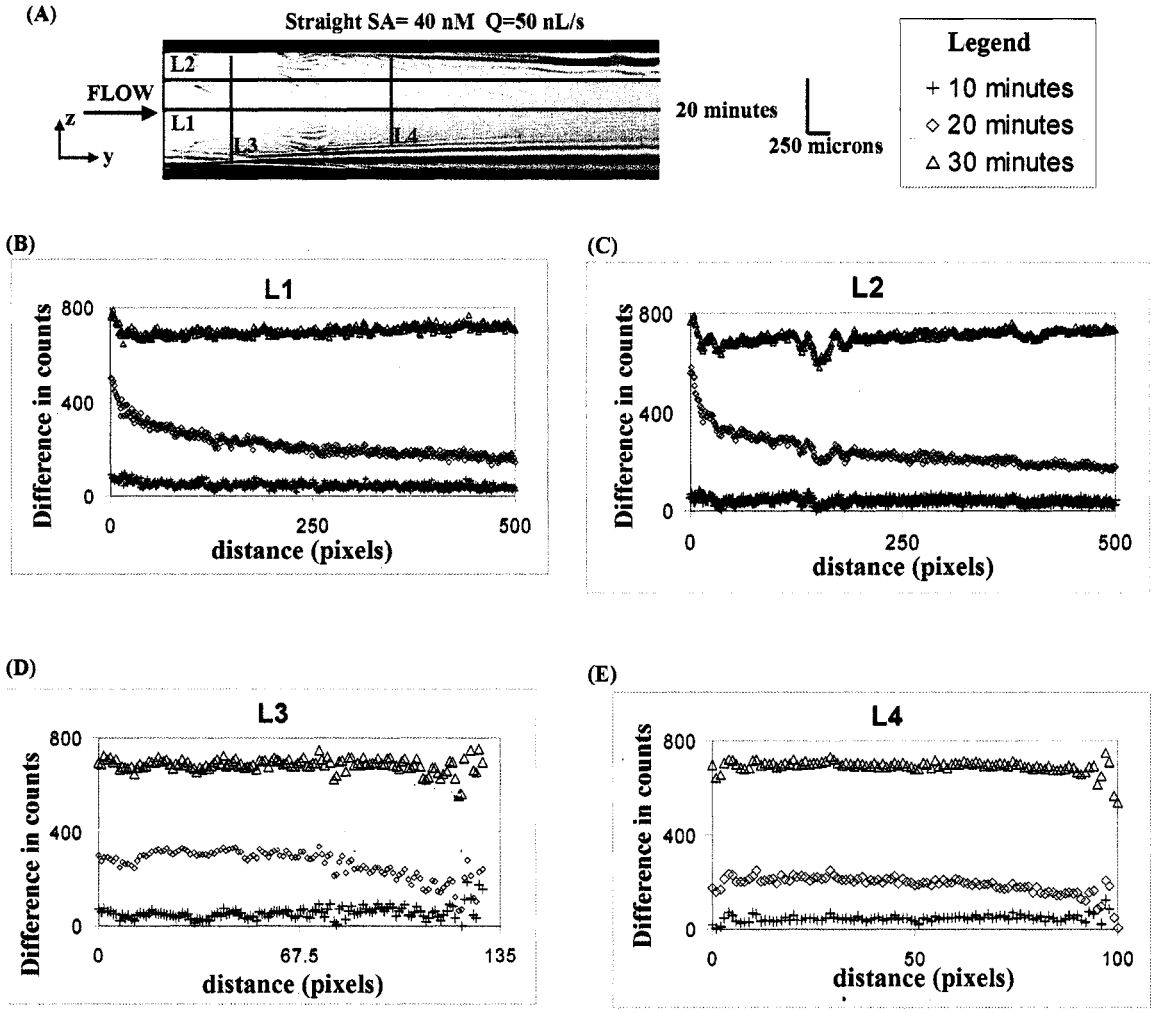

Figure 67. Different line profiles of the surface concentration profile of bound streptavidin in a straight microchannel. Experimental results. (A) SPRM difference image subtracted from initial image. The image has been contrast enhanced for viewing purposes to demonstrate the variation of surface concentration of streptavidin. (B)-(E) Line profiles of surface concentration of streptavidin over time. The location of the line profiles are indicated in (A). The line profiles were calculated from raw TM images. The line profile at time=0 was subtracted from each line profile at the indicated time point. The line profiles L1 and L2 are 5 pixels (~17 microns) in width and L3 and L4 are 10 pixels (70 microns) in width. The difference in pixel to distance ratio on the substrate in each dimension is due to image foreshortening in the y-dimension discussed in Appendix C. Streptavidin inlet concentration = 40 nM. Re= 0.11. Pe=1480. Q=50 nL/s.

Influence of an increased diffusion coefficient on the surface binding profile.

The binding profile also strongly depends on the diffusion coefficient of the binding species. The more rapidly diffusing the binding species, the less transport-limited the binding of the species to the surface. A computational model of a theoretical molecule

with a diffusion coefficient ten times faster than streptavidin was run (Figure 68). The results indicate that the depletion zone is significantly reduced with the increased diffusional coefficient (Figure 68A with $D=10D_{streptavidin}$ versus Figure 57 for $D_{streptavidin}$). Under these conditions, the efficiency of the binding reaction is significantly improved when the binding species diffuses rapidly. The binding profile is also significantly altered (Figure 68B with $D=10D_{streptavidin}$ versus Figure 58 for $D_{streptavidin}$) with not only increased total binding but a more parabolic binding profile (if a line profile was taken transverse to flow – z-dimension). As expected, the binding profile for the fast diffusing analyte reaches saturation before the streptavidin system (Figure 68C).

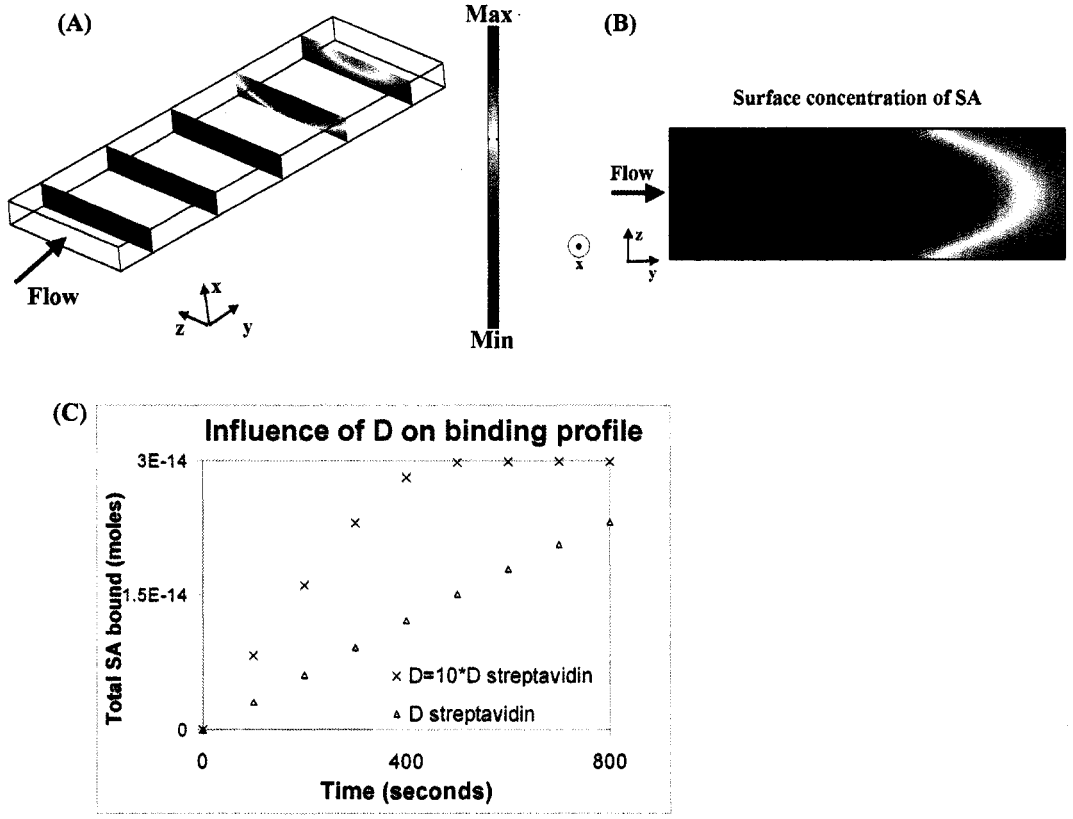

Figure 68. Comparison of the influence of the diffusion coefficient of the binding species on the depletion layer and the surface binding profile. Model results of a species for which $D=10*D_{streptavidin}$. (A) Concentration profile of streptavidin in the channel (moles/m^3) at time= 350 seconds. The maximum concentration is 2.01×10^{-5} moles/m^3. The minimum concentration is 0 moles/m^3. (B) Surface concentration profile of bound streptavidin (moles/m^2) at time=350 seconds. The theoretical maximum surface binding concentration is 3.99×10^{-8} moles/m^2. The maximum surface binding concentration is 3.99×10^{-8} moles/m^2. The minimum surface binding concentration is 0 moles/m^2. (C) Comparison of the total surface binding over time for each species. Binding species inlet concentration = 20 nM = 2×10^{-5} moles/m^3. Re= 0.01. Pe=135.1 and 1.35 respectively. Q=5 nL/s. The theoretical maximum amount of the binding species that can bind to the surface is 3×10^{-14} moles.

Implication of model results on assay design

The model has several important practical implications for the design of microfluidic SPR imaging assays.

1) Size of surface binding area for a given analyte.

The models indicate that large surface patterns of capture molecules are not required for rapid (10 minutes or less) SPR-imaging assays to quantify the nanomolar concentrations protein, since very little binding occurs three hundred microns downstream of the start of the binding region at early time points (time=350 seconds). This is especially true for other assay formats conducted under low flow rates or with slowly diffusing analytes (extremely transport limited conditions). If higher flow rates, quickly diffusing analytes, or very high concentrations of analytes must be quantified, a larger binding region may be required so that the surface is not rapidly saturated.

The small region over which the majority of the binding occurs also has implications for the signal processing procedures employed. The model results indicate that the signal from the first ~ 100 microns should be analyzed to achieve the highest signal. Depending on the quality of the pattern and the resolution of the instrument, this may be the best or most sensitive method for processing images.

2) Location of control surface binding surfaces

A subtle yet significant point that the model aids in understanding is where the patterns of control molecules required to assess the specificity of the binding of the analyte to the experimental pattern (the pattern which recognizes the analyte of interest) should be positioned. As the model indicates, a large depletion zone of analyte exists immediately above the binding region. This depletion zone continues down the length of the channel until the analyte diffuses down the concentration gradient and replenishes the concentration of analyte at the surface. The distance over which this occurs will depend on the diffusion coefficient of the analyte as well as the flow rate. If the control pattern of

molecules closely followed the pattern of capture molecules specific for the analyte of interest, the depletion zone above the surface would reduce, if not eliminate, the potential for binding, even if the molecule could bind to the control pattern. This assumes that the molecule that is binding is recognized by both the experimental and control patterns, as in the case of non-specific binding or a promiscuous molecule capable of binding to both molecules. In this scenario, the control would never show a signal due to transport considerations rather than the actual interaction between the molecules.

3) Location of surface binding patterns.

The parabolic velocity profile has been shown to significantly reduce the total binding of streptavidin at the sidewalls of the microchannel, particularly at low flow rates and streptavidin concentrations. If multiple surface binding patterns for a single analyte are averaged to determine the amount of the analyte in solution, it would be important to ensure that some patterns are not near the sidewalls, as there is the possibility that transport limitations give rise to a reduction in the surface binding in those locations. This would only serve to reduce the average signal and increase the standard deviation of the measurement. Ideally, the patterns should be positioned toward the center of the microchannel or in regions that are similarly affected by mass-transport considerations.

4) Dimensions of the microchannel.

As shown in Figure 59, the parabolic velocity profile – particularly at low analyte concentrations and low flow rates – can give rise to a reduction in the amount of protein bound to the surface near the sidewalls when compared to the centerline of the channel. To avoid this reduction, narrow microchannels (z-dimension) should be avoided to reduce the percentage of the surface affected by the reduced velocity at the sidewalls.

5) Dynamic range of a microfluidic flow assay.

Two potential quantification methods, the measurement of the total amount of analyte bound at a single time point or the measurement of the rate of surface binding, are often used in flow assays. Ideally, to use one of these quantification methods the surface

binding profile should be far from saturation and under the linear regime. Once a concentration of analyte is high enough to saturate the surface, it is impossible to quantify higher concentrations as the surface is also saturated at the higher concentration.

If there is an analyte species at an extremely high concentration and it quickly saturates the surface, the operating dynamic range could be expanded by reducing the flow rate to increase the time to saturation or through the dilution of the sample solution. Alternatively, the binding surface could be increased in size to again increase the amount of time to saturation. Given the importance of operating the assay far from saturation of the surface, it is also important for the binding surface to have a high density of binding sites to achieve the widest possible dynamic range.

6) Multiple analyte detection.

If a SPR-imaging assay is designed to quantify multiple analytes simultaneously (i.e. multiple capture molecules are patterned on the gold surface), the analysis methods and time points of measurements should be tailored to each analyte. As this chapter has illustrated, depending on the concentration of analyte, the diffusion coefficient of the analyte, and the flow rate, the point of surface saturation and in turn the optimal time to collect the measurements varies for each analyte. In this model assay format – streptavidin-biotin – the kinetics dissociation rates are extremely low ($<3\times10^{-6}$ 1/s). On the other hand for immunoassays, the dissociation rates of the antibody and antigen may be much larger and could influence the performance of an assay. The computational model described in this chapter would serve as an excellent tool to optimize the quantification method for a given analyte.

It is possible that for an assay conducted within a single microchannel, the optimal flow rate varies widely for each analyte. As the flow rate cannot be adjusted within a given microchannel, not only the time point of the measurements but also the size of the binding surface can be tailored to each analyte to ensure the measurement is taken far from saturation. If these alterations are not sufficient to quantify the analytes within the

dynamic range of interest, dilution of the sample may be required for the quantification of some analytes.

5.5 Conclusions

A computational model of a standard microfluidic flow assay (streptavidin-biotin model system) was developed and shows qualitative agreement with SPR-imaging experiments. The model and experimental results indicate that under the assay conditions explored, the surface binding reaction was mass transport-limited. As the solution of streptavidin flows across the binding surface and binds to the surface, a depletion zone above the binding surface is established in which little to no protein is present. The depletion zone is reflected in a non-uniform surface binding profile. Models and/or experiments explored the influence of higher concentrations of protein, faster diffusing analytes, and flow rate on the binding profile. The model and experimental results give insight into important assay design parameters, such as the location and size of the binding surface, the position of control binding surfaces in relation to the analyte binding surface, the time point of measurements, and method of quantification for single and multiple analytes. This model has and will serve as a method to efficiently optimize and explore other assay formats. Chapters 6-8 will build upon the results presented in this model.

Chapter 6: Development of computational models of indirect microfluidic flow immunoassays.

6.1 Objectives

1) Develop computational models of the indirect immunoassay.
2) Explore the influence of dispersion, flow rate, antibody concentration, and the incorporation of monovalent versus bivalent approximation of the antibody on the performance of the assay.
3) Use model data to explore methods to quantify the concentration of antigen in a sample.

6.2 Background

One method to quantify the amount of a small molecule analyte using SPR-imaging as a detection method – the indirect microfluidic flow immunoassay – was proposed by Dr. Kjell Nelson (Figure 69). In this assay design, the sample containing an unknown concentration of the small molecule of interest, phenytoin, – a drug to treat epilepsy[201] – is mixed off the microfluidic card with a solution of a known concentration of antibody (Figure 69B). The antibody and antigen (phenytoin) bind to each other (Figure 69A). An antibody molecule has two binding sites. However, some computational models approximated that the antibody was monovalent and could only bind one antigen. After ~15 minutes, the solution of antibody and the sample are introduced to a microfluidic device. The SPR detection surface is functionalized with BSA-phenytoin molecules. Antibody molecules with available binding sites bind to the surface yielding an SPR signal (Figure 69C). The amount of antibody with available binding sites is inversely related to the amount of antigen, phenytoin, in solution. Therefore, there will be an inverse relationship between the SPR signal and the antigen concentration.

The purpose of this research is to develop computational models of this immunoassay to better understand the influence of several variables – dispersion, a monovalent

approximation of the antibody versus a more realistic bivalent approximation of the antibody, flow rate, and antibody concentration. Some of the principles explored in Chapter 5 will be revisited, as the previous model analyzed streptavidin binding, and this model analyzes the binding of antibody to a surface in the presence of an antigen. Two methods (rate of antibody binding versus total antibody binding) to quantify the amount of antigen present in the sample will be explored with the model.

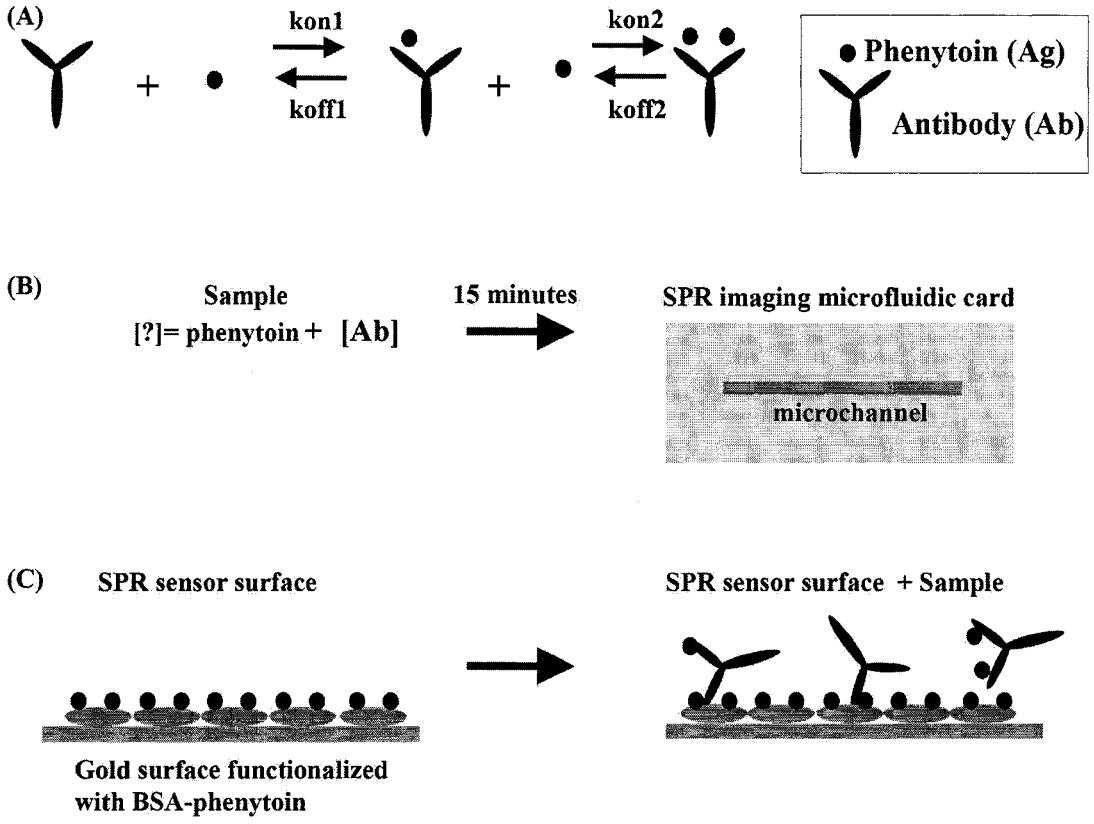

Figure 69. Indirect microfluidic flow SPR imaging immunoassay. (A) Antibody-phenytoin binding interaction. There are two binding sites in an antibody and two sets of kinetic parameters (kon and koff). (B) Schematic for the indirect immunoassay. A sample with an unknown concentration of the analyte, phenytoin (antigen (Ag)), is mixed with a known concentration of antibody (Ab) for fifteen minutes. The solution is introduced to a SPR biosensor. (C) The gold surface is functionalized with BSA-phenytoin to which antibody with free binding sites may bind. Antibody without available binding sites is washed out of the microchannel. The amount of antibody with free binding sites inversely correlates with the total amount of antigen in the sample. The amount of antibody bound to the surface and/or the rate of antibody binding is monitored with SPR imaging and may be used to quantify the amount of analyte in the sample.

Because the purpose of this research is to develop rapid diagnostics, the computational models explored up to 10 minutes after the start of flow. Nanomolar concentrations of antigen (analyte) were the focus of the model given the fact this concentration range is

clinically relevant[202] and/or is near the clinically relevant concentration range for the small molecules of interest (cortisol and phentyoin). The model also serves as a tool to further optimize the indirect immunoassay and explore other assay formats in a rapid and efficient manner. Furthermore, the experimental detection method, SPR imaging, only detects changes in the refractive index near the gold surface. The model gives insight into the concentration profile within the entire microchannel.

6.3 Materials and Methods

Computational Simulations

All computational simulations were completed with the commercially available finite element method software, COMSOL® (Versions 3.2-3.3, Comsol, Inc., Burlington, MA). For a detailed description of the governing equations of each model as well as a detailed explanation of the modeling protocol, see Appendices A and B, respectively. The modeling protocols are described briefly below.

Indirect immunoassay

Due to computational constraints and the high experimental flow rates, the immunoassay was modeled in two dimensions (Figure 70). A parabolic velocity profile was incorporated in the model. A range of flow rates as well as antigen/antibody concentrations were explored (Table 4 and Table 5). Antibodies were modeled as monovalent as well as bivalent (the more accurate description, which requires more computational memory).

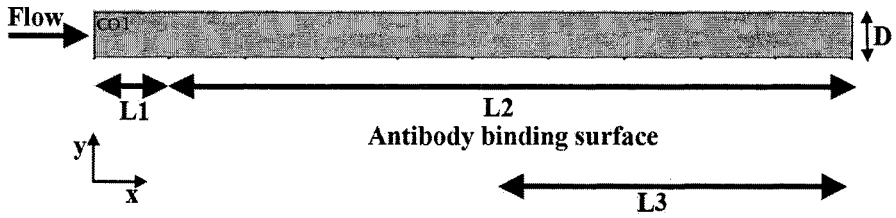

Figure 70. Model geometry for the indirect immunoassay. A pre-mixed solution of sample containing antigen, antibody, antigen-antibody is introduced under flow to the device. The channel depth, *D*, is 90 microns. The upstream channel length, *L1*, is modeled as 22.1 mm or 0.1 mm. The modeled antibody binding surface, *L2*, is 2 mm. To correlate with experimental analysis, the binding region analyzed with the model, *L3*, is a 1 mm patch that is 1 mm downstream of the front of the binding surface.

Table 4. Velocities, Reynolds numbers, and Peclet numbers for the indirect immunoassay models.

	Average velocity (m/s)	Maximum velocity (m/s)	Re	Pe
25 nL/s	3.47E-04	5.21E-04	1.74E-02	484.4
100 nL/s	1.39E-03	2.08E-03	6.94E-02	1937
250 nL/s	3.47E-03	5.21E-03	1.74E-01	4844

Models in the computational matrix were simulated twice (Table 5). In the first series of models, the binding region was located 0.1 mm from the model inlet (L1 Figure 70). In the second series of models, the binding region was located 22.1 mm from the model inlet to help assess the influence of dispersion on the results. The second series of models is a better approximation of the experimental data set. However, the dispersion distance is much longer in the experimental set-up and the geometry is more complex. To simplify the model and the assumptions, the 22.1 mm distance was chosen to approximate the distance from the inlet of the device to the imaging region.

Table 5. Matrix of indirect immunoassays simulated. The dash indicates that those models were not completed.

Antigen (nM) Antibody(nM)	0	25	50	75	100
5	25 nL/s 100 nL/s 250 nL/s	—	—	—	—
100	25 nL/s 100 nL/s 250 nL/s	—	—	—	—
125	25 nL/s 100 nL/s 250 nL/s	25 nL/s 100 nL/s 250 nL/s	25 nL/s 100 nL/s 250 nL/s	25 nL/s 100 nL/s 250 nL/s	25 nL/s 100 nL/s 250 nL/s
250	25 nL/s 100 nL/s 250 nL/s	25 nL/s 100 nL/s 250 nL/s	25 nL/s 100 nL/s 250 nL/s	25 nL/s 100 nL/s 250 nL/s	25 nL/s 100 nL/s 250 nL/s

In the model, a surface is covered with binding sites for the antibody. In solution, antibody, sample antigen, and antibody-antigen complexes flow past the sensor surface. The antibody is assumed to be monovalent or bivalent. No bivalency in terms of attachment of an antibody to the surface was introduced to this model system (i.e., there is no antibody bound to the surface-immobilized antigen via two antigen binding interactions). The inlet is located either 0.1 mm or 22.1 mm upstream of the binding surface (L1 Figure 70). The modeled antigen (Ag) molecule is a small molecule – similar to cortisol or phenytoin. The binding area quantified in the experiment is 1 mm downstream of the beginning of the binding patch to reflect the experimental analysis protocol. The total binding area assessed is 1 mm in length.

The diffusion coefficients, kinetics parameters, and surface densities of binding sites were typical of those found experimentally and used in similar computational studies of immunoassays (Table 6). [182, 183, 186, 191, 197, 198] Similar values are also used in the model presented in Chapter 7.

Table 6. Values of the constants used in the indirect immunoassay models.

Variable	Input value in COMSOL®
$D_{antibody}$ (m^2s^{-1})[54, 203]	4.3×10^{-11}
$D_{antigen}$ (m^2s^{-1})[204]	5×10^{-10}
k_{ads1} (m^3 $moles^{-1}s^{-1}$) (rate for antibody binding to the surface immobilized antigen when bound to no free antigen)	10^5
k_{des1}(s^{-1}) (rate for dissociation of the antibody from the surface immobilized antigen when bound to no free antigen)[205]	10^{-3}
k_{on1} (m^3 $moles^{-1}s^{-1}$) (rate for antibody-antigen binding in solution when the antibody is bound to no antigen)	10^6
k_{off1}(s^{-1}) (rate for antibody-antigen binding dissociation in solution when the antibody is bound to no antigen)	10^{-3}
θ_0 (moles of binding sites/m^2) = 1 binding site every 5 nm × 5nm	6.64×10^{-8}
Theoretical maximum amount of antibody bound to a 1 mm strip (moles/m)	6.64×10^{-11}

To determine the concentrations of the antibody, antigen, and antibody-antigen upon introduction to the device, transient models of the binding under static conditions were completed. It took <180 seconds for the modeled system to reach equilibrium (the actual experimental off-chip incubation time was longer (~15 minutes). The computed concentrations were then inputted into the model (Table 7 and Table 8). When solving the convection-diffusion and surface binding modes in which L1=0.1 mm and only antibody was present in the microchannel, the mesh consisted of 115,188 elements and had 251,536 degrees of freedom. When L1=22.1 mm and four species were present (antibody, antigen, antibody-antigen, and antibody-antigen-antigen), the mesh consisted of 34,315 elements and had 294,882 degrees of freedom.

Table 7. Equilibrium concentrations for all assay conditions for the monovalent model.

Antigen (nM) Antibody (nM)	25	50	75	100
125	Ab 100.2 Ag 0.25 Ab-Ag 24.75	Ab 75.65 Ag 0.65 Ab-Ag 49.35	Ab 51.43 Ag 1.43 Ab-Ag 73.57	Ab 28.4 Ag 3.4 Ab-Ag 96.6
250	Ab 225.1 Ant 0.11 Ab-Ag 24.89	Ab 200.2 Ag 0.25 Ab-Ag 49.75	Ab 175.4 Ag 0.4251 Ab-Ag 74.57	Ab 150.7 Ag 0.66 Ab-Ag 99.34

Table 8. Equilibrium concentrations for all assay conditions for the bivalent model. Assumes the kinetic parameters for binding to antigen in solution and to the surface are the same for antibody bound to one antigen and antibody bound to no antigen.

Antigen (nM) Antibody(nM)	25	50	75	100
125	Ab 103.4 Ag 0.18 Ab-Ag 18.3 Ab-2Ag 3.25	Ab 85.47 Ag 0.34 Ab-Ag 29.41 Ab-2Ag 10.12	Ab 69.56 Ag 0.52 Ab-Ag 36.39 Ab-2Ag 19.04	Ab 55.2 Ag 0.73 Ab-Ag 40.33 Ab-2Ag 29.47
250	Ab 227 Ag 0.09 Ab-Ag 21.02 Ab-2Ag 1.94	Ab 206.7 Ag 0.18 Ab-Ag 36.75 Ab-2Ag 6.53	Ab 188.1 Ag 0.26 Ab-Ag 49.1 Ab-2Ag 12.82	Ab 170.7 Ag 0.35 Ab-Ag 58.95 Ab-2Ag 20.35

6.4 Results and Discussion

Please note that the terms antigen and analyte are used interchangeably in this Chapter.

Units of adsorption

The 2D Comsol model assumes that the binding line extends into and out of the paper – essentially the width of the microchannel. In the model, the binding surface (or rather line) to which antibody binds is a slice within a total channel to which antibody binds. The surface concentration of bound antibody and available binding sites is moles/m^2. The bulk concentration of antibody and antigen are moles/m^3.

When determining the amount of antibody bound to the modeled geometry, the value of c_s (moles/m^2) along the binding line is integrated along then entire length of the line. Therefore, this integrated value, i.e. the total amount of antibody bound, has units of moles/m where the distance "m" represents the channel width. In order to calculate the total moles, this value must simply be multiplied by the channel width. Since this study compares channels of the exact same width, the values remain in the units of moles/m. An important limitation in the assumption that the binding is uniform across the entire width of the channel is that this model does not capture the reduction in binding due to

the reduction in velocity near the sidewalls. Therefore, physically this model will overestimate the amount of antibody bound to the surface.

Influence of Kd and avidity

In this study, we assessed the binding of one antibody to the binding surface. The value of Kd was not varied for this research, and therefore, this value will not be explored in detail in this dissertation as other variables – antigen and antibody concentrations, flow rate, and channel geometry were explored extensively. However, the Kd can significantly impact the binding of the antibody to the surface. When the dissociation constant is high for a given antibody, desorption may be observed even during the course of rapid diagnostic (5-10 minutes). This could have a significant impact on the maximum amount of antibody bound to the surface and in turn the performance of an assay. The values of Kd will vary from antibody to antibody. The kinetic and equilibrium constants for a given antibody and immobilized antigen system may also substantially vary from the values observed in solution phase for a variety of reasons including steric hinderance, repulsive or attractive electrostatics due to the charge of the gold, and the local topography of the immobilized antigen.

Avidity is the strength of a bond when multiple bonds are involved. This contrasts with affinity in which a single bond is involved. Therefore, for a protein such as an IgG is bivalent, the effective strength of the bond to the immobilized antigen could be altered if the IgG binds to the surface with both antigen binding pockets versus a single antigen binding pocket. Therefore, the desorption rate and Kd could be altered. In another protein-immobilized ligand system for which avidity could be significant, the streptavidin-biotin system analyzed by Jung et al[88] and modeled in Chapter 5, the authors attempted to quantify the value of the desorption constant when streptavidin was bound to a single immobilized biotin versus streptavidin bound to two immobilized biotins. The ability of a protein to bind to two immobilized ligand molecules will strongly depend on the topography, distance between ligand binding pockets on the protein receptor, and

distance between the immobilized ligands. When an antibody is bound to two immobilized antigens, the effective dissociation constant will be significantly reduced as when the antibody dissociates from one immobilized ligand, it remains bound to the surface. In order for the antibody to completely dissociate from the surface, both antigen-antibody reactions must be

Impact of continuum assumptions

The COMSOL models do not incorporate any molecular dynamics which would account for any orientational constraints on the binding of the antibody to the surface (i.e. the rotational diffusion of the antibody molecule is not incorporated in the model). The incorporation of molecular dynamics into the COMSOL model is outside the scope of this dissertation. However, several researchers have explored the role of orientational constraints in macromolecular associations when the binding reaction is diffusion limited.[206-208]

Influence of flow rate on the size of the depletion zone and the binding profile

To explore the distribution of antibody within the microchannel as a function of flow rate and relate this to the surface binding profile of antibody, computational models were completed in which no antigen (phenytoin) was present and only the flow rate was varied.

Figure 71A indicates a strong dependence of the depletion zone depth of the antibody near the binding surface (described in Chapter 5) on flow rate. Lower flow rates (Pe=484.4) generate a more significant depleted zone of antibody than higher flow rates (Pe=4844) for two reasons. At lower flow rates, less total antibody is introduced to the device for a given time point. Therefore, it will take more time to saturate the surface and in turn the depletion zone will exist for a longer period of time. Secondly, the velocity gradient is much steeper at higher flow rates. The "unstirred layer" near the binding

surface, in which diffusion dominates over convection, is smaller at high flow rates. In turn, the relative influence of mass transport by diffusion is low compared to mass transport by convection. By reducing the depth at which diffusion dominates transport, the concentration gradient is much higher at higher flow rates, enabling more efficient transport to the surface.

Figure 71A also demonstrates that over time, as the surface becomes saturated with bound antibody molecules, the position of the depleted region will move downstream. This is best illustrated by comparing the location of the beginning of the depletion of the antibody in solution for Pe=484 at time=1 minute and time=5 minutes. Therefore, there is temporal dependence on the location of the depleted region.

As described in Chapter 5, the existence of the depletion zone of antibody affects the surface binding profile of the antibody (Figure 71B). The more significant the depletion zone, the more transport-limited the binding of the antibody to the surface. At lower flow rates (Pe=484), this is observed in the binding profile as a steep drop-off in the amount of antibody bound from the beginning of the binding region to the end of the binding region (i.e., a steeper slope in the graph in Figure 71B). At higher flow rates with a reduction in the depletion zone, the binding profile is much more uniform across the length of the binding surface (reduced sloped in the graph in Figure 71B). This has also been observed experimentally (data not shown) by Dr. Kjell Nelson.

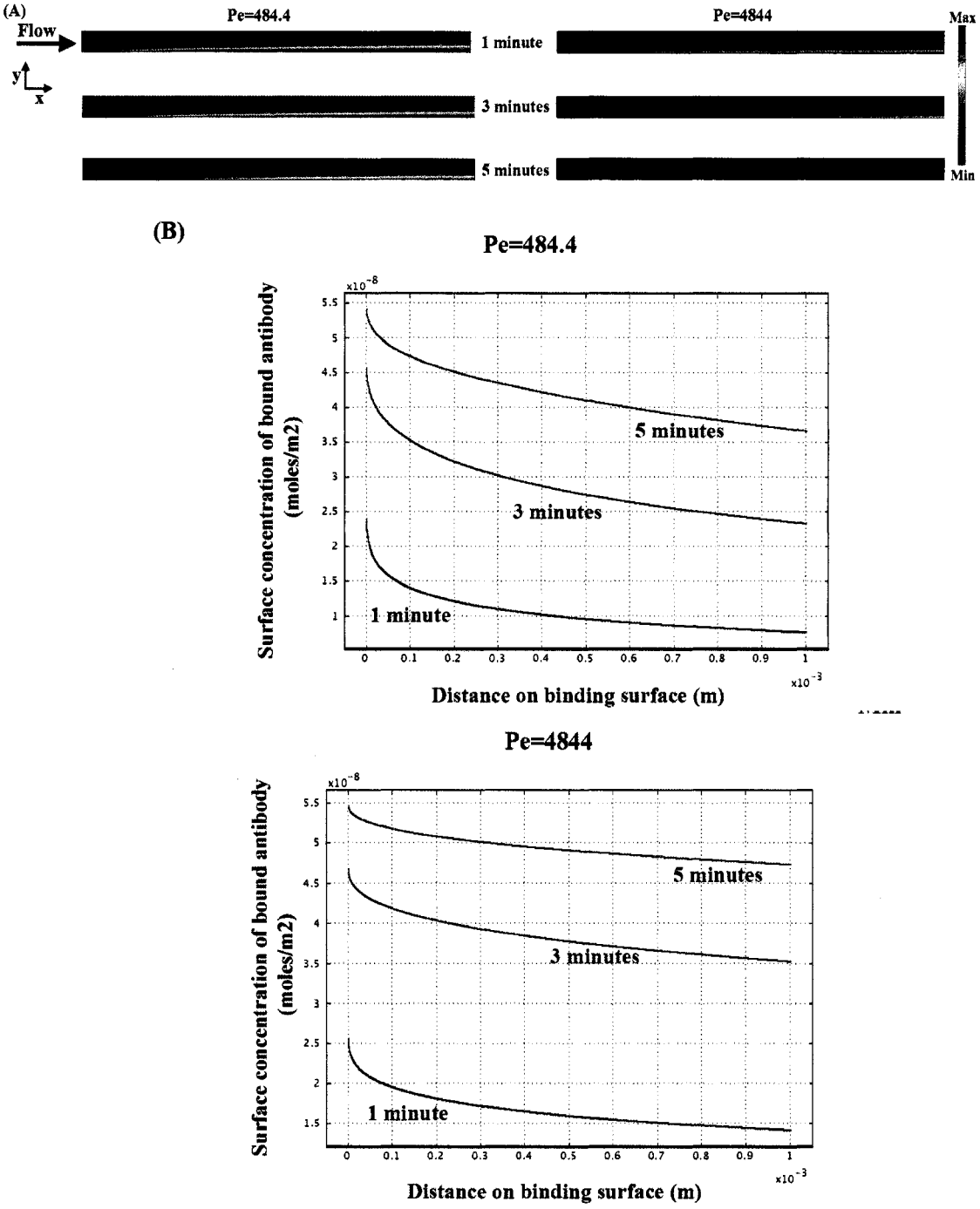

Figure 71. Influence of flow rate on the depletion zone profile over time. Model results. (A) Antibody concentration profile (moles/m^3) within the microchannel at two flow rates: 25 nL/s and 250 nL/s. (B) Surface concentration profile (moles/m^2) of bound antibody along binding surface over time. The inlet concentration of antibody = 100 nM = 1×10^{-4} moles/m^3. Max = 1×10^{-4} moles/m^3 and Min=1.789×10^{-4} moles/m^3. The theoretical maximum antibody surface binding concentration is 6.64×10^{-8} moles/m^2. The antibody is assumed to be monovalent.

Influence of flow rate and antibody concentration on antibody binding profile

To gain an understanding of the influence of antibody concentration and flow rate on the assay, several simulations were completed with no antigen present (Figure 72).

Figure 72B illustrates that at lower flow rates (25 nL/s) the binding profile tends to be linear over the time period investigated with the models. At higher flow rates, the surface tends toward saturation much earlier and the profile is more sigmoidal. This can be attributed to two factors: 1) more material is introduced to the device at high flow rates and 2) the "unstirred layer" is much smaller at higher flow rates, reducing the region in which diffusion dominates the transport to the surface.

The data also indicate that the total of antibody bound does not increase substantially at high flow rates. This is an important fact when considering that in Figure 72B, increasing the flow rate by a factor of 2.5 (250 nL/s – green data versus 100 nL/s – pink data) does not result in a significant change in a binding profile. When designing a diagnostic, the total volume introduced to the device is an important design parameter. The ability to reduce the sample required from the patient is important, and if a signal gain is not accomplished by increasing the flow rate it only serves to waste reagents and the sample.

An important consideration in the design of an immunoassay is the amount of dead volume (volume the fluid must travel before it reaches the detection area) in the system. Ideally, the sample would be introduced, without dilution, directly to the detection region. However, upstream tubing, valves, and the dead volume within the microchannel itself often make this a difficult task to accomplish. As a result of this dead volume the sample undergoes dispersion, which serves to dilute the sample and alter its concentration profile (for further details on dispersion please see Appendix H).

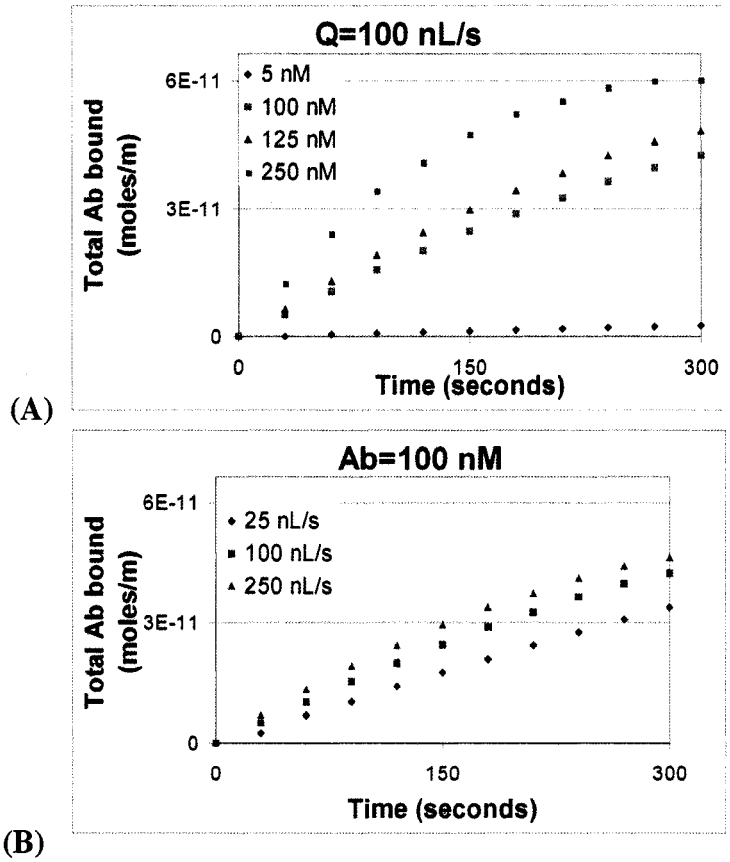

Figure 72. Influence of the concentration of antibody and flow rate on the total amount of antibody binding to the surface. Model results for the indirect immunoassay. No antigen is present. L1 =0.1 mm. The antibody binding was analyzed along L3 (see Figure 70 for diagram of model geometry). The theoretical maximum binding concentration for the 1mm surface is 6.64×10^{-11} moles/m.

Influence of dispersion on the antibody binding profile

To explore the influence of dispersion on the total binding of the antibody to the surface, two upstream distances before the binding surface were modeled – L1 = 0.1 mm or L1 = 22.1 mm (see Figure 70). No antigen was introduced to the solution. At time= 0 seconds, only buffer solution is present in the microchannel. The antibody concentration and flow rate were also altered to determine if there was a regime in which the influence of dispersion was most significant (Figure 73).

Figure 73 demonstrates in A and C that an increase in the upstream distance from the inlet and the binding surface alters the binding profile of the antibody to the surface. As

expected, by delaying the entrance of the antibody to the surface binding areas, the time at which to collect the data to quantify the amount of antigen in solution is delayed. An important note is that although the antibody may begin to bind to the surface later, the rate of the binding (slope of the curve) is similar for L1=0.1 mm and L1= 22.1 mm. The most significant difference between the antibody binding profiles for different upstream distances to the binding surface occurs at low flow rates and low antibody concentration (Figure 73C). In this scenario, the antibody is most transport-limited. At high flow rates (250 nL/s Figure 73B), the difference between the binding curves is negligible. As shown previously (Figure 72B), at very high flow rates, the transport to the surface is not as diffusion limited and it quickly saturates. Furthermore as discussed in Appendix H, the higher the concentration of the antibody the more quickly the protein will diffuse down the steep concentration gradient at the center of the microchannel toward the walls. Therefore, dispersion at high flow rates can be expected to have a negligible affect on the binding profile of the antibody to the surface.

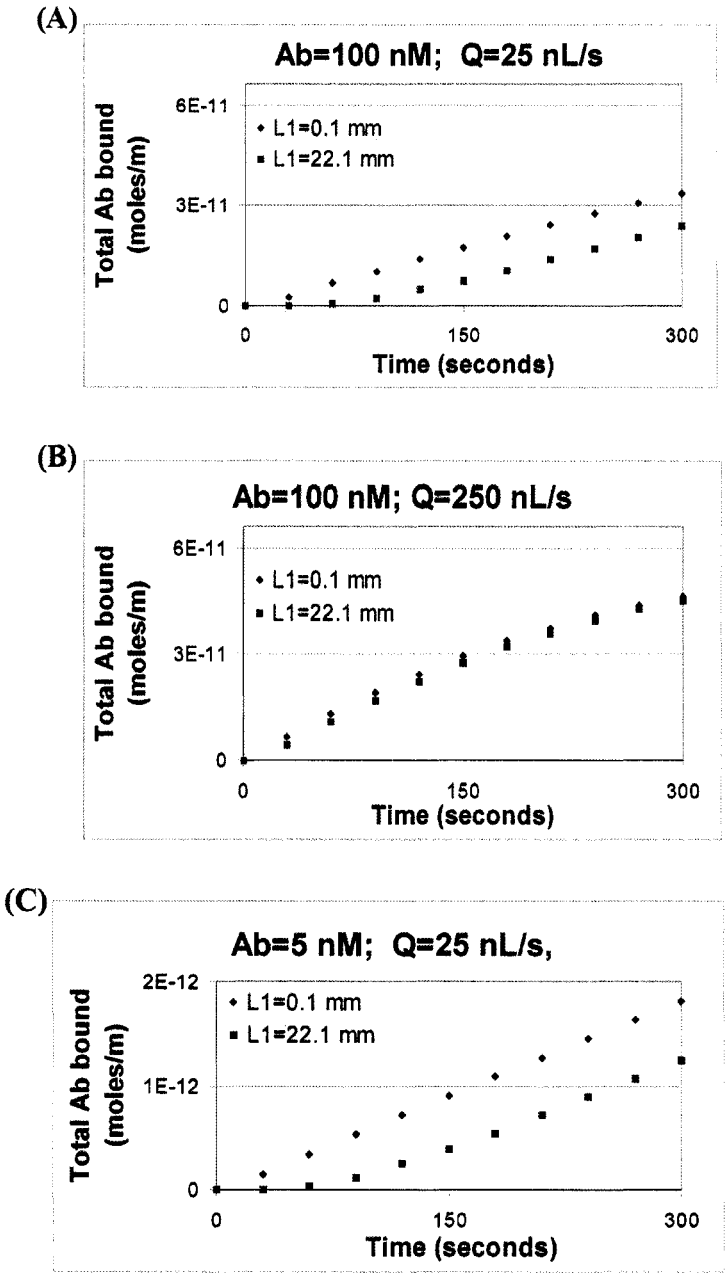

Figure 73. Influence of dispersion on the total amount of antibody bound to a surface. Two flow rates and two concentrations of Ab were examined. Model results for the indirect immunoassay. No antigen was present. L1 (see Figure 70 for the diagram of the model geometry) refers to the distance of the microchannel upstream of the binding surface. The theoretical maximum for total antibody binding to the 1 mm line is 6.64×10^{-11} moles/m. Note that the maximum in (C) is not the true maximum due to the low concentration of antibody and the low flow rate. The surface binding of the antibody is analyzed along L3 (see Figure 70 for the diagram of the model geometry).

Surface binding of antibody with antigen present in solution

The change in the binding profile of antibody to the surface as a function of antigen concentration is presented in Figure 74. In this model, the antibody is assumed to be monovalent (i.e. each antibody can bind only one antigen). Since the amount of antibody with available binding sites is inversely related to the amount of antigen present in the sample solution, it is expected that there will be a reduction in the amount of antibody binding to the surface with increased antigen concentration. The model results (Figure 74) clearly support this hypothesis.

An ideal assay would be operated under conditions such that either the total amount of antibody bound to the surface or the rate of antibody binding to the surface would relate linearly to the amount of antigen present in solution. The more sensitive the assay (the steeper the slope of the calibration curve), the better it is able to distinguish antigen concentrations. For the assay to be practically implemented, the assay also must be operated far from the saturation of the surface but with enough antibody molecules binding to the surface so that the SPR signal is above the detection limit of the instrument.

The influence of the flow rate on the binding profile (Figure 74A and B) indicates that at low flow rates (25 nL/s) the surface binding profile is far from saturation. There is a relatively inverse linear relationship between the total antibody bound to the surface and antigen present in the sample (see Figure 75 for further detail) for more than the first 8 minutes of the assay (not all data shown) assuming the assay's optimal dynamic range is between 25-100 nM. At higher flow rates (250 nL/s), more material is introduced to the device and the antibody surface binding profile is much more sigmoidal as the antibody quickly saturates the surface. Furthermore, the relationship between the amount of bound antibody to the surface at a given time point and the antigen concentration in solution is no longer linear (see Figure 75 for further detail). For example, the difference in the amount of antibody bound to the surface when the antigen concentration is doubled from

25 nM to 50 nM is not the same as when the antigen concentration changes from 75 nM to 100 nM, even though the absolute difference in concentration (25 nM) is the same. Therefore, to operate the assay under linear conditions, the data must be collected earlier for faster flow rates. The antibody concentration has a similar influence on the assay as the flow rate (Figure 74A and C) for a given dynamic range of antigen. Higher antibody concentrations result in more antibody available to bind to the surface so the surface will reach saturation in less time.

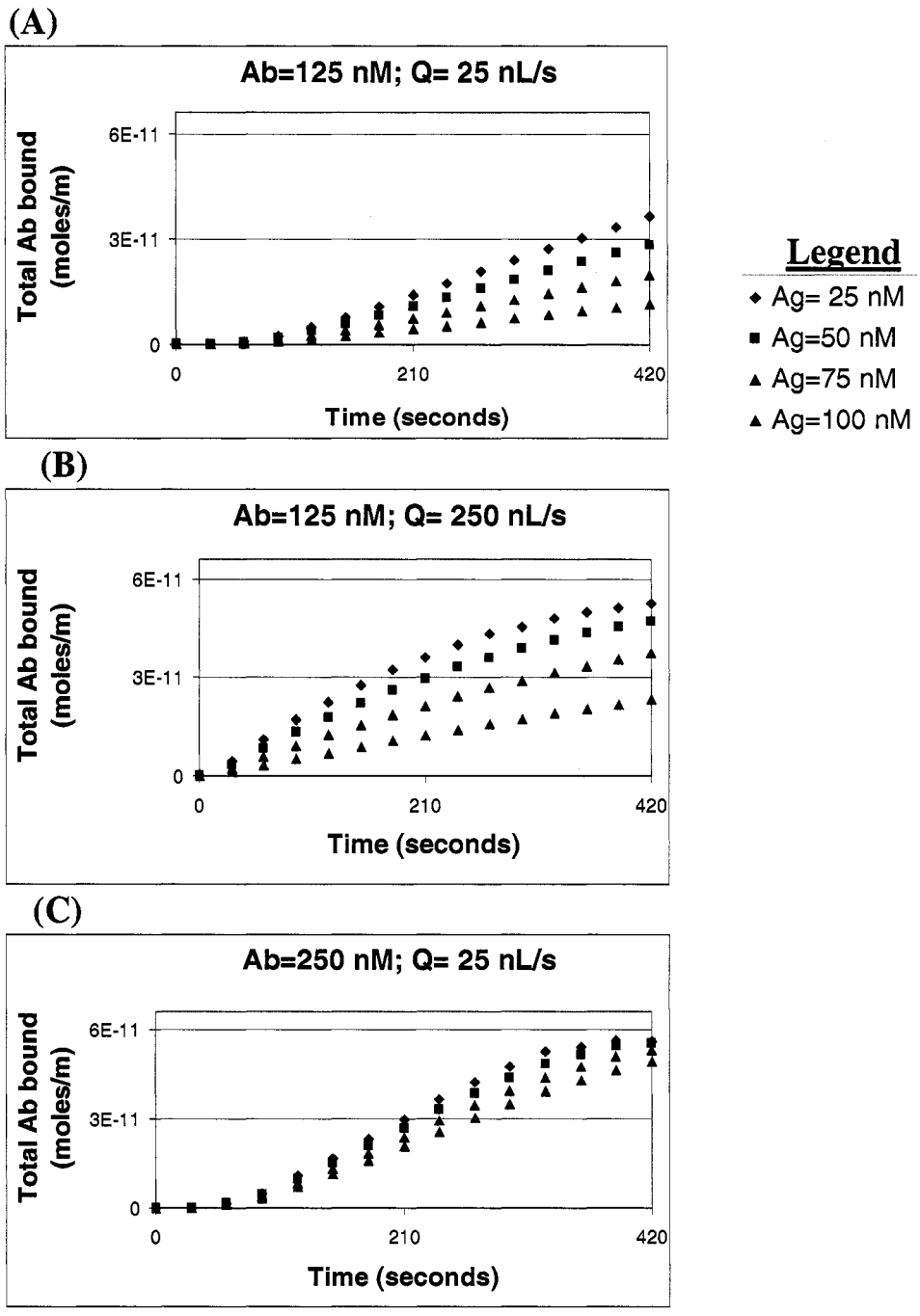

Figure 74. Total amount of antibody bound over time for a range of antigen concentrations. Model results. The influence of the flow rate and the antibody concentration are presented. L1 =22.1 mm (see Figure 70 for the diagram of the model geometry). The theoretical maximum for the total amount of antibody bound to the 1mm line is 6.64×10^{-11} moles/m. The antibody was assumed to be monovalent. The binding of the antibody was analyzed along L3 (see Figure 70 for the diagram of the model geometry).

Quantification of the antigen concentration by measuring the total amount of antibody bound to the detection surface

As previously mentioned, one method to quantify the amount of antigen (also termed analyte in the following figures) is to measure the amount of antibody bound at a given time point as a function of analyte concentration (Figure 75A-C). This potential method of quantification was qualitatively explored in the previous section. Figure 75 presents calibration curves generated with the model data. Three time points are presented. Linear fits for the data were plotted in Excel and the R^2 values are indicated for the 1 minute and 7 minutes time points. When the surface is far from saturation (time=1 minute), there is a strongly linear relationship for all assay conditions present (R^2 ~1 Figure 75A-C). As the surface tends toward saturation (time=7 minutes), the linear relationship between analyte concentration and total antibody bound is reduced (R^2 <1).

As previously mentioned, higher flow rates (Figure 75A at 25 nL/s versus Figure 75B at 250 nL/s) result in a binding surface that becomes saturated in a shorter amount of time, thereby reducing the linear relationship between the antigen concentration and total amount of bound antibody. There is only a small difference in sensitivity of the assay (the slope of a linear fit to the calibration curve at time= 7 minutes as computed by Excel) between 250 nL/s and 25 nL/s, which are -4×10^{-13} moles/(m nM) and -3×10^{-13} moles/(m nM) respectively, but the 250 nL/s data set is not as linear as the 25 nL/s data set.

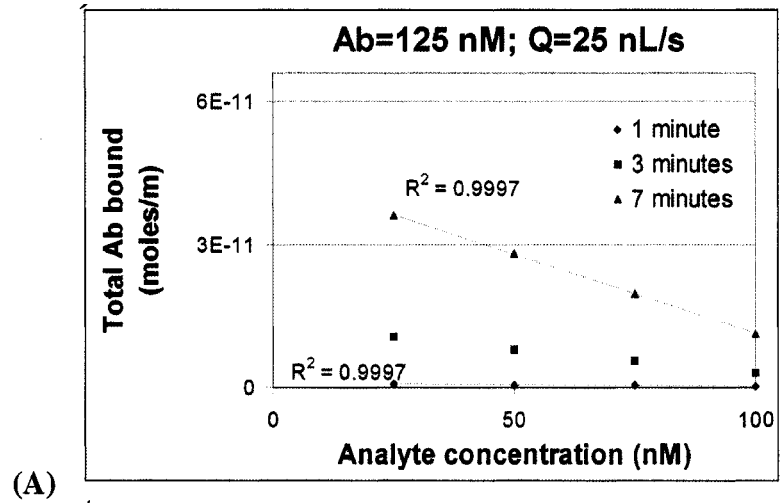

(A)

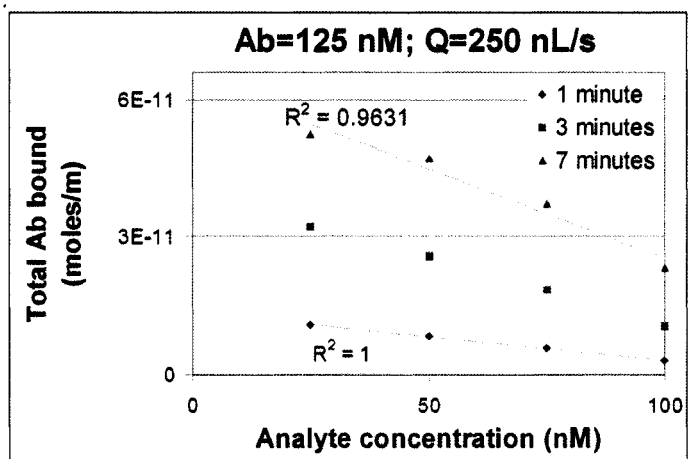

(B)

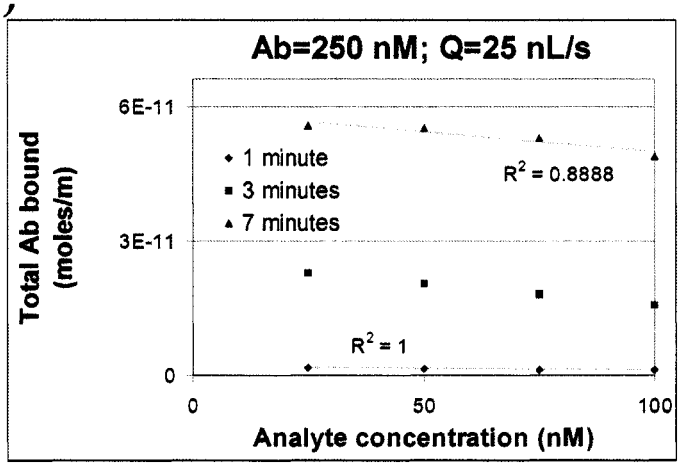

(C)

Figure 75. Quantification of the analyte (antigen) concentration using the total amount of antibody bound to the surface. Model results for the indirect immunoassay. The influence of the concentration of antibody and the flow rate are presented in (A)-(C). For the 1 minute and 7 minutes data sets, linear fits were plotted in Excel and the R^2 values are listed. The antibody is assumed to be monovalent. L1 =22.1 mm (see Figure 70 for the diagram of the model geometry). The theoretical maximum for the total the amount of antibody bound to the 1mm line is 6.64×10^{-11} moles/m. The surface binding of the antibody is analyzed along L3 (see Figure 70 for the diagram of the model geometry).

The higher the antibody concentration (Figure 75A at 125 nM versus Figure 75C at 250 nM), the more quickly the surface reaches saturation (i.e., R^2 value at time=7 minutes is ~0.89 for 250 nM Ab concentration versus ~0.9997 for 125 nM Ab concentration). The sensitivity of the assay is also markedly different. At time=7 minutes the slopes of the calibration curves are -9×10^{-14} moles/(m nM) for an antibody concentration of 250 nM and -3×10^{-13} moles/(m nM) for an antibody concentration of 125 nM. The change in sensitivity can be attributed to the amount of total free antibody available to bind the surface. When the antibody concentration is doubled from 125 nM to 250 nM and the range of analyte concentrations being measured remains 25 nM to 100 nM, there is a much larger percentage of the total antibody bound to analyte. Therefore, the ability of the analyte concentration to modulate the SPR signal is reduced. Ideally, the concentration of analyte and antibody would be comparable.

Quantification of the antigen concentration by measuring the rate of antibody binding

Another method to quantify the amount of analyte present in a sample is to measure the rate of antibody binding, not the total amount of antibody bound to the surface. In Figure 76, calibration curves were generated with model data that explore the influence of the flow rate and the antibody concentration on this quantification method. Once again, linear fits of the calibration curves as well as slopes (Table 9) were calculated in Excel. The rate of binding is the local rate of binding over a 30 second period calculated by subtracting the total amount of antibody bound at t_x from the total amount bound at t_x + 30 seconds and dividing by 30 seconds.

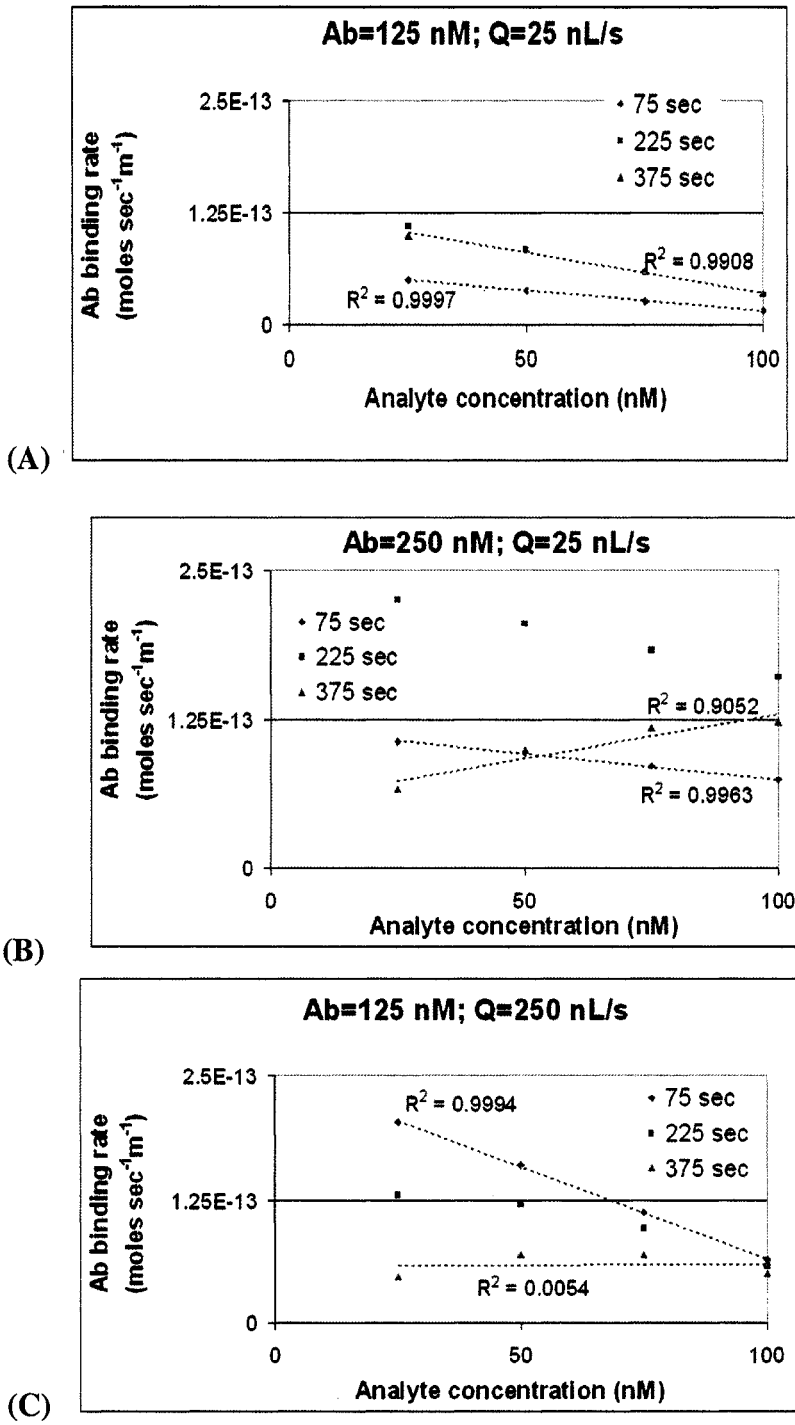

Figure 76. Quantification of the analyte concentration using the rate of binding of the antibody to the surface. Model results for the indirect immunoassay. The influence of the concentration of antibody and the flow rate are presented in (A)-(C). For the 75 second and 375 seconds data sets, linear fits were plotted in Excel and the R^2 values are listed. The antibody was assumed to be monovalent. L1 =22.1 mm (see Figure 70 for the diagram of the model geometry). The binding surface was located at L3 (see Figure 70 for the diagram of the model geometry).

Once again, approaching saturation of the surface with antibody complicates this method of analysis. When the surface approaches saturation, the rate of antibody binding is greatly reduced (see the slopes of the binding profile in Figure 74). For a given analyte concentration and a given time point, the amount of antibody bound to the surface is different, and in turn, the rate of binding varies. Ideally, the relationship between the rate of binding and analyte concentration would be linear.

At early time points and far from saturation, the low analyte concentrations (in turn high concentrations of antibody available to bind the surface) have the fastest rate of binding due to the steeper concentration gradient of antibody near the surface (Figure 74 A-C at time = 75 and 225 seconds). The higher analyte concentrations have a lower rate of binding due to the reduced concentration of antibody available to bind to the surface. However, at later time points (time=375 seconds), at low analyte concentrations the surface has nearly reached saturation of bound antibody and the rate of binding of the antibody to the surface approaches zero, whereas for the higher analyte concentrations the rate of antibody is substantially higher. Therefore, there can be an inversion of the calibration plot (Figure 74B time=375 seconds) with the faster rate of binding of antibody to the surface occurring at higher analyte concentrations. On the other hand, at lower antibody concentrations and lower flow rates (Figure 74A time= 225 and 375 seconds), the binding rate remains relatively constant.

Dispersion also can have a strong influence on the rate of binding, particularly at low flow rates (25 nL/s) and low antibody concentrations (125 nM) (Figure 74A time=75 seconds). Because the antibody has yet to reach the binding surface due to the upstream dead volume, the initial binding rates (time=75 seconds) are lower when compared to later time points (time=225 seconds). At higher flow rates (Figure 74C time=75 seconds), the earliest time point presented has the highest rate of binding as the antibody reaches the binding surface quickly.

The sensitivity of the assay (Table 9) shows a strong dependence on the antibody concentration and the flow rate. The larger the magnitude of the slope, the more sensitive the assay. As previously mentioned, at higher antibody concentrations and later time points (Ab=250 nM and time= 375 seconds and Q= 250 nL/s) the linear relationship is inverted (the higher analyte concentrations have faster binding rates) and the slope transitions from a negative to a positive value. The analysis time point that yields the most sensitive calibration curve varies for each assay design explored and changes dramatically over the course of a few minutes. The model results suggest that lower antibody concentrations (125 nM) and higher flow rates (250 nL/s) yield the most sensitive assay at early time points.

Table 9. Sensitivity of the indirect immunoassay when using rate of antibody binding to quantify the analyte (antigen) concentration. Model results.

	Slope of calibration curve (moles/(m second nM))		
Assay parameters/ time (seconds)	75 seconds	225 seconds	375 seconds
monovalent [Ab]=125 nM; Q=250 nL/s	-2E-15	-1E-15	3E-17
monovalent [Ab]=125 nM; Q=25 nL/s	-5E-16	-1E-15	-9E-16
monovalent [Ab]=250 nM; Q=25 nL/s	-4E-16	-9E-16	8E-16
bivalent [Ab]=125 nM; Q=25 nL/s	-2E-16	-4E-16	-2E-16

Comparison of model results when the antibody is assumed to be monovalent versus bivalent.

An important assumption in the previous models is that the antibody can only bind to a single antigen. Therefore, for a given antibody concentration, the modeled number of analyte binding sites is actually half of the actual number of analyte binding sites. To better understand the implication of this assumption on the binding profiles and methods of quantification, computational models in which bivalency was incorporated (assuming the binding kinetics to antigen in solution and to the surface is the same for antibody bound to a single free antigen from solution as antibody bound to no antigen from solution) were compared to previous monovalent models (Figure 77).

Unlike the surface binding profile of antibody over time for the monovalent model (Figure 77A), in which there is a significant difference in the total amount of antibody bound for a given analyte concentration, the binding profiles for the bivalent model (Figure 77C) do not vary significantly between different analyte concentrations. In effect, the incorporation of bivalency in the model increases the amount of antibody available to bind to the surface. Because antibody bound to one antigen is still capable of binding to the surface, a given analyte concentration does not modulate the binding of the antibody to the surface as much as a monovalent molecule, which when bound to a single analyte is incapable of binding to the surface.

The use of the rate of binding as a quantification method is also very different for the bivalent model versus the monovalent model (Figure 77B and D). In the bivalent model, more antibody is capable of binding to the surface at a given time point. Therefore, the bivalent model tends toward saturation before the monovalent model. At later time points (time=375 seconds), the antibody binding rates are reduced. The sensitivity of the assay is also significantly reduced (a factor of ~5-10 as shown in Table 9) in the bivalent model due to the ability of antibody bound to one analyte to bind to the surface. These results suggest that Fab fragments or a reduction in the antibody concentration will be required in order to develop a more sensitive immunoassay.

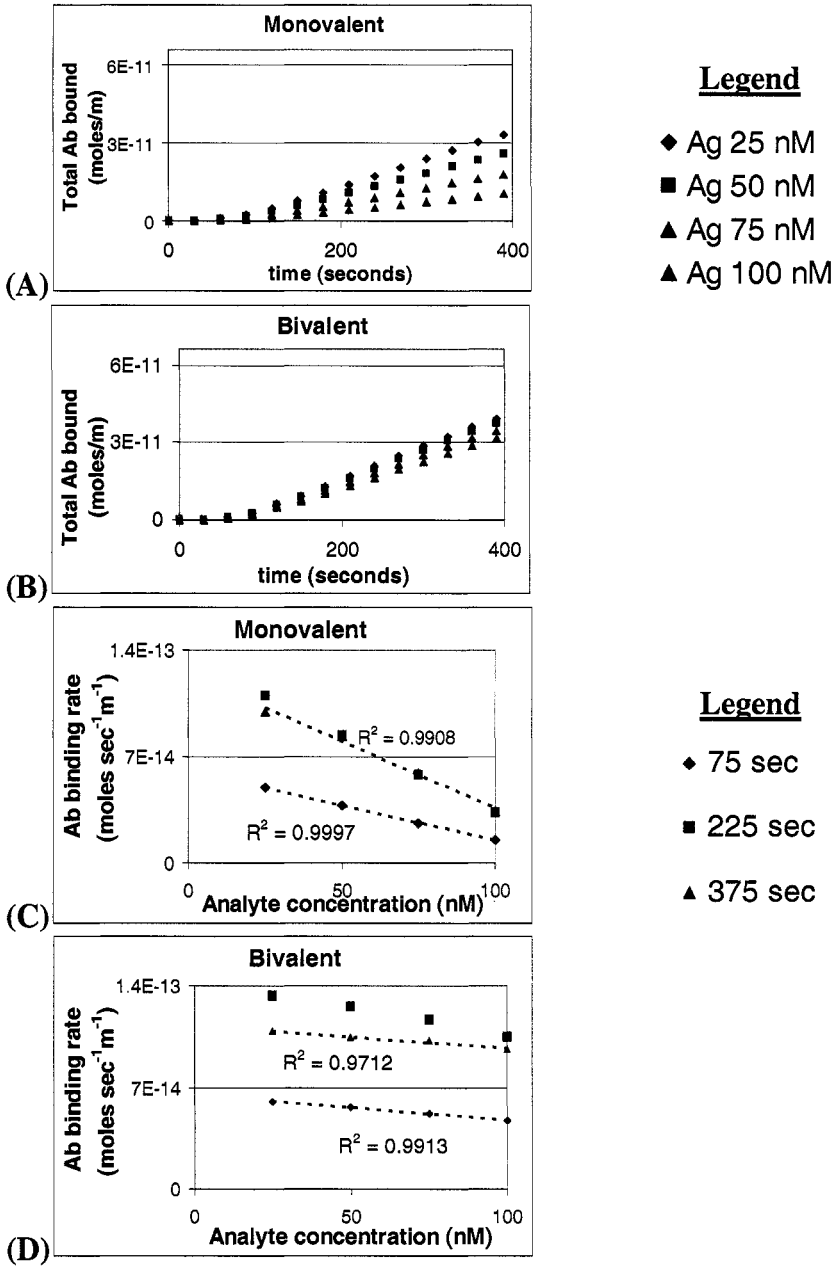

Figure 77. Incorporation of a bivalent antibody in the computational model. Comparison of the total amount of antibody bound to the surface over time ((A) and (B)) and the calibration curve when the rate of antibody binding to the surface was used to quantify the amount of analyte ((C) and (D)) for a monovalent antibody versus a bivalent antibody. Model results. The bivalent model assumes $k_{on1}=k_{on2}$, $k_{off1}=k_{off2}$, $k_{des1}=k_{des2}$, and $k_{ads1}=k_{ads2}$. For the 75 second and 375 seconds data, linear fits were plotted in Excel and the R^2 values are listed. L1 =22.1 mm (see Figure 70 for the diagram of the model geometry). The antibody concentration was 125 nM and the flow rate was 25 nL/s. The theoretical maximum for the total amount of antibody bound to the 1mm line was 6.64×10^{-11} moles/m. The surface binding of the antibody was analyzed along L3 (see Figure 70 for the diagram of the model geometry).

Comparison of model results when the kinetic binding rates for a bivalent antibody were altered when it was bound to one versus two antigen molecules

(A)

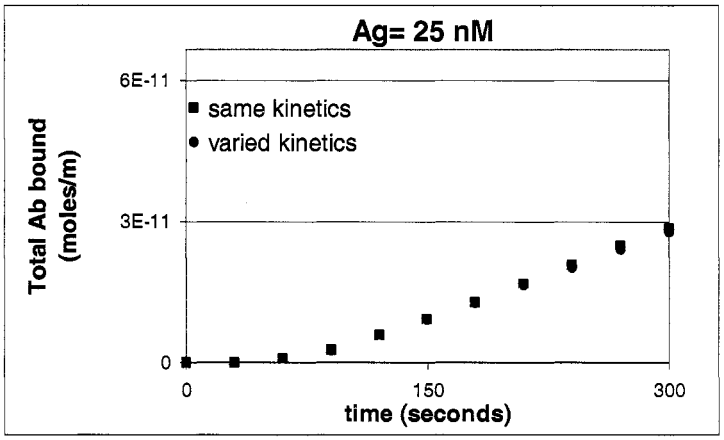

(B)

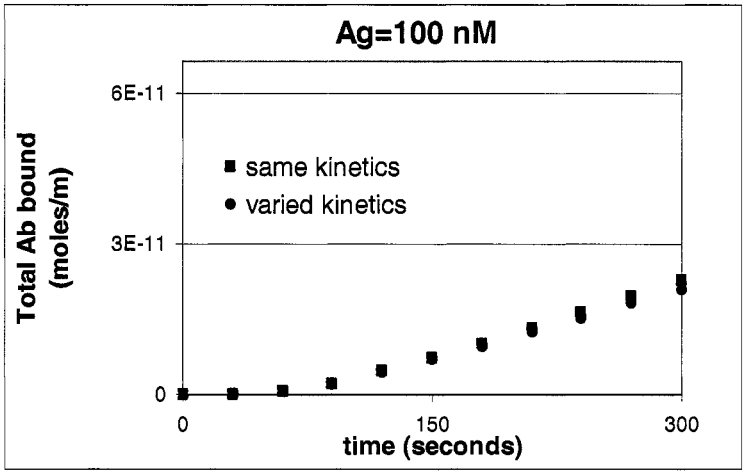

Figure 78. Influence of varied kinetic parameters on the total amount of antibody bound to the surface over time for the indirect immunoassay for two concentrations of antigen (analyte). Model results. The models assume the antibody is bivalent (see Figure 69A). The model with the *same kinetic parameters* assumed $k_{on1}=k_{on2}$, $k_{off1}=k_{off2}$, $k_{des1}=k_{des2}$, and $k_{ads1}=k_{ads2}$. The model with *varied kinetic parameters* assumed $k_{on1}=k_{on2}$, $k_{off1}=0.5k_{off2}$, $k_{des1}=0.5k_{des2}$, and $k_{ads1}=2k_{ads2}$. L1 =22.1 mm (see Figure 70 for the diagram of the model geometry). The theoretical maximum for the total amount of antibody bound to the 1mm line was 6.64×10^{-11} moles/m. The surface binding of the antibody was analyzed along L3 (see Figure 70 for the diagram of the model geometry). The antibody concentration was 125 nM, and the flow rate was 25 nL/s.

In the previous bivalent model (Figure 77), the binding kinetics of antibody bound to a single antigen were assumed to be the same as an antibody bound to no antigen. This assumption may not be accurate. Depending on the rotational diffusion of the antibody molecule and the size of the antigen, the kinetic parameters may not be the same for free

antibody and antibody bound to a single antigen molecule. A thorough literature search found no completed experimental measurements of the kinetic rates for antibody bound to no antigen and bound to one antigen. To determine if this assumption significantly changes the expected binding profile, models with varied kinetic parameters were completed. Without experimental measurements to guide the model parameters, several assumptions were made. The adsorption rate of antibody bound to a single antigen was assumed to be half of the binding rate of antibody bound to no antigen as the number of available binding sites is halved. The desorption and off rates for antibody bound to no antigen are half that of antibody bound to a single antigen, as there is another binding site in close proximity that can rebind the analyte molecule released, thereby effectively reducing the off rate and desorption rates.

The model results (Figure 78) for two antigen concentrations suggest that there is very little difference in the binding of the antibody to the surface for a given flow rate (125 nL/s) and antibody concentrations (125 nM). There is only a very slight reduction in the amount of binding with the varied kinetic parameters. These results suggest that the potential for varied kinetic parameters does not completely alter the expected binding profiles. However, at higher antigen concentrations and/or lower antibody concentrations, a larger population of antibody molecules will be bound to one and two antigen molecules. Under those conditions it would be expected that the varied kinetic parameters will alter the binding profile to a greater extent.

6.5 Conclusions

Computational models of the indirect immunoassay have been developed. The model results confirm experimental results (data not shown and collected by Dr. Kjell Nelson) that indicate that at low flow rates there is substantial binding of the antibody to the upstream edge of the binding surface, with a steep reduction in binding downstream. At higher flow rates, when the antibody is less transport-limited, the binding profile is more uniform down the length of the channel.

The model results indicate that the binding profile of the antibody to the surface as a function of time is sigmoidal. At early time points, the total binding of antibody to the surface is linear. As the surface becomes saturated with the antibody, the relationship becomes highly non-linear. When higher flow rates and higher antibody concentrations are used, the surface will quickly reach saturation.

Two methods of quantification of the analyte concentration (rate and total binding of antibody) were analyzed. Due to the reduction in the amount of binding when the surface approaches saturation, the point at which the binding rate or total amount of bound antibody is measured is critical to achieve a sensitive and rapid immunoassay result. Ideally, the SPR instrument should have a low limit of detection and be extremely sensitive to enable the measurements to be taken at early time points when the binding curve of the antibody to the surface is linear as a function of a time.

Given the complex relationship between flow rate, antibody concentration, and the quantification method (rate analysis or total binding of antibody analysis), a computational model that efficiently explores the influence of these parameters on assay performance will be extremely useful.

Chapter 7: Computational model of the concentration gradient immunoassay

7.1 Objectives

1) Develop a computational model of the CGIA.

2) Use model results to explore a method to quantify the amount of analyte in a sample.

7.2 Related Publications

All figures (except the last figure in the chapter) and captions in this chapter were copied from the following articles. The majority of the text is also reproduced.

1) Foley, J., Nelson, K., Mashadi-Hossein, A., Finlayson, B., and P. Yager. "Concentration Gradient Immunoassay (CGIA) II. Computational Modeling for Analysis and Optimization." *Analytical Chemistry.* (in press).

2) Nelson, K., Foley, J. and P. Yager. "The Competition Gradient Immunoassay (CGIA): A Rapid Competitive Immunoassay Based on Interdiffusion and Surface Binding in a Microchannel." *Analytical Chemistry.* (in press).

7.3 Background

As described in Chapter 2 of this dissertation, the Yager group has proposed a novel surface-based microfluidic flow immunoassay – the concentration gradient immunoassay (CGIA)[15] – to quantify small molecules using surface sensitive techniques such as SPR imaging. This assay extends the principles of the diffusion immunoassay (DIA)[51, 54, 209] – an assay that utilizes the unique transport characteristics of microfluidic devices like the T-sensor.[47, 49] Like the DIA, this assay relies upon the interdiffusion and binding of an antibody and analyte to quantify the concentration of the analyte. In contrast to the DIA,

which uses fluorescence to observe the assay outcome, the CGIA uses SPR imaging to measure changes in mass at a surface to quantify the analyte.[12-14]

In the CGIA (Figure 79), solutions of antibody and antigen (the analyte) are introduced to a T-sensor under laminar flow conditions. The solutions mix by diffusion across the interface, allowing the antibody and analyte to bind to form an antibody-analyte complex. This diffusion-based mixing establishes a spatially-dependent concentration gradient of antibody-analyte complex that can be directly related to the concentration of analyte for a given antibody concentration. The example presented herein illustrates how, twenty-two millimeters downstream of the inlet, antibody with open binding sites binds to a surface functionalized with immobilized analyte. The amount of antibody available to bind inversely relates to the concentration of analyte in solution. SPR imaging detects the spatial distribution of surface bound antibody.

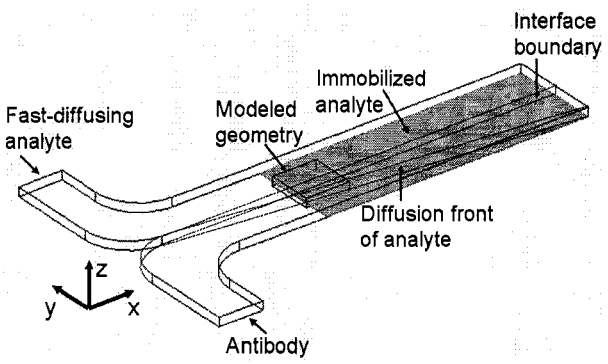

Figure 79. Schematic of the concentration gradient immunoassay (not drawn to scale). Antibody and a fast-diffusing analyte (e.g., phenytoin) are introduced to a T-sensor. Antibody and analyte interdiffuse and bind at the fluidic interface. The diffusion front of the fast-diffusing analyte traverses into the antibody stream (y-dimension) as the fluids travel down the length of the channel where it binds to the relatively slow-diffusing antibody to form antibody-analyte complex. The surface downstream is functionalized with immobilized analyte. Free antibody binds to the surface and is detected with a surface-sensitive technique – SPR imaging. Due to computational limitations, only the central 1.6 mm of the 3 mm wide (y-dimension) device located 22 mm downstream of the inlet could be modeled in three dimensions. A two-dimensional model that was connected to the three-dimensional model simulated the upstream portion of the assay.

A finite element model was developed to give insight into the important physical parameters of the assay. Given computational constraints, only the central 1.6 mm of the 3 mm wide (y-dimension) microchannel positioned twenty-two millimeters downstream of the inlet could be modeled in three-dimensions (Figure 79). Because of its reduced

complexity in the absence of surface binding, a two-dimensional model simulated the convective and diffusive mass transport and antibody antigen binding from the inlet to the binding surface. The solution to this two-dimensional model was coupled to a full three-dimensional model that includes binding of antibody (assumed to be monovalent) to the SPR sensing surface. The governing equations within the microchannel are the Navier-Stokes equation,[52] which describes the behavior of the fluids, and the convection-diffusion equation,[52] which describes the transport and reaction of the antibody, analyte, and antibody-analyte complex. The surface reaction of the antibody binding to a surface-immobilized analyte (Equation 9 and Equation 10) was coupled to the convection-diffusion equation for the antibody within the microchannel. See Appendix for further information.

$$c_{Ab} + \theta \underset{k_{des}}{\overset{k_{ads}}{\Leftrightarrow}} c_s \qquad \text{Equation 9}$$

$$\frac{dc_s}{dt} = k_{ads} c_{Ab}(\theta_0 - c_s) - k_{des} c_s \qquad \text{Equation 10}$$

where c_{Ab} is the antibody concentration in the bulk of the microchannel, cs is the surface concentration of bound antibody, θ_0 is the surface concentration of antibody binding sites, and k_{ads} and k_{des} are the adsorption and desorption kinetic parameters.

This model compared to other computational models of assays is novel in that it 1) assesses the binding profile in three-dimensions and 2) incorporates dispersion (i.e.. the three-dimensional geometry at t=0 is filled with buffer). Although the model accounts for dispersion, the upstream distance between the binding surface and the sample fluid is significantly larger for the experimental system (at least 10 cm versus <0.1 mm). However, even given this discrepancy, the model should still be able to predict the qualitative behavior of the immunoassay.

7.4 Materials and Methods

Computational Simulations

All computational simulations were completed with the commercially-available finite element method software, COMSOL® (Version 3.3, Comsol, Inc., Burlington, MA) on a G5 PowerMAC with 8 GB of RAM and a dual 2.5 GHz processor. The models build upon a two-dimensional example in COMSOL®'s model library.[210]

A two-dimensional cross-section (y- and z-dimensions) of the microfluidic device simulated the concentration profiles of the antibody, analyte, and antibody-analyte complex as a function of the x-dimension for the 22 mm portion of the device upstream of the binding region. In these simulations, the entire width of the microchannel (3 mm in the y-dimension) was modeled. The Poisson equation solved the laminar flow parabolic velocity profile. A pseudo-3d convection-diffusion mode used this velocity profile to determine the concentration profiles of the analyte, antibody, and antibody-analyte complex as the streams flow down the length of the device. The concentration and velocity profiles were mapped to the inlet of the three-dimensional geometry to connect the two- and three-dimensional models.

The three-dimensional geometry (Figure 79) contained the binding surface and was 1 mm (x-dimension) × 1.6 mm (y-dimension) × 0.1 mm (z-dimension) for analyte concentrations ranging from 1 nM to 500 nM. Additional simulations (data not shown) demonstrated that the model results are representative of the assay for this range of analyte concentrations. For higher analyte concentrations, the modeled three-dimensional geometry was 0.3 mm (x-dimension) × 3 mm (y-dimension) × 0.1 mm (z-dimension) to accurately capture the steep concentration gradient of the analyte. When solving the Navier-Stokes mode, the mesh consisted of 7,870 elements and 166,487 degrees of freedomen. When solving the convection-diffusion and surface binding modes, the mesh consisted of 10,948 elements and 200,891 degrees of freedom.

The steady-state Navier-Stokes equation was solved using a mapped two-dimensional velocity profile at the inlet thereby ensuring fully-developed flow throughout the device. COMSOL®'s weak-boundary mode solved the surface reaction and coupled it to the flux of antibody through the binding surface in boundary conditions of the COMSOL®'s convection-diffusion mode solved in the bulk of microchannel. Using the mapped two-dimensional concentration profiles at the inlet and the solved three-dimensional velocity profile, the transient convection-diffusion mode and weak boundary mode were solved simultaneously. The initial conditions specified that the concentration of all species was zero within the microchannel and no antibody was bound to the surface. For the portion of the microchannel modeled using the pseudo-3d mode, it was assumed that the diffusion was minimal in the axial direction (x-dimension) compared to convection; this is an acceptable description for this model. In the experimental design,[15] bovine serum albumin (BSA) molecules functionalized with multiple analytes are adsorbed to a surface and bind antibody from solution. Given the dimensions of an antibody (14.2 nm × 8.5 nm × 3.8 nm)[211] and bovine serum albumin (BSA) (~71 nm^2 when adsorbed to a surface)[212] and taking into account steric constraints and that multiple analyte binding sites are available on a single BSA molecule, the surface density was estimated to be 1 binding site every 5 nm × 5 nm (6.64×10^{-8} moles/m^2). The diffusion coefficient for the model analyte, phenytoin (MW 243), used in experimental tests of this system was estimated as 5×10^{-6} cm^2s^{-1}. This is comparable to the diffusion coefficient of other small molecules such as sucrose (MW 342 Da) with a reported diffusion coefficient of 4.6×10^{-6} cm^2s^{-1}.[204] The modeled diffusion coefficient of the antibody was 4.3×10^{-7} cm^2s^{-1} based on molecular weight (150 kDa).[54, 211] The diffusion coefficient of the antibody-analyte complex was assumed to be the same as the antibody given the large size of the antibody relative to the phenytoin molecule. The k_{ads} (10^5 1/(Ms)) was estimated to be an order of magnitude smaller than the k_{on} (10^6 1/(Ms)) due to the reduction of binding efficiency of an immobilized analyte versus an analyte free in solution.[203] The k_{off} and k_{des} were estimated to be 10^{-2} 1/s. These kinetic parameters are within the range for typical antibodies.[213-215] The flow rate is 53 nL/s. The average velocity in the channel was

0.000177 m/s corresponding to a Reynolds number of 0.01767 and Peclet numbers of $Pe_{antibody}$=375.9, $Pe_{analyte}$=35.33, and $Pe_{antibody\text{-}analyte\ complex}$=375.9.

7.5 Results and Discussion

As the solutions flow down the length of the channel, the antibody and analyte solutions mix by diffusion across the fluid interface; antibody and antigen molecules bind to form antibody-analyte complex (Figure 80A-C). The analyte diffuses an order of magnitude faster than the antibody and the antibody-analyte complex. This relative difference in diffusion coefficients results in a bias in the location of the antibody-analyte complex to the side (y-dimension) of the microchannel on which the antibody was introduced (Figure 80B), as the analyte diffuses a greater distance into the antibody stream than vice versa. The immobilized analyte depletes the concentration of antibody near the surface at the beginning of the binding region (Figure 80C). The highest surface concentration of bound antibody (Figure 80D) is located at the leading edge of the binding surface where the antibody present near the microchannel wall binds. Downstream of the beginning of the immobilized analyte surface, the depletion of solution antibody molecules reduces the rate of binding to the surface, resulting in a reduced surface concentration of bound antibody. These results suggest that under the simulated assay conditions the surface reaction is mass-transport limited. Experimental results presented by Nelson et al. reveal a similar binding profile in support of this model result.

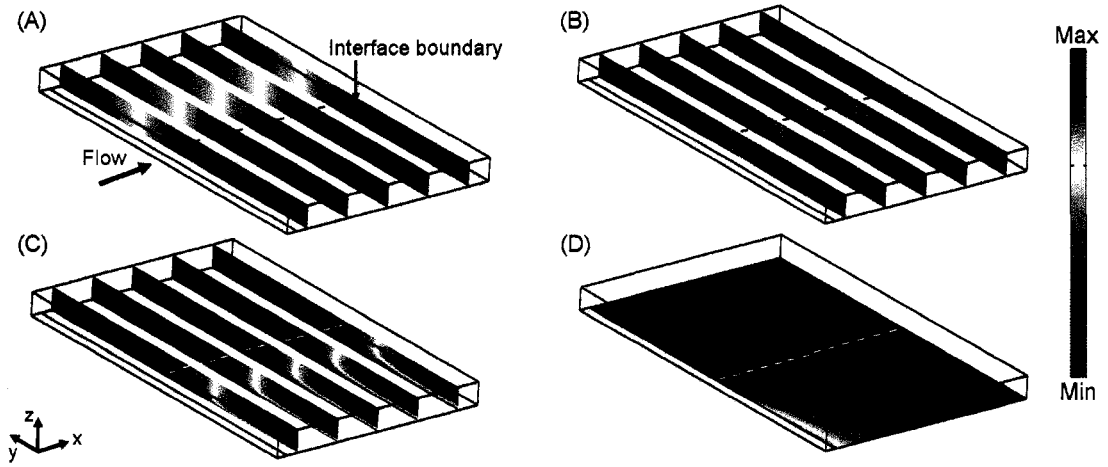

Figure 80. Concentration profiles of species in a typical CGIA. (A)-(C) The concentration profiles for the analyte, antibody-analyte complex, and antibody respectively at time=4.25 minutes where the maximum concentration is 100 nM and minimum concentration is -2.2×10^{-5} nM. (D) Surface concentration of bound antibody at time=4.25 minutes where the maximum concentration is 1.342×10^{-8} moles of bound antibody/ m^2 and the minimum concentration is -7.334×10^{-14} moles of bound antibody/ m^2. The arrow and dashed line indicate the direction of flow and the interface boundary of the microchannel for each image. The initial analyte and antibody concentrations were 100 nM. The modeled geometry is 1 mm (x-dimension) × 1.6 mm (y-dimension) × 0.1 mm (z-dimension).

The surface concentration of bound antibody (Figure 81) increases beyond the front of the binding surface (x-dimension) over time. However, the highest surface concentration of antibody remains at the upstream edge of the binding patch. As the solutions flow across the immobilized analyte, the antibody and analyte in solution continue to mix by diffusion and bind to each other to generate antibody-analyte complex. The difference in diffusivities of the antigen and the antibody gives rise to an increasing concentration of complex on the side of the channel to which the antibody was introduced, as previously shown in Figure 80B. The position of the complex within the microchannel along the length of the channel (x-dimension) moves towards the side of the channel (y-dimension) to which the antibody was introduced due to diffusive mixing and reaction. The amount of antibody available to bind to the surface is reduced and is reflected in the binding profile as a slight slope in the surface concentration of bound antibody (indicated by the red arrow in Figure 81).

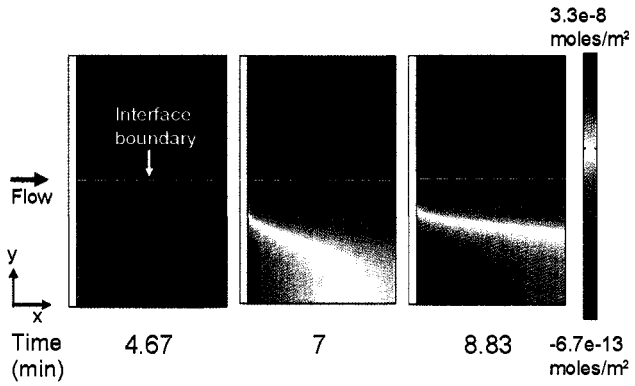

Figure 81. Surface concentration of bound antibody over time. The solution analyte and antibody concentrations were set to 100 nM. The red arrow indicates the direction of the slope in the binding profile of antibody to the surface due to the continued formation and diffusion of complex above the immobilized analyte. The results present a 1 mm (x-dimension) × 1.6 mm (y-dimension) region of the binding surface located in the center of the 3 mm wide (y-dimension) microchannel.

A critical element in the development of this assay is the establishment of a quantitative analysis method. Simulations explored the influence of analyte concentration on the binding of the antibody to immobilized analyte (Figure 82). As shown in Figure 82, for a given antibody concentration, the analyte concentration modulates spatial distribution of the concentration gradient of antibody-analyte complex within the microchannel. At higher analyte concentrations, more antibody-analyte complex is formed, thereby reducing the concentration of antibody with binding sites available to react with the immobilized analyte.

The analyte concentration also modulates the location of the antibody-analyte complex within the microchannel. Relatively higher analyte concentrations increase diffusional transport of the analyte into the antibody stream where it reacts to form antibody-analyte complex. This shifts the location on the surface to which antibody with available binding sites can react with the immobilized analyte.

Figure 82A illustrates this shift in the position on the surface where antibody is available to bind to immobilized analyte. When the analyte concentration is 1 nM and the antibody concentration is 100 nM, very little antibody-analyte complex is formed at the fluidic interface. The majority of antibody in solution is available to bind to the surface.

Therefore, antibody is available to bind to the surface near the interface boundary. When the analyte concentration is 100 nM, a significant amount of complex is formed at the fluidic interface and the location on the surface where free antibody can bind shifts away from the interface boundary (y-dimension).

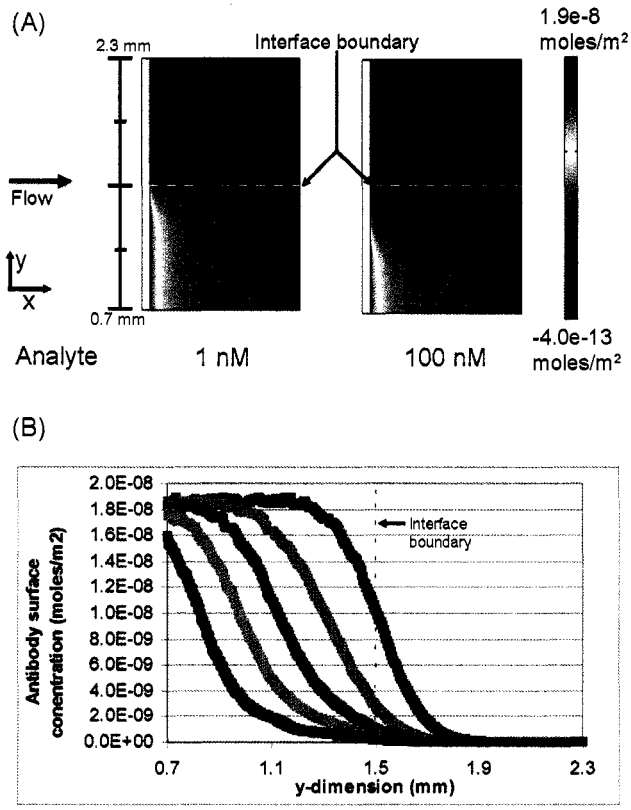

Figure 82. Influence of the concentration of analyte on the surface concentration of antibody. (A) Comparison of the surface binding profiles of antibody when the analyte concentration is 1 nM and 100 nM. The black bar at the left indicates the actual y-dimension distance within the microchannel. (B) The surface concentration of antibody as a function of position in the y-dimension at the leading edge of the binding surface. The analyte concentrations plotted are 0 (+), 100 (+), 250(+), 500 (+), and 1000 (+) nM. The concentration of antibody was 100 nM and t=4.67 minutes.

A range of analyte concentrations (1 nM to 1000 nM) was simulated to further explore the influence of analyte on the surface binding profile. The graph in Figure 82B plots the surface concentration of bound antibody at the leading edge of the immobilized analyte patch as a function of the width (y-dimension) of the microchannel. The results indicated that there was a significant shift away from the interface boundary in the binding profile of the antibody with increasing analyte concentration.

This assay shift, defined as the distance from the interface "boundary" at which 50% of maximal surface concentration of bound antibody occurs, may be used to quantify the total concentration of analyte in solution. In Figure 83, the assay shift is plotted as a function of the analyte concentration. The simulation results indicated that there was a linear relationship between the assay shift and analyte concentration at low analyte concentrations (1 nM - 100 nM). The influence of analyte concentration on assay shift was also measured experimentally by Nelson et al. The experimental and model results correlate extremely well indicating that the model accurately captures the relevant experimental parameters.

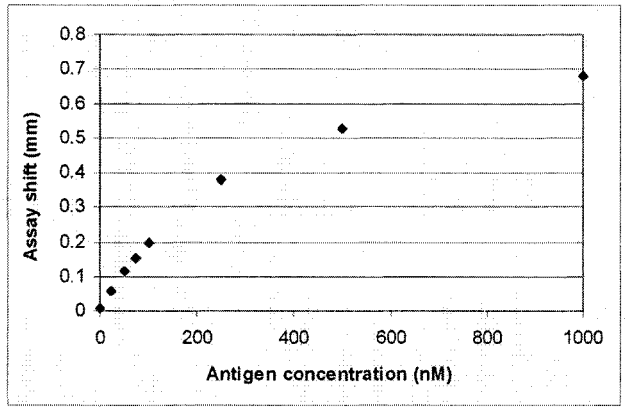

Figure 83. Assay shift dependence on analyte concentration. The assay shift was for an antibody surface concentration that was half the maximal surface concentration at that time point (0.9×10^{-8} moles/m^2). The concentration of antibody was 100 nM and t=4.67 minutes.

Given the similarity between the model and experimental results, measuring the assay shift may represent a viable method for quantifying the analyte concentration. A plot similar to Figure 83 would be used to calibrate an instrument's response. The position at which a given surface concentration of antibody occurs would then be used to determine the analyte's concentration in a sample. A major benefit of this type of analysis is that it is rapid and does not require extensive calculations or transformation of the data.

It should be noted that the model presented in this work assumed that the antibody was monovalent, rather than bivalent, due to computational constraints. An IgG molecule with one bound analyte (defined as the complex in the model) can in theory bind to the surface. Therefore, the model underestimates the amount of antibody available to bind to

the surface and gives only a semi-quantitative understanding of the experimental results. However, with the current assumptions, the experimental and model results show strong agreement, suggesting that this simplifying assumption does not eliminate the validity of the model. With increased computational resources, bivalency may be incorporated in the 3D model in future work.

The results for the finite element models presented above exhibit some numerical noise given the complex nature of the model. In particular, some of the results indicate that slightly negative concentrations of species (0.002% of the magnitude of the maximum concentration of 100 nM) are present in the microchannel. This non-physical result occurs in a relatively small portion of the model (<<5%) and arises in regions where the species is unlikely to occur – for example the antibody concentration on the side of the channel to which analyte – not antibody – was introduced. Therefore, these negative concentrations do not detract from the validity of the model results.

The noise and the negative concentrations can be attributed to several factors including (1) a mesh which is not dense enough to generate a smooth data set and (2) discontinuities at the initial conditions that would include surface concentrations and solution concentrations that are zero at time = 0. Given the nature of the assay and the computational limitations, the noise in the data and the negative concentrations could not be completely eliminated.

The previous model results assumed that the antibody was monovalent. In effect, this assumption increased the response of the assay for a given analyte concentration thereby overestimating the "assay shift." To overcome the computational limitations resulting from the incorporation of two new species in the model (1) antibody molecules bound to two analytes in solution and (2) antibody molecules bound to one analyte from solution and a surface immobilized analytes) a much smaller geometry was modeled (in the x-dimension it was 0.3 mm as opposed to 1 mm for previous model results – see Figure 79).

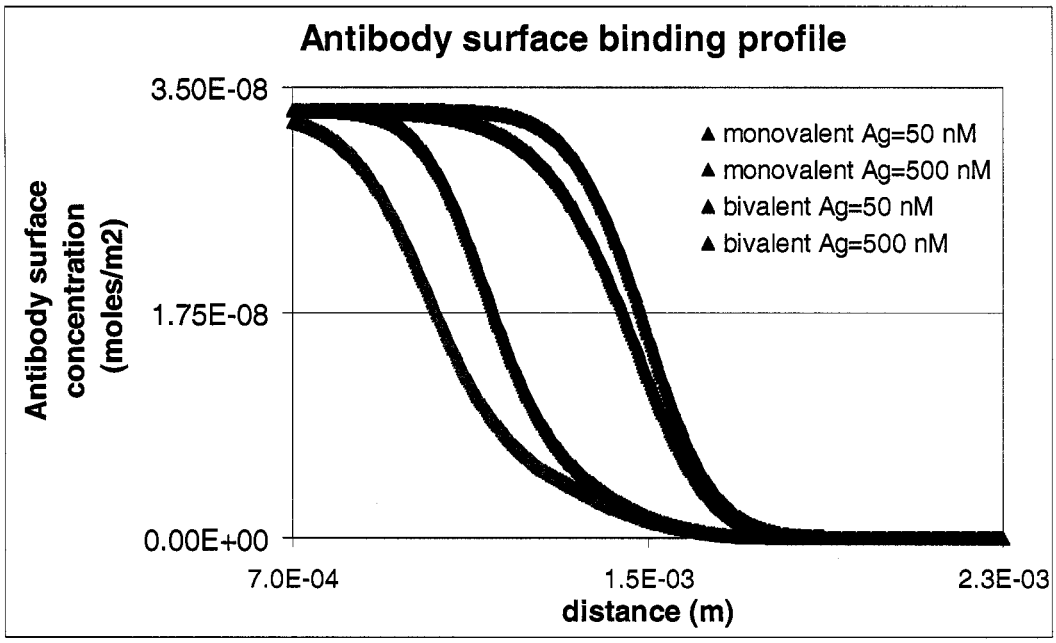

Figure 84. Influence of incorporating a bivalent antibody into the model on the surface binding profile of the antibody. Model Results. Surface binding profile of antibody at the leading edge of the binding surface transverse to flow (y-dimension). The results for the central 1.6 mm of the microchannel are presented. Antibody concentration = 100 nM. Time = 400 seconds.

Like Figure 82B, the binding profile of the antibody across the leading edge of the binding surface transverse to flow (y-dimension) was plotted as a function of the distance across the channel for the bivalent and monovalent models (Figure 84). As expected, the bivalent model results indicated that more antibody binds to the surface, and the assay shift was reduced for a given analyte concentration. The implication is that the sensitivity of the assay was reduced. Two potential methods to circumvent this reduction in sensitivity are to: (1) reduce the antibody concentration so that there is an increase in the population of antibody molecules bound to two analyte molecules or (2) incorporate Fab fragments instead of antibodies thereby eliminating the use of a bivalent recognition species.

7.6 Conclusions

A computational model has been presented that describes a novel surface-based immunoassay – the CGIA – that relies on the inter-diffusion and reaction of antibody and analyte and the binding of an antibody to surface immobilized antigen to quantify the concentration of analyte in a sample. The model data give insight into the underlying transport and reaction mechanisms in the assay and support a quantitative analysis method directly related to the key feature of this method, namely a diffusion-generated spatial concentration gradient. Strong qualitative agreement between the model and experimental results enable us to use this model to explore methods to optimize the dynamic range and sensitivity of the assay as well as tailor assay parameters for specific analytes at medically relevant concentrations. Future work could explore those topics by altering the device geometry, the antibody concentration, the K_d of the antibody, the analyte species (i.e. explore the potential to quantify large slowly diffusing species using the CGIA), and flow rates.

Chapter 8: Surface binding of proteins in a chevron microfluidic mixer.

8.1 Objectives

1) Simulate a microfluidic flow assay (streptavidin-biotin system detailed in Chapter 5) that incorporates a chevron mixer with fluid introduced in a forward and reverse configuration.
2) Relate the model results for the velocity profile within the chevron microchannel to the surface binding profile of streptavidin.
3) Microfabricate chevron microchannels.
4) Complete SPR imaging streptavidin-biotin flow assay experiments using the chevron microchannel.
5) Compare the pattern of binding and the total amount of binding of streptavidin to a straight microchannel with experimental and computational results.

8.2 Background

The purpose of this work is to determine if a passive microfluidic mixer shown to mix solutions in the bulk of the device will be able to improve the performance of a model system of a microfluidic flow assay – streptavidin binding to immobilized biotin from solution. A passive microfluidic mixer is defined as a mixer which does not require external actuators to cause the solutions to stir.[216] Given the constraints of a point-of-care diagnostic, external actuators add complexity, cost, moving parts, and increased power consumption. Therefore, for a point-of-care diagnostic, a passive mixer would be more suitable and cost-effective.

In Chapter 5, the computational model of the streptavidin assay in a rectangular duct indicated that a depletion zone above the binding region exists in which the concentration of analyte is extremely low. To bind to the surface, streptavidin must diffuse toward the surface while being convected down the length of the channel. As a result, a significant

amount of the binding of streptavidin occurs at the edge of the binding region, particularly at low flow rates or low streptavidin concentrations.

The chevron microchannel, a passive microfluidic mixer, should stir the solution and in theory should replenish the concentration of streptavidin near the binding surface. The purpose of this research is to determine if the stirring caused by the chevron microchannel 1) alters the binding profile and 2) increases the rate of binding of streptavidin to the surface.

This work does not represent the first attempt to use a passive microfluidic mixer to improve the performance of a microfluidic assay to detect a protein analyte. Vijayendran et al.[217] introduced a serpentine mixer to a conventional SPR assay in which protein from solution binds to a functionalized surface (for this system, IgG from solution bound to immobilized protein A). The results indicated that there was only a marginal improvement in the initial binding rate (~2× faster for the serpentine microchannel versus the straight microchannel) (Figure 85). The authors suggest that the "unstirred" region at the wall of the device where the velocity of the solution is zero prevents the mixing of the solution at the surface, thereby resulting in little to no difference in the rate of binding and total amount of antibody bound. However, only a limited range of flow rates was explored, and the detection method averaged the signal over the entire channel, thereby ignoring any localized concentrations of surface binding.

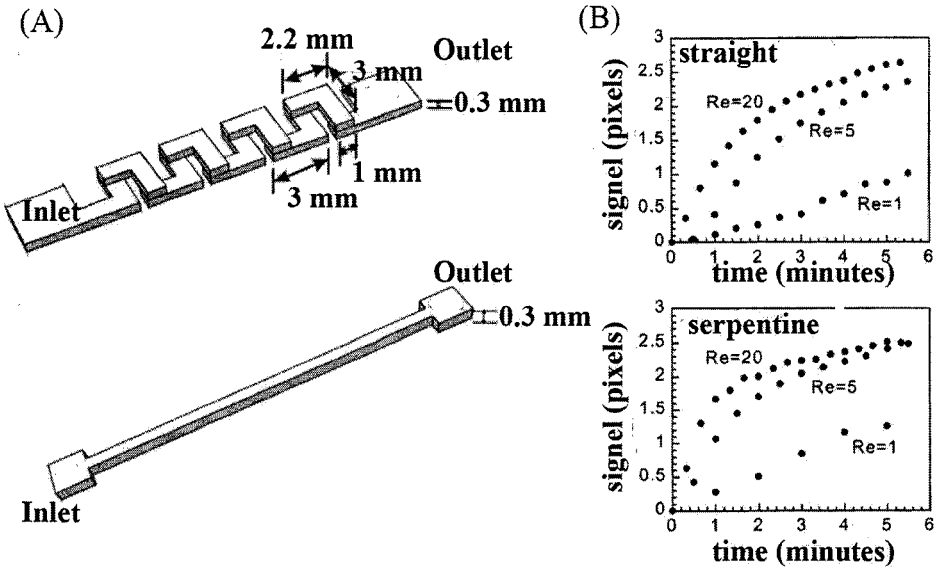

Figure 85. Influence of a serpentine mixer on flow immunoassay.[217] (A) Geometries for the serpentine mixer device and the rectangular device that served as the control. (B) SPR signal generated by the binding of a protein to the surface over time for the two channel geometries shown in (A). Images are modified from the cited reference.

Liu et al.[218] have explored the use of staggered herringbone mixers to improve the DNA hybridization in fluorescence microarrays. Their assays typically were conducted overnight under pseudo-equilibrium conditions. The solutions, containing attomolar concentrations of cDNA, were recirculated over a DNA microarray surface. To reduce mass transport limitations, a staggered herringbone mixer was incorporated in the bridge channel (Figure 86) that connected the hybridization chambers. The time required to achieve the same sensitivity as under static conditions was reduced by a factor of three. The authors reported up to an eight-fold increase in the signal at the same time point.

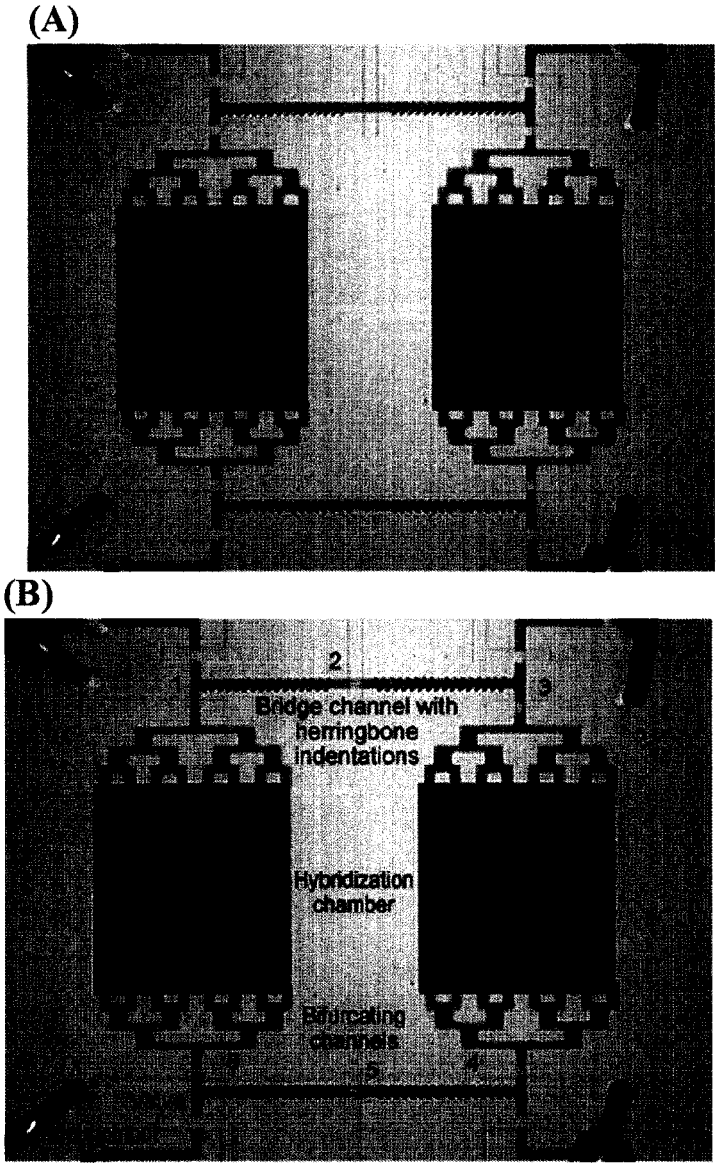

Figure 86. Incorporation of a staggered herringbone mixer in a fluorescence DNA microarray.[218] (A) and (B) Optical micrographs of the PDMS device. (A) Distribution of two solutions at time=0. The chambers were loaded half with the red and half with the blue solution. (B) Peristaltic pumps (1–3 and 4–6) circulated the solutions clockwise in the device. The bridge channel contained herringbone channels for mixing the solution between the hybridization chambers. The images are reproduced from the cited reference.

Yoon et al.[219] also incorporated a staggered herringbone mixer to improve a surface electrochemical reaction (conversion of ferrocyanide to ferricyanide) (Figure 87). The reaction occurred at the sidewalls of the device. The herringbone mixer (with ridges) increased the conversion of ferrocyanide to ferricyanide over the entire range of flow rates explored (Figure 87C).

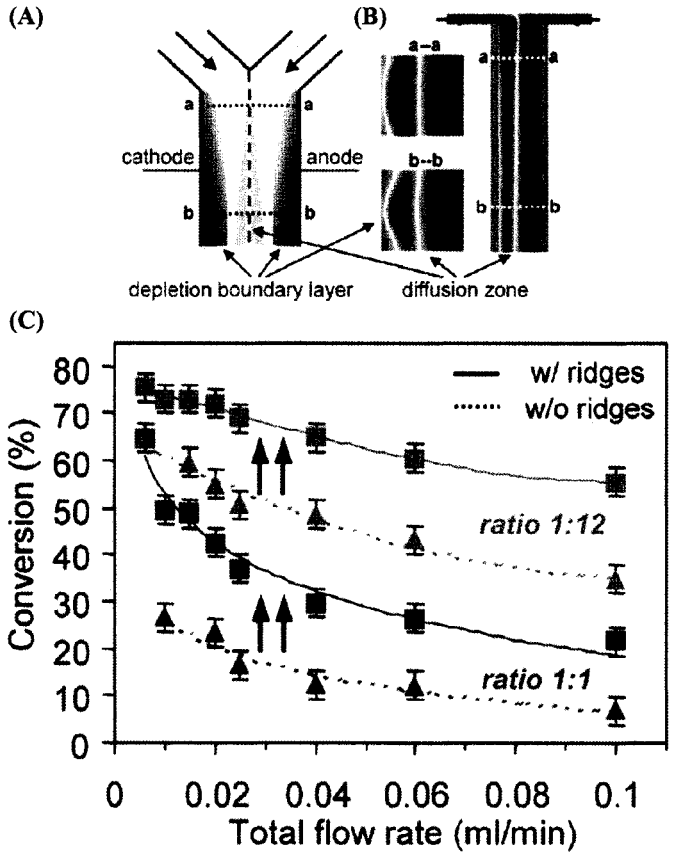

Figure 87. Redox reaction of ferrocyanide to ferricyanide in a microfluidic device under laminar flow and mass transport limited conditions.[219] (A) Schematic of the device – a T-sensor with electrodes embedded at the side walls. To one inlet, ferrocyanide was introduced (near the cathode side). To the other inlet, buffer was introduced. The second stream was focused the ferrocyanide solution toward the cathode. The relative flow rates of the fluid streams were altered. At the cathode, the ferrocyanide is converted to ferricyanide. (B) COMSOL results of the concentration of ferrocyanide. Dark red indicates the maximum concentration, and dark blue indicates the minimum concentration. (C) Conversion percentage of ferrocyanide to ferricyanide as a function of flow rate measured by UV-vis spectroscopy. Ridges or a staggered herringbone mixer was introduced to a T-sensor device. The noted ratios are the ratio of the velocity for the ferrocyanide stream and the buffer stream respectively. The images were reproduced from the cited reference.

Computational work by Roper[220] suggested that the introduction of microspheres or fibers with micron-sized diameters into a microchannel will produce eddies which will serve to improve the binding of a protein (cytochrome *c*) in a SPR sensor. However, this method has yet to be explored experimentally.

Other methods to improve the performance of a microfluidic assay for a biomolecule (DNA and protein) analyte using active mixing methods (mixing methods which rely on outside actuators rather than the geometry of the microchannel) have also been studied. They showed comparable increases (~2× to ~10×) in the binding of the analyte to the surface when they were compared to passive microfluidic mixers. Pulsed peristaltic pumping has been examined experimentally and computationally for the binding of a protein (insulin) to antibodies immobilized in a hydrogel.[221] The results suggested that there can be up to a 5× increase in the binding of insulin to the surface. A computational model indicated that electrothermal forces (induced by AC electrokinetics) could yield a 3× increase in the rate of the binding of an antigen or antibody to the surface in a heterogeneous immunoassay for Damkohler and Peclet numbers comparable to those examined in the research presented in this Chapter.[222] (Related experimental results have yet to be published.) Pulsed chaotic flow has been shown to increase signal intensities 3 to 4× higher than static conditions for a DNA microarray.[223] Computational models of the influence of pulsed flow on the binding of DNA to microarrays have also been completed by other research groups.[224-226] Experimental results have yet to be published. Magnetic beads have been incorporated in a microfluidic ELISA. The magnetic beads mixed the solution. Biomolecules were immobilized to the surface of the bead where the enzymatic reaction occurred.[227] The authors did not compare the performance of the assay when the solution was mixed versus when the solution was stagnant. However, the authors reported a 10× increase in sensitivity compared to other reported microfluidic ELISAs. The influence of a planetary centrifugal mixer on the binding of DNA to a microarray was described by Bynum et al. (Agilent Laboratories)[228]. At extremely high g forces (100*g* of acceleration) and an incubation time of 17 hours, the authors reported a 10× increase in the sensitivity and dynamic range of the assay. A 2× to 3× increase in sensitivity was reported for a DNA microarray in which mixing was accomplished by two air-driven bladders.[229]

Given the advantages of incorporating a passive versus an active microfluidic mixer in a point-of-care microfluidic assay, this work has focused on the incorporation of a passive

mixer – a chevron mixer – in a model microfluidic assay. In this work, SPR imaging assesses the influence of the mixer on the performance of the streptavidin-biotin assay[88, 101] as described in detail in Chapter 5. This method, unlike conventional SPR, can monitor localized increases in surface binding and give insight into the binding pattern of streptavidin at the surface. Furthermore, unlike the previous work by Liu et al.[218] and Yoon et al.,[219] this work assesses in real-time the binding of a protein to the entire surface underneath the chevron microchannel. In the work by Liu et al.,[218] the chevron microchannel was not incorporated above the hybridization chamber but in a microchannel bridging the two hybridization chambers. In the research presented by Yoon et al.,[219, 230] the redox reaction in which ferrocyanide was converted to ferricyanide occurred at an electrode located at the sidewall (cathode side) of the microchannel, and the concentration was measured off-chip using UV-vis spectroscopy. The concentration range (attomolar for Liu et al.[218] and 5 mM for Yoon et al.[219]), the flow rate (~5 nL/s for Liu et al.[218] and ~100 nL/s to ~1000 nL/s for Yoon et al.[219]) and surface reacting species (DNA for Liu et al.[218] and redox reaction of ferrocyanide for Yoon et al.[219]), and in turn surface reaction kinetics are different for this system (Q = [5, 25 and 50 nL/s] and [streptavidin] =20 nM and 40 nM). Furthermore, unlike the streptavidin-biotin reaction at the surface, the DNA hybridization reaction[218] occurred under pseudo-equilibrium conditions.

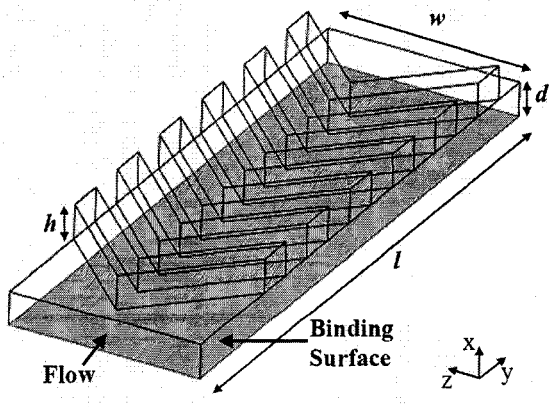

Figure 88. Chevron microchannel. For the modeled microchannel d=90 microns, h= 90 microns, w=500 microns, and l=1.5 mm. For the experimental device, d=82 microns, h= 56 microns, w=500. The biotin-functionalized gold surface to which streptavidin bound is indicated.

Most of the research and modeling of chevron mixers assessed the performance of mixing the solutions in the bulk and generally did not study the mixing of the solutions at or near the surface.[16, 216, 231-242] For this research, it is critical to understand what occurs at the surface of the device. To aid in this understanding, computational models of the streptavidin assay using a chevron mixer microchannel were completed. The models explored the velocity profile and the binding of streptavidin from solution to a surface, and they can relate the velocity profiles to the surface binding profile. Since the experimental methods only yield information about local refractive index changes near the surface over time, the models are extremely important for gaining an understanding of the transport of streptavidin in the bulk solution. Furthermore, the following models yield more quantitative information regarding the velocity profile within the chevron microchannel.

In sum, this research represents the first attempt (1) to model a surface binding reaction in a chevron microchannel, (2) to assess the influence of the chevron microchannel on the surface binding of a protein, and (3) to monitor in real-time the binding of a protein with an SPR-imaging system.

Due to computational constraints, only a 1.5 mm downstream distance (y-dimension) of the device (Figure 88) was modeled. Experimentally, a much larger area was interrogated (~7 mm). For reference, the work by Yoon et al.[219] (Figure 87) assessed the redox reaction over a distance of 25 mm.

8.3 Initial Design Considerations

An important experimental design concern was the exact geometry of the control microchannel. The control microchannel was a rectangular geometry that served as a control for evaluating the performance of the surface binding assay with a microfluidic mixer. The depth of microfluidic device had a significant impact on the efficiency of the binding of analytes from solution to the surface and was an important parameter to

control. However, the depth of the chevron mixer varied throughout the channel and consequently determining the appropriate depth of the control microchannel became non-trivial. One potential solution was to fabricate rectangular microchannels with the same average depth or fluidic diameter as the chevron mixer. However, given the complicated fabrication process of the mixer and the fact that it would be ideal to run the control and the experiment on the same device, the control straight microchannel has a depth (*d* in Figure 55) equal to the base microchannel (*d* in Figure 88) of the chevron microchannel.

Choosing the appropriate flow conditions was another important design parameter when comparing the mixer geometry to the straight microchannel. Either the flow rate or the average velocity could be constant. Since this overall grant funded by the NIDCR was to develop a rapid point-of-care salivary diagnostics in which total sample volume is also of importance, the flow rate were kept constant in these experiments, ensuring that the assays were completed in the same period of time and used the same volume of sample.

The chevron microchannel had not been optimized for the greatest amount of transverse flow. This optimization problem was difficult given the large number of parameters to be explored (chevron frequency, chevron depth, distance between chevrons, width of the microchannel, relative depth of the chevron to the base microchannel, and flow rate) and was therefore beyond the scope of this dissertation. The dimensions of the chevron were chosen based on previous work by the Whitesides group as well as in consideration of the magnification of the SPR imaging instrument. A 500 micron wide (z-dimension) microchannel was fabricated as opposed to the 200 micron wide (z-dimension) microchannel used by the Whitesides group, as the SPR instrument had very low magnification. For the experimental system, there was a relatively small region (~500 microns) of the SPR image that was in focus as a function of the y-dimension due to the fact that the instrument has not fulfilled the Scheimpflug condition. Furthermore, as described in Appendix C, the image was foreshortened in the y-dimension by a factor of ~0.42. The SPR propagation length in the y-dimension for this instrument (~30 microns) also reduced the resolution in that dimension.[76] Given the instrument's limitations, it was

likely that features that appeared in the model data would not be captured in the experimental data.

8.4 Materials and Methods

Computational Simulation

Simulations were completed exactly described in Chapter 5. The type of geometry drawn was the only difference in the protocol. Please note that the exact geometry (Figure 88) of the modeled system and the experimental system were not the same (an SU8 mold broke over the course of the experiments). Therefore, the flow rates, Reynolds number, and Peclet numbers of the model (Table 11) and experimental system (Table 12) differed. The governing equations for the surface binding reaction are:

$$c_{SA} + \theta \underset{kdes}{\overset{kads}{\rightleftarrows}} c_s \qquad \text{Equation 11}$$

$$\frac{dc_s}{dt} = k_{ads} c_{SA}(\theta_0 - c_s) - k_{des} c_s \qquad \text{Equation 12}$$

where c_{SA} is the streptavidin concentration in the bulk of the microchannel, c_s is the surface concentration of bound streptavidin, θ_0 is the initial surface concentration of antibody binding sites, θ is the surface concentration of antibody binding sites, and k_{ads} and k_{des} are the adsorption and desorption kinetic parameters. When solving the Navier-Stokes mode, the mesh consisted of 10,323 elements and had 98,530 degrees of freedom. When solving the convection-diffusion and surface binding modes, the mesh consisted of 54,245 elements and had 446,448 degrees of freedom.

Table 10. Surface binding parameters for the modeled system.[101] The binding kinetics and surface coverage parameters were measured and calculated from the cited reference.

θ_0 (moles m^{-2}) Initial streptavidin binding sites on the surface calculated based on experimental findings for a similar experimental situation.	3.9867×10^{-8}
c_0 (nM) Initial concentration of streptavidin	20
ρ (kg m^{-3})	1000
μ (kg m^{-1} s^{-1})	1×10^{-3}
Base microchannel depth (m)	90×10^{-6}
Microchannel width (m)	500×10^{-6}
Chevron depth (m)	90×10^{-6}
Chevron width (m)	100×10^{-6}
Distance between chevrons (m)	100×10^{-6}
D_{SA}(m^2 s^{-1}) diffusion coeffient of streptavidin	7.4×10^{-11}
k_{ads} (m^3 $moles^{-1}$ s^{-1})	4000
k_{des} (s^{-1})	3×10^{-6}

Table 11. Velocities, Peclet numbers and Reynolds numbers for the modeled chevron microchannel as a function of flow rate.

Flow rate (nL/s)	Average velocity (m/s) *	Peclet number	Reynolds number
5	1.111×10^{-4}	135.1	0.01
25	5.556×10^{-4}	270.3	0.05
50	1.111×10^{-3}	1351.3	0.1
100	2.222×10^{-3}	2702.7	0.2
200	4.444×10^{-3}	5405.4	0.4
250	5.556×10^{-3}	6756.8	0.5
500	1.111×10^{-2}	13513.5	1

* Calculated for channel depth without chevrons

Table 12. Velocities, Reynolds numbers, and Peclet numbers for the experimental chevron microchannel.

	Average velocity (m/s)	Maximum velocity (m/s)	Reynolds number	Peclet number
50 nL/s	1.22E-03	1.83E-03	1.10E-01	1.48E+03
100 nL/s	2.44E-03	3.66E-03	2.20E-01	2.96E+03

* Calculated for channel depth without chevrons

Experimental methods

Chemicals and reagents

Streptavidin (US Biologics, MA, USA) was diluted in phosphate-buffered saline (PBS, pH 7.4) (Sigma, St. Louis, MO). Deionized water (Barnstead International, Dubuque,

Iowa) was used throughout the work. Biotinylated alkyl thiol (BAT) (Iris BioTECH GmbH, Germany – custom synthesis) and ethylene glycol (Prochimia, Sopot, Poland) were diluted in absolute ethanol.

Microfluidic device fabrication

Molds for PDMS microfluidic channels were fabricated using established soft photolithography methods.[64, 175] The chevron microchannel required two layers of SU8. The two layers of SU8 must be precisely aligned to ensure that device geometry is accurate. A protocol for two-layer SU8 fabrication was adopted from Dr. Elena Garcia. The design of a photolithography mask was completed using AutoCAD 98 (Microsoft, Redmond, WA) and Adobe Illustrator 10 (Adobe Systems Inc., San Jose, CA). The first mask generated the rectangular base of the microchannel. The second mask outlined the chevrons that sit on top of the rectangular duct. When designing the mask, special attention was paid to the placement and geometry of the alignment marks. After several iterations, it was determined that the optimal alignment marks were crosses located on either side of the microchannel along the same axis. Upon exposure to UV light, the first mask generated a small cross. After spinning the second layer of SU8 onto the wafer, the small cross could be visualized. The second mask had a large cross in which the smaller cross on the wafer was centered.

To create the photolithography mask, black and white transparencies were printed (Publication Services, University of Washington, Seattle, WA). At the Washington Technology Center (WTC), the first layer of SU8 (MicroChem, Newton, MA) was spun (Solitec Spinner, Milpitas, CA) onto a clean, three-inch silicon test wafer (Silicon Sense, Nashua, NH). The wafer was pre-baked to densify the SU8 film. A four-inch infrared contact aligner (AB-M, San Jose, CA) exposed the wafer to ultraviolet light, thereby polymerizing the exposed regions of the SU8. Given the viscous and adhesive properties of the SU8, the WTC required that the wafer be placed onto the back of a clean, four-inch test wafer to ensure that SU8 did not contaminate the four-inch infrared contact aligner. After the first exposure, a second layer of SU8 was spun onto the wafer. The wafer was

soft-baked. The wafer was post-baked and then incubated in a solution of SU8 developer (MicroChem, Newton, MA), which removed any unpolymerized SU8. The wafer was once again baked to harden the SU8. The depth of the SU8 features were measured with the P15 surface profilometer (Tencor, San Jose, CA) located in the WTC.

The PDMS microchannels were prepared by dispensing Sylgard 184 prepolymers (Dow Corning, Midland, MI) at a 10:1 ratio of polymer to curing agent onto the SU8 molds. To create inlets and outlets to the microchannel, silicone tubing (Cole Parmer, Vernon Hills, IL) was glued to the inlet and outlet with DuCo Cement (Devcon, Riviera Beach, FL) and allowed to dry. Then, Sylgard 184 prepolymers (Dow Corning, Midland, MI), at a 10:1 ratio of polymer to curing agent, were dispensed onto the SU8 mold to create the PDMS microchannel. Upon drying, the PDMS microchannel was removed with a razor blade. For the initial studies, the PDMS was placed onto the slide substrate. However, bubbles tended to form. In order to overcome this difficulty, the PDMS device was activated in oxygen plasma to create a more hydrophilic surface (oxygen pressure 30 psi for one minute at 600 Watts, Plasma Preen II 973, Plasmatic System, Inc., North Brunswick, NJ). The PDMS was masked such that only the microchannel itself was exposed to the oxygen plasma.

Gold-coated slide preparation

A 1 nm adhesion layer of chromium and a 45 nm of layer gold were electron beam (CHA 600, CHA Industries, Fremont, CA) deposited onto clean glass microscope slides (Fischer Scientific, Pittsburgh, PA) at the Washington Technology Center (WTC). The gold-coated (45 nM Au, 1 nM Cr for adhesion) glass substrates were cleaned under oxygen plasma (oxygen pressure 30 psi) for 1 minute (Plasma Preen II 973, Plasmatic System, Inc., North Brunswick, NJ) at 600 watts. Due to leaks at the PDMS/gold interface, gold was deposited on the gold coated slide only in regions where the microchannels were situated. Stainless steel masks (Precision Image Corporation, Bothell, WA) were placed onto clean gold slides in the electron beam evaporator during the gold deposition. The oxygen plasma-cleaned slide was patterned with thiols using the

"wicking method," a technique developed and optimized by Dr. Kjell Nelson and Neil Geisler. Briefly, a 10 mil sheet of mylar (Fralock, Canoga Park, CA, USA) was cut using a carbon dioxide laser (M25, Universal Laser System, Inc., Scottsdale, AZ) to serve as a wicking mask. In the mask, a 1 mm diameter hole was cut. The mask was placed onto the slide using an alignment jig. A 0.5 mM solution of BAT/PEG (10% BAT, 90% HS-PEG) was introduced to the hole cut in the mylar mask. Capillary forces wicked the solution underneath the mask. The thiol solution evaporated. A 0.5 mM solution of HS-PEG was pipetted onto the exposed regions of gold outside of the masked region and allowed to evaporate. The mylar mask was removed. The slide was thoroughly rinsed in ethanol for one minute to remove any excess thiols and then dried with nitrogen gas. The oxygen plasma-activated PDMS microchannel was then aligned and placed on top of the gold substrate.

SPR imaging experiments

SPR images were collected over time as a solution of streptavidin (US Biologics, Swampscott, MA) in PBS (Sigma, St. Louis, MO) was introduced to the microfluidic device (Microflow system, Micronics, Redmond, WA). In the initial images, buffer filled the microchannel. A six-port injection valve (#V451 Upchurch Scientific, Oak Harbor, WA) introduced the solution of streptavidin from the 2 mL sample loop to the microchannel. The 905 nm bandpass filter was tilted 22 degrees from normal as the SPR curve indicated that wavelength was the most sensitive to small changes in refractive index near the surface (data not shown). The integration time was on the order of 0.5 second. Images were collected at a frequency of every 15 or 30 seconds.

Data Analysis

All SPR data were collected and analyzed using Labview software (National Instruments Corp., Austin, TX) developed by Dr. Elain Fu. All changes in reflectivity were dark and TE corrected (See Appendix C for further information).

8.5 Results and Discussion

As noted previously, the chevron depth of the experimental system and the model system was different (h= 90 microns versus h=56 microns where h is detailed in Figure 88) due to the destruction of a wafer during the course of experiments. In this section, the original model results are presented (h= 90 microns). In Appendix G, the influence of altering the chevron depth was explored with the model. The model results indicated that general features of the velocity profile, as well as the surface binding and concentration profiles of streptavidin in the microchannel, will exist in a chevron with a narrower chevron depth. Furthermore, the chevrons on the SU8 mold used for the PDMS microchannel were not perfectly aligned with the base microchannel, yielding a device with chevrons that were off-center (Figure 89).

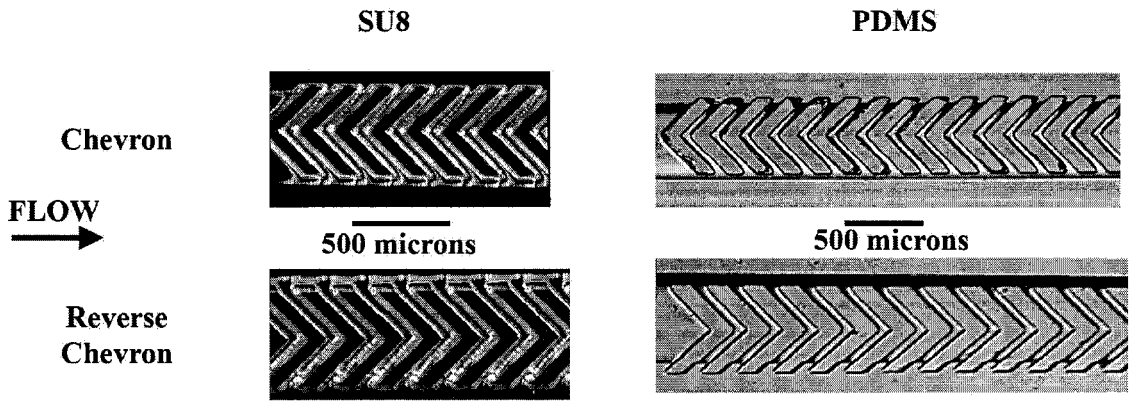

Figure 89. Stereoscopic micrographs of the SU8 mold and PDMS device for the chevron microchannel. The microfluidic channel was imaged in two locations – at the start of the forward chevron configuration and the start of the reverse chevron microchannel. Please note that the SU8 mold and the PDMS images were at different magnifications and hence have different scale bars. The direction of flow is indicated at the left.

As will be shown in the following section, in spite of the slight misalignment, the experimental results still closely resemble the model results for a perfectly aligned system. Therefore, the model system—although not exactly the same as the experimental system— provided valid information on the behavior of the velocity fields and bulk concentration of streptavidin in the chevron microchannel.

Also please note that in some figures, the chevron microchannel is referred to as the herringbone microchannel. This is a vestige of the reference to the off-sided chevron geometry as the staggered herringbone mixer by other groups.

Velocity profiles in the chevron microchannel

The model results for the velocity field for the chevron microchannel (Figure 90) indicated that the velocity of the fluid within the chevron was significantly lower than the velocity in the base microchannel. The velocity profile in the base microchannel (Figure 90A) closely resembled the parabolic velocity profile in the straight microchannel (Figure 56). Due to the increase and decrease in depth of the microchannel, the velocity slightly increased and decreased in the narrower and deeper regions (Figure 90B). A more extreme version of influence of the increase and decrease in the microchannel depth is explored in Appendix H.

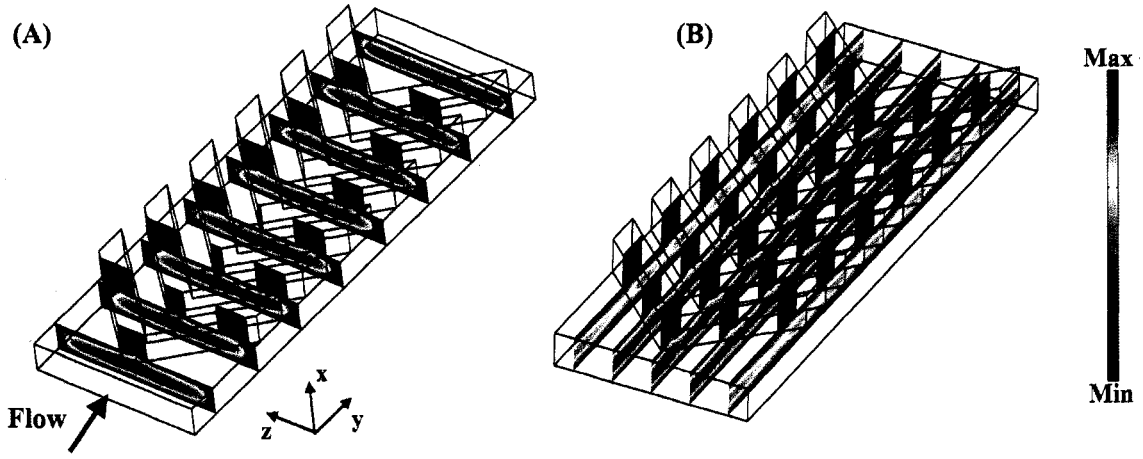

Figure 90. Velocity profile (m/s) for a chevron microchannel. Model results. The flow rate was 5 nL/s. Reynolds number = 0.01. Q=5 nL/s. The maximum velocity and minimum velocity in (A) and (B) were 1.77×10^{-4} m/s and 0 m/s.

Unlike the uni-directional parabolic velocity profile in a straight microchannel, the velocity profile in a chevron microchannel will have components in three dimensions (x-, y-, and z- dimensions instead of only the y-dimension). To best understand the contribution of each component to the velocity field, the velocity fields in the x-, y-, and z-dimensions were assessed and plotted within the microchannel. Particularly important

to the surface binding profile of streptavidin was the velocity profile very near to the binding surface as it was closest to the area of interest and convectively transported the streptavidin molecule to the binding region. Therefore, in the figures, the velocity profile 30 microns from the surface is illustrated (x=30 microns), since at x=0 microns the velocity due to the no-slip condition was zero. Please note that since the purpose of the cross-sections was to indicate that variation in the velocity in that particular slice of the microchannel, the range of velocities plotted within the figures are not identical.

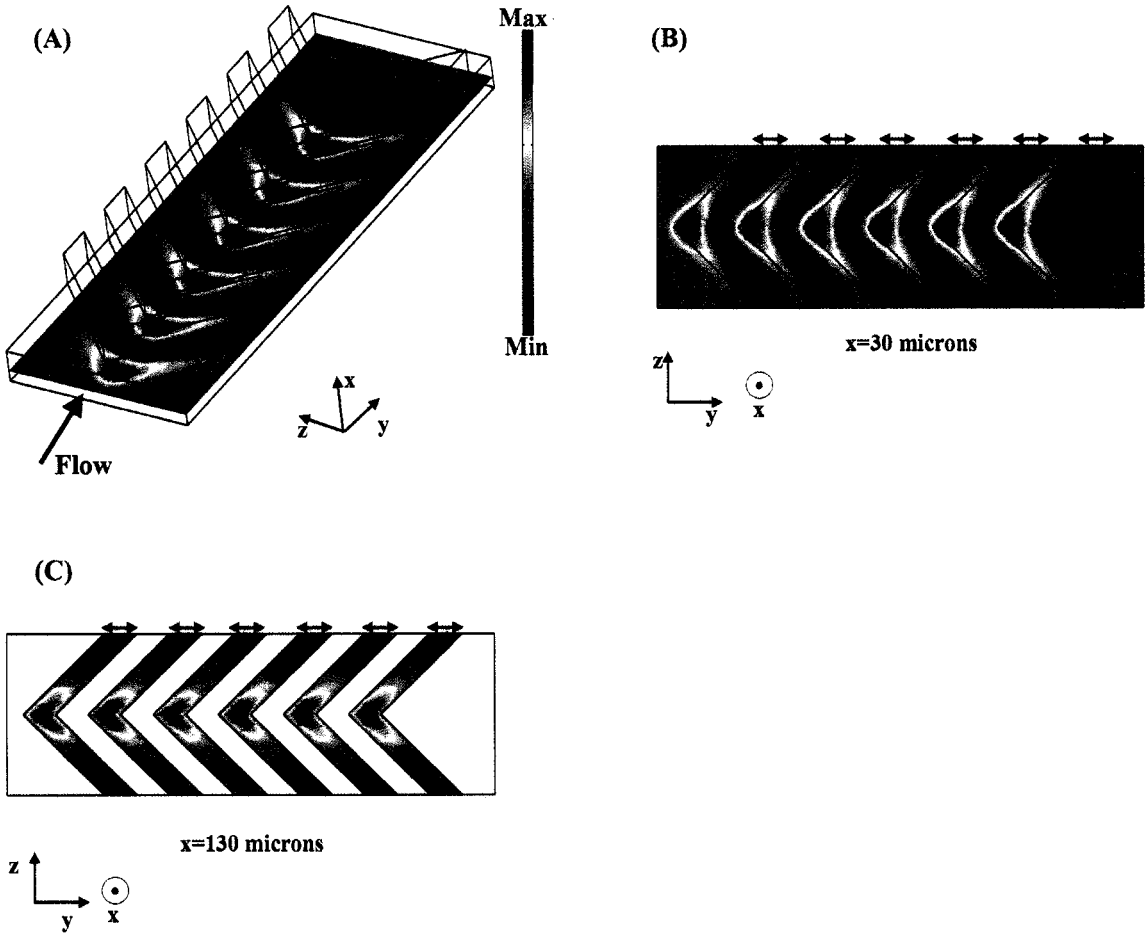

Figure 91. X-velocity profile (m/s) for a chevron microchannel. Model results. (A) 3d image of x-velocity profile at x=30 microns. (B) and (C) 2d images of x-velocity profile at x= 30 microns and x=130 microns respectively. The maximum velocity and minimum velocity in (A) and (B) were 1.32×10^{-5} m/s and -9.68×10^{-6} m/s. The maximum velocity and minimum velocity in (C) were 1.69×10^{-5} m/s and -1.54×10^{-5} m/s. The flow rate was 5 nL/s. Reynolds number = 0.01. Q=5 nL/s. The arrows indicate the deepest portion of the channel where the chevron structure was present.

In the chevron microchannel, the fluid must travel in the upward (x-dimension) to fill the chevron and then must be pushed downward toward the binding surface at the termination of a chevron. This gave rise to an up and down motion in the velocity field (x-velocity profile Figure 91). When the fluid first encountered the chevron at the midline of the channel (z=250 microns), it moved rapidly into the chevron (indicated by the red velocity) and away from the binding surface. At the terminus of the chevron, the fluid was pushed out of the chevron and toward the surface (indicated by the blue velocity). This occurred at the sidewalls of the microchannel. In the rest of the microchannel, the x-velocity was minimal (indicated by the turquoise velocity). The x-velocity behavior was similar near the surface (Figure 91B x=30 microns) and within the chevron (Figure 91C x=130 microns). The upward velocity (red) at the center of the microchannel and at the start of the chevron was higher than the velocity toward the binding surface (blue). At x=30 microns, the maximal upward velocity was ~37% greater than the maximal downward velocity (~1.3e-5 m/s versus ~-0.96 e-6 m/s). At x=130 microns, the maximal upward velocity was ~13% greater than the maximal downward velocity (~1.7e-5 m/s versus ~-1.5 e-5 m/s. The fluid first encountered the chevron microchannel at one location and the fluid must fill the microstructure (z=250 microns – the center point of the microchannel). However, it had two locations to be pushed out of the chevron (at the sidewalls of the device). Therefore, assuming the same volume of fluid entered and left the chevron, the downward velocity should be lower than the upward velocity.

The model results also indicated that the x-velocity was smaller in magnitude near the streptavidin binding surface of the device (x=30 microns) compared to within the chevron microstructure (x=130 microns). This was expected as it was the chevron microstructure that induced the x-velocity component; in turn the fluid in that region was most significantly influenced by the x-velocity.

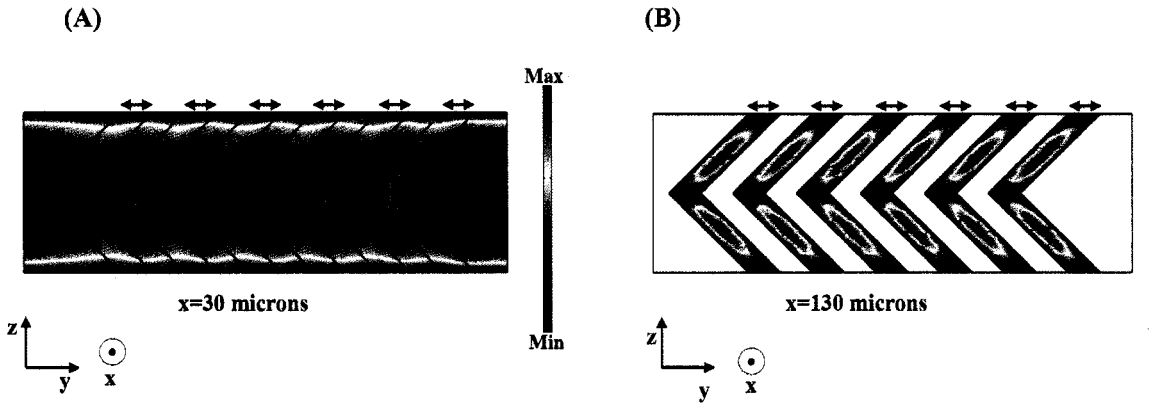

Figure 92. Y-velocity profile (m/s) for a chevron microchannel. Model results. (A)-(B) 2d slices of y-velocity profile at x= 30 microns and x= 130 microns respectively. The maximum velocity and minimum velocity were 1.60×10^{-4} m/s and -6.07×10^{-19} m/s at x=30 microns. The maximum velocity and minimum velocity were 3.02×10^{-5} m/s and -2.28×10^{-19} m/s at x= 130 microns. The flow rate was 5 nL/s. Reynolds number = 0.01. Q=5 nL/s. The arrows indicate the deepest portion of the channel where the chevron structure was present.

The y-velocity profile for the chevron (Figure 92), the velocity down the length of the microchannel, differed from the straight microchannel velocity (Figure 56) in which the y-velocity was the only velocity component. The occurrence of the chevrons served to widen and narrow the microchannel and therefore reduce the velocity in the areas with chevrons near the binding surface (Figure 92A x= 30 microns at locations demarked by the black arrows on the side of the microchannel). This behavior was repeated down the length of the channel. Within the chevrons (x=130 microns Figure 92B), the magnitude of the maximum y-velocity was ~5 times smaller than the velocity at x=30 microns (~1.6e-4 m/s versus ~3e-5 m/s) as expected from the general velocity field (Figure 90). In the chevron, the y-velocity was near zero at the midline of the channel (z=250 microns; x-velocity to the fill the chevron was more dominant – see Figure 91C). For similar reasons, the y-velocity at the sidewalls was near zero due to the no slip condition. In the other regions in the chevron, there was some forward (red velocity) motion with a maximum occurring in the center of the chevron and, due to the no-slip conditions, a velocity of zero at the chevron walls. The maximum magnitude of the y-velocity was significantly reduced within the chevron as compared to the base microchannel (1.6e-4 m/s at x=30 microns versus 3e-5 m/s at x=130 microns), which corroborated the findings

for the general velocity field (Figure 90) indicating that most of the convective transport occurred in the base portion of the microchannel.

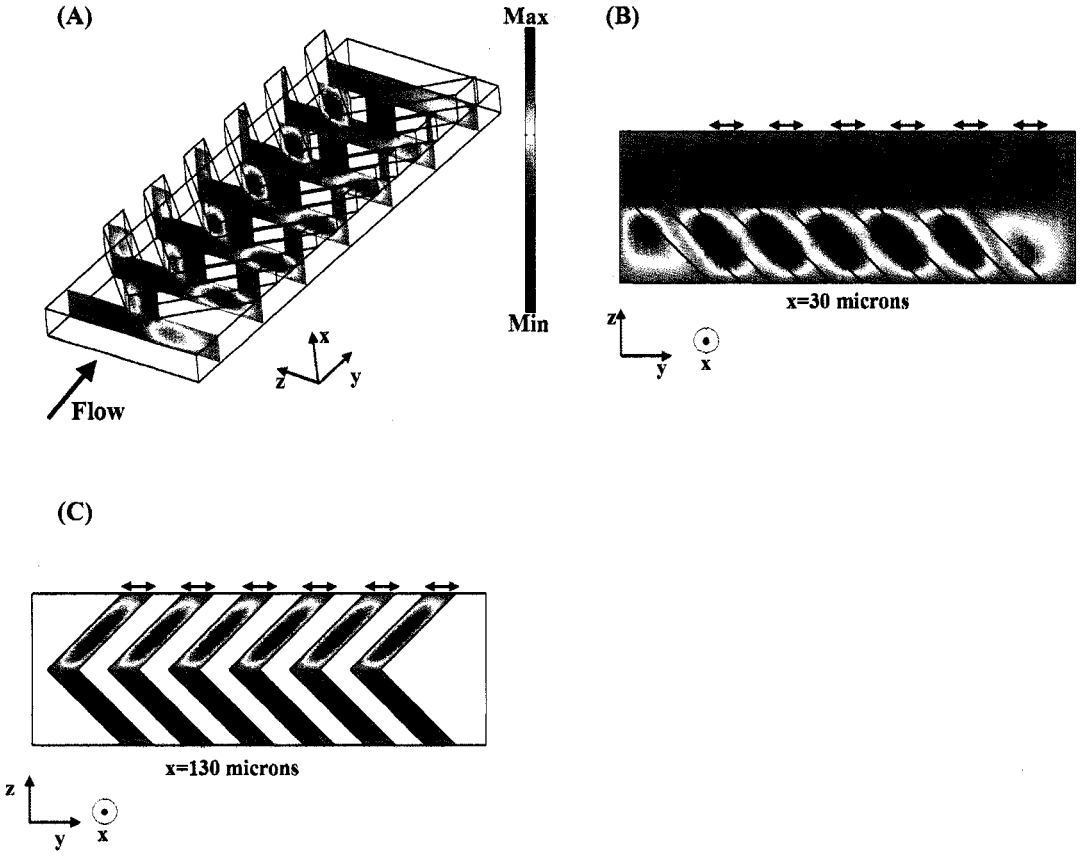

Figure 93. Z-velocity profile (m/s) for a chevron microchannel. Model results. (A) Slices of z-velocity profile in 3d. (B)-(C) 2d slices of the z-velocity profile at x=30 microns and x=130 microns. The maximum velocity and minimum velocity in (A) were 2.94×10^{-5} m/s and -2.91×10^{-5} m/s. The maximum velocity and minimum velocity in (B) were 2.01×10^{-5} m/s and -2.04×10^{-5} m/s. The maximum velocity and minimum velocity in (C) were 3.30×10^{-5} m/s and -3.14×10^{-5} m/s. The flow rate was 5 nL/s. Reynolds number = 0.01. Q=5 nL/s. The arrows indicate the deepest portion of the channel where the chevron structure was present.

The chevron microstructure induced a z-velocity component in the velocity field (Figure 93). The magnitude of the velocity profile is symmetric about the midline of the channel (z=250 microns). The z-velocity at the midline of the channel (z=250 microns) was zero for both depths (x=30 microns and x=130 microns). Within the chevron (x=130 microns Figure 93C), the fluid from the midline of the channel traveled along the chevron microstructure and was convected to the sidewalls. Near the surface (x= 30 microns Figure 93B), the transverse velocity was highest in the narrow regions of the channel

(where the chevron microstructure was not present). The velocity profile indicated that the fluid traveled from the sidewalls of the channel toward the center of the microchannel (i.e., in the opposite direction as in the chevrons).

A more subtle result was that there was transverse flow before the fluid encountered the chevrons. This arises as fluid was pulled upwards (x-dimension) into the point of the chevron microstructure. As a result, the fluid near the surface was pulled transversely across the surface and towards the midline of the microchannel (z=250 microns) where it filled the point of the chevron microstructure (Figure 93B).

Combining the results for Figure 91, Figure 92, and Figure 93 gives insight into the overall influence the chevron microchannel had on the velocity profile and serves to corroborate the qualitative description of the velocity field presented by Whitesides et al. (Figure 9).

Upon encountering a chevron, the fluid moved upward at the point of the chevron in the midline of the microchannel (z=250 microns) to fill the volume (x-velocity component – red). The fluid traveled across the chevron microstructure (z-velocity component and as the overall motion was forward, a y-velocity component as well) to the sidewalls of the microchannel. Upon reaching the sidewalls, the fluid was transported out of the chevron toward the surface (x-velocity component – blue). The fluid once out of the chevron (the narrower portion of the device as indicated by the black arrows in the figure) was swept towards the midline of the channel where it once again encountered a chevron. This cycle repeated itself as the fluid traveled down the length of the channel.

These results indicated that there was a circular nature to the convection within the chevron microstructure. On each half of the chevron microchannel a rotation of the fluid occurred. On the upper half of this image (z=250-500 microns), there was a counter-clockwise circulation as the fluid traveled upward to fill the chevron microstructure at the midline (z=250 microns) and across the top of the chevron towards the sidewalls and then

was pushed from the sidewalls toward the midline once the chevron microstructure was terminated. Similarly on the bottom half of this image (z=0-250 microns) a clockwise circulation of the fluid occurred. In other words, at the midline of the channel (z=250 microns), the chevron microstructure pulled the solution upwards toward to the top of the chevron, across the top of the chevron, down the sidewalls, and back across the binding surface.

How significant this rotation depended on the relative magnitude of the y-velocity component to the z-velocity component. The closer in magnitude these velocities are, the tighter the circulation. However, if the y-velocity was significantly larger than the z-velocity, the recirculation would have been more elliptical in nature so that in the overall velocity profile the fluid will travel down the length of the channel, undergoing a slight twisting motion induced by the x- and z-velocities as qualitatively illustrated by Whitesides et al. (Figure 9).

In Table 13, the maximum and minimum velocities are listed at two depths of the channel and indicate that near the surface the maximum y-velocity was nearly ten times larger than the z-velocity, suggesting that in that region the velocity profile was much more elliptical rather than circular in nature.

Table 13. Maximum and minimum velocities (m/s) in the chevron microstructure (x=130 microns) and near the surface (x=30 microns). Chevron microchannel. Model results.

	x=30 microns		x=130 microns	
(m/s)	maximum	minimum	maximum	minimum
x-velocity	1.3e-5	-9.6e-6	1.7e-5	-1.5e-5
y-velocity	1.6e-4	0	3e-5	0
z-velocity	2.0e-5	2.0 e-5	3.3e-5	-3.2e-5

In the chevron microstructure (x=130 microns), the magnitude of the maximum and minimum z-velocity was comparable to the maximum of the y-velocity (~3e-5 m/s), indicating that in that location, the transverse velocity was more significant. These results depend on the distance from the binding surface, but they yield a qualitative understanding of the relative behavior near the surface and within the chevron microstructure.

Quantification of the velocity components in the chevron microchannel.

To gain a more quantifiable understanding of the relative importance of each velocity component, the following calculations were completed using model results over a range of flow rates.

$$D_n = \frac{velocity_{\max or \min} herringbone}{velocity_{average} straight} * 100 \qquad \text{Equation 13}$$

$$F_{n-velocity} = \frac{(n - velocity)^2}{x - velocity^2 + y - velocity^2 + z - velocity^2} \qquad \text{Equation 14}$$

To normalize the maximum and minimum velocities in each dimension(x-, y- and z-dimensions), they were divided by the average velocity in a straight microchannel and multiplied by 100 yielding a value termed "*D*" (Equation 13 and Table 14). The values of *D* remained constant over a large range of flow rates which could be expected under laminar flow conditions. The data suggest that the maximum magnitude of the $D_{\text{x-velocity}}$ was significant – ~50% of the average velocity of a straight microchannel. As noted earlier in the discussion of the x-velocity profile, $D_{\text{x-velocity}}$ for the maximum and minimum were not equivalent (minimum $D_{\text{x-velocity}}$ – ~30%). The $D_{\text{y-velocity}}$ for the maximum velocity was 160%, which was higher than expected as the maximum velocity in a straight microchannel is 150% of the average velocity. Therefore, the maximum value in the chevron was consistently higher than this. Analysis of the y-velocity profiles indicated that the maximal velocity consistently occurred at the point of the very first chevron, very near the midline of the channel (z ~250 micron; x ~90 micron). This maximal value could potentially have arisen from the initialization of flow in directions besides the downstream direction (y-dimension). The negative value (-1 %) for the $D_{\text{y-velocity}}$ minimum was due to numerical errors, and the minimum value occurred in a small fraction of the microchannel, particularly near the walls and the outlet. The maximal and minimal $D_{\text{z-velocity}}$ ~30% indicated that the transverse flow could be significant in the device. Furthermore, the maximum and minimum values were equal in magnitude

(within the +/-1% numerical error of the model), further indicative of symmetric flow profiles in the z-dimension.

Table 14. D values. Normalized value of the maximum and minimum velocities in each dimension for the chevron microchannel. Model Results.

chevron	5 nL/s		25 nL/s		50 nL/s	
	Max	Min	Max	Min	Max	Min
$D_{x\text{-velocity}}$	46	-32	52	-35	48	-31
$D_{y\text{-velocity}}$	160	0	160	-1	160	0
$D_{z\text{-velocity}}$	31	-32	30	-31	31	-32
$D_{velocity\ field}$	160	0	161	0	160	0

chevron	250 nL/s		500 nL/s	
	Max	Min	Max	Min
$D_{x\text{-velocity}}$	49	-32	48	-32
$D_{y\text{-velocity}}$	160	-1	160	-1
$D_{z\text{-velocity}}$	33	-34	33	-34
$D_{velocity\ field}$	160	0	160	0

F (Equation 14 and Table 15) was the fraction of total kinetic energy contributed by the velocity in the x-, y-, or z-dimensions. The value of *D* gave an understanding of the relative influence of the maximum or minimum value of a velocity component. However, it did not give any insight into how significant to the overall velocity field that velocity component was, as the maximum or minimum velocities could have occurred in a large or small fraction of the microchannel volume. Calculating the fraction of overall kinetic energy each velocity component contributed will give a sense of the relative significance over the entire channel volume of each velocity component.

The results (Table 15) indicated that the most significant velocity component was in the y-dimension, with 98% of the kinetic energy being directed in that dimension (please note that values were rounded to two significant digits). The x-dimension's energy contribution was less than 1%. The value of $F_{z\text{-dimension}}$ indicates that ~1.3% of the entire kinetic energy went into the velocity in the z-dimension. These results corroborated the qualitative results presented in the image of the velocity profile (Figure 90), in which the majority of the velocity field occurred in the downstream (y-dimension) and showed marked similarity to the velocity profile for a straight microchannel (Figure 56). As mentioned in the Initial Design Considerations for this chapter, the modeled and

experimental chevron geometries have not been optimized to achieve maximal transverse flow nor have they been optimized for a surface binding reaction. Instead the design was based on similar chevron geometries presented by Whitesides et al. Therefore, it was not surprising that the significance of the z-velocity was not extremely high.

Table 15. F values. Fraction of energy due to the velocity in each dimension. Model results. Chevron microchannel.

chevron	5 nL/s	25 nL/s	50 nL/s	100 nL/s	250 nL/s	500 nL/s
$F_{x\text{-dimension}}$	8.3E-03	8.5E-03	8.2E-03	8.6E-03	8.6E-03	8.7E-03
$F_{y\text{-dimension}}$	9.8E-01	9.8E-01	9.8 E-01	9.8E-01	9.8E-01	9.8E-01
$F_{z\text{-dimension}}$	1.3E-02	1.3E-02	1.3E-02	1.4E-02	1.4E-02	1.4E-02

Surface binding profile of streptavidin over time in the chevron microchannel

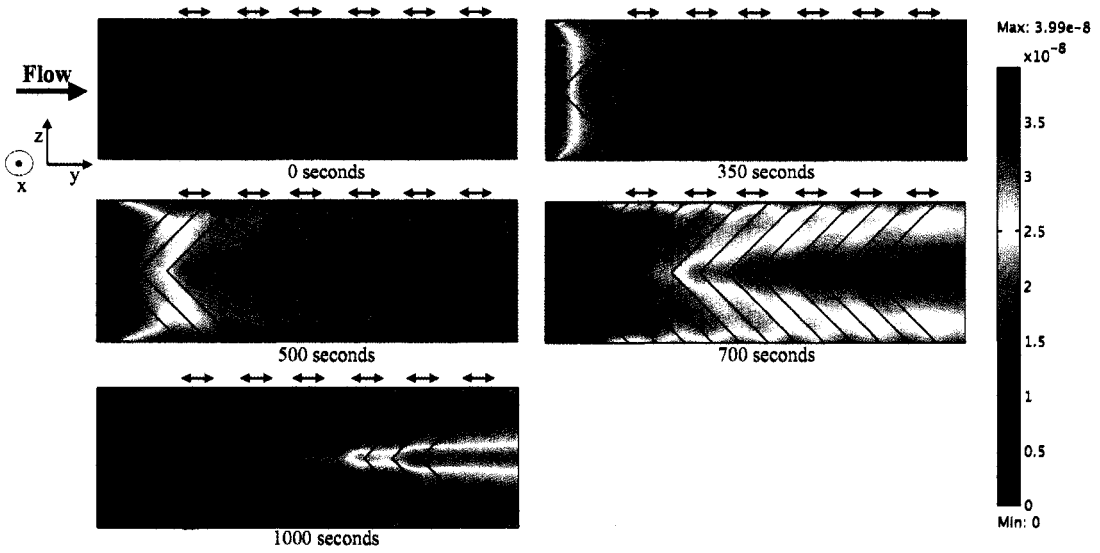

Figure 94. Surface concentration profile of bound streptavidin (moles/m^2) in the chevron microchannel. Model results. Streptavidin inlet concentration = 20 nM = 2×10^{-5} moles/m^3. Time = 350 seconds. Re= 0.01. Pe=135.1. Q=5 nL/s. The arrows indicate the deepest portion of the channel where the chevron structure was present. The theoretical maximum SA surface binding concentration was 3.99 $\times10^{-8}$ moles/m^2.

The model results for the surface binding profile of streptavidin for the chevron microchannel (Figure 94) indicate that like the straight microchannel (Figure 58), there was a surface gradient of bound streptavidin from right to left, reflecting that the streptavidin was introduced at the inlet (left to right). However, the chevron geometry introduces two unique features to the surface binding profile: (1) there was a dramatic reduction in the amount of streptavidin binding in the middle of the microchannel (z=250

microns) and (2) there was a slight decrease in the amount of binding in the chevron regions of the microchannel where the channel was deeper (demarked by the black arrows along the length of the microchannel).

Experimental results (Figure 95) showed strong similarity to the model results (Figure 94). There was a steep reduction in the amount of bound streptavidin in the midline of the microchannel. There was a subtle increase and decrease in the binding down the length of the microchannel (y-dimension). However, as mentioned in the Initial Design Consideration for this chapter, this was the dimension that was foreshortened and the dimension of the SPR propagation length. Furthermore, further downstream (y-dimension) the image became out of focus. When the microchannel was rotated 90 degrees and placed in the line of focus, the midline feature was not visible due to the foreshortening and the SPR propagation length. The irregular features at the front of the binding area were particularly noticeable at time = 10 minutes. These features were a result of irregular patterning of thiols at the front of the binding surface. Due to the misalignment of the chevrons on the base microchannel, they were visible at the bottom (z-dimension) of the image.

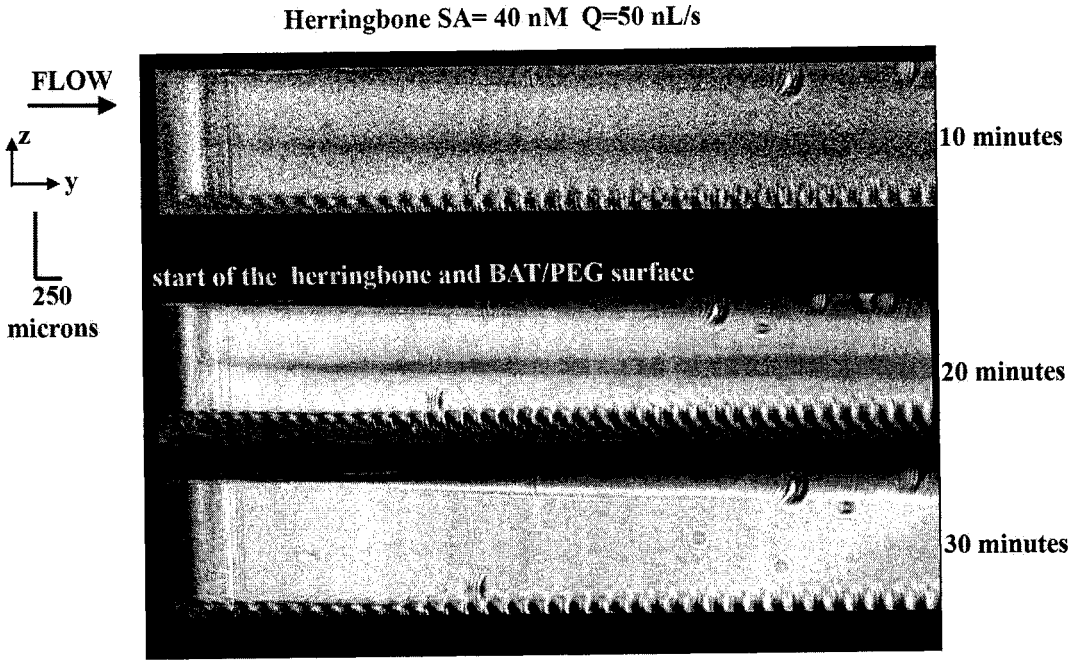

Figure 95. Surface concentration profile of bound streptavidin over time in a chevron microchannel. Experimental results. SPRM difference images subtracted from the initial image. Each image had been contrast enhanced for viewing purposes to demonstrate the variation of surface concentration of streptavidin within each image. Streptavidin inlet concentration = 40 nM. Re= 0.11. Pe=1480. Q=50 nL/s.

In some experiments, the reduction in the streptavidin binding profile was not found at the midline of the channel (Figure 96). The experiments were completed at the same flow rate using the same PDMS microchannel. The misalignment of the chevrons and/or the elastomer properties of the PDMS may be the source of the alteration in the binding pattern. In the model, the chevron structure was immobile – unlike a PDMS elastomer, which for this chevron device was on the order of 100 microns in width. For example, the chevron structures may deteriorate over time, or under flow the chevron structure may be deformed, thereby altering the location of the point of the chevron. Evidence suggesting that the elastomeric properties of the PDMS may be the cause of this behavior is that during the introduction of fluid to the device, the fluid had trouble entering the chevrons (data not shown). Flow-induced deformation of PDMS has been reported in the literature.[243]

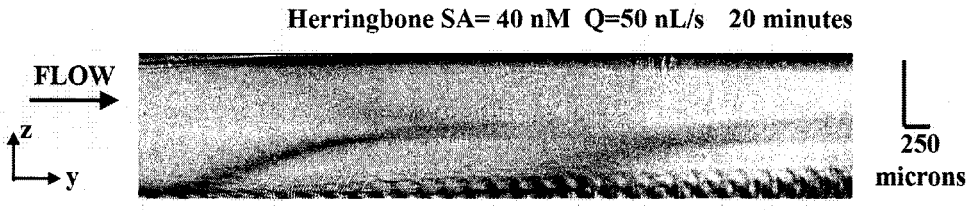

Figure 96. Surface concentration profile of bound streptavidin in a chevron microchannel when the reduction in binding was not centered. Experimental results. SPRM difference image subtracted from initial image. The image has been contrast enhanced for viewing purposes to demonstrate the variation of surface concentration of streptavidin within each image. Streptavidin inlet concentration = 40 nM. Re= 0.11. Pe=1480. Q=50 nL/s.

Relation between the velocity profiles and the SA surface binding profile in the chevron microchannel

To better understand the relationship between the fluid mechanics in the chevron microchannel and the surface binding profile of streptavidin, line profiles of the velocity components (x-, y-, and z-) near the binding surface (x=30 microns) were compared to line profiles of surface-bound streptavidin (Figure 97, Figure 98, and Figure 99). When analyzing these data, it is important to remember the relative magnitude of each velocity component (Table 13).

The x-velocity profile (Figure 97 B-D blue data) – representing the velocity toward (Figure 97A blue) and away from the surface (Figure 97A red) – correlated with the surface binding profile (Figure 97 B-D pink data). In the downstream line profiles, L1 and L2, when the x-velocity was directed towards the binding surface (negative velocity profile in the graphs) there was a slight increase in the amount of surface binding in those regions. For the line profile transverse to flow, L3, the downward velocity (blue) near the sidewalls of the channel correlated with an increase in the total amount of streptavidin bound to the surface in the region. In the regions where the solution was directed away from the surface (x-velocity greater than zero), there was a reduction in the amount of bound streptavidin.

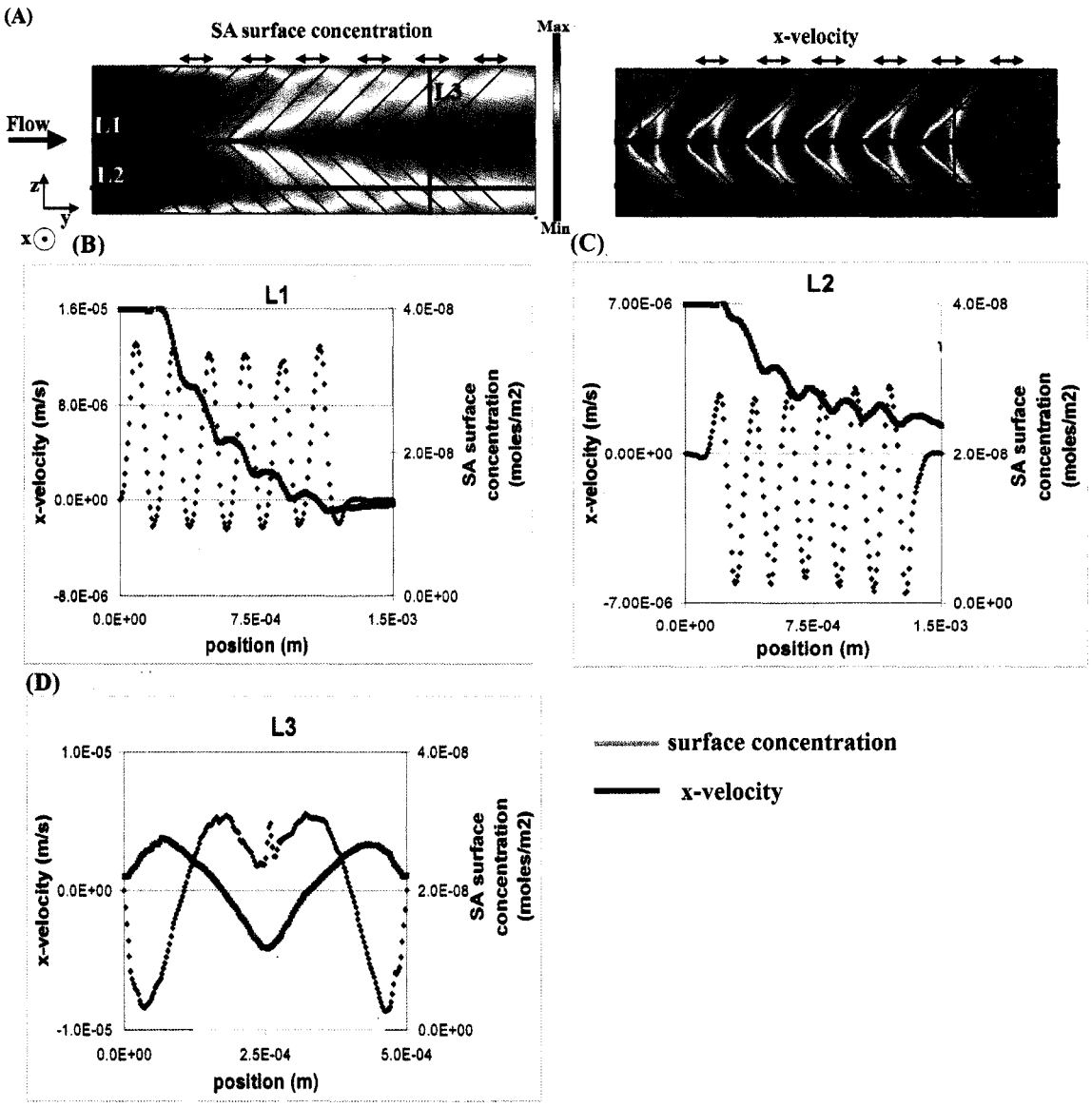

Figure 97. Comparison of the x-velocity profile and the binding profile in the chevron microchannel. Model results. (A) Surface concentration profile of bound streptavidin (moles/m^2). The maximum SA surface binding concentration was 3.99 $\times 10^{-8}$ moles/m^2. The minimum SA surface binding concentration was 0 moles/m^2. Velocity profile (m/s) in the x-dimension at x=30 microns. The maximum velocity and minimum velocity were 1.32 $\times 10^{-5}$ m/s and -9.68 $\times 10^{-6}$ m/s. (B)-(D) Line profiles comparing the SA surface concentration profile and the velocity in the x-dimension. The location of the line profiles are indicated in (A) and are labeled respectively in (B)-(D). The specific coordinates of the lines are L1 (z=250 microns; y[0 to 1.5mm]), L2(z=90 microns; y[0 to 1.5 mm]) and L3 (y=1.15 mm; z[0 to 500 microns]). Streptavidin inlet concentration = 20 nM = 2×10^{-5} moles/m^3. Time = 700 seconds. Re= 0.01. Pe=135.1. Q=5 nL/s. The arrows indicate the deepest portion of the channel where the chevron structure was present. The theoretical maximum SA surface binding concentration was 3.99 $\times 10^{-8}$ moles/m^2.

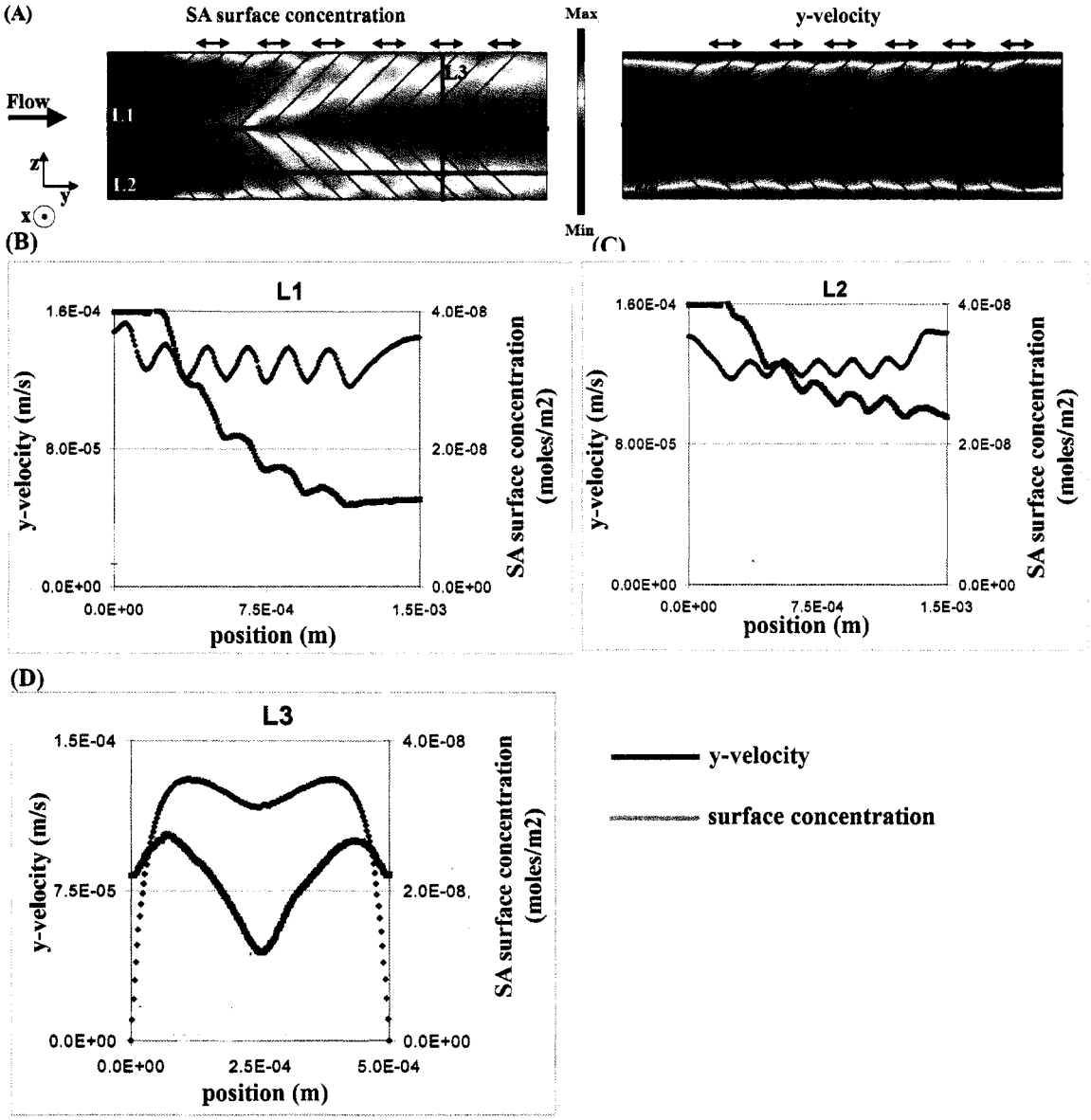

Figure 98. Comparison of the y-velocity profile and the binding profile in the chevron microchannel. Model results. (A) Surface concentration profile of bound streptavidin (moles/m^2). The maximum SA surface binding concentration was 3.99 $\times 10^{-8}$ moles/m^2. The minimum SA surface binding concentration was 0 moles/m^2. Velocity profile (m/s) in the y-dimension at x=30 microns. The maximum velocity and minimum velocity were 1.60 $\times 10^{-4}$ m/s and 6.10 $\times 10^{-19}$ m/s. (B)-(D) Line profiles comparing the SA surface concentration profile and the velocity in the y-dimension. The location of the line profiles are indicated in (A) and are labeled respectively in (B)-(D). The specific coordinates of the lines are L1 (z=250 microns; y[0 to 1.5mm]), L2(z=90 microns; y[0 to 1.5 mm]) and L3 (y=1.15 mm; z[0 to 500 microns]). Streptavidin inlet concentration = 20 nM = 2×10^{-5} moles/m^3. Time = 700 seconds. Re= 0.01. Pe=135.1. Q=5 nL/s. The arrows indicate the deepest portion of the channel where the chevron structure was present. The theoretical maximum SA surface binding concentration was 3.99 $\times 10^{-8}$ moles/m^2.

The y-velocity profile represents the velocity down the length of the channel (Figure 98) and strongly correlates, with the surface binding profile (Figure 98 B-D pink data). At the higher y-velocities, more streptavidin bound to the surface as convection dominated more strongly over diffusion in those regions. As previously mentioned, the y-velocity was higher in the narrow regions of the channel (where the chevrons were not located) and the binding of streptavidin to surface was increased. The repetitive nature of the chevron microchannel gave rise to a repetitive binding pattern.

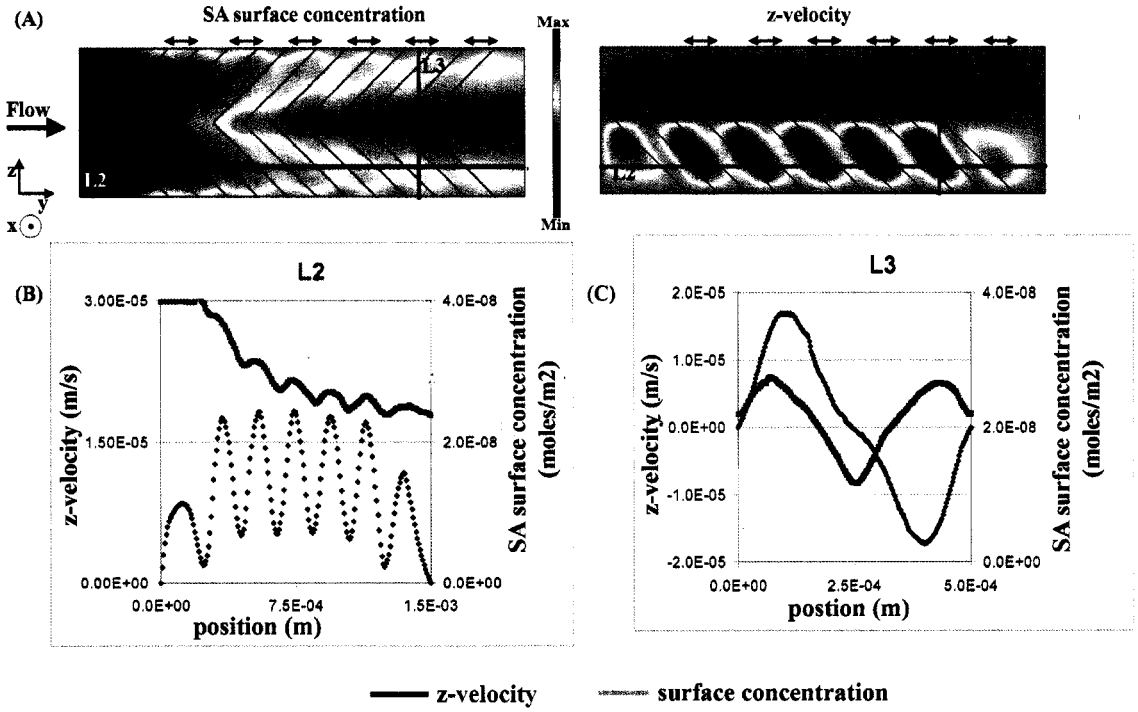

Figure 99. Comparison of the z-velocity profile and the binding profile in the chevron microchannel. Model results. (A) Surface concentration profile of bound streptavidin (moles/m^2). The maximum SA surface binding concentration was 3.99 $\times 10^{-8}$ moles/m^2. The minimum SA surface binding concentration was 0 moles/m^2. Velocity profile (m/s) in the z-dimension at x=30 microns. The maximum velocity and minimum velocity were 2.02 $\times 10^{-5}$ m/s and -2.04$\times 10^{-5}$ m/s. (B)-(C) Line profiles comparing the SA surface concentration profile and the velocity in the z-dimension. The location of the line profiles are indicated in (A) and are labeled respectively in (B) and (C). The specific coordinates of the lines are L2(z=90 microns; y[0 to 1.5 mm]) and L3 (y=1.15 mm; z[0 to 500 microns]). Streptavidin inlet concentration = 20 nM = 2×10^{-5} moles/m^3. Time = 700 seconds. Re= 0.01. Pe=135.1. Q=5 nL/s. The arrows indicate the deepest portion of the channel where the chevron structure was present. The theoretical maximum SA surface binding concentration was 3.99 $\times 10^{-8}$ moles/m^2.

The z-velocity profile represents the velocity transverse to flow (Figure 99 B-C blue), and it also correlated with the surface binding profile of streptavidin (Figure 99 B-C pink). Whether the z-velocity was positive or negative (toward one sidewall of the channel or

the other), there was an increase in the binding of streptavidin to the surface in those locations and a minimum in surface binding when the velocity is zero (Figure 99C). The maximum z-velocity in Figure 99C did not correlate with the maximum concentration of streptavidin at the surface. This may have been the result of the depletion in the concentration of streptavidin as it traveled across the surface and towards the midline of the microchannel.

The experimentally measured SPR difference line profiles indicating the surface binding of streptavidin (Figure 100) strongly resembled the model results of the line profile of the surface-bound streptavidin (Figure 97, Figure 98, and Figure 99). Given the SPR propagation length, foreshortening, and lack of focus downstream, it was not expected that the increase and decrease in the binding of streptavidin would be resolved experimentally given the noise of the measurement (Figure 100C L2). These features were slightly observable in the SPR difference image at time=20 minutes (Figure 95), but when the line profiles were collected the noise within the image overwhelmed the pattern. The midline downstream profile, Figure 100B L1, showed a gradient in the binding profile over time (time=20 minutes) and eventually became saturated (time=30 minutes). The downstream line profile closer to the sidewalls (Figure 100C L2), unlike the midchannel line profile (z=250 microns), did not exhibit a spatial gradient in binding at any time point, which showed some correlation with the model results. The line profile transverse to flow (Figure 100D L3), like the model results, also showed a strong reduction in binding at the center. The experimental, like the model, line profile also showed there was a slight reduction in the binding at the sidewalls. Due to the misalignment of the chevrons on the base microchannel, the large reduction in the streptavidin was not located at the centerline (z=250 microns) but instead occurred where the point of the chevron was located.

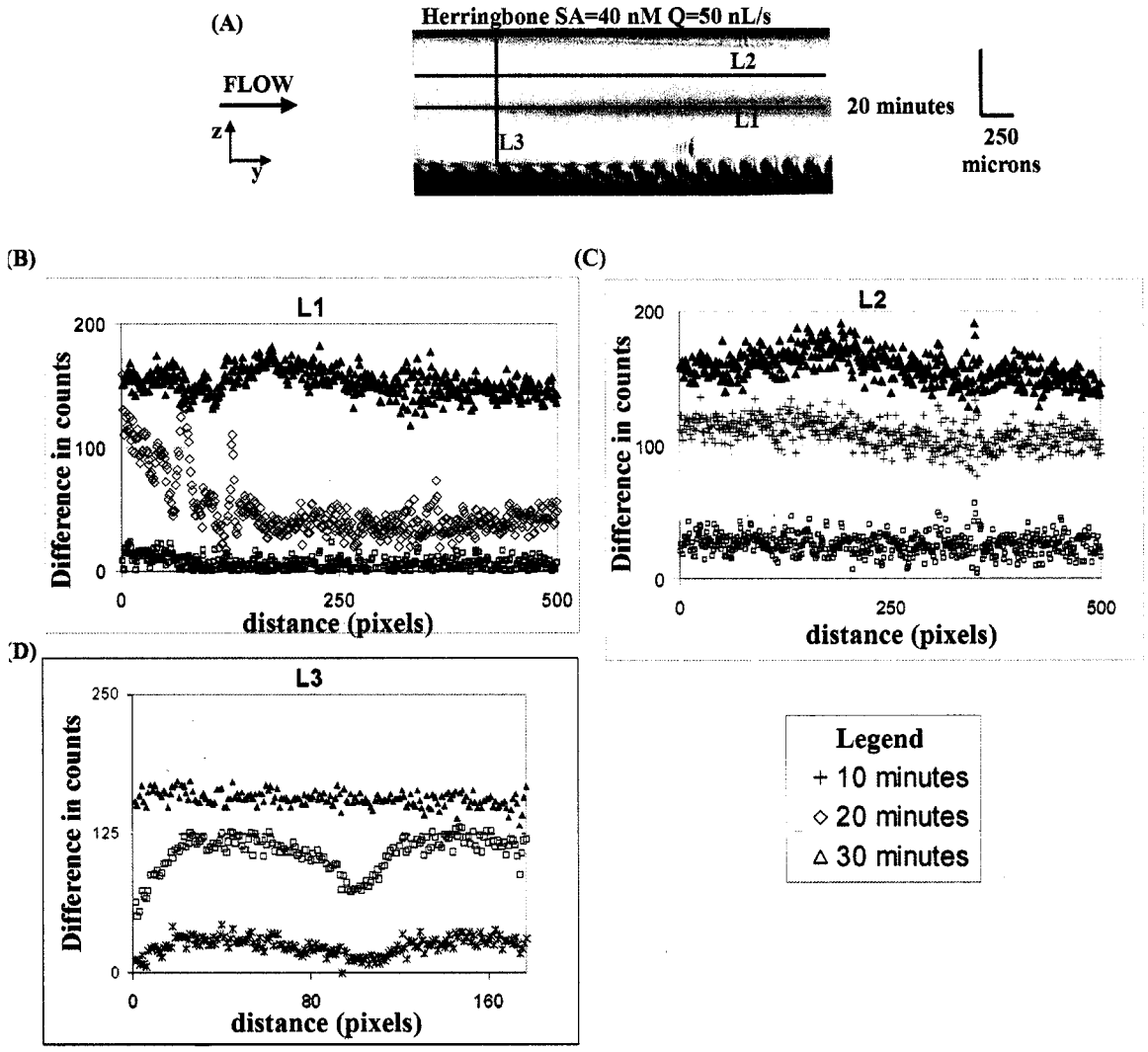

Figure 100. SPRM difference line profiles of the SA surface concentration profile of bound streptavidin. Experimental results. (A) SPRM difference image subtracted from initial image. The image has been contrast enhanced for viewing purposes to demonstrate the variation of surface concentration of streptavidin. (B)-(D) Line profiles of surface concentration of streptavidin over time. The location of the line profiles are indicated in (A). The line profiles were calculated from raw TM images. The line profile at time = 0 was subtracted from each line profile at the indicated time point. The line profiles L1 and L2 are 5 pixels (~17 microns) in width and L3 was 10 pixels (~70 microns) in width. The difference in pixel to distance ratio on the substrate in each dimension was due to image foreshortening in the y-dimension discussed in Appendix C. Streptavidin inlet concentration = 40 nM. Re= 0.11. Pe=1480. Q=50 nL/s.

Bulk concentration profiles of streptavidin in the chevron microchannel.

Unlike SPR-imaging experiments, the model yielded information about the concentration profile of streptavidin within the chevron microchannel (Figure 101). The results indicate that like the straight microchannel (Figure 57), a depletion zone occurred near the binding

surface. However, down the midline of the chevron microchannel (z=250 microns), the depletion zone was much deeper. Furthermore, the concentration of streptavidin at the top of the microchannel was reduced, and near the end of the model geometry, the highest concentration of streptavidin occurred in two cores located in each half of the microchannel, near the middle of the microchannel (x-dimension).

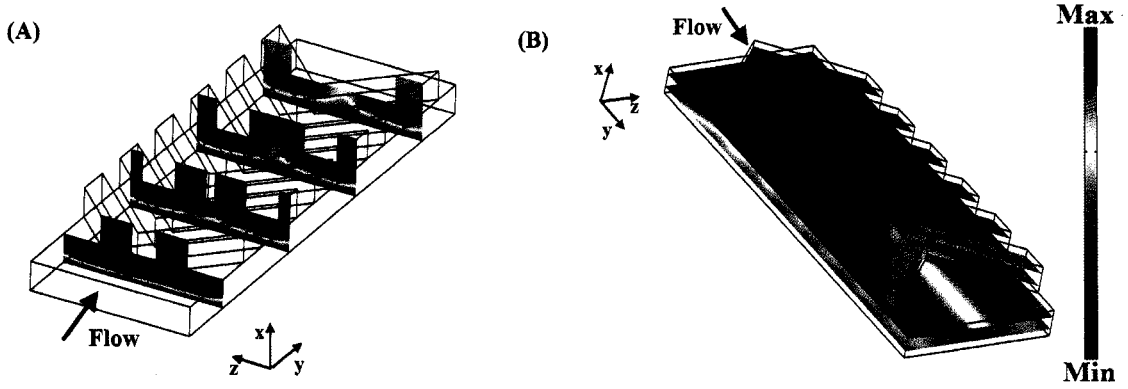

Figure 101. Concentration profile of streptavidin in the chevron microchannel (moles/m^3). Model results. The maximum concentration and minimum concentration were 2.01 $\times 10^{-5}$ moles/m^3 and 0 moles/m^3. Streptavidin inlet concentration = 20 nM = 2×10^{-5} moles/m^3. Time = 350 seconds. Re= 0.01. Pe=135.1. Q=5 nL/s.

As noted earlier, the chevron microchannel introduced two slowly spiraling flows (clockwise and counterclockwise) on each half of the microchannel. The model results of the concentration profiles within the chevron microchannel suggested that the transverse flow (z-dimension) swept the solution near the surface towards the midline of the channel. As the solution swept across binding surface, streptavidin bound to the surface. The solution near the surface, once it reached the center of the channel (z=250 microns), was depleted of streptavidin. Next, the solution swept upward to the top of the chevron, thereby introducing to the top of the chevron microchannel a solution depleted of streptavidin. The solution was then swept across the chevron and once again brought to the sidewalls of the microchannel. This cycle continued down the length of the chevron microchannel and gave rise to two cores of solution in the middle with the highest concentration of streptavidin.

An important parameter to consider is the relative magnitude of the transverse velocity (z-velocity) to the downstream velocity (y-velocity). As described in previous sections, for this chevron microchannel, most of the kinetic energy (98% Table 15) was involved in the downstream velocity. Therefore, even when the solution experienced some transverse flow significant enough to affect the binding profile as experimental and model results indicated, the solution was swept downstream at a much greater velocity. Given this consideration, when the solution was swept across the surface transverse to the flow (z-dimension) and then upward at the midline (z-dimension) of the microchannel, it was pushed rapidly downstream (y-dimension) at the center of the microchannel. Thereby this created a "depletion column," which was rapidly pushed through the chevron microchannel. This depletion column was much more significant at the midline of the chevron microchannel (z=250 microns) than the depth of the depletion zone for the straight microchannel at the midline of the microchannel (z=250 microns).

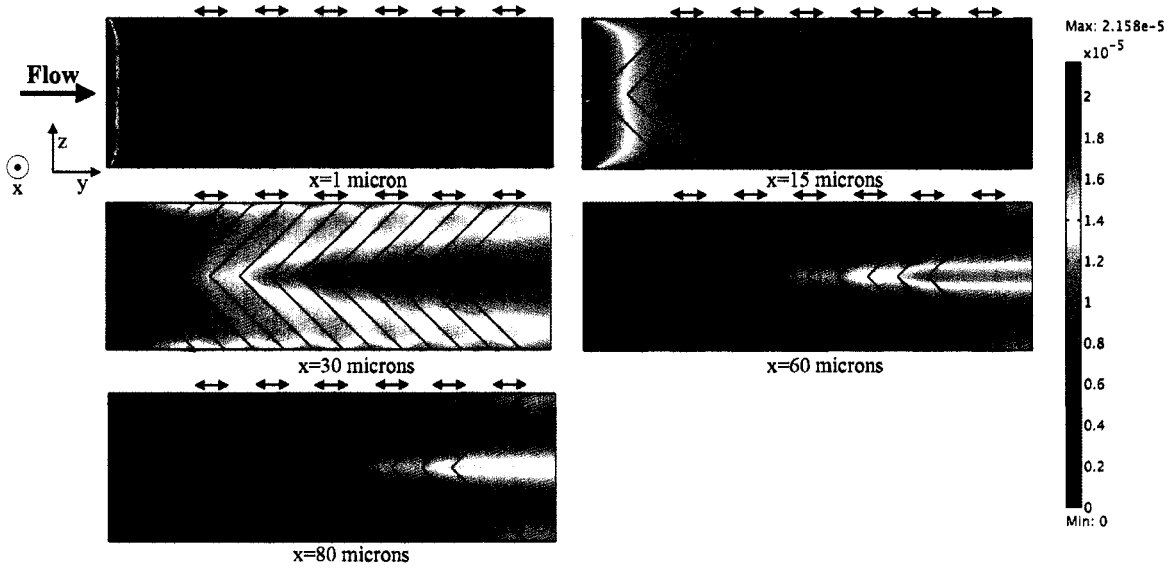

Figure 102. Concentration profile of streptavidin in the channel (moles/m^3) as a function of distance from the binding surface (x-dimension). Model results. Streptavidin inlet concentration = 20 nM = 2×10^{-5} moles/m^3. Time = 350 seconds. Re= 0.01. Pe=135.1. Q=5 nL/s. The arrows indicate the deepest portion of the channel where the chevron structure was present.

The concentration of streptavidin in the chevron microchannel, plotted as a function of depth (x-dimension) (Figure 102), further corroborated and illustrated the interplay of the fluid mechanics and the binding of streptavidin to the surface. The bulk concentration

profile – particularly at x=30 microns – mirrored the binding profile on the surface at time=350 seconds. Very close to the binding surface (x=1 micron), the concentration of streptavidin was nearly zero, indicating that very little of the SPR signal was contributed by the bulk protein. Further from the surface (x=15, 30, 60 and 80 microns), the concentration increased. The streptavidin near the sidewalls and a stripe down the centerline (z=250 microns) was reduced due to the rotation of the fluid, bringing solution depleted of streptavidin near the sidewalls and the centerline (z-dimension) and resulting in two cores of concentration solution.

Influence of increased flow rate on the binding profile of streptavidin in the chevron microchannel

Increased flow rate (Figure 103), as for the straight microchannel (Figure 71), reduced the size of the depletion zone near the surface and increased the amount of streptavidin bound to the surface at a given time point (Figure 103B).

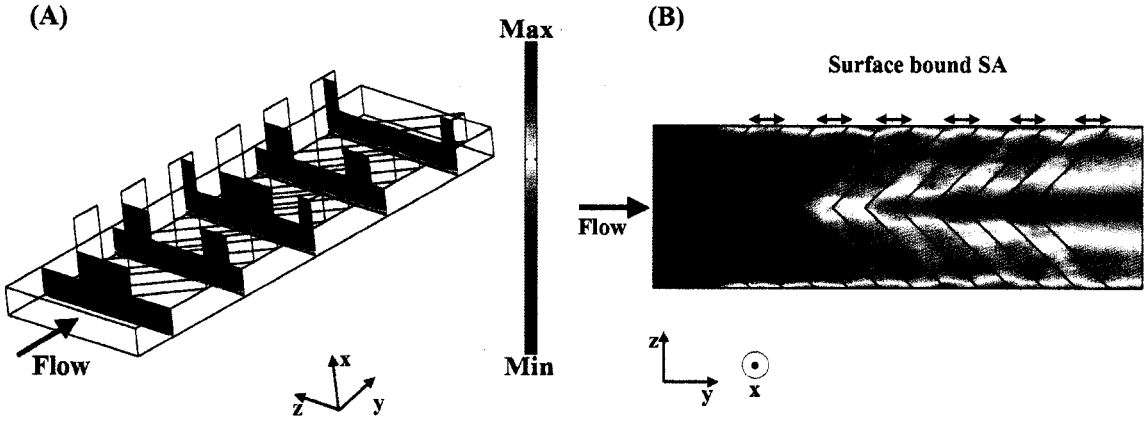

Figure 103. Influence of increased flow rate on SA surface binding in chevron microchannel. Model results. (A) Concentration of streptavidin in the microchannel (moles/m^3). The maximum and minimum concentrations were 2.04 $\times 10^{-5}$ moles/m^2 and 0 moles/m^2. (B) Binding profile of streptavidin to biotinylated surface (moles/m^2). The maximum SA surface binding concentration was 3.99 $\times 10^{-8}$ moles/m^2. The minimum SA surface binding concentration was 0 moles/m^2. The streptavidin concentration introduced to the microchannel was 20 nM= 2×10^{-5} moles/m^3. Time = 350 seconds. Re= 0.1. Pe=1351 Q=50nL/s. The arrows indicate the deepest portion of the channel where the chevron structure was present. The theoretical maximum SA surface binding concentration was 3.99 $\times 10^{-8}$ moles/m^2.

Comparison of binding profiles of streptavidin to the surface in the straight and the chevron microchannels

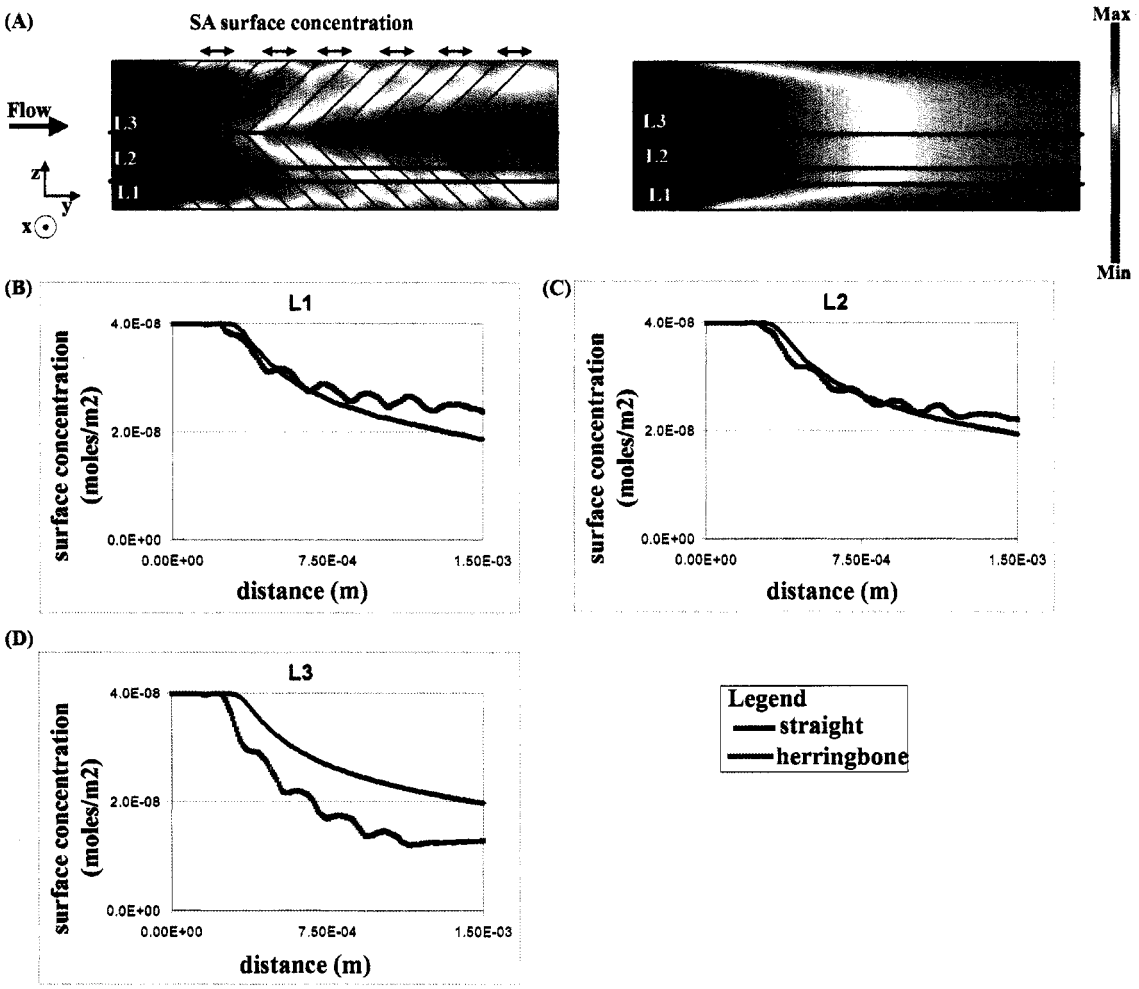

Figure 104. Comparison of the SA surface binding profile for a chevron microchannel and a straight microchannel in the y-dimension. Model results. (A) Surface concentration profiles of bound streptavidin (moles/m^2). The maximum SA surface binding concentration was 3.99 $\times 10^{-8}$ moles/m^2. The minimum SA surface binding concentration was 0 moles/m^2. (B) Line profiles comparing the SA surface concentration profile. The locations of the line profiles are indicated in (A). The specific coordinates of the line profiles are L1(z=250 microns; y[0 to 1.5mm]), L2(z=125 microns; y[0 to 1.5mm]), and L3(z=90 microns; y[0 to 1.5mm]). Streptavidin inlet concentration = 20 nM = 2×10^{-5} moles/m^3. Time = 700 seconds. Re= 0.01. Pe=135.1. Q=5 nL/s. The arrows indicate the deepest portion of the channel where the chevron structure was present. The theoretical maximum SA surface binding concentration was 3.99 $\times 10^{-8}$ moles/m^2.

Comparison of the streptavidin surface binding profile for the straight and chevron microchannel directly highlighted the differences introduced by the chevron microstructure. Near the sidewalls (Figure 104 L1 and L2), the amount bound along those

lines was greater for chevron microchannel. Even for the profile, L2, at upstream positions (y-dimension) the straight channel may bind more streptavidin to the surface, but further downstream more protein bound to the surface. At the centerline of the microchannel (Figure 104 L3 z=250 microns), there was a reduction in the binding profile for the chevron microchannel.

Line profiles transverse to flow (Figure 105) illustrate that the amount of protein binding at midchannel in the chevron (z=250 microns) was significantly reduced down the length of the channel when compared to the straight microchannel with a slight increase in the amount of binding along the sidewalls. The line profiles suggested that initially, the chevron microchannel did not bind as much streptavidin as the straight microchannel (L1). However, down the length of the channel (L4), the data indicate that the amount of streptavidin binding to the surface for the chevron microchannel was greater than the streptavidin binding in the straight microchannel. This suggests that given a larger microchannel (y-dimension), more protein will bind to the surface in the chevron microchannel than in a straight microchannel. However, the transverse line profiles do not capture the fact that in the narrow portion of the chevron microchannel (where the chevron structure is not present) more streptavidin bound and in the wider regions (where the chevrons are present) less streptavidin bound. Depending on where the line profile was located, it may have overestimated or underestimated the average amount of streptavidin bound in that region.

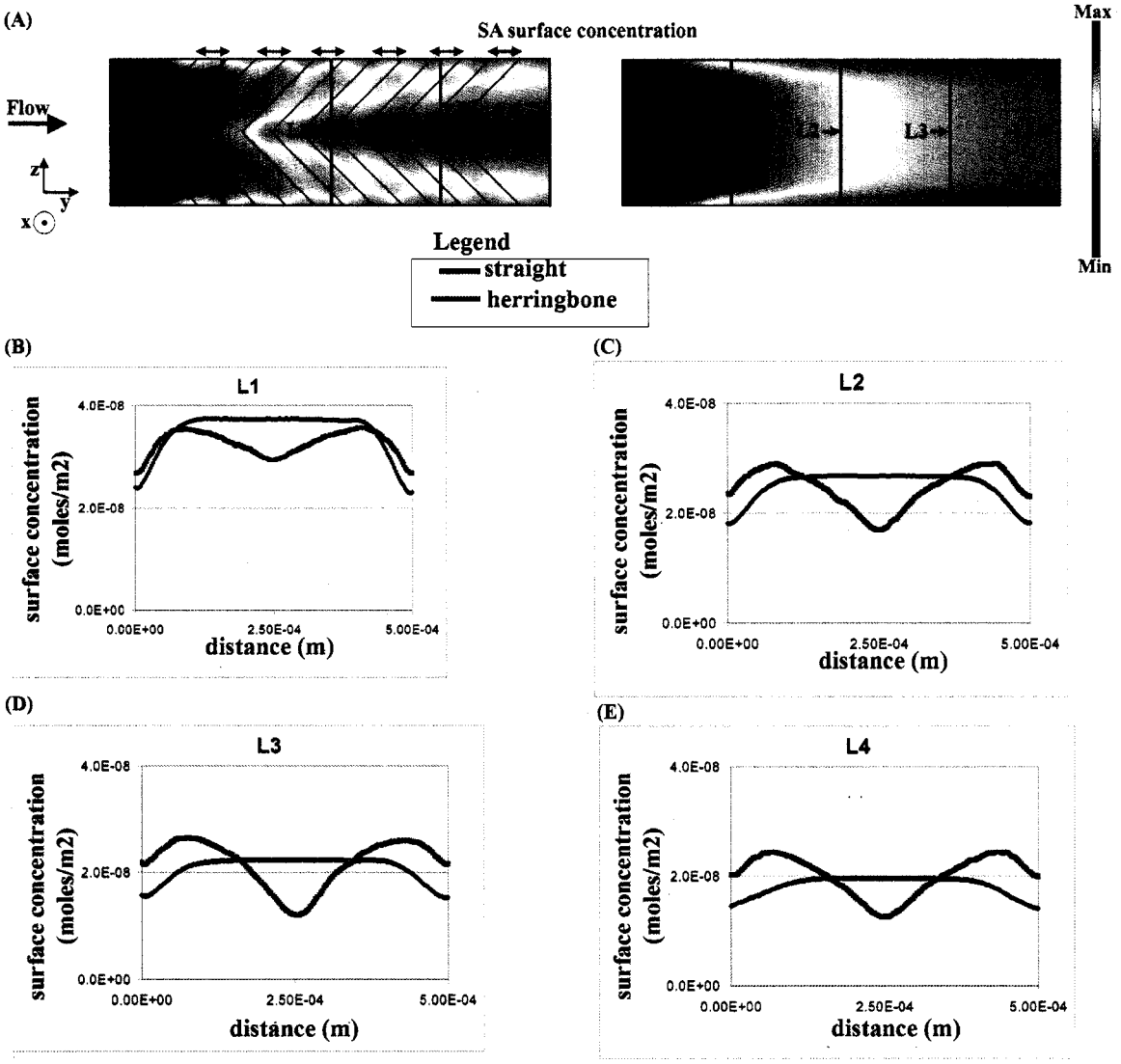

Figure 105. Comparison of the SA surface binding profile for a chevron microchannel and a straight microchannel in the z-dimension. Model results. (A) Surface concentration profiles of bound streptavidin (moles/m^2). The maximum SA surface binding concentration was 3.99 $\times 10^{-8}$ moles/m^2. The minimum SA surface binding concentration was 0 moles/m^2. (B) Line profiles comparing the SA surface concentration profiles. The locations of the line profiles are indicated in (A). The specific coordinates of the line profiles are L1(y=0.375 mm; z[0 to 500 microns]), L2(y=0.75 mm; z[0 to 500 microns]), L3(y=1.125 mm; z[0 to 500 microns]), and L4(y=1.5 mm; z[0 to 500 microns]). Streptavidin inlet concentration = 20 nM = 2×10^{-5} moles/m^3. Time = 700 seconds. Re= 0.01. Pe=135.1. Q=5 nL/s. The arrows indicate the deepest portion of the channel where the chevron structure was present. The theoretical maximum surface binding concentration was 3.99 $\times 10^{-8}$ moles/m^2.

Comparison of total binding of streptavidin for a straight microchannel versus a chevron microchannel

To compare the total amount of binding for the chevron microchannel versus a straight microchannel, the amount of streptavidin over the entire binding surface was plotted as a function of time (Figure 106) at two flow rates. The results indicated that the introduction of transverse flow to recirculate the streptavidin solution over the binding surface in the chevron microchannel did not increase the amount of streptavidin bound to the surface (in Figure 106 the data points for the straight and herringbone microchannel).

A

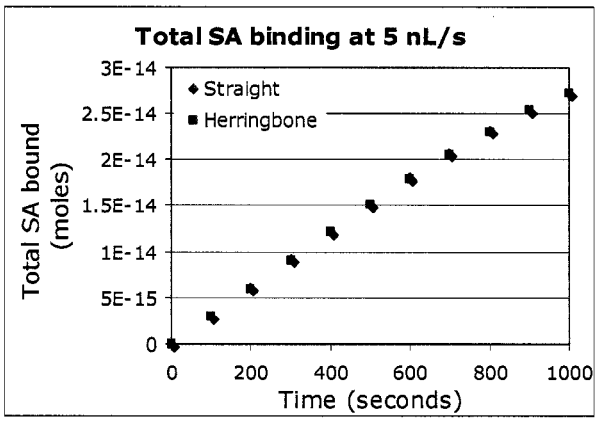

B

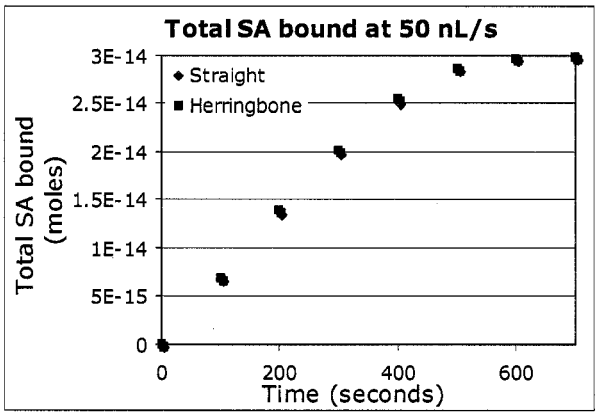

Figure 106. Total streptavidin bound to the surface for the chevron microchannel versus the straight microchannel for two flow rates. Model results. (A) 5 nL/s. (B) 50 nL/s. The streptavidin concentration introduced to the microchannel was 20 nM. The theoretical maximum for total amount of antibody bound to the surface was 3×10^{-14} moles.

At first, this result may be surprising. However, there are several potential reasons why the chevron microchannel may not increase the total amount of streptavidin bound compared to the straight microchannel.

(1) Microchannel volume. For the chevron microchannel, the base microchannel had the same dimensions as the straight microchannel. It was chosen as the control as this microchannel was the easiest for which to complete the experimental controls, due to fabrication issues (described in the Initial Design Considerations). Therefore, the volume of the chevron microchannel was larger than the straight microchannel, thereby increasing the microchannel volume-to-binding surface area ratio and reducing the average velocity. Furthermore, the velocity within the chevron was shown to be dramatically lower than in the base microchannel, and the dispersion profile (Appendix H) varied significantly for the straight versus the chevron microchannel. These considerations would in theory reduce the amount of streptavidin bound to the surface for the chevron microchannel versus the straight microchannel.

(2) Y-velocity dominant in the chevron microchannel. When the transverse flow was introduced to the center of the chevron microchannel solution depleted of streptavidin, a depletion column was rapidly swept downstream. Therefore, in the area of the microchannel in which there was the most significant convective transport (at the midline and far from the sidewalls), the solution was significantly depleted of protein. On the other hand, in the straight microchannel, the depth of the depletion zone in the region of the most significant convective transport was much smaller.

(3) Size of the model microchannel. Due to computational constraints, only 1.5 mm (y-dimension) of the microchannel could be modeled. A larger distance may be required for an increase in the total amount of streptavidin bound to the surface in the chevron microchannel versus the straight microchannel. As previously mentioned, the line profiles (Figure 105, particularly L4) suggest that more protein bound downstream in the chevron microchannel.

(4) Protein molecules are not mass transport-limited enough to observe an increase in streptavidin binding over such a small distance (y-dimension) of a chevron microchannel. Protein molecules may not be transport limited enough to observe an increase in binding compared to perhaps microspheres (0.8 micron streptavidin-covered beads were used in experiments (data not shown), but the beads sedimented out of solution over the course of the experiment). Although there may be an increase in binding of a more slowly diffusing particle to the surface, the focus of this research has been to quantify protein and small molecules in solution. Therefore, this analysis is outside the scope of this research.

(5) Literature precedence. The work by Yoon et al. [219], Vijayendran et al.,[217] and Liu et al.,[218] described in the Background, also used microfluidic mixers to improve the performance of a surface binding reaction. Although they did not analyze the same experimental system, their work indicated that there was not a substantial improvement in the performance of the assays due to the incorporation of the mixer geometry (from ~1.5× to ~8× improvement in binding rates or the amount of material bound to the surface at a given time point). Furthermore, the length of the mixer microchannel (detailed above in #3) for each of these systems was ~6× to ~16.7× larger than the 1.5 mm distance in the y-dimension in this model geometry. For reasons described in #3, these systems may have seen an improvement in the surface reaction which is not observed with this modeled system.

The influence of the location of the binding area, when comparing the straight and chevron microchannel, has been explored with the model. The amount of streptavidin bound down the centerline of the microchannel (Figure 107 A2) compared to the amount bound near the sidewall (Figure 107 A1) indicated that down the midline there was a significant reduction in the amount of streptavidin bound to the chevron (herringbone) microchannel. However, along the sidewalls there was a slight increase in the total amount of streptavidin bound in the straight microchannel versus the chevron microchannel. The increase in streptavidin binding near the sidewalls was less than the

reduction in streptavidin binding along the centerline, due to the fact that there was also a slight increase in binding near the other sidewall of the microchannel.

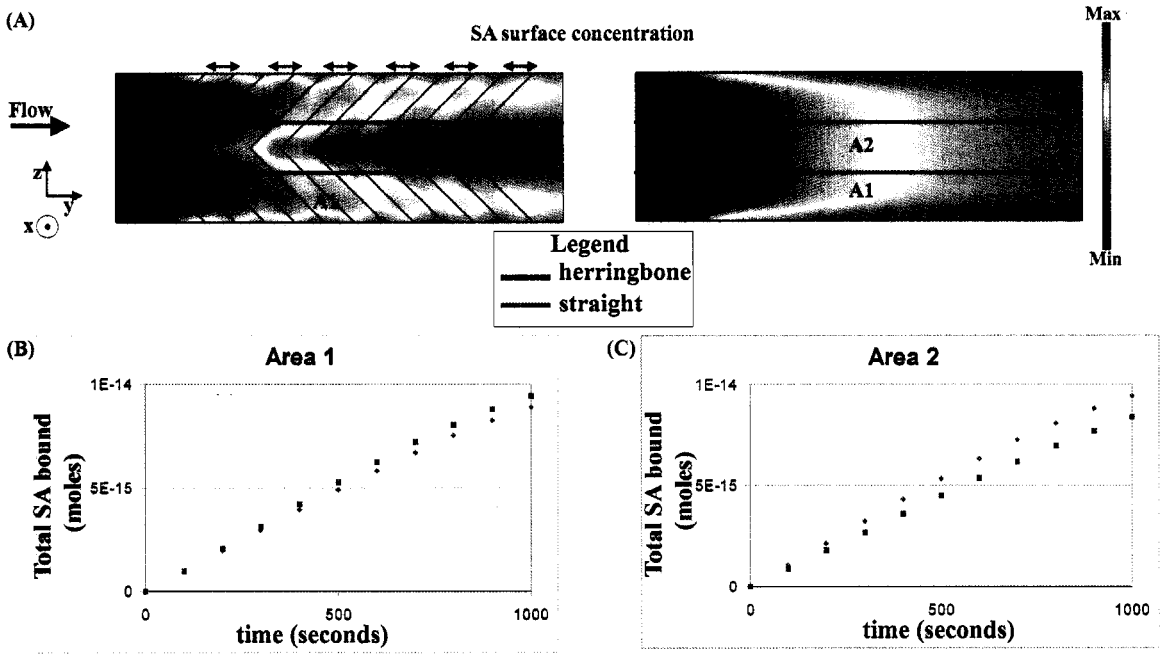

Figure 107. Total SA bound to the surface for several areas of interest in a chevron microchannel versus a straight microchannel. Model results. (A) Surface concentration profiles of bound streptavidin (moles/m^2). (B)-(C) Total SA binding over time in areas 1-2 respectively for the chevron microchannel and straight microchannel. The maximum SA surface binding concentration was 3.99 $\times 10^{-8}$ moles/m^2. The minimum SA surface binding concentration was 0 moles/m^2.The locations of the areas analyzed are indicated in (A). The specific coordinates of the areas are A1 (y[0 to 1.5 mm]; z[0 to 167 microns]) and A2 (y[0 to 1.5 mm; z[167 to 333 microns]). Streptavidin inlet concentration = 20 nM = 2×10^{-5} moles/m^3. Time = 700 seconds. Re= 0.01. Pe=135.1. Q=5 nL/s. The arrows indicate the deepest portion of the channel where the chevron structure was present. The theoretical maximum amount of SA that can bind to the surfaces was 9.97 $\times 10^{-15}$ moles. The theoretical maximum SA surface binding concentration was 3.99 $\times 10^{-8}$ moles/m^2.

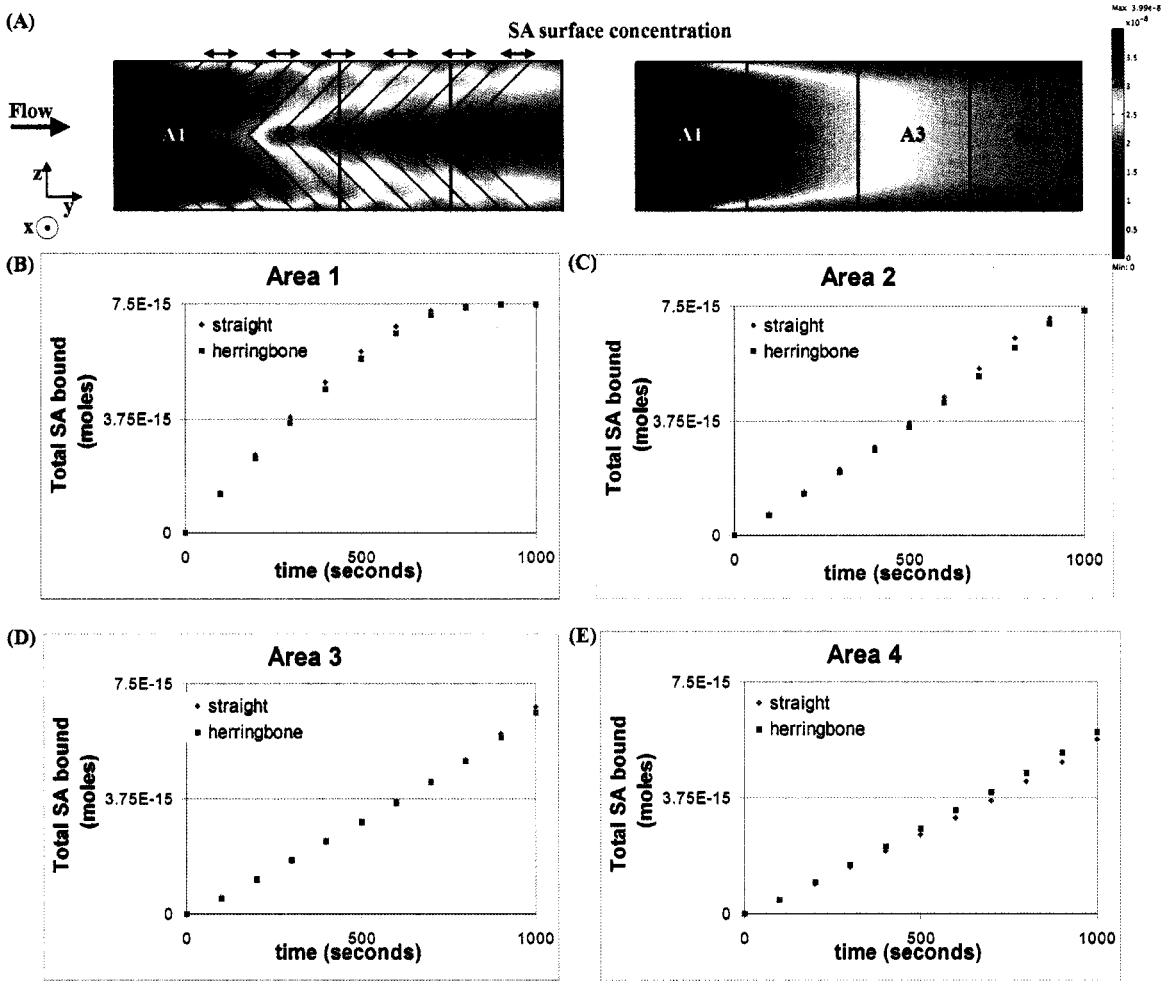

Figure 108. Total SA bound to the surface for several areas of interest for a chevron microchannel versus a straight microchannel. Model results. (A) Surface concentration profiles of bound streptavidin (moles/m^2). (B)-(E) Total SA binding over time in areas 1-4 respectively for the reverse chevron microchannel and straight microchannel. The maximum SA surface binding concentration was 3.99 $\times 10^{-8}$ moles/m^2. The minimum SA surface binding concentration was 0 moles/m^2.The locations of the areas analyzed are indicated in (A). The specific coordinates of the areas are A1 (y[0 to 0.375 mm]; z[0 to 500 microns]), A2 (y[0 to 0.75 mm]; z[0 to 500 microns]), A3 (y[0 to 1.125 mm]; z[0 to 500 microns]), and A4 (y[0 to 1.5 mm]; z[0 to 500 microns]). Streptavidin inlet concentration = 20 nM = 2×10^{-5} moles/m^3. Time = 700 seconds. Re= 0.01. Pe=135.1. Q=5 nL/s. The arrows indicate the deepest portion of the channel where the chevron structure was present. The theoretical maximum amount of SA that binds to the surfaces was 7.48 $\times 10^{-15}$ moles. The theoretical maximum SA surface binding concentration was 3.99 $\times 10^{-8}$ moles/m^2.

The total amount of streptavidin bound to the surface was also analyzed as a function of distance downstream (y-dimension Figure 108) and indicated that there was very little difference in the amount of streptavidin bound in each area of the straight and chevron (herringbone) microchannel. However, in the last area – Area 4 – there was a slight increase in the total amount of streptavidin bound to the surface of the chevron

(herringbone) microchannel, suggesting that further downstream (y-dimension) there could be an increase in the total amount of streptavidin bound for the chevron (herringbone) microchannel versus the straight microchannel.

To explore distances further downstream of the inlet (y-dimension) in the binding profile for the herringbone microchannel versus the straight microchannel as compared to that explored by the modeled microchannel, experiments were completed that analyzed three discrete areas downstream of the start of the streptavidin binding surface (Figure 109 and Figure 110). The areas were ~1.8 mm in the y-dimension (downstream distance) with area 1 located at the start of the binding surface. The average change in reflectivity for that region was plotted over time. For reference, the model system was only 1.5 mm in the y-dimension. Therefore, the experimental data explored an area that was ~3.6 times larger than the model system. The experimental results clearly indicated there was a more significant delay in the binding as a function of distance down the channel for the straight microchannel (Figure 109) versus chevron microchannel (Figure 110). These results suggested that further downstream in the chevron microchannel, more streptavidin bound to the surface versus the straight microchannel.

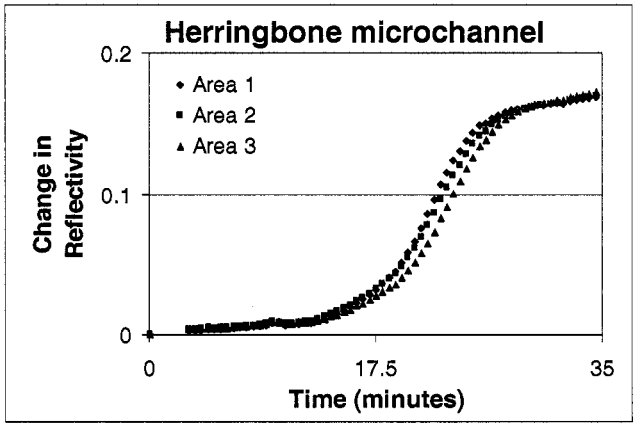

Figure 109. Change in reflectivity over time in three areas as a function of distance from the inlet for the chevron (herringbone) microchannel. Experimental results – SPR imaging. Area 1 was closest to the inlet. Each area was 300 pixels in the y-dimension and the width of the entire channel in the other dimension. Streptavidin inlet concentration = 40 nM. Re= 0.11. Pe=1480. Q=50 nL/s. The missing data points were the result of a bubble entering the microchannel.

An important experimental detail needed to accurately compare the data results is that the upstream distance in the device before the binding surface (distance from the inlet to the biotinylated alky thiol – hence the dead volume) was slightly different for straight microchannel and the chevron microchannel. The upstream distance in the straight microchannel was 8.43 mm, corresponding to 356 nL of dead volume before the binding area. In the chevron microchannel, the distance was 20 mm, which corresponded to 820 nL of dead volume. Therefore, there was some discrepancy between the time the solution reached the binding surface as well as the influence of dispersion for the chevron and the straight microchannels. The streptavidin solution reached the straight channel binding area before the chevron microchannel. However, the comparison of the time to half saturation for the streptavidin surface binding profile within a single microchannel (chevron or straight) would not be affected by the discrepancy. Furthermore, given the fact that the upstream dead volume is ~35 microliters, the difference between the geometries was not that significant as a percent of the total dead volume.

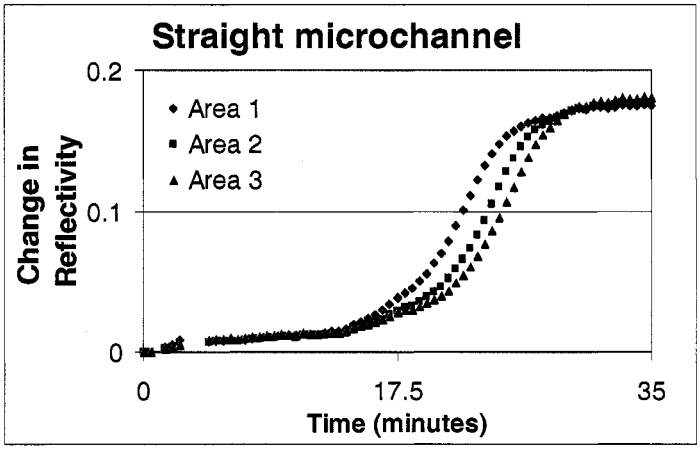

Figure 110. Change in reflectivity over time in three areas as a function of distance from the inlet for the straight microchannel. Experimental results. Area 1 was closest to the inlet. Each area was 300 pixels in the y-dimension and the entire width of the channel in the other dimension. Streptavidin inlet concentration = 40 nM. Re= 0.11. Pe=1480. Q=50 nL/s. The missing data points were the result of a bubble entering the microchannel.

To obtain a more quantitative understanding of the difference in the binding profile between the chevron and straight microchannel, the time point at which the change in reflectivity was half of the maximum change in reflectivity was calculated for the straight microchannel and the chevron microchannel (Table 16). The standard deviation for both

microchannels was the largest for Area 1, which may be a result of the variation in the amount of thiols at the front of the binding surface (an artifact of the thiol patterning method). However, binding of streptavidin to the surface was faster in the straight microchannel at the other locations (Area 2 and Area 3).

Table 16. Time (minutes) at which the surface concentration reached half maximum. Experimental results. (n=3)

	Straight microchannel		Chevron microchannel	
	average	standard deviation	average	standard deviation
Area 1	21.8	1.0	20.4	1.7
Area 2	23.5	0.5	21.8	0.4
Area 3	24.2	0.3	22.0	0.9

To understand the relationship between the binding profiles within each microchannel, the difference in the time between each area's point of half saturation is listed in Table 17. The results indicated that the time between half saturation for Areas 1 and 2 is much greater for the straight microchannel, even with consideration of the relatively large standard deviation. For the time difference between Areas 2 and 3, the large standard deviation made it impossible to determine if there was a difference between the straight and chevron microchannels.

Table 17. Difference in time for reaching half maximum surface concentration (minutes). Experimental results. (n=3)

	Straight microchannel		Chevron microchannel	
	average	standard deviation	average	standard deviation
Area 1 and Area 2	1.6	0.5	0.42	0.1
Area 2 and Area 3	0.70	0.2	1.2	0.8

These results suggest that for a longer chevron microchannel there would be an improvement in the binding of streptavidin to the surface.

Reverse chevron microchannel

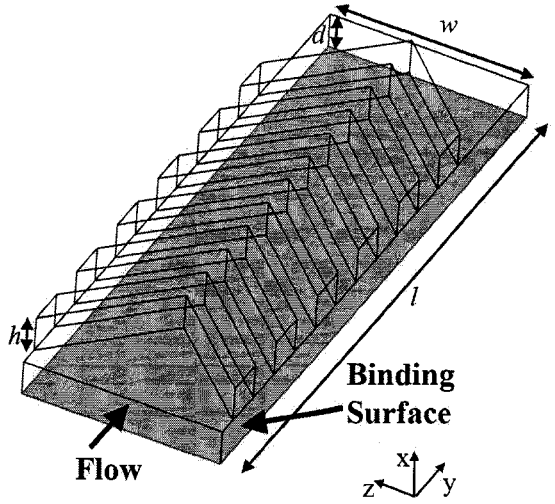

Figure 111. Reverse chevron microchannel. In the model microchannel d=90 microns, h= 90 microns, w=500 microns, and l=1.5 mm. In the experimental microchannel d=82 microns, h= 56 microns, and w=500 microns. The binding surface is indicated.

Typically in chevron microchannels, the solution is introduced into the device so that the fluid first encounters the front point of the chevron. This typical format was explored in the previous section. Alternatively, the fluid could be introduced in the reverse format (Figure 111).

Since the assay operates under laminar flow conditions, the velocity profile should be the same whether the fluid enters in the front (described in the previous sections of the chapter) or back (detailed in this section). However, the direction of the velocity to and from the surface (x-velocity) as well as the transverse velocity (z-velocity) will be in the opposite direction when the fluid enters the device from the rear.

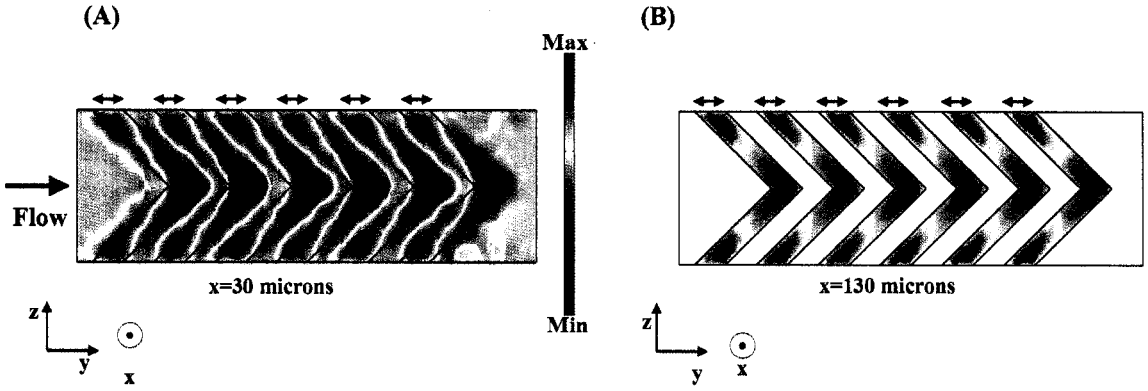

Figure 112. X-velocity profile (m/s) in the reverse chevron microchannel. Model results. (A) The maximum velocity and minimum velocity were 1.05 $\times 10^{-5}$ m/s and -1.49$\times 10^{-5}$ m/s at=30 microns. (B) The maximum velocity and minimum velocity were 1.50 $\times 10^{-5}$ m/s and -2.16 $\times 10^{-5}$ m/s at x=130 microns. The flow rate was 5 nL/s. Reynolds number = 0.01. Q=5 nL/s. The arrows indicate the deepest portion of the channel where the chevron structure was present.

When the fluid entered the reverse chevron, it entered the chevron microstructure from the back so that the fluid moved away from the surface (Figure 112 x-velocity in red) at the tails of the chevron and was pushed toward the binding surface (Figure 112 x-velocity in blue) at the terminus of the chevron at the chevron point at the midline of the channel (z= 250 microns). As expected, the results were comparable near the surface (x=30 microns) and within the chevron (x=130 microns) and mirrored the results for the forward chevron with the direction of the x-velocity.

The y-velocity profile (Figure 113) mirrored the previous velocity profile (Figure 92 chevron microchannel) near the surface (x=30 microns) with a decrease in velocity in the location of the chevron (black arrows), with the maximal velocity located near the terminus of the chevron microstructure at the point of the last chevron encountered. Within the chevron (x=130 microns), the velocity profile was also remarkably similar to the previous results and indicated that maximal velocity occurred in the middle of the chevron structure and was zero at the structure walls (as dictated by the no slip boundary condition).

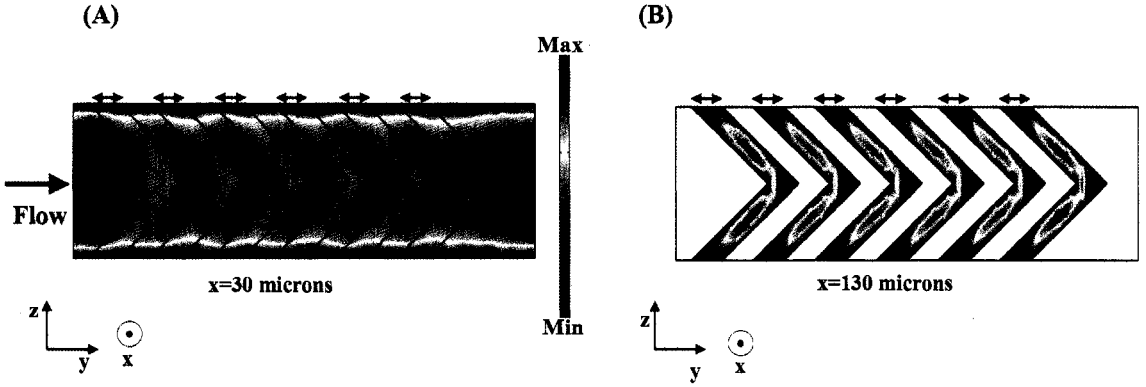

Figure 113. Y-velocity profile (m/s) in the reverse chevron microchannel. Model results. (A) The maximum velocity and minimum velocity were 1.60×10^{-4} m/s and -6.07×10^{-19} m/s at=30 microns. (B) The maximum velocity and minimum velocity were 3.48×10^{-5} m/s and -5.59×10^{-19} m/s at x=130 microns. The flow rate was 5 nL/s. Reynolds number = 0.01. Q=5 nL/s. The arrows indicate the deepest portion of the channel where the chevron structure was present.

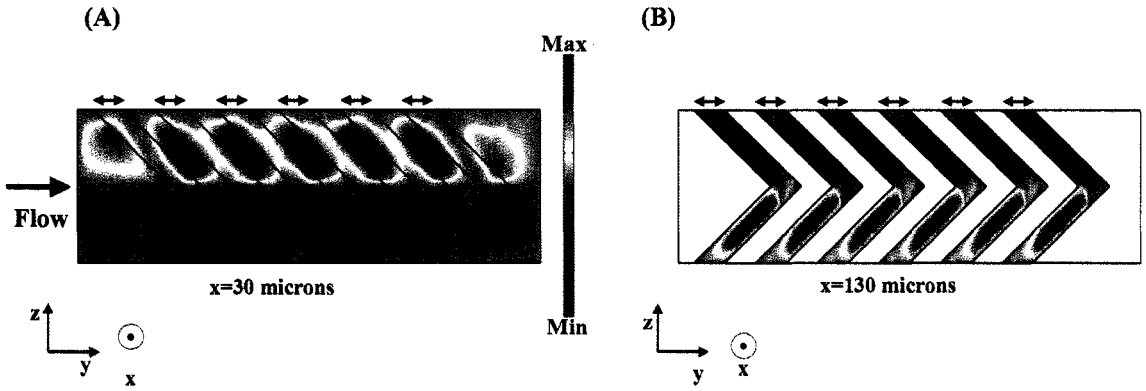

Figure 114. Z-velocity profile (m/s) in the reverse chevron microchannel. Model results. (A) The maximum velocity and minimum velocity were 2.15×10^{-5} m/s and -2.15×10^{-5} m/s at=30 microns. (B) The maximum velocity and minimum velocity were 3.20×10^{-5} m/s and -3.12×10^{-5} m/s at x=130 microns. Q=5 nL/s. Reynolds number = 0.01. Q=5 nL/s. The arrow indicates the deepest portion of the channel where the chevron structure was present.

In the reverse chevron, the transverse velocity (Figure 114 z-velocity) swept the fluid near the surface (Figure 114A x=30 microns) from the midline (z= 250 microns) towards the channel sidewalls. Within the chevron (Figure 114B x=130 microns), the fluid was swept from the sidewalls toward the midline (z= 250 microns).

Once again, these results indicate that the chevron microchannel generated two spiraling flows on each half of the microchannel but their direction was reversed in the opposite direction as compared to the forward chevron microchannel – clockwise for z=250-500 microns and counterclockwise for z=0-250 microns. Therefore, at the sidewalls, the solution was pulled from the binding surface towards the chevron in the top of the microchannel. The fluid moved along the chevron to the centerline (z= 250 microns) of the channel, where it was pushed down the binding surface. Near the surface, the fluid was swept from the midline toward the sidewalls.

Quantification of the velocity components in the reverse chevron microchannel

The values of D and F (Equation 13 and Equation 14) were calculated for the reverse chevron microchannel to give quantifiable measures to the velocity field. As expected for laminar flow conditions, the magnitudes of these values for the forward and reverse chevron microchannels were comparable within the error of the model (Table 18 and Table 19). The maximum and minimum values for the x-velocity were reversed.

Table 18. D values. Normalized value of the maximum and minimum velocities in each dimension.

reverse chevron	5 nL/s		50 nL/s	
	max	min	Max	min
$D_{\text{x-velocity}}$	35	-49	35	-50
$D_{\text{y-velocity}}$	165	-1	165	-1
$D_{\text{z-velocity}}$	32	-34	32	-34
$D_{\text{velocity field}}$	165	0	165	0
reverse chevron	5 nL/s		50 nL/s	
	max	min	Max	min
$D_{\text{x-velocity}}$	35	-49	35	-50
$D_{\text{y-velocity}}$	165	-1	165	-1
$D_{\text{z-velocity}}$	32	-34	32	-34
$D_{\text{velocity field}}$	165	0	165	0

Table 19. F values. Fraction of energy due to the velocity in each dimension. Model results. Reverse chevron microchannel.

reverse chevron	5 nL/s	25 nL/s	50 nL/s
Fraction of Energy in x-dimension	9.1E-03	9.2E-03	9.2E-03
Fraction of Energy in y-dimension	9.8E-1	9.8E-1	9.8E-1
Fraction of Energy in z-dimension	1.3E-2	1.4E-2	1.4E-2

Surface binding profile of streptavidin over time in the reverse chevron microchannel

The binding profile of the streptavidin in the reverse chevron (Figure 115) was the inverse of the forward chevron binding profile (Figure 94) with significant binding at the midline (z=250 microns) and a reduction in the binding near the sidewalls. In the deeper portions of the microchannel (indicated by the black arrows and where the chevrons were located) the streptavidin binding was reduced compared to the narrow portions of the channel.

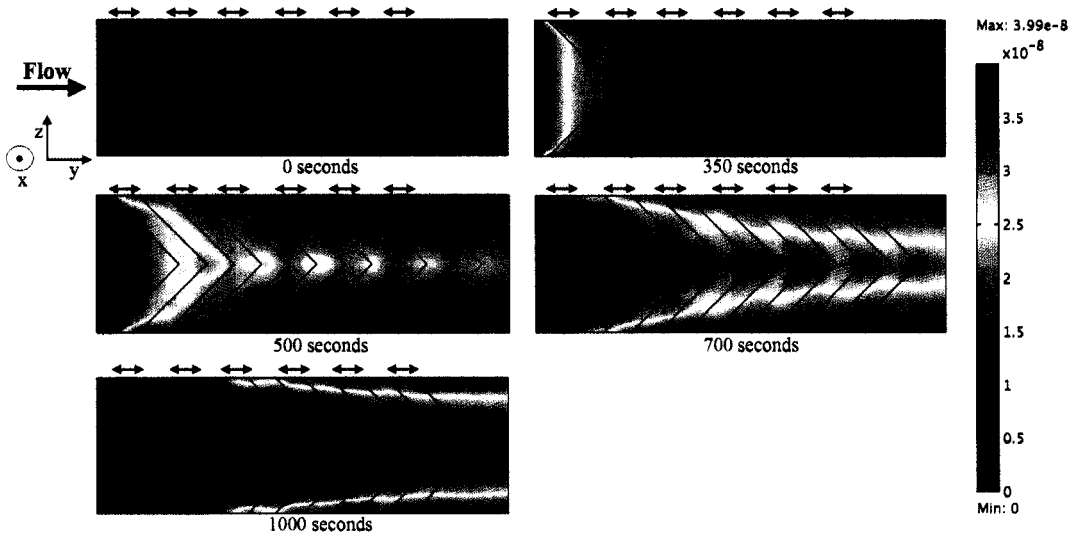

Figure 115. Surface concentration profile of bound streptavidin (moles/m^2) in the reverse chevron microchannel. Model results. Streptavidin inlet concentration = 20 nM = 2×10^{-5} moles/m^3. Time = 350 seconds. Re= 0.01. Pe=135.1. Q=5 nL/s. The arrows indicate the deepest portion of the channel where the chevron structure was present. The theoretical maximum SA surface binding concentration was 3.99 $\times10^{-8}$ moles/m^2.

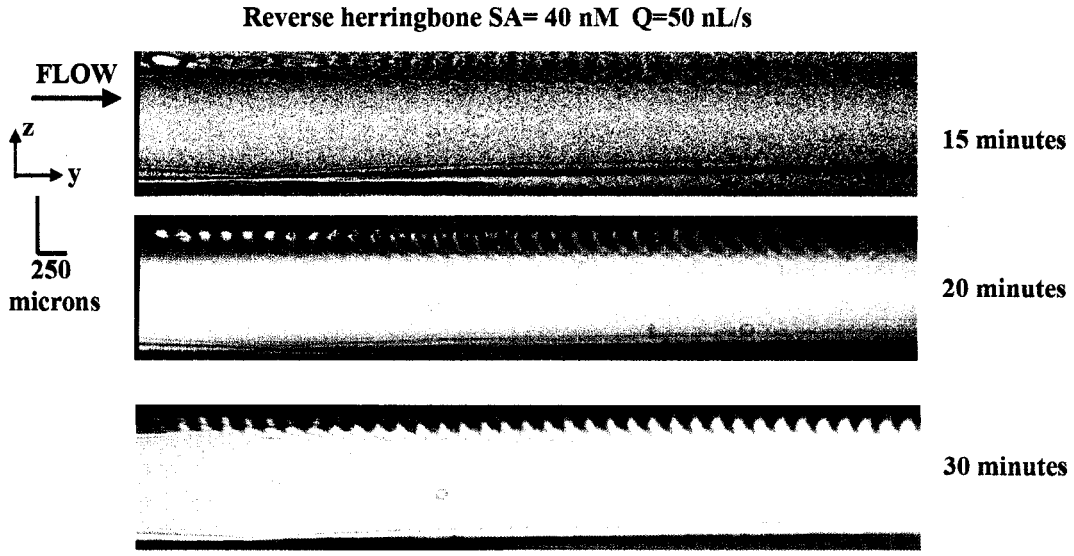

Figure 116. Surface concentration profile of bound streptavidin over time in a reverse chevron microchannel. Experimental results. SPRM difference images subtracted from the initial image. Each image has been contrast enhanced for viewing purposes to demonstrate the variation of surface concentration of streptavidin within each image. Streptavidin inlet concentration = 40 nM. Re= 0.11. Pe=1480. Q=50 nL/s.

SPR difference images (Figure 116) that monitored the binding of streptavidin to the surface corroborated the model results. There was much more binding in the center of the channel than at the sidewalls (particularly at time=20 minutes). Once again, given the focus, image foreshortening, and SPR propagation length, the subtle increase and decrease in the binding profile in the y-dimension could not be resolved with this instrument.

Relationship between the streptavidin surface binding profile and the velocity profiles.

Figure 117 correlates the x-velocity profile with the surface binding profile – particularly L1. When the x-velocity was directed to the binding surface (Figure 117B and C), the negative value indicates that the fluid was being pushed towards the binding surface and the positive value indicates the fluid was pulled away from the binding surface. In the line profile transverse to flow, L2, there was a significant increase in the binding profile at the midline (z=250 microns). The amount of protein bound to the surface was reduced when the fluid was pulled away from the binding surface.

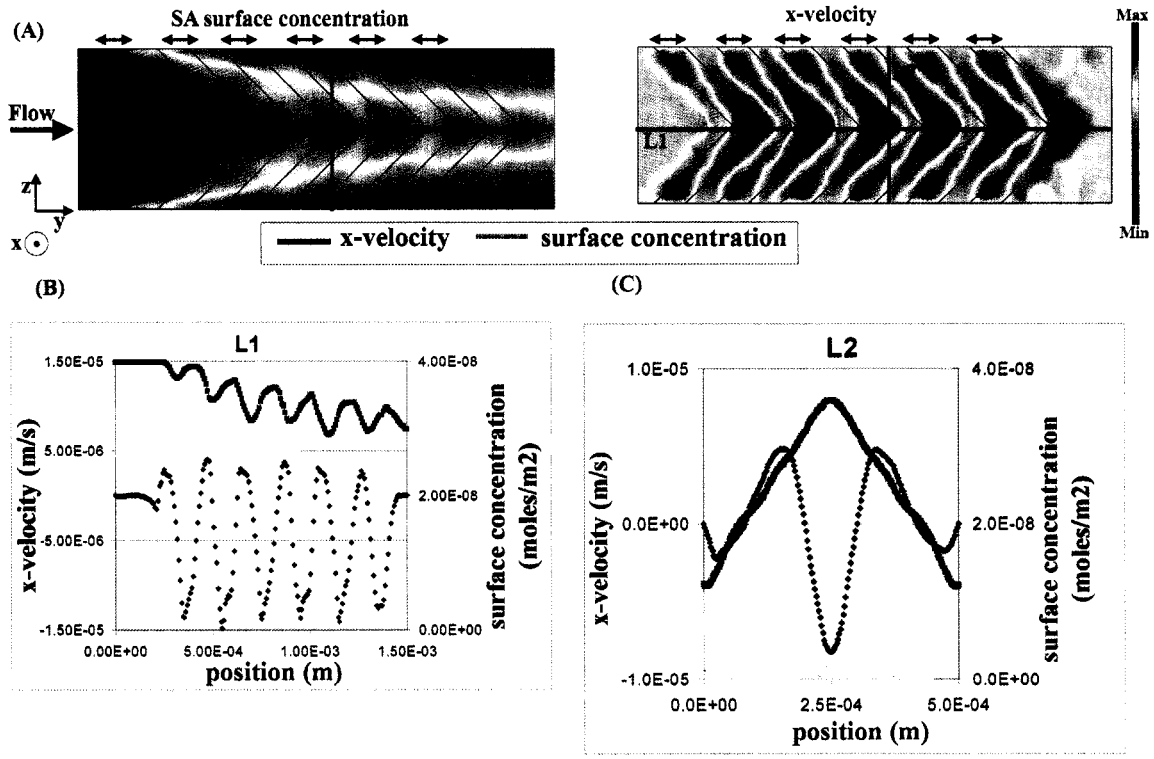

Figure 117. Comparison of the x-velocity profile and the SA surface binding profile in the reverse chevron microchannel. Model results. (A) Surface concentration profile of bound streptavidin (moles/m^2). The maximum SA surface binding concentration was 3.99 $\times 10^{-8}$ moles/m^2. The minimum SA surface binding concentration was 0 moles/m^2. Velocity profile (m/s) in the x-dimension at x=30 microns. The maximum velocity and minimum velocity were 1.05 $\times 10^{-5}$ m/s and -1.49 $\times 10^{-5}$ m/s. (B)-(C) Line profiles comparing surface concentration profile and velocity in the x-dimension. The locations of the line profiles are indicated in (A) and are labeled respectively in (B) and (C). The specific coordinates of the lines are L1(z=250 microns; y[0 to 1.5 mm]) and L2 (y=0.8 mm; z[0 to 500 microns]). Streptavidin inlet concentration = 20 nM = 2×10^{-5} moles/m^3. Time = 700 seconds. Re= 0.01. Pe=135.1. Q=5 nL/s. The arrows indicate the deepest portion of the channel where the chevron structure was present. The theoretical maximum SA surface binding concentration was 3.99 $\times 10^{-8}$ moles/m^2.

Similarly, increases in the y-velocity (Figure 118) correlated with increases in the total binding of streptavidin to the surface down the length of the channel (y-dimension) and transverse to flow (z-dimension).

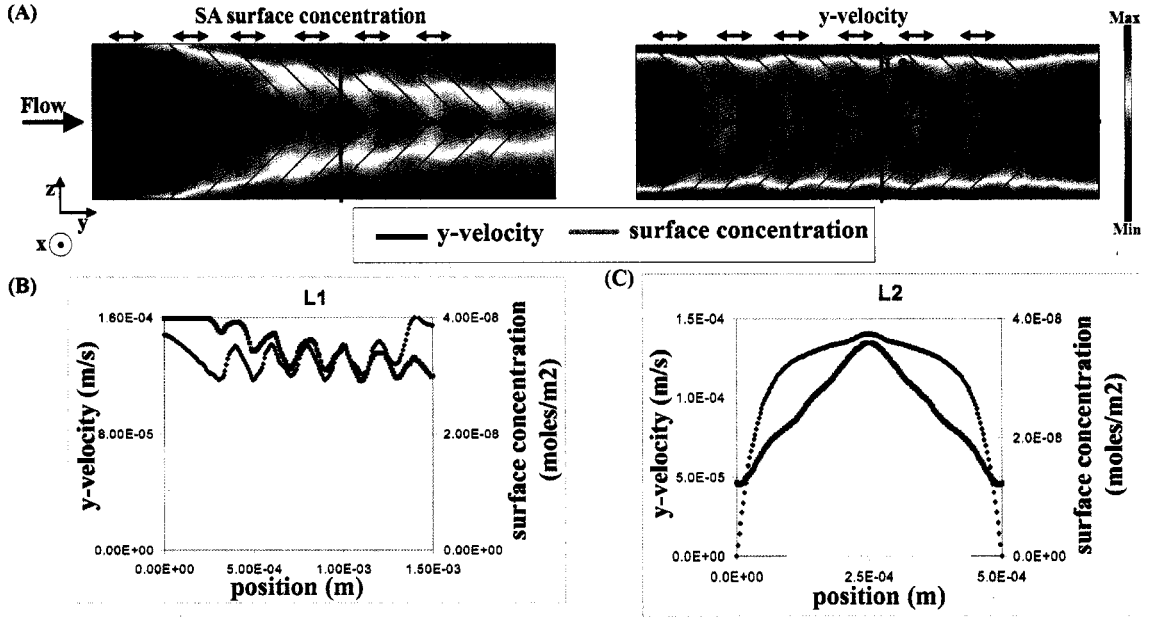

Figure 118. Comparison of the y-velocity profile and the SA surface binding profile in the reverse chevron microchannel. Model results. (A) Surface concentration profile of bound streptavidin (moles/m^2). The maximum SA surface binding concentration was 3.99 $\times 10^{-8}$ moles/m^2. The minimum SA surface binding concentration was 0 moles/m^2.Velocity profile (m/s) in the y-dimension at x=30 microns. The maximum velocity and minimum velocity were 1.60 $\times 10^{-4}$ m/s and -6.0 $\times 10^{-19}$ m/s. (B)-(C) Line profiles comparing surface concentration profile and velocity in the y-dimension. The locations of the line profiles are indicated in (A) and are labeled respectively in (B) and (C). The specific coordinates of the lines are L1 (z=250 microns; y[0 to 1.5 mm]) and L2 (y=0.8 mm; z[0 to 500 microns]). Streptavidin inlet concentration = 20 nM = 2×10^{-5} moles/m^3. Time = 700 seconds. Re= 0.01. Pe=135.1. Q=5 nL/s. The arrows indicate the deepest portion of the channel where the chevron structure was present. The theoretical maximum SA surface binding concentration was 3.99 $\times 10^{-8}$ moles/m^2.

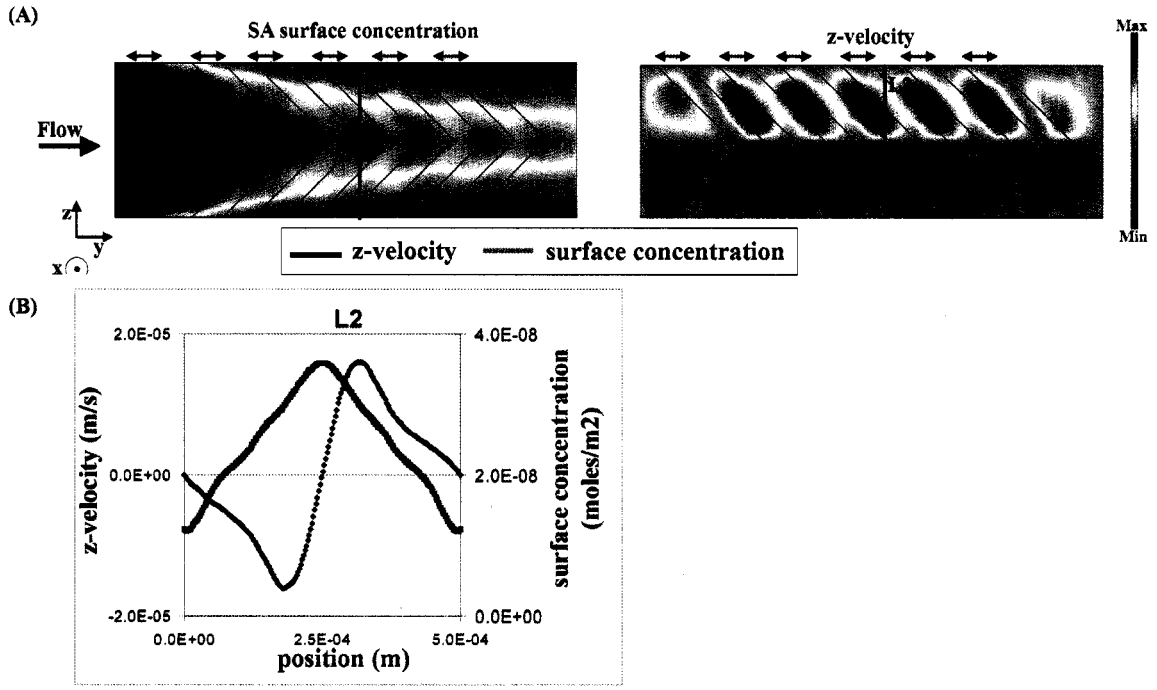

Figure 119. Comparison of the z-velocity profile and the SA surface binding profile in the reverse chevron microchannel. Model results. (A) Surface concentration profile of bound streptavidin (moles/m^2). The maximum SA surface binding concentration was 3.99 $\times 10^{-8}$ moles/m^2. The minimum SA surface binding concentration was 0 moles/m^2. Velocity profile (m/s) in the z-dimension at x=30 microns. The maximum velocity and minimum velocity were 2.15 $\times 10^{-5}$ m/s and -2.15 $\times 10^{-5}$ m/s. (B) Line profile comparing surface concentration profile and velocity in the z-dimension. The location of the line profiles is indicated in (A). The specific coordinates of L2 is y=0.8 mm and z[0 to 500 microns]. Streptavidin inlet concentration = 20 nM = 2×10^{-5} moles/m^3. Time = 700 seconds. Re= 0.01. Pe=135.1. Q=5 nL/s. The arrows indicate the deepest portion of the channel where the chevron structure was present. The theoretical maximum SA surface binding concentration was 3.99 $\times 10^{-8}$ moles/m^2.

The sharpness in the z-velocity profile (Figure 119) also strongly correlated with the binding profile. At the channel midline (z= 250 microns), the transverse velocity rapidly fell to zero but the most streptavidin binding occurred. This increase in the amount of bound streptavidin could be attributed to an increase in the velocity of another velocity component (x- and y- dimensions).

Comparison of the streptavidin surface binding profiles in reverse chevron and straight microchannels

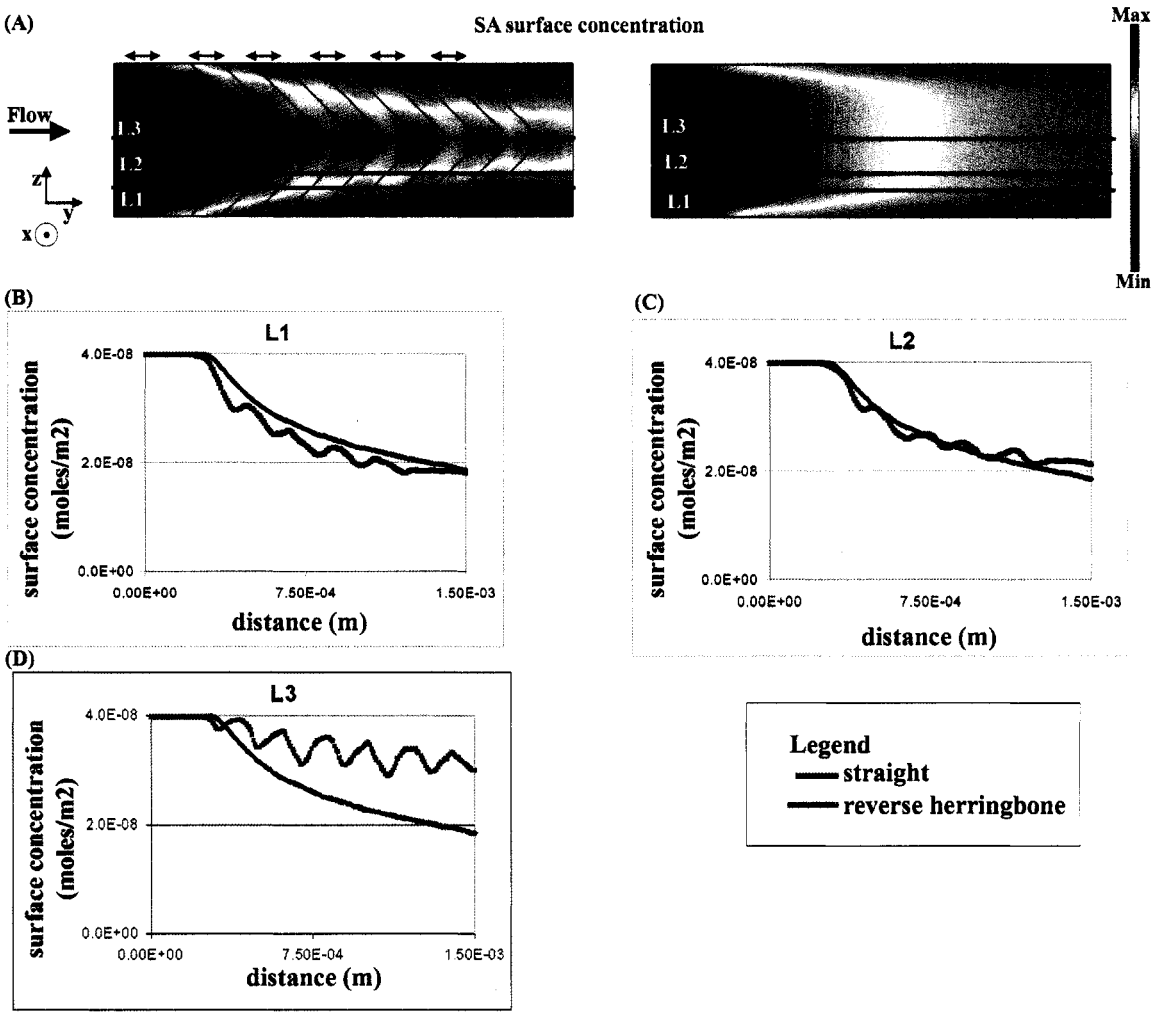

Figure 120. Comparison of the SA surface binding profile for a reverse chevron microchannel and a straight microchannel. Model results. (A) Surface concentration profiles of bound streptavidin (moles/m^2). The maximum SA surface binding concentration was 3.99 $\times 10^{-8}$ moles/m^2. The minimum SA surface binding concentration was 0 moles/m^2. (B) Line profiles comparing the SA surface concentration profiles. The locations of the line profiles are indicated in (A). The specific coordinates of the line profiles are L1(z=250 microns; y[0 to 1.5mm]), L2(z=125 microns; y[0 to 1.5mm]), L3(z=90 microns; y[0 to 1.5mm]). Streptavidin inlet concentration = 20 nM = 2×10^{-5} moles/m^3. Time = 700 seconds. Re= 0.01. Pe=135.1. Q=5 nL/s. The arrows indicate the deepest portion of the channel where the chevron structure was present. The theoretical maximum SA surface binding concentration was 3.99 $\times 10^{-8}$ moles/m^2.

Comparing the surface binding profile of streptavidin downstream of the microchannel (Figure 120 y-dimension) for the straight and chevron microchannels indicates that along the midline of the channel (z=250 microns), there was a significant increase in the

binding for the reverse chevron (L3) whereas near the sidewalls (L1) less streptavidin bound in the chevron microchannel. Along L2, at upstream positions, the reverse chevron microchannel bound less streptavidin, but at the outlet of the device the chevron began to bind more streptavidin.

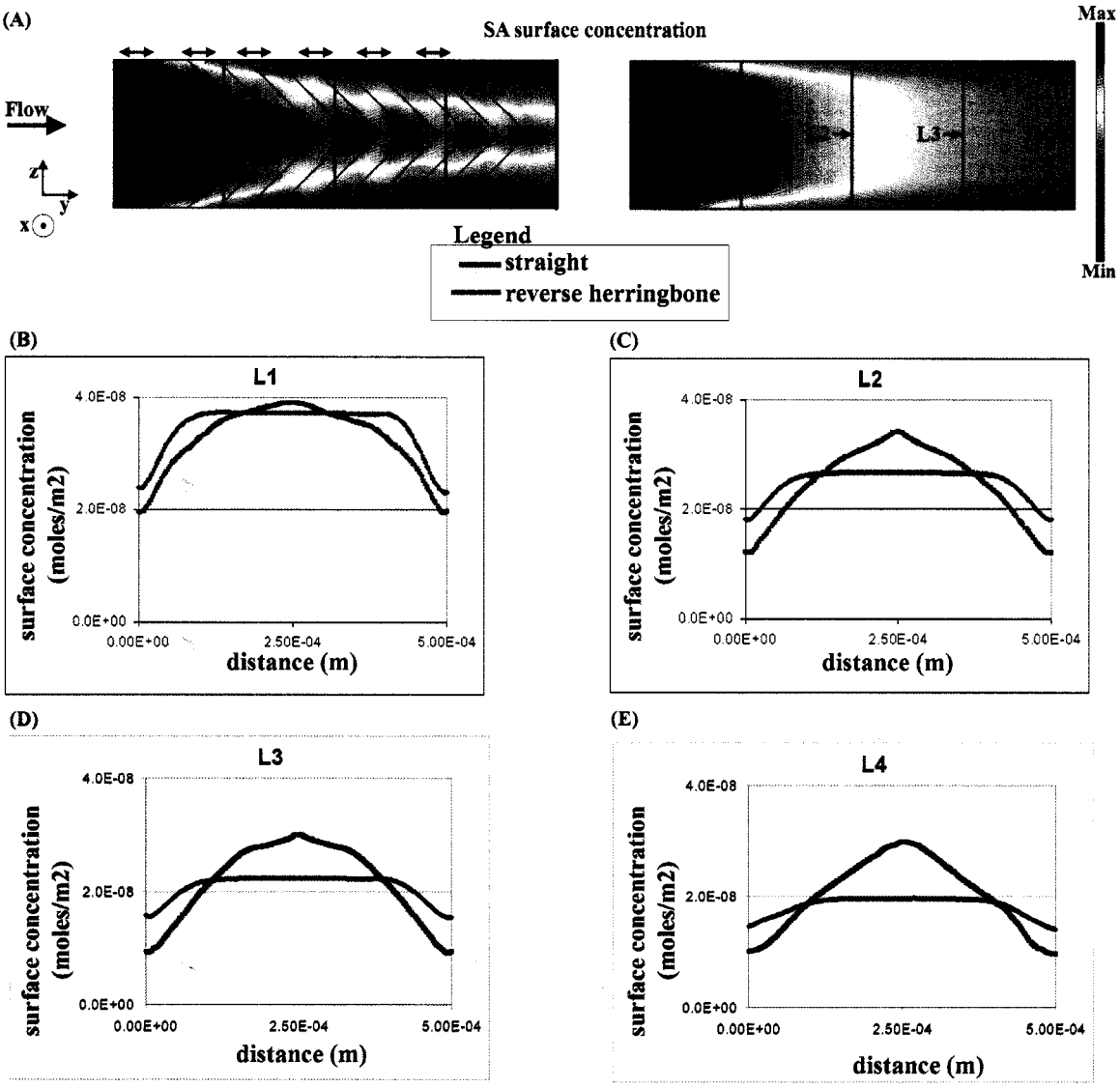

Figure 121. Comparison of the SA surface binding profile for a reverse chevron microchannel and a straight microchannel in the z-dimension. Model results. (A) Surface concentration profiles of bound streptavidin (moles/m^2). The maximum SA surface binding concentration was 3.99 $\times 10^{-8}$ moles/m^2. The minimum SA surface binding concentration was 0 moles/m^2. (B)-(E) Line profiles comparing the SA surface concentration profile. The locations of the line profiles are indicated in (A). The specific coordinates of the line profiles are L1(y=0.375 mm; z[0 to 500 microns]), L2(y=0.75 mm; z[0 to 500 microns]), L3(y=1.125 mm; z[0 to 500 microns]), and L4(y=1.5 mm; z[0 to 500 microns]). Streptavidin inlet concentration = 20 nM = 2×10^{-5} moles/m^3. Time = 700 seconds. Re= 0.01. Pe=135.1. Q=5 nL/s. The arrows indicate the deepest portion of the channel where the chevron structure was present. The theoretical maximum SA surface binding concentration was 3.99 $\times 10^{-8}$ moles/m^2.

The line profiles transverse to flow of the streptavidin surface concentration (Figure 121) indicate that at the centerline of the channel (z=250 microns), more streptavidin was bound in the reverse chevron microchannel. Along L1, the straight microchannel bound more streptavidin whereas along L4, the reverse chevron microchannel bound more streptavidin. The line profiles suggest that as the solution travels downstream (y-dimension), more streptavidin bound to the reverse chevron surface. However, as mentioned in the discussion of the forward chevron microchannel, there were locations of increased and reduced binding arising from the chevron microstructure; depending where the line profile was located, it could over- or underestimate the average amount of protein binding in that area.

Line profiles of the SPR difference images (Figure 122) corroborate the model findings. Transverse to flow (L1 and L2), there was an increase in streptavidin binding at the midline of the channel (z=250 microns). Eventually, the surface became saturated with the protein (time=30 minutes), and no binding features were visible. The experimental streptavidin binding profile, like the model results, was parabolic in nature. The peak in the binding profile in the SPR images did not occur exactly at midline of the channel (z= 250 microns) due to the misalignment of the chevron features. The downstream binding profile (L1) does not corroborate the increase and decrease in the binding profile illustrated in the model results. This was expected given the SPR instrument's focus, image foreshortening, and SPR propagation length issues. The fact that at the 10 minute time point very little streptavidin bound to the surface was due to the large dead volume upstream of the binding surface. Therefore, the solution which had passed the surface by the 10 minute time point was predominantly buffer without streptavidin.

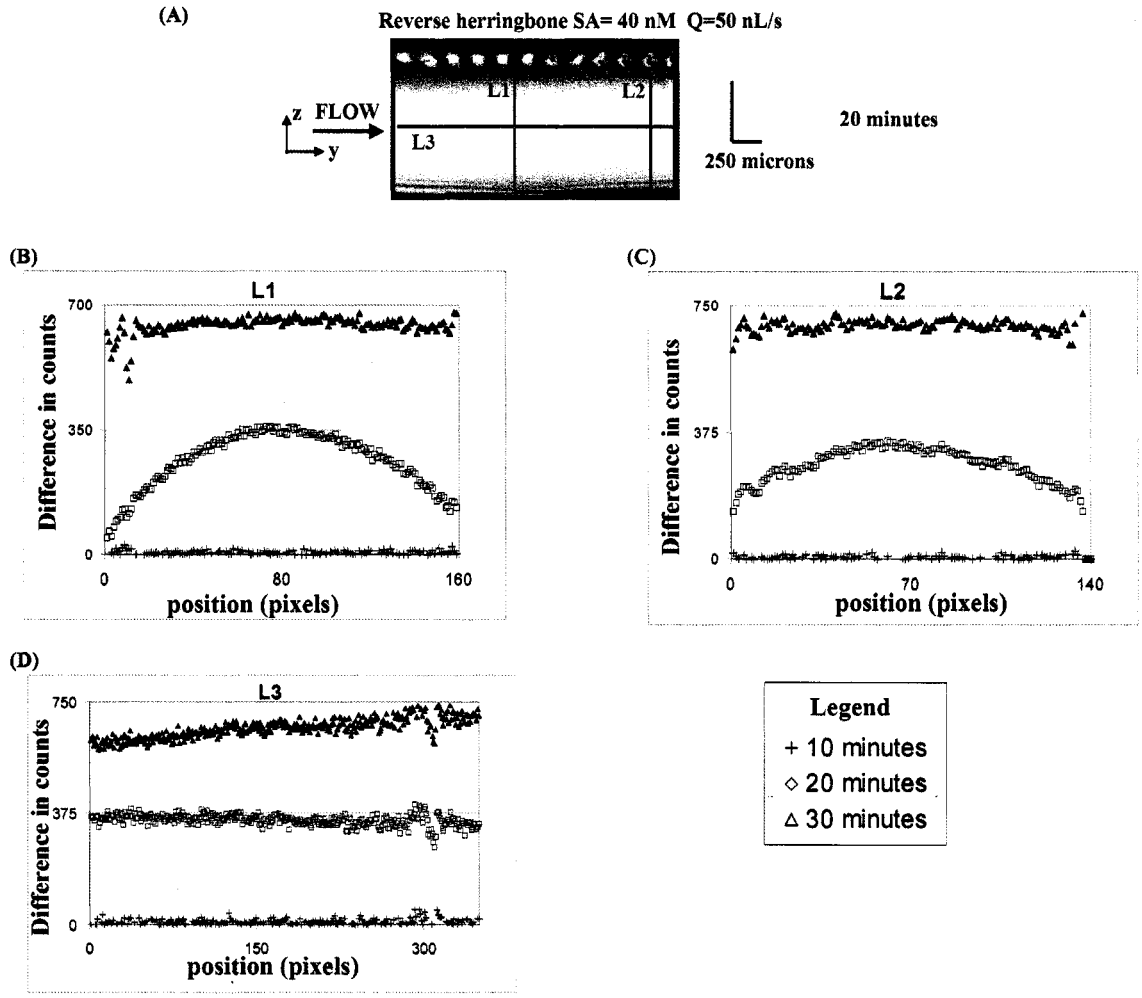

Figure 122. Difference line profiles of the surface concentration profile of bound streptavidin in a reverse chevron microchannel. Experimental results. (A) SPRM difference image subtracted from the initial image. The image has been contrast enhanced for viewing purposes to illustrate the variation of surface concentration of streptavidin. (B) - (D) Line profiles of surface concentration of streptavidin over time. The location of the line profiles are indicated in (A). The line profiles were calculated from raw TM images. The line profile at time = 0 was subtracted from each line profile at the indicated time point. The line profile L3 is 5 pixels (~17 microns) in width, and L1 and L2 are 10 pixels (~70 microns) in width. The difference in pixel to distance ratio on the substrate in each dimension is due to image foreshortening in the y-dimension discussed in Appendix C. Streptavidin inlet concentration = 40 nM. Re= 0.11. Pe=1480. Q=50 nL/s.

Calculation of the total amount of streptavidin bound to the surface over time in the reverse chevron microchannel

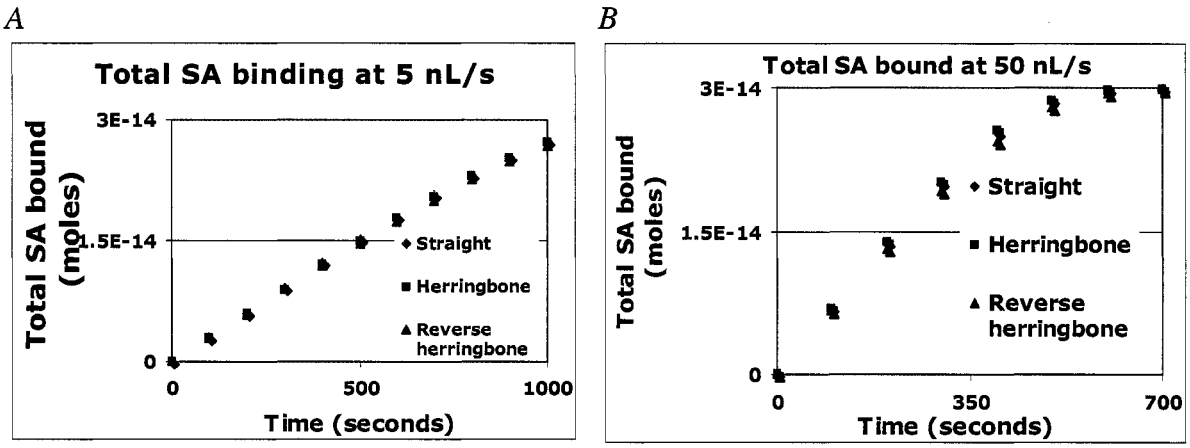

Figure 123. Total streptavidin bound to the surface for the reverse chevron microchannel versus a straight microchannel and a chevron microchannel. Model results. (A) 5 nL/s, Re=0.01, Pe=135.1 and (B) 50 nL/s, Re=0.1, Pe=1351. The streptavidin concentration introduced to the microchannel was 20 nM = 2×10^{-5} moles/m^3. The theoretical maximum for total SA binding to the surface was 3×10^{-14} moles.

A critical question in the analysis of the reverse chevron microchannel is whether more protein bound to the surface than in the forward chevron or straight microchannel (Figure 123). At two different flow rates, the model results suggested that there was no difference in the total binding of streptavidin. As elaborated in the previous section, this surprising result may have been the result of the larger volume in the reverse chevron or the size of the modeled microchannel.

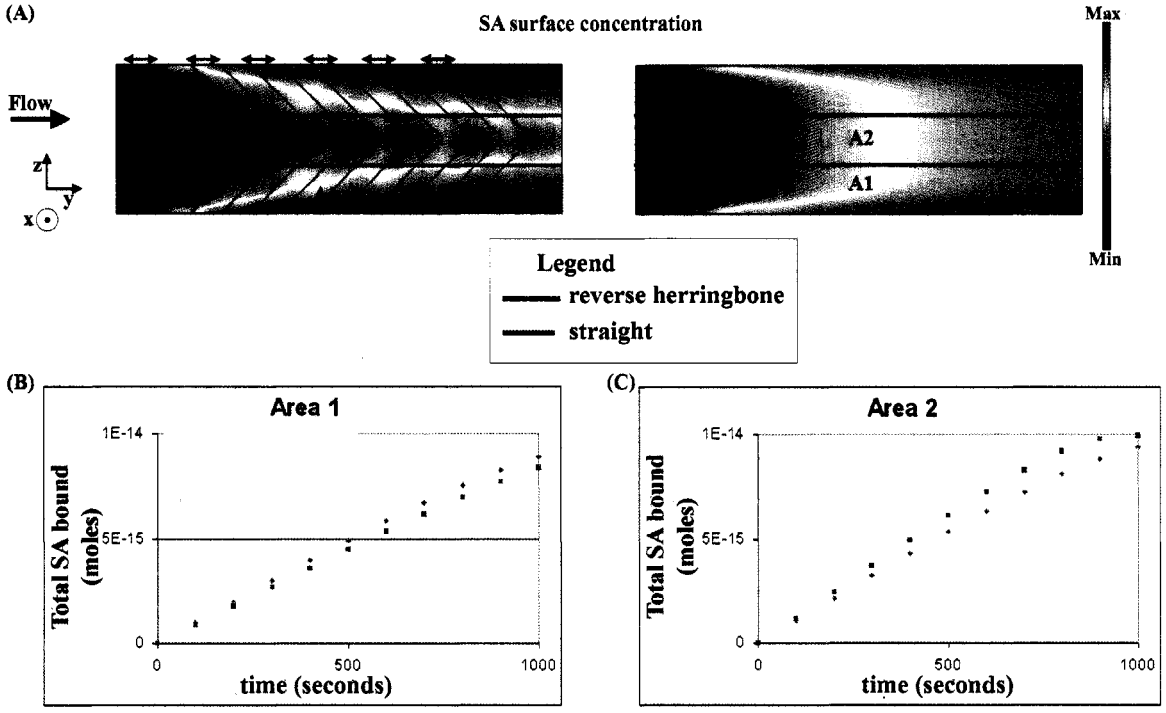

Figure 124. Total SA bound to the surface for several areas of interest for a reverse chevron microchannel versus a straight microchannel. Model results. (A) Surface concentration profiles of bound streptavidin (moles/m^2). The maximum SA surface binding concentration was 3.99 $\times 10^{-8}$ moles/m^2. The minimum SA surface binding concentration was 0 moles/m^2. (B)-(C) Total SA binding over time in areas 1-2 respectively for the reverse chevron microchannel and straight microchannel. The locations of the areas analyzed are indicated in (A). The specific coordinates of the areas are A1 (y[0 to 1.5 mm]; z[0 to 167 microns]) and A2 (y[0 to 1.5 mm; z[167 to 333 microns]). Streptavidin inlet concentration = 20 nM = 2×10^{-5} moles/m^3. Time = 700 seconds. Re= 0.01. Pe=135.1. Q=5 nL/s. The arrows indicate the deepest portion of the channel where the chevron structure was present. The theoretical maximum total amount of SA that can bind to the surface was 9.97 $\times 10^{-15}$ moles. The theoretical maximum SA surface binding concentration was 3.99 $\times 10^{-8}$ moles/m^2.

To explore the total amount of streptavidin bound in localized areas, the amount of streptavidin bound along the center of the reverse chevron microchannel and straight microchannel were compared. The results indicate that as expected, more streptavidin bound along the centerline (z= 250 microns) for the reverse chevron microchannel whereas near the side wall, less streptavidin bound in the reverse chevron microchannel (Figure 124).

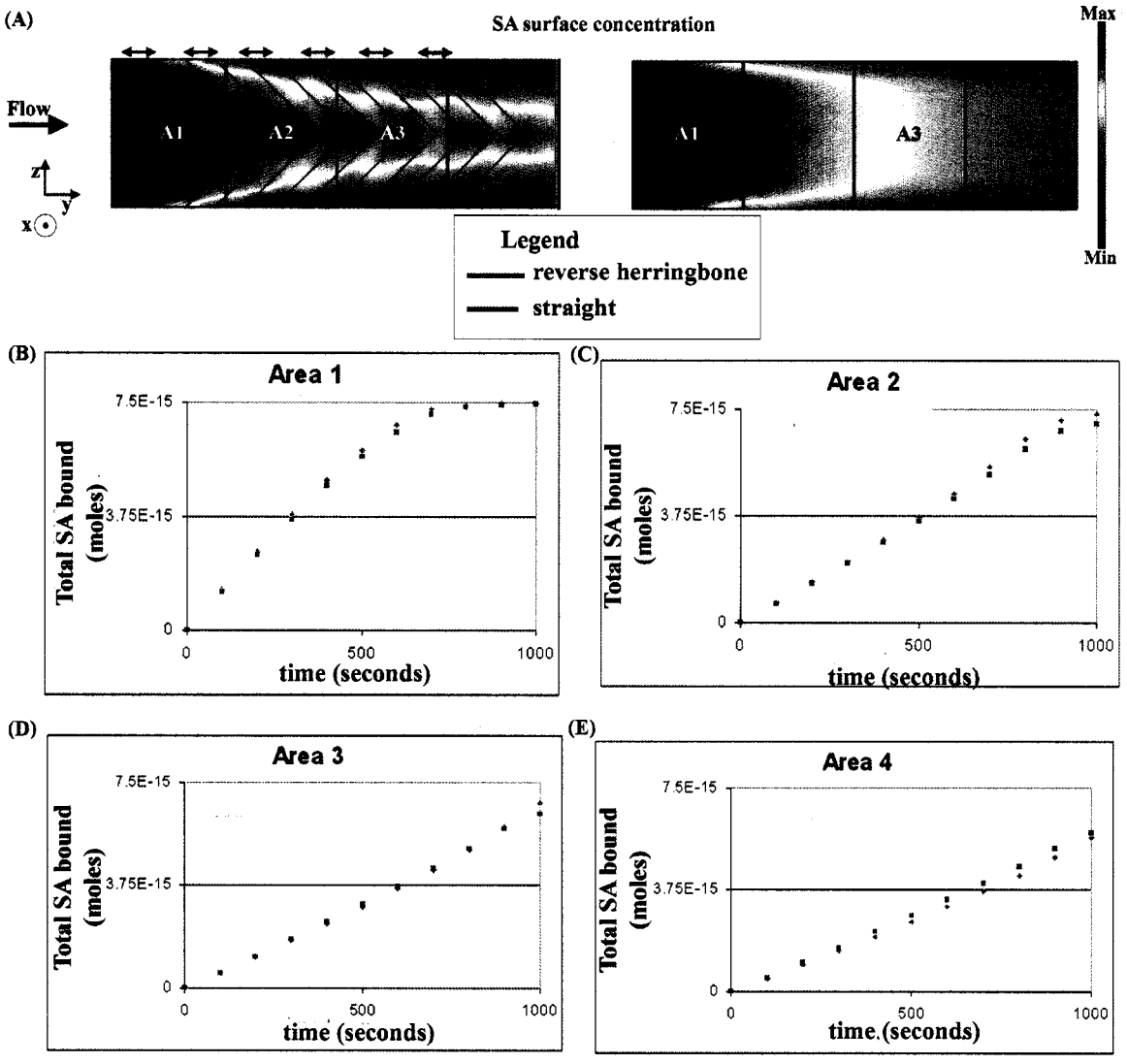

Figure 125. Total SA bound to the surface for several areas of interest for a reverse chevron microchannel versus a straight microchannel. Model results. (A) Surface concentration profiles of bound streptavidin (moles/m^2). The maximum SA surface binding concentration was 3.99 $\times 10^{-8}$ moles/m^2. The minimum SA surface binding concentration was 0 moles/m^2. (B)-(E) Total SA binding over time in areas 1-4 respectively for the reverse chevron microchannel and straight microchannel. The locations of the areas analyzed are indicated in (A). The specific coordinates of the areas are A1 (y[0 to 0.375 mm]; z[0 to 500 microns]), A2 (y[0 to 0.75 mm; z[0 to 500 microns]), A3 (y[0 to 1.125 mm]; z[0 to 500 microns]), and A4 (y[0 to 1.5 mm]; z[0 to 500 microns]). Streptavidin inlet concentration = 20 nM = 2×10^{-5} moles/m^3. Time = 700 seconds. Re= 0.01. Pe=135.1. Q=5 nL/s. The arrows indicate the deepest portion of the channel where the chevron structure was present. The theoretical maximum for the total amount of SA that can bind to the surface was 7.48×10^{-15} moles. The theoretical maximum SA surface binding concentration was 3.99 $\times 10^{-8}$ moles/m^2.

The amount of streptavidin binding to the surface was calculated as a function of distance downstream (Figure 125). The amount of streptavidin bound to the surface was very

similar for the straight microchannel and the reverse chevron in all areas. However, in area 1, there was a small increase in the binding rate for the straight microchannel. Further downstream (area 4), slightly more streptavidin bound in the chevron microchannel. This suggested that if a larger region was interrogated experimentally, the amount of bound streptavidin might have been significantly greater in the reverse chevron microchannel versus straight microchannel.

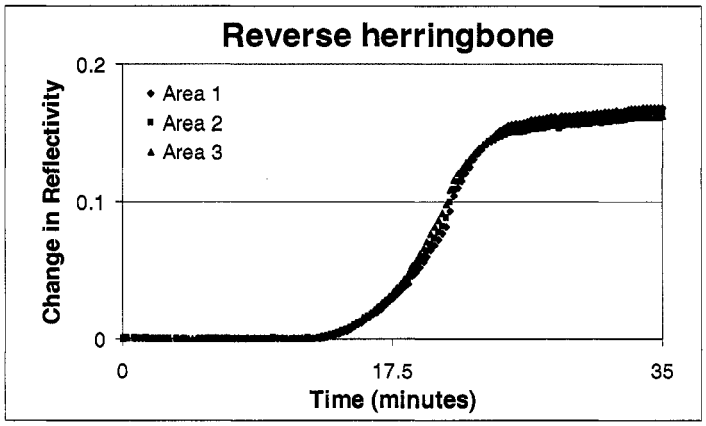

Figure 126. Change in reflectivity over time in three areas as a function of distance from the inlet for the reverse chevron microchannel. Experimental results – SPR imaging. Area 1 was closest to the inlet. Each area was 300 pixels in the y-dimension. Streptavidin inlet concentration = 40 nM. Re= 0.11. Pe=1480. Q=50 nL/s.

Just as for the straight and chevron microchannels, the average change in reflectivity over time was plotted as a function of time for three discrete areas downstream of the binding surface (Figure 126). The results for the reverse chevron (herringbone) microchannel indicated that the streptavidin binding profiles were extremely similar and showed little to no variation in streptavidin binding down the length of the channel. Compared with the straight and chevron microchannels (Figure 109 and Figure 110), in which there was a delay in the binding profiles for the areas further downstream, the reverse chevron data did not have this time delay, indicating the device geometry resulted in more efficient surface binding of streptavidin to the surface than either the straight or the chevron microchannel.

Please note that the volume of fluid upstream of the binding surface for the reverse chevron was 369 nL (9 mm distance from the inlet to the binding surface) versus 346 nL

(8.43 mm distance from the inlet to the binding surface) for the straight microchannel. Therefore, the influence of dispersion and time for binding was not significantly different, enabling a more accurate comparison of the chevron and the straight microchannels.

Bulk concentration profile of streptavidin in the reverse chevron microchannel

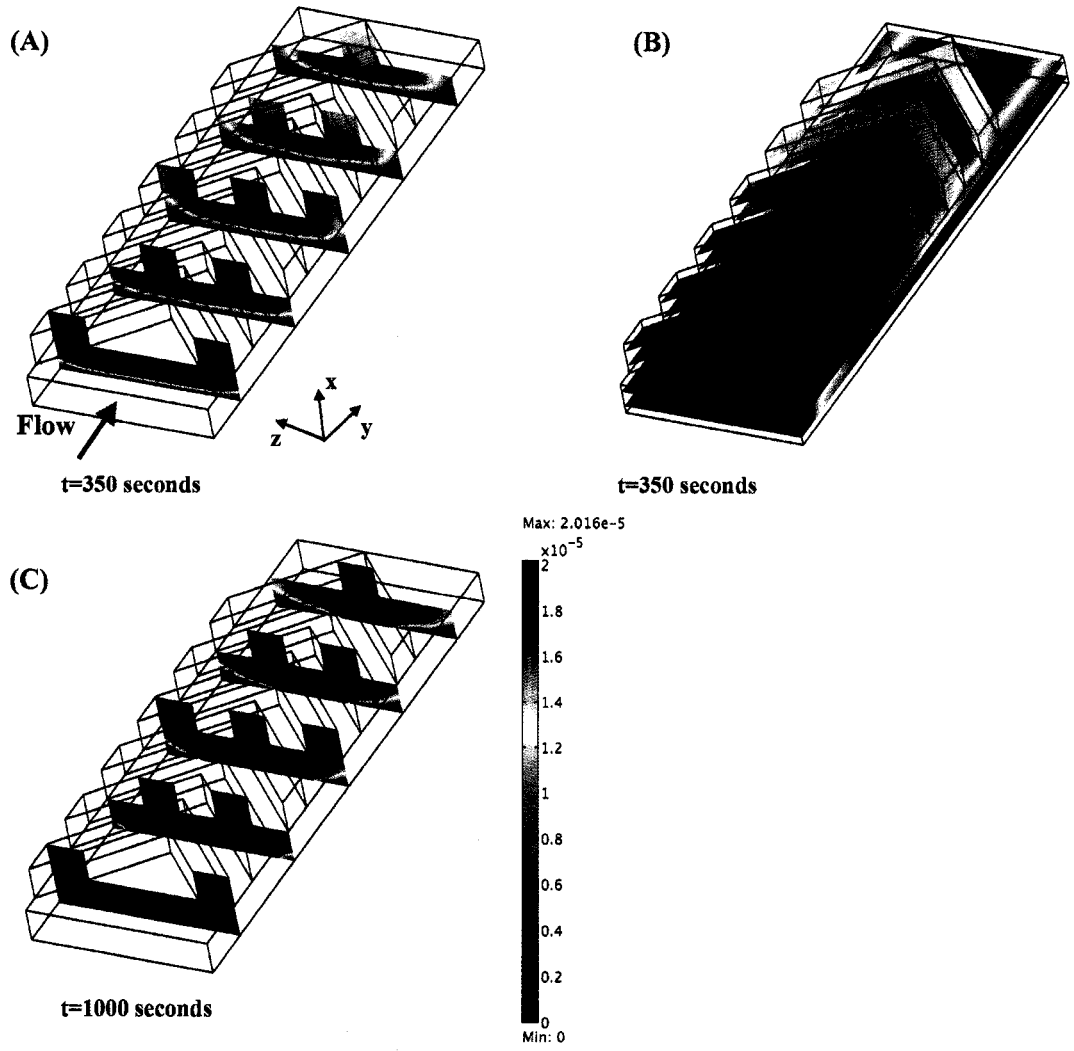

Figure 127. Concentration profile of streptavidin in the reverse chevron microchannel (moles/m^3). Model results. Streptavidin inlet concentration = 20 nM = 2×10^{-5} moles/m^3. Re= 0.01. Pe=135.1. Q=5 nL/s.

The bulk concentration for streptavidin (Figure 127) reflects the interconnection between the fluid mechanics in the reverse chevron microchannel and the surface binding reaction.

In the reverse chevron microchannel, the solution was swept from the midline of the microchannel (z=250 microns) across the binding surface giving rise to a deeper depletion zone at the sidewalls than observed for the forward chevron microchannel (Figure 101). The solution was then passed up into and across the chevron microstructure and towards the surface at the center of the microchannel (z=250 microns). The presence of a reduced concentration in the reverse chevron microchannel within the chevron microstructures and at the centerline is evidence of the rotation of the fluid. Over time (Figure 127 time=1000 seconds), the surface became saturated and the depletion zone was reduced in size.

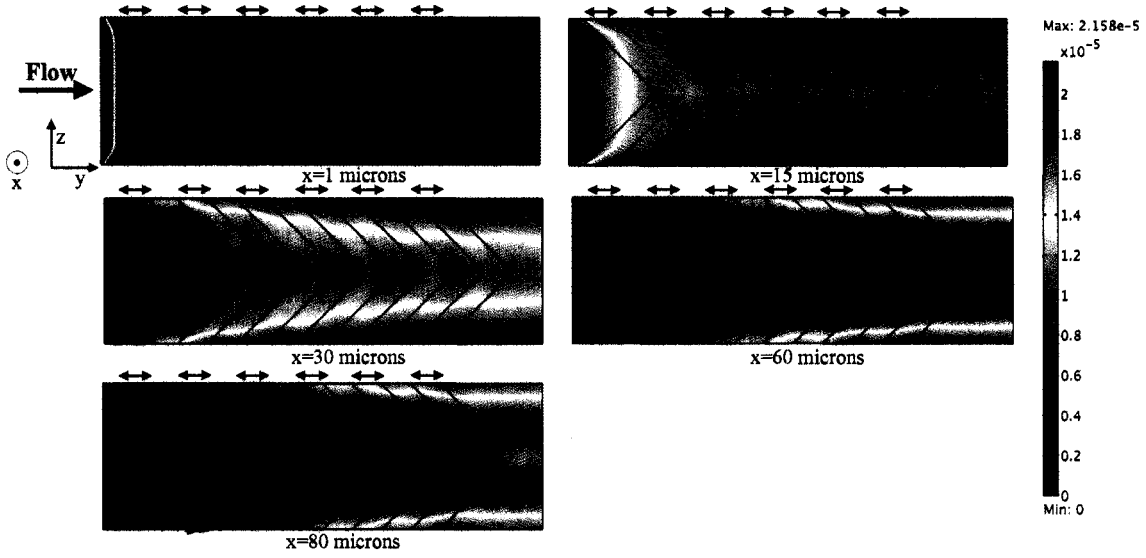

Figure 128. Concentration profile of streptavidin in the channel (moles/m^3) as a function of distance from the binding surface (x-dimension) in the reverse chevron microchannel. Model results. Streptavidin inlet concentration = 20 nM = 2×10^{-5} moles/m^3. Time=350 seconds. Re=0.01. Pe=135.1. Q=5 nL/s. The arrows indicate the deepest portion of the channel where the chevron structure was present.

The concentration profile of streptavidin within the microchannel (Figure 128) as a function of channel depth (x-dimension) was similar to that for the straight and forward chevron microchannels in that it reflects the binding profile of streptavidin. The highest streptavidin concentrations were located at the center of the microchannel (z=250 microns) and again in the narrow locations of the channel (where the black arrows are not located). An interesting feature near the outlet of the channel was that at x=60 microns and x=80 microns from the surface, the concentration of streptavidin was reduced at the

midline of the channel (z=250 microns). This result suggests that at this point down the length of the microchannel, the solution had passed over the binding surface (hence depleting the solution of streptavidin) up the sidewalls, across the chevron, and toward the center of the microchannel.

Influence of increased flow rate on the reverse chevron microchannel

Like for the forward chevron microchannel and the straight microchannel, an increase in flow rate (Figure 129) (1) reduced the depletion depth in the microchannel and (2) increased the amount of protein bound to the surface. However, the general binding pattern remained unchanged (Figure 129B) with an increase in binding along the centerline (y-dimension).

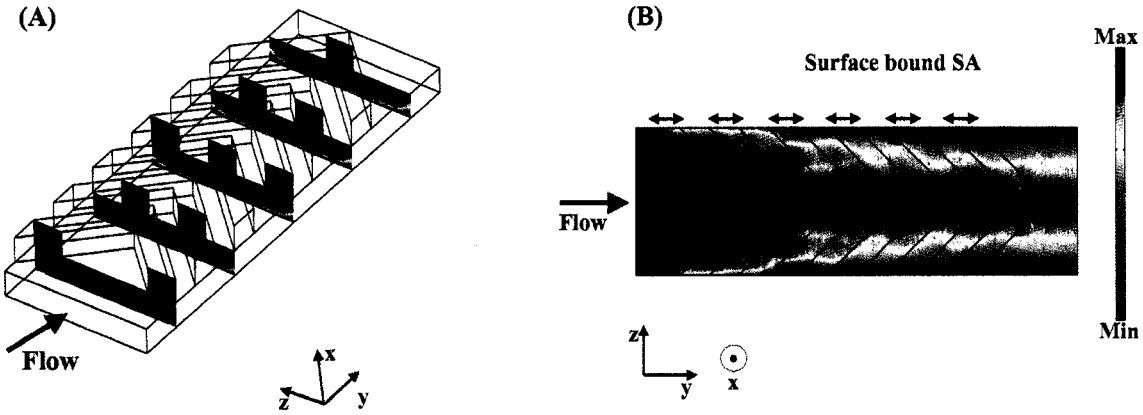

Figure 129. Influence of increased flow rate in the reverse chevron microchannel. Model results. (A) Concentration of streptavidin in the microchannel (moles/m^3). The maximum concentration was 2.02 $\times 10^{-5}$ moles/m^3. The minimum concentration was 0 moles/m^3. (B) Binding profile of streptavidin to the biotinylated surface (moles/m^2). The streptavidin concentration introduced to the microchannel was 20 nM. The maximum SA surface binding concentration was 3.99 $\times 10^{-8}$ moles/m^2. The minimum SA surface binding concentration was 0 moles/m^2. Time = 350 seconds. Re= 0.1. Pe=1351 Q=50nL/s. The arrows indicate the deepest portion of the channel where the chevron structure was present. The theoretical maximum SA surface binding concentration was 3.99 $\times 10^{-8}$ moles/m^2.

8.6 Conclusions

Forward and reverse chevron microchannels give rise to unique streptavidin surface binding profiles that reflect the fluid mechanics in the microchannel. The model results give a clear understanding of the velocity components in the chevron microchannel. In the forward chevron microchannel, there was an increase in the binding near the sidewalls compared to a similar location in a straight microchannel. On the other hand, in the reverse chevron, the pattern was the inversion of the forward chevron microchannel – an increase in streptavidin binding along the midline of the channel and a reduction in binding near the sidewalls. The SPR imaging experiments show strong agreement with model results. The concentration profiles of streptavidin within the bulk solution of the forward and reverse chevron microchannels (model results) also serve to illustrate that there were two spiraling flows down the length of the microchannel.

Comparison of model results for the total amount of streptavidin binding over time for the straight microchannel and forward chevron microchannel did not indicate that the chevron mixer significantly increased the amount of streptavidin binding. This surprising result may be a consequence of varied channel volume or the fact that the model microchannel was not large enough (a computational limitation). However, experimental evidence suggested that the amount of streptavidin bound at a given time point at locations further downstream (y-dimension) for the forward chevron microchannel would be higher than the amount of binding for the straight microchannel. Experiments also suggested similar results for the reverse chevron microchannel.

Conclusions

Microfluidic assays have several advantages over conventional assays, making this technology suitable for POC diagnostics. These advantages include a reduction in sample and reagent volumes, the potential to reduce the size of the instrumentation in order to develop portable diagnostic equipment, and the potential to use affordable and disposable polymeric devices. This dissertation focused on the design development of SPR-imaging microfluidic assays to quantify nanomolar concentrations of small molecules (cortisol and phenytoin) in saliva.

A critical component of an SPR-imaging assay is the immobilized capture molecule. One method of patterning a capture molecule onto a gold surface – microcontact printing – is extensively explored in Chapter 3 with SPR-imaging, XPS, and XPS-imaging. The microcontact printed protein was relatively homogenous across the patterned surface, had little to no non-specific binding, and retained enough of its structure to be recognized by an antibody. However, the binding of an antibody to the patterned protein was not uniform when compared to a traditional patterning method (physical adsorption). The data also indicate that protein and silicone oligomers transferred to the patterned surface.

Microcontact printing also generated well-defined protein patterns inside of microstructures by uniformly pressing a PDMS elastomer inked with a protein solution into the structure (Chapter 4). The protein patterned with this method retained enough of its structure to be recognized by an antibody, suggesting that this patterning method is feasible for a microfluidic flow assay.

Computational models of several microfluidic assay formats were developed to achieve a more thorough understanding of both the mass transport of the analyte within the microchannel and the binding profile of the analyte to the immobilized capture molecule. In Chapter 5, a standard microfluidic assay was modeled – streptavidin binding to biotin immobilized to a gold surface. The model indicated that immediately above the binding

surface, the solution was significantly depleted of streptavidin. This "depletion zone" influenced the binding profile of streptavidin to the surface by significantly reducing the amount of bound streptavidin downstream of the start of the binding surface. The model results showed qualitative agreement with experiments. In future, this model will serve as an efficient method to quickly explore a range of assay parameters (type of analyte, concentration of analyte, flow rate, and device geometry) and assess their influence on the performance of a microfluidic assay.

Computational models of two microfluidic flow immunoassays were developed – the indirect immunoassay (Chapter 6) and the concentration gradient immunoassay (Chapter 7). In Chapter 6, two methods of analysis, end point analysis and rate analysis, were explored as methods to quantify the concentration of a small molecule antigen in solution. In Chapter 7, the model gave insight into the concentration profile of the species within the microchannel. The model showed strong qualitative agreement with experimental results and yielded insight into one method of quantifying the concentration of a small molecule analyte. In future, this model will be used as a rapid method to explore other CIGA assay formats.

A herringbone microchannel was incorporated in a microfluidic flow assay to assess its influence on the performance of an assay (Chapter 8). The model results indicated that the chevron microchannel geometry substantially altered the surface binding profile of streptavidin. These results showed strong qualitative agreement with experimental results. The model indicated that the herringbone microchannel did not increase the rate of binding of streptavidin to the surface. However, experimental results for the herringbone microchannel operated in forward and reverse mode indicated that for microchannel distances greater than the modeled microchannel geometry there was a modest increase in the rate of binding.

References

(1) Shumaker-Parry, J. S.; Aebersold, R.; Campbell, C. T. *Analytical Chemistry* **2004**, *76*, 2071-2082.

(2) Jung, L. S.; Campbell, C. T.; Chinowsky, T. M.; Mar, M. N.; Yee, S. S. *Langmuir* **1998**, *14*, 5636-5648.

(3) Nelson, B. P.; Grimsrud, T. E.; Liles, M. R.; Goodman, R. M.; Corn, R. M. *Analytical Chemistry* **2001**, *73*, 1-7.

(4) Kanda, V.; Kariuki, J. K.; Harrison, D. J.; McDermott, M. T. *Analytical Chemistry* **2004**, *76*, 7257-7262.

(5) Piscevic, D.; Lawall, R.; Veith, M.; Liley, M.; Okahata, Y.; Knoll, W. *Applied Surface Science* **1995**, *90*, 425-436.

(6) Gobi, K. V.; Tanaka, H.; Shoyama, Y.; Miura, N. *Biosensors and Bioelectroics* **2004**, *20*, 350-357.

(7) Jung, L. S.; Shumaker-Parry, J. S.; Campbell, C. T.; Yee, S. S.; Gelb, M. H. *Journal of the American Chemical Society* **2000**, *122*, 4177-4184.

(8) Yu, F.; Persson, B.; Lofas, S.; Knoll, W. *Analytical Chemistry* **2004**, *76*, 6765-6770.

(9) Vareiro, M. L. M.; Liu, J.; Knoll, W.; Zak, K.; Williams, D.; Jenkins, A. T. A. *Anaytical Chemistry* **2005**, *77*, 2426-2431.

(10) Fang, S.; Lee, H. J.; Wark, A. W.; Kim, H. M.; Corn, R. M. *Analytical Chemistry* **2005**, *77*, 6528-6534.

(11) Battaglia, T. M.; Masson, J.-F.; Sierks, M. R.; Beaudoin, S. P.; Rogers, J.; Foster, K. N.; Holloway, G. A.; Booksh, K. S. *Analytical Chemistry* **2005**, *77*, 7016-7023.

(12) Fu, E.; Chinowsky, T.; Foley, J.; Weinstein, J.; Yager, P. *Review of Scientific Instruments* **2004**, *75*, 2300-2304.

(13) Fu, E.; Foley, J.; Yager, P. *Review of Scientific Instruments* **2003**, *74*, 3182-3184.

(14) Davies, J. *Surface Analytical Techniques for Probing Biomaterial Processes*, 1st ed.; CRC Press: Boca Raton, FL, 1996.

(15) Nelson, K., Foley, J., and P. Yager. *Analytical Chemistry* **in press.**

(16) Stroock, A. D.; Dertinger, S. K. W.; Ajdari, A.; Mezic, I.; Stone, H. A.; Whitesides, G. M. *Science* **2002**, *295*, 647-651.

(17) Jeon, N. L.; Baskaran, H.; Dertinger, S. K. W.; Whitesides, G. M.; Van de Water, L.; Toner, M. *Nature Biotechnology* **2002**, *20*, 826-830.

(18) Chen, C. S.; Jiang, X. Y.; Whitesides, G. M. *MRS Bulletin* **2005**, *30*, 194-201.

(19) Jiang, X. Y.; Bruzewicz, D. A.; Wong, A. P.; Piel, M.; Whitesides, G. M. *Proceedings of the National Academy of Sciences of the United States of America* **2005**, *102*, 975-978.

(20) Lee, J. N.; Jiang, X.; Ryan, D.; Whitesides, G. M. *Langmuir* **2004**, *20*, 11684-11691.

(21) Kane, R. S.; Takayama, S.; Ostuni, E.; Ingber, D. E.; Whitesides, G. M. *Biomaterials* **1999**, *20*, 2363-2376.

(22) Bernard, A.; Michel, B.; Delamarche, E. *Analytical Chemistry* **2001**, *73*, 8-12.

(23) Sapsford, K. E.; Shubin, Y. S.; Delehanty, J. B.; Golden, J. P.; Taitt, C. R.; Shriver-Lake, L. C.; Ligler, F. S. *Journal of Applied Microbiology* **2004**, *96*, 47-58.

(24) Delehanty, J. B.; Ligler, F. S. *Analytical Chemistry* **2002**, *74*, 5681-5687.

(25) Taitt, C. R.; Golden, J. P.; Shubin, Y. S.; Shriver-Lake, L. C.; Sapsford, K. E.; Rasooly, A.; Ligler, F. S. *Microbial Ecology* **2004**, *47*, 175-185.

(26) Whelan, J. P.; Kusterbeck, A. W.; Wemhoff, G. A.; Bredehorst, R.; Ligler, F. S. *Analytical Chemistry* **1993**, *65*, 3561-3565.

(27) Juncker, D.; Michel, B.; Hunziker, P.; Delamarche, E. *Biosensors and Bioelectronics* **2004**, *19*, 1193-1202.

(28) Khan, S. A.; Gunther, A.; Schmidt, M. A.; Jensen, K. F. *Langmuir* **2004**, *20*, 8604-8611.

(29) Gunther, A.; Khan, S. A.; Thalmann, M.; Trachsel, F.; Jensen, K. F. *Lab on a Chip* **2004**, *4*, 278-286.

(30) Stone, H. A.; Kim, S. *AIChE Journal* **2001**, *47*, 1250-1254.

(31) Figeys, D.; Pinto, D. *Analytical Chemistry* **2000**, *72*, 330A-335A.

(32) USDiagnostics, http://www.usdiagnostics.net/index.php, accessed November 5th, **2005**.

(33) Glick, B. R.; Pasternak, J.J. *Molecular Biotechnology: Principles and Applications or Recombinant DNA*, 2nd ed.; ASM Press: Washington, D.C., 1998.

(34) Castellion, M. *Fundamentals of General, Organic, and Biological Chemistry*; Prentice Hall: New York, NY, 2002.

(35) Engvall, E.; Perlmann, P. *Immunochemistry* **1971**, *8*, 871-&.

(36) Hennion, M. C.; Barcelo, D. *Analytica Chimica Acta* **1998**, *362*, 3-34.

(37) Weber, P. C.; Wendoloski, J. J.; Pantoliano, M. W.; Salemme, F. R. *Journal of the American Chemical Society* **1992**, *114*, 3197.

(38) Green, N. M. *Methods in Enzymology* **1990**, *184*, 51-67.

(39) Wilchek, M.; Bayer, E. A. *Methods in Enzymology* **1990**, *184*, 5-13.

(40) Kulkarni, S.; Schilli, C.; Grin, B.; Muller, A. H. E.; Hoffman, A. S.; Stayton, P. S. *Biomacromolecules* **2006**, *7*, 2736-2741.

(41) Hamblett, K. J.; Press, O. W.; Meyer, D. L.; Hamlin, D. K.; Axworthy, D.; Wilbur, D. S.; Stayton, P. S. *Bioconjugate Chemistry* **2005**, *16*, 131-138.

(42) Malmstadt, N.; Hoffman, A. S.; Stayton, P. S. *Lab on a Chip* **2004**, *4*, 412-415.

(43) Olsvik, O.; Popovic, T.; Skjerve, E.; Cudjoe, K. S.; Hornes, E.; Ugelstad, J.; Uhlen, M. *Clinical Microbiology Reviews* **1994**, *7*, 43-54.

(44) Freitag, S.; LeTrong, I.; Klumb, L.; Stayton, P.S.; Stenkamp, R.E. *Protein Science* **2006**, *6*, 1157-1166.

(45) Kusterbeck, A. W.; Wemhoff, G. A.; Charles, P. T.; Yeager, D. A.; Bredehorst, R.; Vogel, C. W.; Ligler, F. S. *Journal of Immunological Methods* **1990**, *135*, 191-197.

(46) Rabbany, S. Y.; Kusterbeck, A. W.; Bredehorst, R.; Ligler, F. S. *Sensors and Actuators B-Chemical* **1995**, *29*, 72-78.

(47) Weigl, B. H.; Yager, P. *Science* **1999**, *283*, 346-347.

(48) Kamholz, A. E.; Yager, P. *Biophysical Journal* **2001**, *80*, 155-160.

(49) Kamholz, A. E.; Weigl, B. H.; Finlayson, B. A.; Yager, P. *Analytical Chemistry* **1999**, *71*, 5340-5347.

(50) Weigl, B.; Yager, P.; Brody; J. ; Holl, M.; Forster, F.; Altendorf, E.; Galambos; P.; Kenny, M.; Schutte, D.; Hixson, G.; Zebert, D.; Kamholz, A.; Wu, C. *Microfabricated devices and methods* **2002**, *U.S. Patent # 6,454,945.*

(51) Weigl, B; Yager, P.; Kamholz, A; Hatch, A.*Microscale diffusion immunoassay* **2000**, *U.S. Patent #574797.*

(52) Bird, R. B.; Stewart, W.E.; Lightfoot, E.N. *Transport Phenomena*, 2nd ed.; Wiley Publishing: New York, NY, 2002.

(53) Deen, W. M. *Analysis of Transport Phenomena*; Oxford University Press: New York, NY, 2002.

(54) Hatch, A.; Kamholz, A. E.; Hawkins, K. R.; Munson, M. S.; Schilling, E. A.; Weigl, B. H.; Yager, P. *Nature Biotechnology* **2001**, *19*, 461-465.

(55) Nelson, K.; Foley, J.; Mashadi-Hossein, A.; Yager, P. *Simultaneous, multiple analyte immunoassays on a disposable microfluidic device* Microtas conference presentation. Boston, MA **2005**.

(56) Kim, D. S.; Lee, S. H.; Kwon, T. H.; Ahn, C. H. *Lab on a Chip* **2005**, *5*, 739-747.

(57) Neils, C.; Tyree, Z.; Finlayson, B.; Folch, A. *Lab on a Chip* **2004**, *4*, 342-350.

(58) Spearing, S. M. *Acta Materialia* **2000**, *48*, 179-196.

(59) Kawata, S.; Sun, H. B.; Tanaka, T.; Takada, K. *Nature* **2001**, *412*, 697-698.

(60) McDonald, J. C.; Duffy, D. C.; Anderson, J. R.; Chiu, D. T.; Wu, H. K.; Schueller, O. J. A.; Whitesides, G. M. *Electrophoresis* **2000**, *21*, 27-40.

(61) Raiteri, R.; Grattarola, M.; Butt, H. J.; Skladal, P. *Sensors and Actuators B-Chemical* **2001**, *79*, 115-126.

(62) Liang, Z. H.; Chiem, N.; Ocvirk, G.; Tang, T.; Fluri, K.; Harrison, D. J. *Analytical Chemistry* **1996**, *68*, 1040-1046.

(63) Madou, M. *Fundamentals of Microfabrication*, 2nd ed.; CRC press: Boca Raton, FL, 2002.

(64) Xia, Y.; Whitesides, G.M. *Angew. Chem. Int. Ed* **1998**, *37*, 550-575.

(65) Campbell, D. J.; Beckman, K.J.; Calderon, C.E.; Doolan, P.W.,; Moore, R.H.; Ellis, A.B.; Lisensky, G.C. *J. Chem. Educ.* **1999**, *76*, 537.

(66) Becker, H.; Locascio, L. E. *Talanta* **2002**, *56*, 267-287.

(67) Becker, H.; Gartner, C. *Electrophoresis* **2000**, *21*, 12-26.

(68) Finlayson, B. *Nonlinear Analysis in Chemical Engineering*; Ravenna Park Publishing: Seattle, WA, 2003.

(69) Knoll, W. *Annual Review of Physical Chemistry* **1998**, *49*, 569-638.

(70) Rothenhausler, B.; Knoll, W. *Nature* **1988**, *332*, 615-617.

(71) Ekgasit, S.; Thammacharoen, C.; Knoll, W. *Analytical Chemistry* **2004**, *76*, 561-568.

(72) Biacore, *http://www.biacore.com*, accessed June **2002**.

(73) Smith, E. A.; Thomas, W. D.; Kiessling, L. L.; Corn, R. M. *Journal of the American Chemical Society* **2003**, *125*, 6140-6148.

(74) Smith, E. A.; Erickson, M. G.; Ulijasz, A. T.; Weisblum, B.; Corn, R. M. *Langmuir* **2003**, *19*, 1486-1492.

(75) Shumaker-Parry, J. S.; Campbell, C. T. *Analytical Chemistry* **2004**, *76*, 907-917.

(76) Nelson, B. P.; Frutos, A. G.; Brockman, J. M.; Corn, R. M. *Analytical Chemistry* **1999**, *71*, 3928-3934.

(77) Ulman, A. *Chemical Reviews* **1996**, *96*, 1533-1554.

(78) Whitesides, G. M.; Grzybowski, B. *Science* **2002**, *295*, 2418-2421.

(79) Schwatrz, D. *Annual Review of Physical Chemistry* **2001**, *52*, 107-137.

(80) Bilic, A.; Reimers, J. R.; Hush, N. S. *Journal of Chemical Physics* **2005**, *122*.

(81) Ford, M. J.; Hoft, R. C.; Gale, J. D. *Molecular Simulation* **2006**, *32*, 1219-1225.

(82) Rousseau, R.; De Renzi, V.; Mazzarello, R.; Marchetto, D.; Biagi, R.; Scandolo, S.; del Pennino, U. *Journal of Physical Chemistry B* **2006**, *110*, 10862-10872.

(83) Bain, C. D.; Whitesides, G. M. *Science* **1988**, *240*, 62-63.

(84) Bain, C. D.; Biebuyck, H. A.; Whitesides, G. M. *Langmuir* **1989**, *5*, 723-727.

(85) Prime, K. L.; Whitesides, G. M. *Journal of the American Chemical Society* **1993**, *115*, 10714-10721.

(86) Prime, K. L.; Whitesides, G. M. *Science* **1991**, *252*, 1164-1167.

(87) Folkers, J. P.; Laibinis, P. E.; Whitesides, G. M. *Langmuir* **1992**, *8*, 1330-1341.

(88) Jung, L. S.; Nelson, K. E.; Stayton, P. S.; Campbell, C. T. *Langmuir* **2000**, *16*, 9421-9432.

(89) Haussling, L.; Ringsdorf, H.; Schmitt, F. J.; Knoll, W. *Langmuir* **1991**, *7*, 1837-1840.

(90) Anselmetti, D.; Baratoff, A.; Guntherodt, H. J.; Delamarche, E.; Michel, B.; Gerber, C.; Kang, H.; Wolf, H.; Ringsdorf, H. *Europhysics Letters* **1994**, *27*, 365-370.

(91) Delamarche, E.; Michel, B. *Thin Solid Films* **1996**, *273*, 54-60.

(92) Tsao, M. W.; Hoffmann, C. L.; Rabolt, J. F.; Johnson, H. E.; Castner, D. G.; Erdelen, C.; Ringsdorf, H. *Langmuir* **1997**, *13*, 4317-4322.

(93) Wolf, H.; Ringsdorf, H.; Delamarche, E.; Takami, T.; Kang, H.; Michel, B.; Gerber, C.; Jaschke, M.; Butt, H. J.; Bamberg, E. *Journal of Physical Chemistry* **1995**, *99*, 7102-7107.

(94) Zheng, J.; Li, L. Y.; Chen, S. F.; Jiang, S. Y. *Langmuir* **2004**, *20*, 8931-8938.

(95) Xia, N.; Hu, Y. H.; Grainger, D. W.; Castner, D. G. *Langmuir* **2002**, *18*, 3255-3262.

(96) Chapman, R. G.; Ostuni, E.; Takayama, S.; Holmlin, R. E.; Yan, L.; Whitesides, G. M. *Journal of the American Chemical Society* **2000**, *122*, 8303-8304.

(97) Harder, P.; Grunze, M.; Dahint, R.; Whitesides, G. M.; Laibinis, P. E. *Journal of Physical Chemistry B* **1998**, *102*, 426-436.

(98) Herrwerth, S.; Eck, W.; Reinhardt, S.; Grunze, M. *Journal of the American Chemical Society* **2003**, *125*, 9359-9366.

(99) Ostuni, E.; Chapman, R. G.; Liang, M. N.; Meluleni, G.; Pier, G.; Ingber, D. E.; Whitesides, G. M. *Langmuir* **2001**, *17*, 6336-6343.

(100) Wang, R. Y.; Himmelhaus, M.; Fick, J.; Herrwerth, S.; Eck, W.; Grunze, M. *Journal of Chemical Physics* **2005**, *122*.

(101) Nelson, K. E.; Gamble, L.; Jung, L. S.; Boeckl, M. S.; Naeemi, E.; Golledge, S. L.; Sasaki, T.; Castner, D. G.; Campbell, C. T.; Stayton, P. S. *Langmuir* **2001**, *17*, 2807-2816.

(102) Delamarche, E.; Bernard, A.; Schmid, H.; Bietsch, A.; Michel, B.; Biebuyck, H. *Journal of the American Chemical Society* **1998**, *120*, 500-508.

(103) Delamarche, E.; Bernard, A.; Schmid, H.; Michel, B.; Biebuyck, H. *Science* **1997**, *276*, 779-781.

(104) Hermanson, G. *Bioconjugate Techniques*; Academic Press: Burlington, MA, 1996.

(105) Delamarche, E.; Sundarababu, G.; Biebuyck, H.; Michel, B.; Gerber, C.; Sigrist, H.; Wolf, H.; Ringsdorf, H.; Xanthopoulos, N.; Mathieu, H. J. *Langmuir* **1996**, *12*, 1997-2006.

(106) Ryan, D.; Parviz, B. A.; Linder, V.; Semetey, V.; Sia, S. K.; Su, J.; Mrksich, M.; Whitesides, G. M. *Langmuir* **2004**, *20*, 9080-9088.

(107) Hong, S. H.; Zhu, J.; Mirkin, C. A. *Science* **1999**, *286*, 523-525.

(108) Lee, K. B.; Park, S. J.; Mirkin, C. A.; Smith, J. C.; Mrksich, M. *Science* **2002**, *295*, 1702-1705.

(109) Piner, R. D.; Zhu, J.; Xu, F.; Hong, S. H.; Mirkin, C. A. *Science* **1999**, *283*, 661-663.

(110) Pardo, L.; Wilson, W. C.; Boland, T. J. *Langmuir* **2003**, *19*, 1462-1466.

(111) Wilson, W. C.; Boland, T. *Anatomical Record Part a-Discoveries in Molecular Cellular and Evolutionary Biology* **2003**, *272A*, 491-496.

(112) Kumar, A.; Biebuyck, H. A.; Whitesides, G. M. *Langmuir* **1994**, *10*, 1498-1511.

(113) Bernard, A.; Renault, J. P.; Michel, B.; Bosshard, H. R.; Delamarche, E. *Advanced Materials* **2000**, *12*, 1067-1070.

(114) Workman, R. K.; Manne, S. *Langmuir* **2005**, *20*, 805-815.

(115) Foley, J.; Schmid, H.; Stutz, R.; Delamarche, E. *Engineering microfluidic chips with integrated binding sites for ultraminiaturized immunoassays* Microtas conference proceedings, Boston, MA 2005.

(116) Renaultt, J. P.; Bernard, A.; Bietsch, A.; Michel, B.; Bosshard, H. R.; Delamarche, E.; Kreiter, M.; Hecht, B.; Wild, U. P. *Journal of Physical Chemistry B* **2003**, *107*, 703-711.

(117) Mrksich, M.; Whitesides, G. M. *Trends in Biotechnology* **1995**, *13*, 228-235.

(118) Graber, D. J.; Zieziulewicz, T. J.; Lawrence, D. A.; Shain, W.; Turner, J. N. *Langmuir* **2003**, *19*, 5431-5434.

(119) Bernard, A.; Renault, J.; Michel, B.; Bosshard, R.; Delamarche, E. *Advanced Materials* **2000**, *12*, 1067-1070.

(120) Graham, D.; Ratner, B. B. *Langmuir* **2002**, *18*, 1518-1527..

(121) Glasmastar, K.; Gold, J.; Andersson, A. S.; Sutherland, D. S.; Kasemo, B. *Langmuir* **2003**, *19*, 5475-5483.

(122) Tan, J. L.; Tien, J.; Chen, C. S. *Langmuir* **2002**, *18*, 519-523.

(123) Ross, E. E.; Joubert, J. R.; Wysocki, R. J.; Nebesny, K.; Spratt, T.; O'Brien, D. F.; Saavedra, S. S. *Biomacromolecules* **2006**, *7*, 1393-1398.

(124) Langowski, B. A.; Uhrich, K. E. *Langmuir* **2005**, *21*, 6366-6372.

(125) Hale, P. S.; Kappen, P.; Prissanaroon, W.; Brack, N.; Pigram, P. J.; Liesegang, J. *Applied Surface Science* **2007**, *253*, 3746-3750.

(126) Sharpe, R. B. A.; Burdinski, D.; vanderMarel, C.; Jansen, J. A. J.; Huskens, J.; Zandvliet, H. J. W.; Reinhoudt, D. N.; Poelsema, B. *Langmuir* **2006**, *22*, 5945-5951.

(127) Graham, D. J.; Price, D. D.; Ratner, B. D. *Langmuir* **2002**, *18*, 1518-1527.

(128) Sharpe, R. B. A.; Burdinski, D.; van der Marel, C.; Jansen, J. A. J.; Huskens, J.; Zandvliet, H. J. W.; Reinhoudt, D. N.; Poelsema, B. *Langmuir* **2006**, *22*, 5945-5951.

(129) Vickerman, J. C., Ed. *Surface Analysis: the Principal Techniques*; John Wiley: New York, 1997.

(130) Gunther, S., Kaulich, B., Gregoratti, L., and M. Kiskinova *Progress in Surface Science* **2002**, *70*, 187-360.

(131) Inerowicz, H. D.; Howell, S.; Regnier, F. E.; Reifenberger, R. *Langmuir* **2002**, *18*, 5263-5268.

(132) Veiseh, M.; Wickes, B. T.; Castner, D. G.; Zhang, M. Q. *Biomaterials* **2004**, *25*, 3315-3324.

(133) Rozkiewicz, D.I.; Kraan, Y.; Werten, M.; de Wolf, F.; Subramaniam, V.; Ravoo, B.; Reinhoudt, D. *Chemistry - A European Journal* **2006**, *12*, 6290-6297.

(134) delaFuente, J. M.; Andar, A.; Gadegaard, N.; Berry, C. C.; Kingshott, P.; Riehle, M. O. *Langmuir* **2006**, *22*, 5528-5532.

(135) Vidic, J.; Pla-Roca, M.; Grosclaude, J.; Persuy, M.-A.; Monnerie, R.; Caballero, D.; Errachid, A.; Hou, Y.; Jaffrezic-Renault, N.; Salesse, R.; Pajot-Augy, E.; Samitier, J. *Analytical Chemistry* **2007**.

(136) Rozhok S. C.; Littler, P.L.; Fan, Z.; Liu, C.; Mirkin, C.A.; Holz, R.C. *Small* **2005**, *4*, 445-51.

(137) Wang, D.; Chiang, H.; Wo, A.; Huang, Y. *Journal of Biomedical Materials Research Part B: Applied Biomaterials* **2007**, *80B*, 447-453.

(138) Chen, C. S.; Mrksich, M.; Huang, S.; Whitesides, G. M.; Ingber, D. E. *Biotechnology. Progress* **1998**, *14*, 356-363.

(139) Na, K.; Jung, J.; Shin, B.; Hyun, J. *Langmuir* **2006**, *22*, 10889-10892.

(140) von Philipsborn, A.C.; L. S.; Bernard, A.; Loeschinger, J.; David, C.; Lehnert, D.; Bastmeyer, M.; Bonhoeffer, F. *Nature Protocols* **2006**, *1*, 1322-8.

(141) Brock, A.; Chang, E.; Ho, C. C.; LeDuc, P.; Jiang, X. Y.; Whitesides, G. M.; Ingber, D. E. *Langmuir* **2003**, *19*, 1611-1617.

(142) LaGraff, J. R.; Chu-LaGraff, Q. *Langmuir* **2006**, *22*, 4685-4693.

(143) Bessueille, F.; Pla-Roca, M.; Mills, C. A.; Martinez, E.; Samitier, J.; Errachid, A. *Langmuir* **2005**, *21*, 12060-12063.

(144) Mrksich, M.; Dike, L. E.; Tien, J.; Ingber, D. E.; Whitesides, G. M. *Experimental Cell Research* **1997**, *235*, 305-313.

(145) Larsen, N. B.; Biebuyck, H.; Delamarche, E.; Michel, B. *Journal of the American Chemical Society* **1997**, *119*, 3017-3026.

(146) Wilbur, J. L.; Kumar, A.; Biebuyck, H. A.; Kim, E.; Whitesides, G. M. *Nanotechnology* **1996**, *7*, 452-457.

(147) Xia, Y.; Kim, E.; Whitesides, G. M. *Journal of the Electrochemical Society* **1996**, *143*, 1070-1079.

(148) Balmer, T. E.; Schmid, H.; Stutz, R.; Delamarche, E.; Michel, B.; Spencer, N. D.; Wolf, H. *Langmuir* **2005**, *21*, 622-632.

(149) Delamarche, E.; Schmid, H.; Bietsch, A.; Larsen, N. B.; Rothuizen, H.; Michel, B.; Biebuyck, H. *Journal of Physical Chemistry B* **1998**, *102*, 3324-3334.

(150) Delamarche, E.; Geissler, M.; Bernard, A.; Wolf, H.; Michel, B.; Hilborn, J.; Donzel, C. *Advanced Materials* **2001**, *13*, 1164-+.

(151) Wilkop, T.; Wang, Z. Z.; Cheng, Q. *Langmuir* **2004**, *20*, 11141-11148.

(152) Park, T. J.; Lee, S. Y.; Lee, S. J.; Park, J. P.; Yang, K. S.; Lee, K. B.; Ko, S.; Park, J. B.; Kim, T.; Kim, S. K.; Shin, Y. B.; Chung, B. H.; Ku, S. J.; Kim, D. H.; Choi, I. S. *Analytical Chemistry* **2006**, *78*, 7197-7205.

(153) Lahiri, J.; Ostuni, E.; Whitesides, G. M. *Langmuir* **1999**, *15*, 2055-2060.

(154) Cho, Y.; Ivanisevic, A. *Journal of Physical Chemistry B* **2005**, *109*, 6225-6232.

(155) Foley, J.; Schmid, H.; Stutz, R.; Delamarche, E. *Langmuir* **2005**, *21*, 11296-11303.

(156) Feng, C. L.; Vancso, G. J.; Schonherr, H. *Advanced Functional Materials* **2006**, *16*, 1306-1312.

(157) Kim, H. S.; Bae, Y. M.; Kim, Y. K.; Oh, B. K.; Choi, J. W. *Journal of Microbiology and Biotechnology* **2006**, *16*, 141-144.

(158) Wang, B.; Feng, J.; Gao, C. Y. *Macromolecular Bioscience* **2005**, *5*, 767-774.

(159) Cho, Y.; Ivanisevic, A. *Langmuir* **2006**, *22*, 8670-8674.

(160) Schmalenberg, K. E.; Buettner, H. M.; Uhrich, K. E. *Biomaterials* **2004**, *25*, 1851-1857.

(161) Yang, Z.; Belu, A. M.; Liebmann-Vinson, A.; Sugg, H.; Chilkoti, A. *Langmuir* **2000**, *16*, 7482-7492.

(162) Runge, A. F.; Saavedra, S. S. *Langmuir* **2003**, *19*, 9418-9424.

(163) James, C. D.; Davis, R. C.; Kam, L.; Craighead, H. G.; Isaacson, M.; Turner, J. N.; Shain, W. *Langmuir* **1998**, *14*, 741-744.

(164) Bernard, A.; Delamarche, E.; Schmid, H.; Michel, B.; Bosshard, H. R.; Biebuyck, H. *Langmuir* **1998**, *14*, 2225-2229.

(165) Rozkiewicz, D. I.; Kraan, Y.; Werten, M. W. T.; de Wolf, F. A.; Subramaniam, V.; Ravoo, B. J.; Reinhoudt, D. N. *Chemistry-A European Journal* **2006**, *12*, 6290-6297.

(166) Bernard, A. R., J. P.; Michel, B.; Bosshard, H. R.; Delamarche, E. *Advanced Materials* **2000**, *12*, 1067.

(167) Kwak, S. K.; Lee, G. S.; Ahn, D. J.; Choi, J. W. *Materials Science & Engineering C-Biomimetic and Supramolecular Systems* **2004**, *24*, 151-155.

(168) Biasco, A.; Pisignano, D.; Krebs, B.; Cingolani, R.; Rinaldi, R. *Synthetic Metals* **2005**, *153*, 21-24.

(169) Wang, D. Y.; Huang, Y. C.; Chiang, H. S.; Wo, A. M.; Huang, Y. Y. *Journal of Biomedical Materials Research Part B-Applied Biomaterials* **2007**, *80B*, 447-453.

(170) Mack, N. H.; Dong, R.; Nuzzo, R. G. *Journal of the American Chemical Society* **2006**, *128*, 7871-7881.

(171) Wang, L. K.; Feng, X. Z.; Hou, S.; Chan, Q. L.; Qin, M. *Surface and Interface Analysis* **2006**, *38*, 44-50.

(172) Feng, C. L.; Embrechts, A.; Bredebusch, I.; Schnekenburger, J.; Domschke, W.; Vancso, G. J.; Schonherr, H. *Advanced Materials* **2007**, *19*, 286-+.

(173) Foley, J.; Schmid, H.; Stutz, R.; Delamarche.E. *Langmuir* **2005**, *21*, 11296-11303.

(174) Gamble, L.; personal communication, 2005.

(175) Duffy, D. C.; McDonald, J. C.; Schueller, O. J. A.; Whitesides, G. M. *Analytical Chemistry* **1998**, *70*, 4974-4984.

(176) Juncker, D.; Schmid, H.; Drechsler, U.; Wolf, H.; Wolf, M.; Michel, B.; de Rooij, N.; Delamarche, E. *Analytical Chemistry* **2002**, *74*, 6139-6144.

(177) Lionello, A.; Josserand, J.; Jensen, H.; Girault, H. *Lab on a Chip* **2005**, *5*, 1096-1103.

(178) Lionello, A.; Josserand, J.; Jensen, H.; Girault, H. *Lab on a Chip.* **2005**, *5*, 254-260.

(179) Mason, T.; Pineda, A.R.; Wofsy, C.; Goldstein, B. *Mathematical Biosciences* **1999**, *159*, 123-144.

(180) Myszka, D. G.; He, X.; Dembo, M.; Morton, T. A.; Goldstein, B.*Biophysical Journal* **1998**, *75*, 583-594.

(181) Sadana, A. *Analytical Biochemistry* **2001**, *291*, 34-47.

(182) Sigmundsson, K.; Masson, G.; Rice, R. H.; Beauchemin, N.; Obrink, B. *Biochemistry* **2002**, *41*, 8263-8276.

(183) Vijayendran, R. A.; Ligler, F. S.; Leckband, D. E. *Analytical Chemistry* **1999**, *71*, 5405-5412.

(184) Sikavitsas, V.; Nitsche, J.M.; Mountziaris, T. J.*Biotechnology Progress* **2002**, *18*, 885-897.

(185) Yarmush, M. L.; Patankar, D.B.; Yarmush, D.M. *Molecular Immunology* **1996**, *33*, 1203-1214.

(186) Zimmermann, M.; Delamarche, E.; Wolf, M.; Hunziker, P. *Biomedical Microdevices* **2005**, *7*, 99-110.

(187) Karlsson, R.; Michaelsson, A.; Mattsson, L. *Journal of Immunological Methods* **1991**, *145*, 229-240.

(188) Karlsson, R.; Falt, A. *Journal of Immunological Methods* **1997**, *200*, 121-133.

(189) Edwards, D. A. *Bulletin of Mathematical Biology* **2006**, *68*, 627-654.

(190) Fong, C. C.; Wong, M.S.; Fong, W.F.; Wang, M.S. *Analytica Chimica Acta* **2002**, *456*, 201-208.

(191) Gervais, T.; Jensen, K. F. *Chemical Engineering Science* **2006**, *61*, 1102-1121.

(192) Glaser, R. W. *Analytical Biochemistry* **1993**, *213*, 152-161.

(193) Goldstein, B.; Coombs, D.; He, X. Y.; Pineda, A. R.; Wofsy, C.*Journal of Molecular Recognition* **1999**, *12*, 293-299.

(194) He, X.; Coombs, D.; Myszka, D.; Goldstein, B. *Bulletin of Mathematical Biology* **2006**, *68*, 1125-1150.

(195) Jenkins, J.; Prabhakarpandian, B.; He, X. Y.; Pineda, A. R.; Wofsy, C. *Analytical Biochemistry* **2004**, *331*, 207-215.

(196) Lebedev, K.; Mafe, S.; Stroeve, P. *Journal of Colloid and Interface Science* **2006**, *296(2): 527-537.*, 527-537.

(197) Christensen, L. L. H. *Analytical Biochemistry* **1997**, *249*, 153-164.

(198) Edwards, P. R.; Gill, A.; Pollardknight, D. V.; Hoare, M.; Buckle, P. E.; Lowe, P. A.; Leatherbarrow, R. J. *Analytical Biochemistry* **1995**, *231*, 210-217.

(199) Deegan, R.B.; Dupont, G.; Huber, S. R.; Nagel, T. A. *Nature* **1997**, *389*.

(200) Berg, J. C. *Surface and Colloid Science*; University of Washington: Seattle, 2002.

(201) Kerrick, J. M.; Wolff, D. L.; Graves, N. M. *Annals of Pharmacotherapy* **1995**, *29*, 470-474.

(202) Putignano, P.; Dubini, A.; Toja, P.; Invitti, C.; Bonfanti, S.; Redaelli, G.; Zappulli, D.; Cavagnini, F. *European Journal of Endocrinology* **2001**, *145*, 165-171.

(203) Stenberg, M.; Nygren, H. *Journal of Immunological Methods* **1988**, *113*, 3-15.

(204) Holde, K. E. V. *Physical Biochemistry*, 2nd ed.; Prentice Hall: Englewood Cliffs, NJ, 1985.

(205) Ekins, R. *Nuclear Medicine Biology* **1994**, *21*, 495–521.

(206) Berg, O.; von Hippel, P. H. *Annual Review of Biophysics and Biophyical Chemistry* **1985**, *14*, 131-160.

(207) Berg, O. *Biophysical Journal* **1985**, *47*, 1-15.

(208) Schurr, J. M. *Biophysical Journal* **1970**, *10*, 700.

(209) Hatch, A.; Garcia, E.; Yager, P. *Proc. IEEE* **2004**, *92*, 126-139.

(210) COMSOL *FEMLAB Transport Phenomena Course* **2003**, 38-48.

(211) Sarma, V. R.; Silverto, E. W.; Davies, D. R.; Terry, W. D. *J. of Biol. Chem.* **1971**, *246*, 3753.

(212) Peters, T. *All About Albumin: Biochemistry, Genetics, and Medical Applications*; Academic Press: San Diego, 1996.

(213) Polzius, R.; Diessel, E.; Bier, F. F.; Bilitewski, U. *Analytical Biochemistry* **1997**, *248*, 269-276.

(214) Kaufman, E. N.; Jain, R. K. *Biophysical Journal* **1991**, *60*, 596-610.

(215) Griffiths, A. D. *EMBO J.* **1993**, *12*, 725–734.

(216) Hardt, S.; Drese, K.S.; Hessel, V.; Schonfeld, F. *Microfluidics and Nanofluidics* **2005**, *1*, 108-118.

(217) Vijayendran, R. A.; Motsegood, K. M.; Beebe, D. J.; Leckband, D. E. *Langmuir* **2003**, *19*, 1824-1828.

(218) Liu, J., Williams, B.A., Gwirtz, R.M.; Wold, B. J. a. S. Q. *Angewandte Chemie-International Edition* **2006**, *45*, 3618.

(219) Yoon, S. K.; Fichtlb, G.W.; Kenis, P. *Lab on a Chip* **2006**, *6*, 1516.

(220) Roper, D. K. *Chemical Engineering Science* **2006**, *61*, 2557-2564.

(221) Zubtsov, D. A.; Ivanov, S.M.; Rubina, A. Y.; Dementieva, E. I.; Chechetkin, V.R.; Zasedatelev, A. S. *Journal of Biotechnology* **2006**, *122*, 16-27.

(222) Sigurdson, M.; Wang, D.; Meinhart, C. *Lab on a Chip* **2005**, *5*, 1366.

(223) McQuain, M. K.; Seale, K.; Peek, J.; Fisher, T. S.; Levy, S.; Stremler, M. A.; Haselton, F. R. *Analytical Biochemistry* **2004**, *325*, 215-226.

(224) Raynal, F.; Beuf, A.; Plaza, F.; Scott, J.; Carriere, P.; Cabrera, M.; Cloarec, J. P.; Souteyrand, E. *Physics of Fluids* **2007**, *19*, 17112.

(225) Raynal, F.; Plaza, F.; Beuf, A.; Carriere, P.; Souteyrand, E.; Martin, J. R.; Cloarec, J. P.; Cabrera, M. *Physics of Fluids* **2004**, *16*, L63-L66.

(226) Hertzsch, J. M.; R. Sturman, R.; Wiggins, S. *Small* **2007**, *3*, 202-218.

(227) Herrmann, M.; Veres, T.; Tabrizian, M. *Lab on a Chip* **2006**, *6*, 555-560.

(228) Bynum, M. A.; Gordon, G. B. *Analytical Chemistry* **2004**, *76*, 7039-7044.

(229) Adey, N. B.; Lei, M.; Howard, M. T.; Jensen, J. D.; Mayo, D. A.; Butel, D. L.; Coffin, S. C.; Moyer, T. C.; Slade, D. E.; Spute, M. K.; Hancock, A. M.; Eisenhoffer, G. T.; Dalley, B. K.; McNeely, M. R. *Analytical Chemistry* **2002**, *74*, 6413-6417.

(230) Yoon, S. K.; Choban, E.R.; Kane, C.; Tedakis, T.; Kenis, P. *Journal of the American Chemical Society* **2005**, *127*, 10466.

(231) Stroock, A. D.; Dertinger, S. K.; Whitesides, G. M.; Ajdari, A. *Analytical Chemistry* **2002**, *74*, 5306-5312.

(232) Floyd-Smith, T. M.; Golden, J.P.; Howell, P.B.; Ligler, F. *Microfluidics and Nanofluidics* **2006**, *2*, 180-183.

(233) Fu, X.; Liu, S.F.; Ruan, X.D.; Yang, H.Y. *Sensors and Actuators B-Chemical* **2006**, *114*, 618-624.

(234) Ghaleb, K. A.; Stephan, K. *Applied Spectroscopy* **2006**, *60*, 564-567.

(235) Hassell, D. G.; Zimmerman, W. B.*Chemical Engineering Science* **2006**, *61*, 2977-2985.

(236) Howell, P.; Mott, D.; Fertig, S.; Kaplan, C.; Golden, J.; Oran, E.; Ligler, F. *Lab on a Chip* **2005**, *5*, 524-530.

(237) Li, C.A.; Chen, T. N. *Sensors and Actuators B-Chemical* **2005**, *106*, 871-877.

(238) Sato, H.; Ito, S.; Tajima, K.; Orimoto, N.; Shoji, S. *Sensors and Actuators A-Physical* **2005**, *119*, 365-371.

(239) Stroock, A. D.; McGraw. G.J. *Philosophical Transactions of the Royal Society of London Series A-Mathematical Physical and Engineering Sciences* **2004**, *362*, 971-986.

(240) Stroock, A. D.; Dertinger, S. K.; Whitesides, G. M. Ajdari, A. *Analytical Chemistry* **2002**, *74*, 5306-5312.

(241) Li, C. A.; Chen, T. N. *Sensors and Actuators B-Chemical* **2005**, *106*, 871-877.

(242) Yang, J. T.; Huang, K. J.; Lin, Y. C. *Lab on a Chip* **2005**, *5*, 1140-1147.

(243) Gervais, T.; El-Ali, J.; Gunther, A.; Jensen, K. F. *Lab on a Chip* **2006**, *6*, 500-507.

(244) Jackson, N.; Finlayson, B.A. *Journal of Non-Newtonian Fluid Mechanics.* **1982**, *10*, 55-69.

Appendix A: Governing equations and boundary conditions used in the COMSOL® models

Detailed below are the governing equations and boundary conditions for the equations solved in COMSOL®. Each model solved the Poisson and Navier-Stokes equations (A.1-A.2). The models for the indirect immunoassay and the streptavidin-biotin assay solved the convection-diffusion equations described in A.3. The description in A.3. details a 3D model even though the indirect immunoassay model was completed in 2D due to computational constraints. Simply enter a parabolic velocity profile in the 2D model and do not solve the Navier-Stokes equation. The concentration gradient immunoassay model solved the convection-diffusion equations described in A.4. The streptavidin-biotin model was less complex than the indirect immunoassay in that there was no reaction term in the convection-diffusion equation. In the binding reaction, substitute streptavidin for the antibody. Input the appropriate reaction and transport parameters but neglect the reaction term when you attempt to solve this model. To incorporate bivalency in any of the models, incorporate additional species in the convection-diffusion mode and the weak boundary mode. Include other reaction terms in the bulk of the solution and the surface reaction. All parameters were entered using SI units. All of the equations were derived from general chemical engineering texts[52, 53] and an example model described in the COMSOL® manual[210] as well as discussions with Prof. Bruce Finlayson.

Table 20. List of variables in the COMSOL model.

Variable	Description
k_{on} ($m^3 moles^{-1} s\ s^{-1}$)	binding rate of an antibody and antigen molecules in solution
k_{off}(s^{-1})	dissociation rate of an antibody and antigen molecules in solution
k_{ads} ($m^3 moles^{-1}\ s^{-1}$)	binding rate of an antibody molecule from solution to the surface
k_{des}(s^{-1})	dissociation rate of a an antibody molecule bound to the surface
θ (moles/m^2)	the available binding sites per unit area
θ_0 (moles/m^2)	total number of initial binding sites per unit area
p ($kg\ m^{-1}\ s^{-2}$)	pressure
x_s (m)	characteristic length (typically defined as the smallest dimension of the channel)
u_s ($m\ s^{-1}$)	characteristic velocity (typically defined as the average velocity in the microchannel)
u_0 ($m\ s^{-1}$)	inlet velocity
t_s (s)	characteristic time scale
ρ ($kg\ m^{-3}$)	density
μ ($kg\ m^{-1}\ s^{-1}$)	viscosity
c_s ($moles\ m^{-2}$)	surface concentration of bound antibody
c_{Ab} ($moles\ m^{-3}$)	concentration of antibody in solution
c_{Ag} ($moles\ m^{-3}$)	concentration of analyte in solution
$c_{Ag\text{-}Ab}$ ($moles\ m^{-3}$)	concentration of antibody-analyte (complex) in solution
D ($m^{-2}\ s^{-1}$)	diffusion coefficient

A.1 Poisson Equation

Solves the pseudo-3d velocity and is mapped to the inlet of 3d geometries (u_0).

$$-\nabla \bullet (\nabla \boldsymbol{u}) = \left(\frac{\partial p}{\partial x}\right) / \mu \quad \text{Equation 15}$$

A.2 Navier-Stokes equation

Navier-Stokes equation*

$$\rho \frac{\partial \boldsymbol{u}}{\partial t} + \rho \boldsymbol{u} \bullet \nabla \boldsymbol{u} = -\nabla p + \mu \nabla^2 \boldsymbol{u} \quad \text{Equation 16}$$

Reynolds number

$$\mathrm{Re} = \frac{\rho u_s x_s}{\mu} \quad \text{Equation 17}$$

* At this size scale, gravitational effects are negligible and the gravity term drops out of the Navier-Stokes equation.

Table 21. Boundary conditions for the Navier-Stokes equation.

Wall	Slip plane	Inlet	Outlet
$\boldsymbol{u} = 0$;	$\boldsymbol{n} \bullet \boldsymbol{u} = 0$;	$\boldsymbol{u} = u_0$;	Normal outflow; v=0, w=0;

A.3 Governing equations and boundary conditions for the indirect immunoassay and the streptavidin-biotin assay

Table 22. Initial conditions for the convection-diffusion mode.

$c_s = 0$	$c_{AB0} = X$ *	$c_{ANT0} = Y$ *	$c_{ANT-AB0} = Z$ *

*where X and Y and Z are determined by the equilibrium concentration of antibody, antigen, and antibody-antigen (Table 7 and Table 8) solved in 2-dimensions when they were allowed to react under no flow for 15 minutes (concentration distribution of the species was found to be the same for a 15 minute transient solution as the steady-state solution.)

** for the streptavidin-biotin model c_{SA0}=0.

Reaction between antibody and analyte in solution

$$c_{Ab} + c_{Ag} \underset{k_{off}}{\overset{k_{on}}{\Leftrightarrow}} c_{Ab-Ag} \qquad \text{Equation 18}$$

Convection-diffusion equations for each species in solution

$$\frac{dc_{Ab}}{dt} + \nabla \bullet \left(-D\nabla c_{Ab} + c_{Ab}\boldsymbol{u}\right) = k_{off}c_{Ag-Ab} - k_{on}c_{Ab}c_{Ag} \qquad \text{Equation 19}$$

$$\frac{dc_{Ag}}{dt} + \nabla \bullet \left(-D\nabla c_{Ag} + c_{Ag}\boldsymbol{u}\right) = k_{off}c_{Ag-Ab} - k_{on}c_{Ab}c_{Ag} \qquad \text{Equation 20}$$

$$\frac{dc_{Ag-Ab}}{dt} + \nabla \bullet \left(-D\nabla c_{Ag-Ab} + c_{Ag-Ab}\boldsymbol{u}\right) = k_{on}c_{Ab}c_{Ag} - k_{off}c_{Ag-Ab} \qquad \text{Equation 21}$$

Peclet number for each species

$$Pe_{Ab} = \frac{x_s u_s}{D_{Ab}} \qquad \text{Equation 22}$$

$$Pe_{Ag} = \frac{x_s u_s}{D_{Ag}} \qquad \text{Equation 23}$$

$$Pe_{Ag-Ab} = \frac{x_s u_s}{D_{Ag-Ab}} \qquad \text{Equation 24}$$

Table 23. Boundary conditions for the antibody and analyte for the convection-diffusion equation.

	Antibody	Analyte
Wall/Plane of symmetry	$\boldsymbol{n} \bullet (-D\nabla c_{Ab} + c_{Ab}\boldsymbol{u}) = 0$	$\boldsymbol{n} \bullet (-D\nabla c_{Ag} + c_{Ag}\boldsymbol{u}) = 0$
Binding surface	$\boldsymbol{n} \bullet (-D\nabla c_{Ab} + c_{Ab}\boldsymbol{u}) = N_0$; $N_0 = -k_{ads}c_{Ab}(\theta_0 - c_s) + k_{des}c_s$	$\boldsymbol{n} \bullet (-D\nabla c_{Ag} + c_{Ag}\boldsymbol{u}) = 0$
Outlet	$\boldsymbol{n} \bullet (-D_{Ab}\nabla c_{Ab}) = 0$	$\boldsymbol{n} \bullet (-D_{Ag}\nabla c_{Ag}) = 0$

Table 24. Boundary conditions for the antibody-analyte complex for the convection-diffusion equation.

	Antibody-Analyte complex
Wall/Plane of symmetry	$\boldsymbol{n} \bullet (-D\nabla c_{Ag-Ab} + c_{Ag-Ab}\boldsymbol{u}) = 0$
Binding surface	$\boldsymbol{n} \bullet (-D\nabla c_{Ag-Ab} + c_{Ag-Ab}\boldsymbol{u}) = 0$
Outlet	$\boldsymbol{n} \bullet (-D_{Ag-Ab}\nabla c_{Ag-Ab}) = 0$

Surface binding reaction

$$c_{Ab} + \theta \underset{k_{des}}{\overset{k_{ads}}{\Leftrightarrow}} c_s \qquad \text{Equation 25}$$

$$\frac{dc_s}{dt} = k_{ads}c_{Ab}(\theta_0 - c_s) - k_{des}c_s \qquad \text{Equation 26}$$

A.4.Governing equations and boundary conditions for the concentration gradient immunoassay

Table 25. List of variables for the CGIA model.

Variable	Description
c_s (moles m^{-2})	surface concentration of bound antibody
c_{Ab} (moles m^{-3})	concentration of antibody in solution
c_{Ag} (moles m^{-3})	concentration of analyte in solution
$c_{Ag\text{-}Ab}$ (moles m^{-3})	concentration of antibody-analyte (complex) in solution
c_{Ab0} (moles m^{-3})	initial concentration of antibody in solution
c_{Ag0} (moles m^{-3})	initial concentration of analyte in solution
$c_{Ag\text{-}Ab0}$ (moles m^{-3})	initial concentration of antibody-analyte (complex) in solution
c_{s0} (moles m^{-2})	initial surface concentration of bound antibody
$c_{Ag\ 22\ mm}$(moles m^{-3})	concentration of antigen 22 mm downstream of inlet solved for at the end of the pseudo-3d model
$c_{Ab\_22\ mm}$ (moles m^{-3})	concentration of analyte 22 mm downstream of inlet solved for at the end of the pseudo-3d model
$c_{Ag\text{-}Ab\_22\ mm}$ (moles m^{-3})	concentration of antibody-analyte complex 22 mm downstream of inlet solved for at the end of the pseudo-3d model
k_{ads} (m^3moles$^{-1}s^{-1}$)	binding rate of an antibody from solution to the surface
k_{des}(s^{-1})	dissociation rate of an antibody bound to the surface
θ (moles m^{-2})	available antibody binding sites per unit area
θ_0 (moles m^{-2})	total number of initial antibody binding sites per unit area
p (kg m^{-1} s^{-2})	pressure
x_s (m)	characteristic length (the depth of channel)
u (m s^{-1})	velocity in x-dimension
u_s (m s^{-1})	characteristic velocity (average velocity)
u_0 (m s^{-1})	parabolic inlet velocity for 3d model solved in pseudo-3d mode
v(m s^{-1})	velocity in y-dimension
W(m s^{-1})	velocity in z-dimension
ρ (kg m^{-3})	density
μ (kg m^{-1} s^{-1})	viscosity
D (m^2 s^{-1})	diffusion coefficient

Table 26. Initial conditions for the pseudo-3d convection-diffusion mode in the CGIA model.

$c_{Ab0} = X$ *	$c_{Ag0} = Y$ *	$c_{Ag\ -\ Ab0} = 0$

*where X and Y are arbitrary concentrations.

$$c_{Ab} + c_{Ag} \underset{k_{off}}{\overset{k_{on}}{\Leftrightarrow}} c_{Ab\ -\ Ag}$$ Equation 27

Convection-diffusion equations for each species in solution

$$\frac{dc_{Ab}}{dt} + \nabla \bullet \left(-D\nabla c_{Ab} + c_{Ab}\boldsymbol{u}\right) = k_{off}c_{Ag\ -\ Ab} - k_{on}c_{Ab}c_{Ag}$$ Equation 28

$$\frac{dc_{Ag}}{dt}+\nabla\bullet\left(-D\nabla c_{Ag}+c_{Ag}\boldsymbol{u}\right)=k_{off}C_{Ag\,-\,Ab}-k_{on}C_{Ab}C_{Ag}$$ Equation 29

$$\frac{dc_{Ag\,-\,Ab}}{dt}+\nabla\bullet\left(-D\nabla c_{Ag\,-\,Ab}+c_{Ag\,-\,Ab}\boldsymbol{u}\right)=k_{on}C_{Ab}C_{Ag}-k_{off}C_{Ag\,-\,Ab}$$ Equation 30

Peclet number for each species

$$Pe_{Ab}=\frac{x_s u_s}{D_{Ab}}$$ Equation 31

$$Pe_{Ag}=\frac{x_s u_s}{D_{Ag}}$$ Equation 32

$$Pe_{Ag\,-\,Ab}=\frac{x_s u_s}{D_{Ag\,-\,Ab}}$$ Equation 33

Table 27. Boundary conditions for the pseudo-3D mode in the CGIA model.

	Wall/Plane of symmetry
Antibody	$\boldsymbol{n}\bullet(-D\nabla c_{Ab}+c_{Ab}\boldsymbol{u})=0$
Analyte	$\boldsymbol{n}\bullet(-D\nabla c_{Ag}+c_{Ag}\boldsymbol{u})=0$
Antibody-Analyte complex	$\boldsymbol{n}\bullet(-D\nabla c_{Ag\,-\,Ab}+c_{Ag\,-\,Ab}\boldsymbol{u})=0$

Table 28. Initial conditions for the convection-diffusion and surface binding modes in the 3D CGIA model.

$c_{Ab0}=0$	$c_{Ag0}=0$	$c_{Ag\,-\,Ab0}=0$	$c_s=0$

Table 29. Boundary conditions for the analyte and antibody for convection-diffusion and surface binding modes in the 3D model.

	Antibody	Analyte
Wall/ Slip plane	$\boldsymbol{n} \bullet (-D\nabla c_{Ab} + c_{Ab}\boldsymbol{u}) = 0$	$\boldsymbol{n} \bullet (-D\nabla c_{Ag} + c_{Ag}\boldsymbol{u}) = 0$
Inlet**	$c_{Ab} = c_{Ab\,22mm}$	$c_{Ag} = c_{Ag\,22mm}$
Outlet	$\boldsymbol{n} \bullet (-D_{Ab}\nabla c_{Ab}) = 0$	$\boldsymbol{n} \bullet (-D_{Ag}\nabla c_{Ag}) = 0$
Binding Surface	$\boldsymbol{n} \bullet (-D\nabla c_{Ab} + c_{Ab}\boldsymbol{u}) = N_0$ $N_0 = -k_{ads}c_{Ab}(\theta_0 - c_s) + k_d$	$\boldsymbol{n} \bullet (-D\nabla c_{Ag} + c_{Ag}\boldsymbol{u}) = 0$

**The inlet concentration profile is the solution to the pseudo-3d model after traveling 22 mm downstream of the inlet.

Table 30. Boundary conditions for the analyte-antibody complex for the convection-diuffusion and surface binding modes in the 3D model.

	Antibody-Analyte complex
Wall/ Slip plane	$\boldsymbol{n} \bullet (-D\nabla c_{Ag-Ab} + c_{Ag-Ab}\boldsymbol{u}) = 0$
Inlet**	$c_{Ag-Ab} = c_{Ag-Ab\,22mm}$
Outlet	$\boldsymbol{n} \bullet (-D_{Ag-Ab}\nabla c_{Ag-Ab}) = 0$
Binding Surface	$\boldsymbol{n} \bullet (-D\nabla c_{Ag-Ab} + c_{Ag-Ab}\boldsymbol{u}) = 0$

**The inlet concentration profile is the solution to the pseudo-3d model after traveling 22 mm downstream of the inlet.

Surface binding reaction

There is no surface binding reaction for the pseudo-3d model. The surface reaction is relevant only for the 3d model.

$$c_{Ab} + \theta \underset{k_{des}}{\overset{k_{ads}}{\Leftrightarrow}} c_s \qquad \text{Equation 1}$$

$$\frac{dc_s}{dt} = k_{ads}c_{Ab}(\theta_0 - c_s) - k_{des}c_s \qquad \text{Equation 2}$$

A.5 Conservation of mass calculations

An essential step in verifying the accuracy of a computational model is to determine whether mass is conserved. This is particularly important in models in which one surface (the binding surface) depletes mass from solution. Listed below are two methods of verifying that mass is conserved in the standard immunoassay models. The first method was described by Professor Bruce Finlayson in a meeting. The second was pursued by Afshin Moshadi-Hossein.

Method 1

A mass balance must be completed to determine that the amount of material that enters the device is equivalent to what binds to the surface and what flow out of the device. Below are listed the boundary conditions for the different regions of the device. Using these boundary conditions as well as the governing equations, it can be determined if mass is conserved.

Convection-diffusion equation for molecules in solution

$$\frac{\partial c}{\partial t} + \nabla \cdot \left(-D\nabla c + c\boldsymbol{u}\right) = 0 \qquad \text{Equation 3}$$

Integrate over the entire volume of the microchannel:

$$\int \frac{\partial c}{\partial t} dV + \int \nabla \cdot \left(-D\nabla c + c\boldsymbol{u}\right) dV = 0 \qquad \text{Equation 4}$$

Rearrange the equation:

$$\frac{d}{dt}\int_V c dV + \int_V \nabla \cdot \left(-D\nabla c + c\boldsymbol{u}\right) dV = 0 \qquad \text{Equation 5}$$

Apply the divergence theorem to the second term:

$$\frac{d}{dt}\int_V c\,dV + \int_S \left(-D\boldsymbol{n}\bullet\nabla c + \boldsymbol{u}\bullet\boldsymbol{n}c\right)dS = 0 \qquad \text{Equation 6}$$

Specify each of the surfaces (Note: the dot products of the conditions at the walls and plane of symmetry with the gradient equals zero. Therefore, those terms drop out of the equation.)

$$\frac{d}{dt}\int_V c\,dV + \int_{Spatch}\left(-D\boldsymbol{n}\bullet\nabla c\right)dS + \int_{Sinlet}\left(\boldsymbol{u}\bullet\boldsymbol{n}c_0\right)dS \int_{Soutlet}\left(\boldsymbol{u}\bullet\boldsymbol{n}c_{out}\right)dS = 0 \qquad \text{Equation 7}$$

Next, the equations governing the binding reaction at the surface is manipulated.

Surface reaction differential equation

$$\frac{dc_s}{dt} = k_{ads}c(\theta_0 - c_s) - k_{des}\theta c_s \qquad \text{Equation 8}$$

Integrate over the entire surface

$$\int_{Spatch}\frac{dc_s}{dt}dS = \int_{Spatch}\left(k_{ads}c(\theta_0 - c_s) - k_{des}\theta c_s\right)dS \qquad \text{Equation 9}$$

Because c_s is not defined elsewhere and c becomes c_s upon binding to the surface and the velocity (**u**) at the surface is zero:

$$\int_V\left(-D\boldsymbol{n}\bullet\nabla c\right)dV = \int_{Spatch}\frac{\partial c_s}{\partial t}dS \qquad \text{Equation 10}$$

Therefore, for mass to be conserved:

$$\frac{d}{dt}\int_V c\,dV + \int_{Spatch}\left(-D\boldsymbol{n}\bullet\nabla c\right)dS + \int_{Sinlet}\left(\boldsymbol{u}\bullet\boldsymbol{n}c_0\right)dS \int_{Soutlet}\left(\boldsymbol{u}\bullet\boldsymbol{n}c_{out}\right)dS = 0 \qquad \text{Equation 11}$$

The value of $\frac{d}{dt}\int_V c\,dV$ must be calculated from data points within the model to account for depletion of c from the solution as it binds to the binding patch surface. To do this, the amount of analyte in the bulk of the device (integrated over the entire device) must be plotted as a function of time. The slope must be taken to find $\frac{d}{dt}\int_V c\,dV$. To find the other

values, use COMSOL® to calculate the flux through each surface for a given time point. If mass is conserved, these mathematical relationships should hold.

Method 2

The second method eliminates the need to determine the slope to find the value of $\frac{d}{dt}\int_V cdV$. The amount of mass that flows out of the device can be computed over time by introducing a weak boundary form modes at the inlet and the outlet. By integrating a weak boundary form mode at these surfaces, calculating the amount that has entered and flowed out of the device as well as bound to the surface simply requires integration over the surface.

Appendix B: Protocols to solve the COMSOL® models

The following section serves as a practical guide for completing COMSOL® models of the indirect immunoassay in three-dimensions and the standard flow assay (streptavidin-biotin) as well as the concentration gradient immunoassay. Several bugs were discovered in the COMSOL® software while developing these models. The purpose of this section is to explain the exact order of operations to generate a working model so that in future these errors are avoided. If an input is not described in this protocol, it indicates that the default value is appropriate. Appendix A describes the equations and boundary conditions solved in further detail.

B.1 Indirect immunoassay in three-dimensions or the streptavidin-biotin assay

This protocol can be applied to the streptavidin-biotin system if you do not enter reaction terms and do not include c2 and c3. Streptavidin would be represented by c1 and cs would represent surface bound streptavidin.

1) Draw:

A) The geometry of the microchannel in three dimensions. If there is a plane of symmetry incorporate it in the model to reduce the computation required. Also, integrate lines in the geometry to denote the binding surface.

B) The geometry of the inlet in two dimensions.

2) Open four modes within COMSOL®:

Three-dimensional modes (**for the indirect immunoassay you could reduce the memory usage by completing it in 2D which is what is presented in Chapter 6. To detail a more complicated model which would be more useful for future users, the 3D model is detailed here.)

A) Transient Convection Diffusion (variable *c1* (antibody or streptavidin), *c2* (antigen), *c3* (antibody-antigen))

B) Steady state incompressible Navier-Stokes (variables *u, v, w* velocities in the x, y, and z dimensions)

C) Weak Boundary Mode [variable *cs* (surface bound antibody or streptavidin)]

Two-dimensional mode

D) Poisson Equation (variable *u2* (inlet parabolic velocity profile))

3) Enter the following constants

Table 31. List of variables in the COMSOL model.

c1 (moles m^{-3})
c2 (moles m^{-3})
c3 (moles m^{-3})
D1 (m^2s^{-1})
D2 (m^2s^{-1})
D3 (m^2s^{-1})
k_{ads} ($m^3moles^{-1}s^{-1}$)
k_{des}(s^{-1})
θ (moles/m^2)
θ_0 (moles/m^2)
ρ (kg m^{-3})
μ (kg m^{-1} s^{-1})

4) Enter the following boundary expression for the three-dimensional geometry

Table 32. Boundary expression for the surface binding reaction.

react_surf	k_{ads} *c(θ_0 - cs)- k_{des} *cs

5) Input the boundary conditions and subdomain parameters for the Poisson equation.

Table 33. Boundary conditions for the Poisson equation.

Walls	Dirichlet (no slip condition)
Plane of symmetry	Neumann (slip condition)

Table 34. Subdomain parameters for the Poisson mode.

c	12
f	1/(depth of channel)^2

6) Input the boundary conditions, initial conditions and subdomain parameters for the convection-diffusion equation.

Table 35. Boundary conditions for the convection-diffusion mode.

Inlet	Concentration = c_1, c_2, c_3
Outlet	Convective flux
Wall	Insulation symmetry
Binding surface	Flux = -react_surf
Plane of symmetry	Insulation symmetry

Table 36. Subdomain parameters for the convection-diffusion mode.

D	D1, D2, D3
u	u
v	v
w	w
R** (c1)	koff*c3- kon*c1*c2
R** (c2)	koff*c3- kon*c1*c2
R** (c3)	kon*c1*c2 – koff*c3

** for the streptavidin-biotin assay there is no R term in the convection-diffusion mode.

Table 37. Initial conditions for the convection-diffusion mode.

c1, c2, c3	0

7) Input the boundary conditions and subdomain parameters for the steady-state Navier-Stokes mode.

Table 38. Subdomain parameters for the Navier-Stokes mode.

ρ	ρ
μ	μ

Table 39. Boundary conditions for the Navier-Stokes mode.

Inlet**	u0=0; v0=u_map; w0=0
Outlet	Normal outflow; w0=0
Wall	No slip
Binding surface	No slip
Plane of symmetry	Slip/symmetry

** Depending on the geometry, either u, v, or w may be non-zero. It is important to remember that in COMSOL® u represents velocity in the x direction, v represents velocity in the y direction, and w represents velocity in the z direction. Therefore, the parameters listed must be consistent with the geometry.

8) Input the parameters for the weak boundary form.

Ensure that only the binding surface is activated.

Table 40. Weak boundary mode.

weak	cs_test*react_surf
dweak	cs_test*cs_time

9) Mesh the two-dimensional geometry.

10) Mesh the three dimensional geometry to solve the steady-state Navier-Stokes equation. This mesh should be relatively uniform throughout the entire channel with a slight bias in the smallest dimension of the channel to ensure that enough nodes exist to get a smooth solution for the velocity profile.

11) Click "Get initial value" for the two dimensional and three dimensional models.

12) Solve the Poisson mode with the linear solver which calculates the two dimensional fully developed parabolic flow profile.

13) Map the Poisson velocity profile to 3D system

NOTE: ***BEFORE*** this step

1) Mesh the three-dimensional geometry to solve the Navier-Stokes equation.
2) Highlight the appropriate solver (Nonlinear, General)
3) Input all the parameters to solve the Navier-Stokes equation.
4) Highlight "Current solution" and "Navier-Stokes" in the solver manager.

A) In the two-dimensional geometry:

i) Click "Options" → "Extrusion coupling variables" → "Subdomain variables."

ii) Name the mapping variable and variable in two-dimensions it refers to (i.e.,, u_map → u2).

iii) Map the variable (u2) to the inlet of three-dimensional microchannel.

iv) Select "Update model."

v) To verify that the variable (u2) has been mapped to the inlet of the device: Click "Post–processing" → "Domain plot parameters"

→ "Surface" → select the Inlet → type in "u_map" → click zx plane** (The particular plane depends on the way the geometry was drawn.)

14) Solve the steady-state Navier-Stokes equation with the nonlinear solver ensuring that "Current solution" is selected.

15) Click "Store solution" in the solver manager.

16) Remesh the three-dimensional geometry such that you bias it toward the surface. If the relatively uniform mesh is used to solve the Navier-Stokes equation, the model is not likely to converge.

17) Solve the convection-diffusion and weak boundary modes together selecting the "Stored solution" and the time dependent solver.

B.2 Concentration Gradient Immunoassay

The major differences between this model and the previous model are:

1) The binding patch is a significant distance from the inlet of the geometry during which the antibody and antigen fluid streams mix. Given the large distance (~22 mm) downstream of the inlet that the antibody binding patch is situated and the computational limits of the computer, the microchannel upstream of the binding patch could not be incorporated into the three-dimensional model. Therefore, another mode (the pseudo three-dimensional mode) is required to describe the entire immunoassay.

2) Due to computational memory constraints, the entire width of the microchannel could not be modeled. Therefore, the central 1.6 mm of a 3 mm wide channel was simulated and slip boundary conditions were applied to two walls of the geometry.

3) The antibody and antigen are not mixed before the introduction to the device.

4) The antibody and antigen are introduced in separate streams.

1) Draw:

A) The geometry of the microchannel in three dimensions. Also, integrate two lines in the geometry to denote the binding surface.

B) The geometry of the inlet in two dimensions. Divide the inlet in half with a line segment.

2) Open five modes within COMSOL®:

Three-dimensional modes

A) Transient Convection Diffusion (variable *c1, c2, c3* where *c1* represents the antibody (or streptavidin), *c2* represents the antigen, and *c3* represents the antibody-antigen complex)

B) Steady state incompressible Navier-Stokes (variables *u, v, w* velocity in the x, y, and z dimensions)

C) Weak Boundary Mode (variable *cs* (surface bound antibody))

Two-dimensional modes

D) Poisson Equation (variable *u2* parabolic velocity profile)

E) Pseudo-3d convection-diffusion (variables *c4, c5, c6* where *c4* represents the antibody, *c5* represents the antigen, and *c6* represents the antibody-antigen complex)

3) Enter the following constants (values used for the constants are located in the Materials and Methods in Chapter 7.)

Table 41. List of variables for the CGIA model.

D1 (m^2s^{-1}) (antibody)
D2 (m^2s^{-1}) (antigen)
D3 (m^2s^{-1}) (antibody-antigen complex
c_{40}(moles m^{-3}) (antibody initial concentration)
c_{50} (moles m^{-3}) (antigen initial concentration)
k_{ads} (s^{-1})
k_{des}(m^3s^{-1}moles $^{-1}$)
k_{on} (s^{-1})
k_{off} (m^3s^{-1}moles $^{-1}$)
θ (moles m^{-2})
θ_0 (moles m^{-2})
ρ (kg m^{-3})
μ (kg m^{-1} s^{-1})

4) Enter the following boundary expression for the three-dimensional geometry

Table 42. Boundary expression for the surface binding reaction.

react_surf	k_{ads} *c1(θ_0 - cs)- k_{des} *cs

5) Input the boundary conditions and subdomain parameters for the Poisson equation.

Table 43. Boundary conditions for the Poisson mode.

Walls	Dirichlet (no slip condition)
Plane of symmetry	Neumann (slip condition)

Table 44. Subdomain parameters for the Poisson mode.

c	12
f	1/(depth of the microchannel)^2

6) Input the boundary conditions, initial conditions and subdomain parameters for the pseudo-3d convection-diffusion mode.

Table 45. Subdomain parameters for the pseudo-3D convection-diffusion mode.

D^{**}(c1)	D1
D^{**}(c2)	D2
D^{**}(c3)	D3
R^{**}(c1)	koff*c3- kon*c1*c2
R^{**}(c2)	koff*c3- kon*c1*c2
R^{**}(c3)	kon*c1*c2 – koff*c3
u	u
v	v
w	w

** Note: There are three boundary conditions for each species (c1, c2, and c3).

Table 46. Initial conditions for the pseudo-3D convection-diffusion mode.

	Left half of the channel	Right half of the channel
c40	0	c40
c50	c50	0
c60	0	0

Table 47. Boundary conditions for the pseudo-3D convection diffusion mode

Walls	Insulation symmetry
Plane of symmetry	Insulation symmetry

** Note: There are three boundary conditions for each species (c1, c2, and c3) and the mapped concentrations are from the pseudo-3d model.

7) Input the boundary conditions, initial conditions and subdomain parameters for the convection-diffusion equation.

Table 48. Subdomain parameters for the 3D convection-diffusion mode.

Subdomain Parameters	
D^{**}(c4)	D1
D^{**}(c5)	D2
D^{**}(c6)	D3
R^{**}(c4)	koff*c6- kon*c4*c5
R^{**}(c5)	koff*c6- kon*c4*c5
R^{**}(c6)	kon*c1*c2 – koff*c3
u	u2

** Note: There are three subdomain parameters for each species (c4, c5, and c6)

Table 49. Initial conditions for the 3D convection-diffusion mode.

c10	0
c20	0
c30	0

Table 50. Boundary conditions for the 3D convection diffusion mode

Inlet (c1)**	Concentration = c4map
Inlet (c2)**	Concentration = c5map
Inlet (c3)**	Concentration = c6map
Outlet	Convective flux
Wall	Insulation symmetry
Binding surface	Flux = -react_surf
Plane of symmetry	Insulation symmetry

** Note: There are three boundary conditions for each species (c1, c2, and c3) and the mapped concentrations are from the pseudo-3d model.

8) Input the boundary conditions and subdomain parameters for the steady-state Navier-Stokes mode.

Table 51. Subdomain parameters for the 3D Navier-Stokes mode.

ρ	ρ
μ	μ

Table 52. Boundary conditions for the 3D Navier-Stokes mode.

Inlet **	u0=0; v0=u_map; w0=0
Outlet	Outflow/pressure p0=0
Wall	No slip
Binding surface	No slip
Plane of symmetry	Slip/symmetry

** Depending on the geometry, either u, v, or w may be non-zero. It is important to remember that in COMSOL® u represents velocity in the x direction, v represents velocity in the y direction, and w represents velocity in the z direction. Therefore, the parameters listed must be consistent with the geometry.

9) Input the parameters for the weak boundary form.

Ensure that only the binding surface is activated.

Table 53. Weak boundary mode.

weak	cs_test*react_surf
dweak	cs_test*cs_time

10) Mesh the two-dimensional geometry. To achieve the best results, it is important to bias the mesh at the interface between the two streams.

11) Mesh the three dimensional geometry to solve the steady-state Navier-Stokes equation. This mesh should be relatively uniform throughout the entire channel with a slight bias in the smallest dimension of the channel to ensure that enough nodes exist to get a smooth solution for the velocity profile.

12) Click "Get initial value" for the two dimensional and three dimensional models.

13) Solve the Poisson mode with the linear solver which calculates the two-dimensional fully developed parabolic flow profile.

14) Solve the transient pseudo-3d convection-diffusion equation. The length of time required to solve the mode can be calculated using the average velocity rate and the distance traveled to the binding surface from the inlet.

15) Map the velocity profile and the concentration profiles of the antibody (c4), antigen (c5), and antibody-antigen complex (c6) to the three-dimensional model geometry.

NOTE: ***BEFORE*** this step

1) Mesh the three-dimensional geometry to solve the Navier-Stokes equation.
2) Highlight the appropriate solver (Nonlinear, General).
3) Input all the parameters to solve the Navier-Stokes equation.
4) Highlight "Current solution" and "Navier-Stokes" in the solver manager.

A) In the two-dimensional geometry

i) Click "Options" → "Extrusion coupling variables" → "Subdomain variables."

ii) Name the mapping variable and variable in two-dimensions it refers to (i.e.,, u_map → u2, c4map → c4, c5map → c5, and c6map → c6).

iii) Map the variables u2, c4, c5, and c6 to the inlet of the three-dimensional microchannel.

iv) Select "Update model."

v) To verify that the variable (u2, c4, c5, or c6) has been mapped to the inlet of the device: Click "Post–processing" → "Domain plot parameters" → "Surface" → select the Inlet → type in "u_map" or "c4_map" or "c5_map" or "c6_map" → click zx plane** (The particular plane depends on the way the geometry was drawn.)

16) Solve the steady-state Navier-Stokes equation with the nonlinear solver ensuring that "Current solution" is selected.

17) Click "Store solution" in the solver manager.

18) Remesh the three-dimensional geometry such that you bias it toward the surface. If the relatively uniform mesh used to solve the Navier-Stokes equation, the model is not likely to converge.

19) Solve the convection-diffusion and weak boundary modes together selecting the "stored solution" and the time dependent solver.

Appendix C: Surface plasmon resonance microscopy

Dr. Elain Fu developed the following image correction methods for surface plasmon resonance microscopy used in this dissertation.

C.1 Spatial and background signal processing

In any imaging system, there are spatial variations in the amount of light that reaches a particular location of the detector. Many of these differences arise from aberrations in the optical elements, blemishes on the optics, and spatial variations in the light source. In SPR, only the transverse magnetic (TM) component of light excites plasmons and thus generates the image. The transverse electric (TE) component of light does not excite plasmons on the gold surface. Because the TE image is subject to the same spatial variations in incident light as the TM image, it can serve as the reference image. TE normalization can be accomplished by dividing the TM image by the TE image, pixel by pixel. In addition, correction of the background signal due to stray light and the dark signal of the detector must be accomplished. A 'dark' image in which the source light is blocked from passage to the detector (a piece of black felt is placed between the polarizer and the bandpass filter) is recorded. The dark image is subtracted pixel by pixel from the TM and TE images. These processing steps are described by the equation below.

$$TM_{ij}{}^{\theta}{}_{processed} = \left(\frac{TM_{ij} - Dark_{ij}}{TE_{ij} - Dark_{ij}} \right) \qquad \text{Equation 45}$$

where $TM_{i,j}$ denotes pixel i,j in the TM image, $TE_{i,j}$ denotes pixel i,j in the TE image, and $Dark_{i,j}$ denotes pixel i,j in the 'dark' image.

The wavelength tuning method utilized by the SPRM used in this dissertation requires another image correction step. In this SPRM, the wavelength of light is altered by rotating a bandpass filter about an axis perpendicular to the axis of light propagation. It has been shown that as the filter is rotated, the ratio of TM to TE light increases from an expected value of 1 at normal incidence to ~5 at a filter angle of 40 degrees (Figure 130). To correct for the polarization dependent transmission of the filter, a correction factor

that is dependent on the angle between the collimated light and the filter face must be added to Equation 46.

$$TM_{ij}{}^{\theta}{}_{final} = \left(\frac{TM_{ij}{}^{\theta}{}_{correction}}{TE_{ij}{}^{\theta}{}_{correction}} \right) TM_{ij}{}^{\theta}{}_{processed} \qquad \text{Equation 46}$$

where $TM^{\theta}{}_{final\ i,j}$ is the final processed image, $TM_{ij}{}^{\theta}{}_{correction}$ is the intensity value of the TM correction image, $TE_{ij}{}^{\theta}{}_{correction}$ is the intensity value of the TM correction image, and $TM^{\theta}{}_{processed\ i,j}$ is the TE and background corrected image. The θ indicates that each image must be corrected with the TM and TE correction files of the appropriate filter angle.

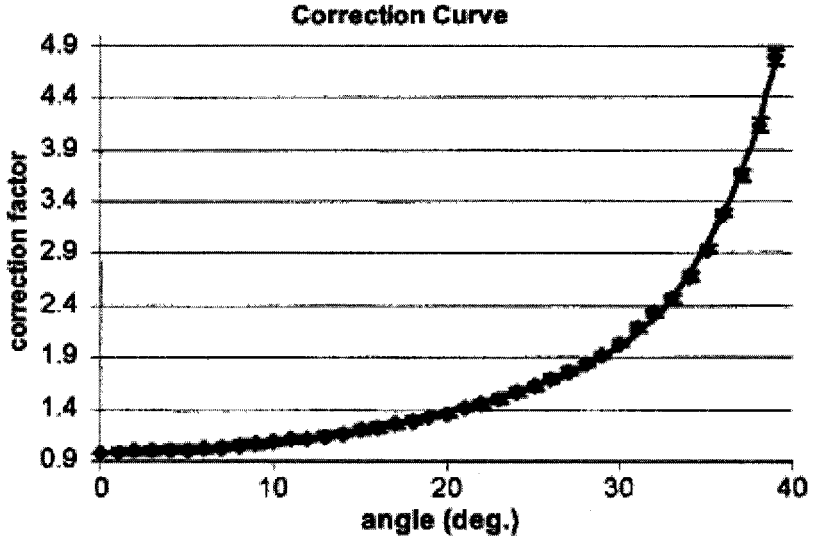

Figure 130. The correction factor shown above is the value of $\frac{TM_{ij}{}^{\theta}{}_{correction}}{TE_{ij}{}^{\theta}{}_{correction}}$ for a 905 nm bandpass filter as it is tilted off-normal.[12] Image is reproduced from the cited reference.

C.2 Temporal signal processing

The light intensity from the quartz halogen light source of the SPRM varies over time. The temperature of the substrate may also change during the time course of the experiment. Each of these contributes to temporal variations in the signal. To reduce this noise, Dr. Elain Fu and Dr. Tim Chinowsky have determined that a reference region – a portion of the image in which the refractive index does not change over time such as the

regions outside of the microchannel (i.e., the adhesive region for mylar devices or the PDMS areas for PDMS devices) – can be used to correct for these variations.[12] Average intensity values for the reference regions as well as the regions of interest (i.e., an antigen or antibody binding region) are calculated over the time course of the experiment. The initial average intensity value in the reference region corrects for the temporal variations in the signal with the following equation.

$$\overline{TM^{\theta}{}_{sample\_corrected}{}^{t_n}} = \left(\frac{\overline{TM^{\theta}{}_{sample}{}^{t_n}}}{\overline{TM^{\theta}{}_{reference}{}^{t_n}}} \right) \overline{TM^{\theta}{}_{reference}{}^{t_0}} \qquad \text{Equation 47}$$

where $\overline{TM^{\theta}{}_{sample\_corrected}{}^{t_n}}$ is the corrected average intensity value for the sample region of interest, $\overline{TM^{\theta}{}_{reference}{}^{t_0}}$ is the average intensity value for a reference region outside of the microchannel at time zero, $\overline{TM^{\theta}{}_{sample}{}^{t_n}}$ is the average intensity value for a sample region at a later time point "n", $\overline{TM^{\theta}{}_{reference}{}^{t_n}}$ is the average intensity value for a reference region outside of the microchannel at a later time point "t_n".

It is important to note this correction method is most effective when the reference region is located near the region of interest in the microchannel. This suggests that spatial and temporal variations are not entirely independent.

C.3 Calibration

To convert changes in reflectivity to changes in refractive index or changes in the percentage surface coverage, the SPRM must be calibrated. A five channel microfluidic device was placed onto a bare gold substrate. The buffer solution used during the experiment was introduced to one channel. Sodium chloride solutions of a variety of refractive indexes (typically ranging up to 0.01 refractive index units greater than the buffer solution) are introduced to the other four channels. A refractometer measures the refractive index of each solution. SPR images are taken at the appropriate imaging conditions. The images are processed as described in C.1 and the average intensity value

for each of the solution is calculated. From these measurements, a calibration curve relating the change in the refractive index to the change in reflectivity can be generated.

C.4 Calculation of change in reflectivity

To calculate the percent change in reflectivity of a region on a substrate, two SPRM images must be collected under the same imaging conditions and with the same bulk solution in the microchannel. Each image may be processed as described in C.1 or the images maybe be processed for spatial and temporal noise as described in C.1 and C.2. The processed images are subtracted, pixel by pixel yielding a difference image. Using Labview software developed by Dr. Elain Fu, a region of interest can be selected and the average change in intensity and the standard deviation are calculated. The regions of interest used in this dissertation were typically on the order of ~20 pixels x ~20 pixels. The average intensity values in the regions are calculated and subtracted from each other yielding the change in reflectivity in that region of the SPRM image.

C.5 Image foreshortening

The geometry of the SPRM foreshortens the images in one direction. Below is a trigonometric description of this effect courtesy of Dr. Elain Fu. Lengths in the x dimension are reduced by a factor of $cos\ \alpha$ where α is the angle of incidence equaling 64.8° in this SPRM. To accurately present the dimensions of an image, scale crosses – not scale bars – are used. Equations 1 and 2 are calculated from the yellow triangle. Equation 3 is the trigonometric relation for the red triangle.

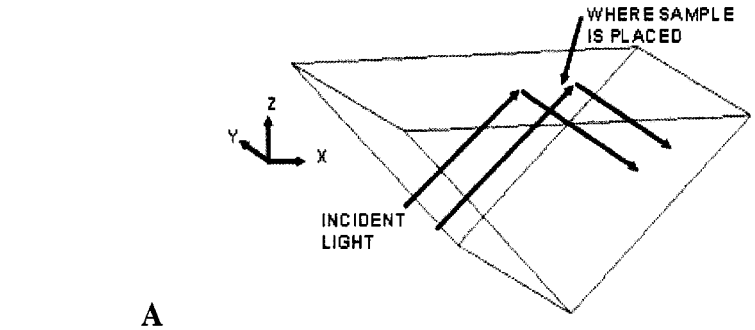

A

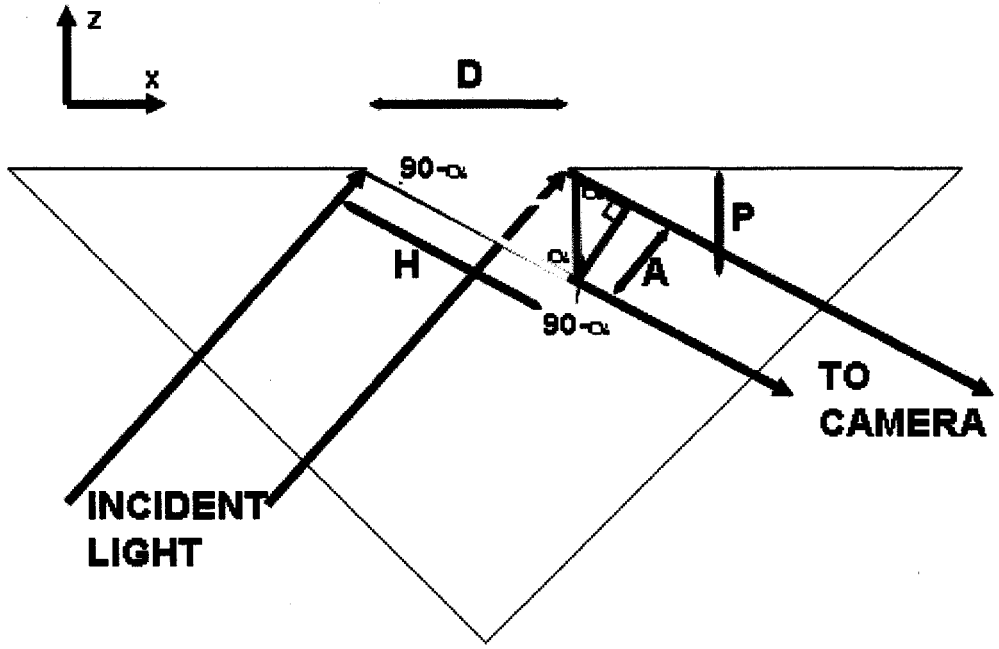

B

Figure 131. Diagram of the geometric constraints which result in image foreshortening. (A) Cartoon of the entire prism. (B) Cross-sectional view of the prism indicating geometric relationships.

(1) $\sin\alpha = \left(\frac{D}{H}\right)$
(2) $\cos\alpha = \left(\frac{P}{H}\right)$
(3) $\sin\alpha = \left(\frac{A}{P}\right)$
Combining equations (2) and (3) yields (4) $\sin\alpha\cos\alpha = \left(\frac{A}{H}\right)$
Combining equations (1) and (4) yields (5) $D\cos\alpha = A$

Appendix D: Non-specific adsorption of proteins to HS-PEG and bare gold surfaces

The following SPRM data give insight into the typical amounts of non-specific adsorption of bovine serum albumin (0.2 mg/mL) to two types of surfaces – a bare gold surface and HS-PEG monolayer on gold. Solutions of BSA were incubated in the microchannels for 20 minutes and then rinsed with PBS. The HS-PEG monolayer significantly reduced the non-specific adsorption. Each set of curves represents a region of interest on the substrate that was monitored. The data underwent TE and temporal correction (in Appendix C.1 and C.2 see Equation 45 and Equation 47).

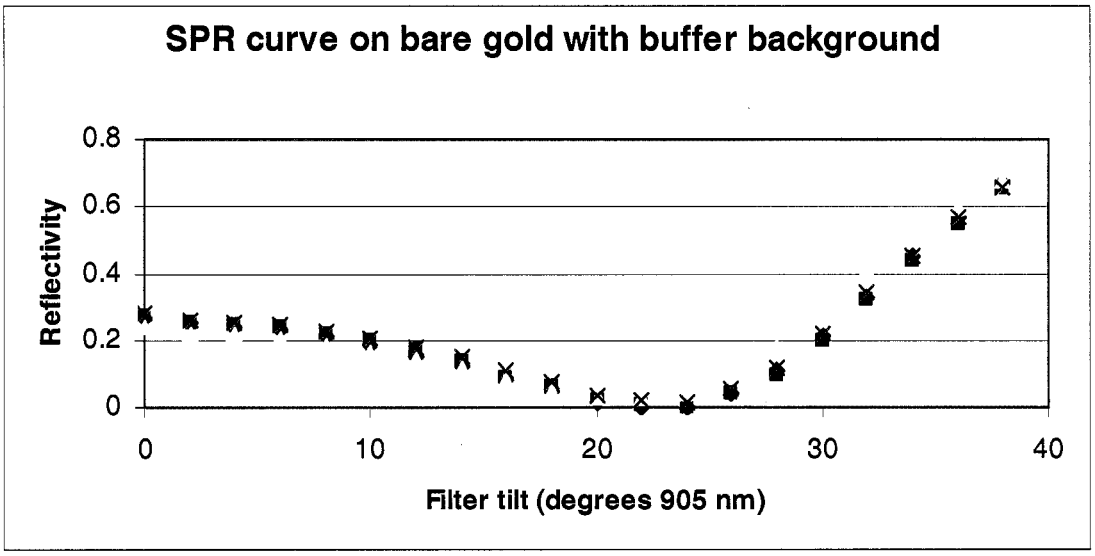

Figure 132. SPR curve as a function of the tilt of the interference filter on a bare gold surface with buffer background.

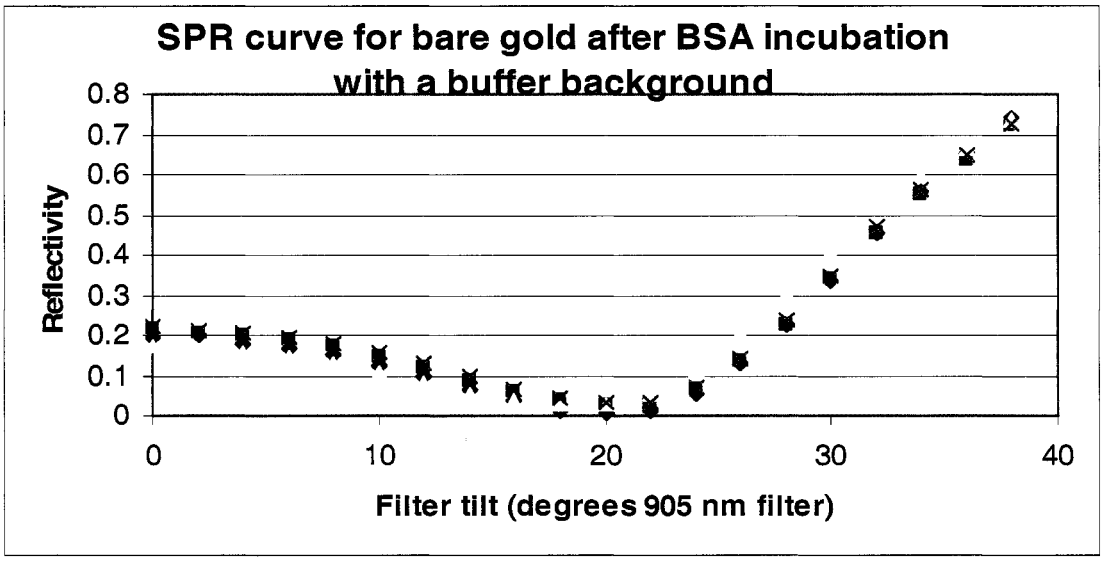

Figure 133. SPR curve as a function of the tilt of the interference filter on a bare gold surface with buffer background after incubation with BSA.

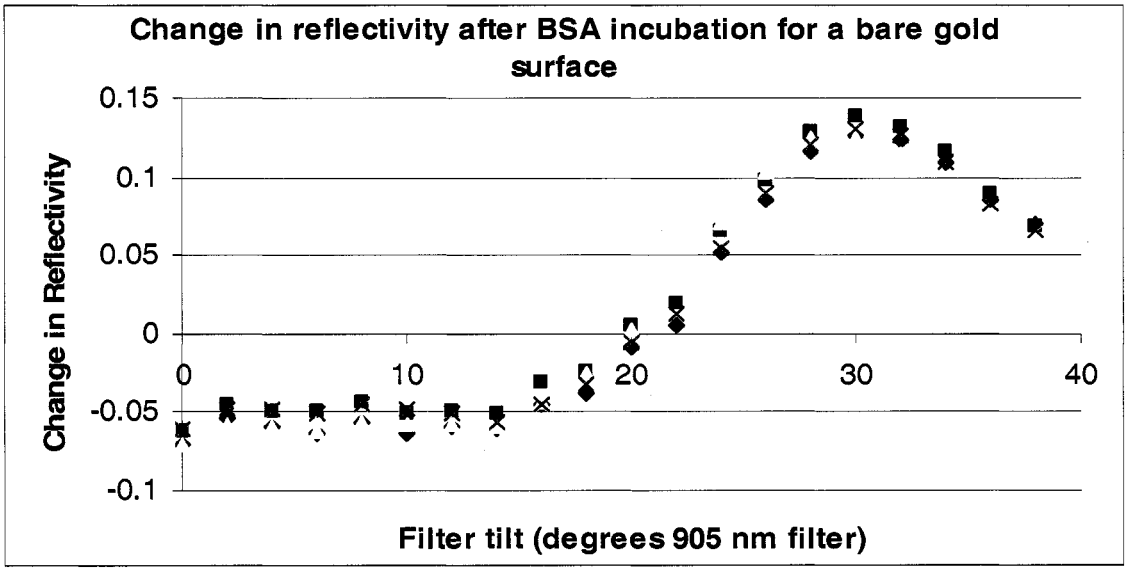

Figure 134. Change in SPR reflectivity as a function of the tilt of the interference filter on a bare gold surface with buffer background after incubation with BSA The curves from Figure 132 and Figure 133 were subtracted.

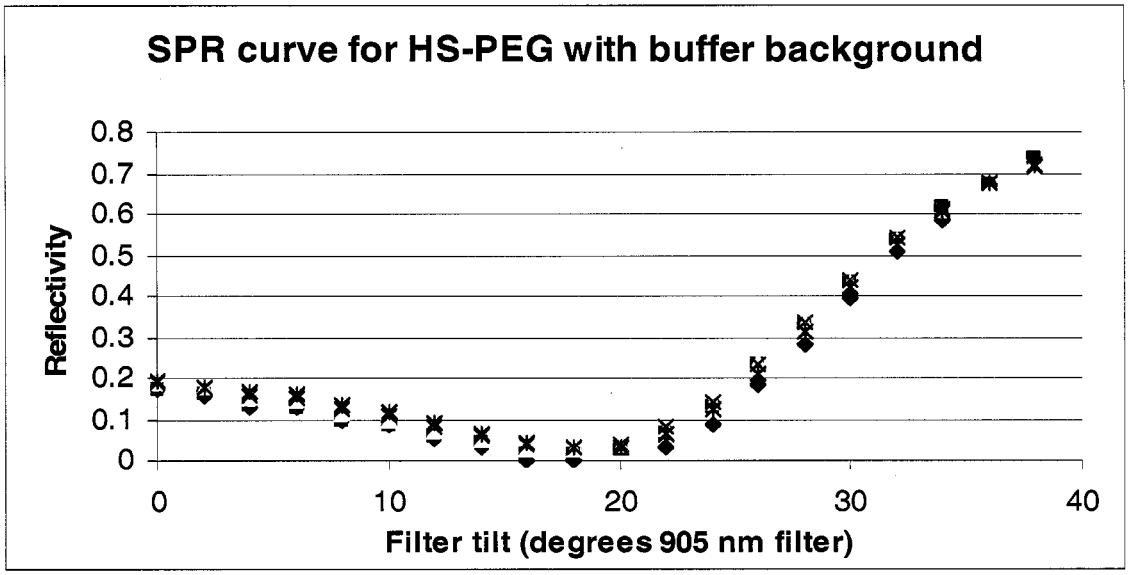

Figure 135. SPR curve as a function of the tilt of the interference filter on a HS-PEG gold surface with buffer background.

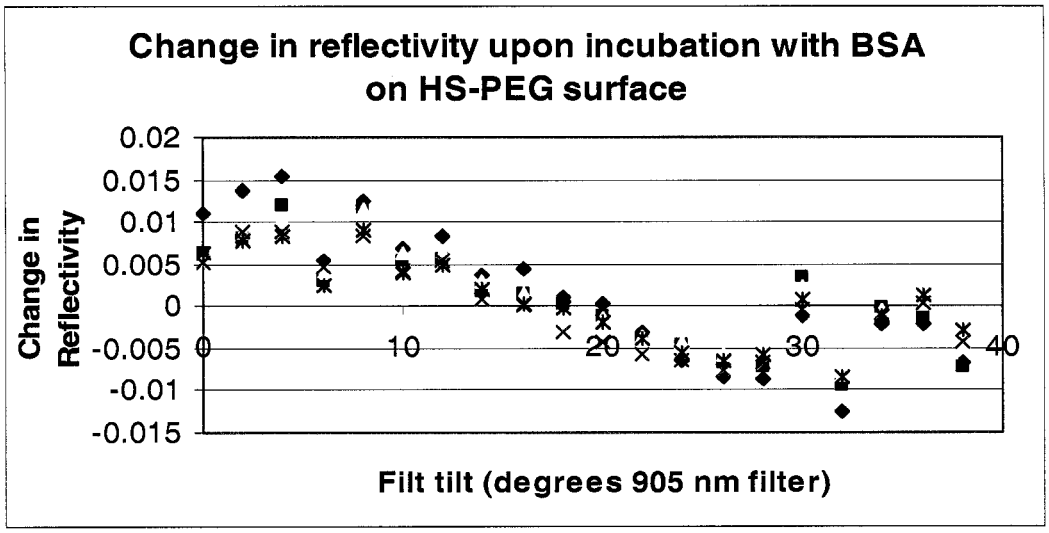

Figure 136. Change in SPR reflectivity as a function of the tilt of the interference filter on a HS-PEG gold surface after incubation with BSA.

Appendix E: List of manuscripts and proceedings

E.1 List of published articles and proceedings

Articles

1) Fu, E., Foley, J., and Yager, P. (2003). "Wavelength-tunable surface plasmon resonance microscope." *Review of Scientific Instruments*. **74**: 3182.
2) Fu, E., Chinowsky, T., Foley, J., Weinstein, J. and Yager, P. (2004). "Characterization of a wavelength -tunable surface plasmon resonance microscope." *Review of Scientific Instruments*. **75**: 2300.
3) Foley, J., Schmid, H., Stutz, R., and E. Delamarche. "Microcontact printing of proteins inside microstructures." *Langmuir*. **21**:11296.
4) Foley, J., Nelson, K., Mashadi-Hossein, A., Finlayson, B., and P. Yager. "Concentration Gradient Immunoassay (CGIA) II. Computational Modeling for Analysis and Optimization." *Analytical Chemistry*. (in press).
5) Nelson, K., Foley, J. and P. Yager. "The Competition Gradient Immunoassay (CGIA): A Rapid Competitive Immunoassay Based on Interdiffusion and Surface Binding in a Microchannel." *Analytical Chemistry*. (in press).

Conference Proceedings

1) Foley, J., Fu, E., and P. Yager. "T-sensor generated refractive index gradients: calibration of a SPR microscope." Microtas 2003 Proceedings, Oct 5-9, 2003.
2) Foley, J., Finlayson, B., and P. Yager. "Spatial and temporal variations in antigen binding to immobilized antibodies for determining diffusion coefficients." Chips to Hits Conference. September 20-23, 2004. Boston, MA.
3) Foley, J., Schmid, H., Stutz, R. and E. Delamarche. "Engineering microfluidic chips with integrated binding sites for ultraminiaturized immunoassays." Microtas 2005 Proceedings, Oct 9-12, 2005.
4) Fu, E., Foley, J., Chen, J., Wiley, B., Xia, Y., and P. Yager. "Wavelength-dependent signal amplification of fold nanocage tags for surface plasmon resonance imaging." Microtas 2005 Proceedings, Oct. 9-12, 2005.
5) Nelson, K., Foley, J., Mashadi-Hossein, A., and P. Yager. "Simultaneous,

multiple analyte immunoassays on a disposable microfluidic device." Microtas 2005 Proceedings, Oct. 9-12, 2005.

E.2 List of planned manuscripts

1. A manuscript or chapter entitled "Insights into the design of microfluidic immunoassays: Experiment and computational model of an indirect standard flow immunoassay" will be submitted. This manuscript will include work from Chapter 6.
2. A manuscript entitled "Surface characterization of microcontact printed proteins on gold surfaces" will be submitted. This manuscript will include work from Chapter 3.
3. A manuscript entitled "Influence of a chaotic microfluidic mixer on analyte binding in flow immunoassays" will be submitted. This manuscript will include work from Chapter 8.

Appendix F: Surface binding profile in chevron microchannels with different chevron depths.

The chevron depth (*h* in Figure 88) in the experimental system (56 microns) is different than the chevron depth in the model geometry (90 microns), detailed in Chapter 8, due to the fact that the original SU8 mold broke during the course of experiments. To determine if the change in the chevron depth significantly alters the surface binding pattern of the streptavidin, two computational models were completed. The depth of the base microchannel was constant in the models (90 microns – indicated as the "standard" chevron depth). Two chevron depths were studied (h=30 microns and h=120 microns).

F.1 Velocity profiles in chevron microchannels

The overall velocity profiles mirror previous results presented in Chapter 8. Therefore, the quantitative measures *D* and *F* are more valuable than the images of the velocity profile in each dimension when comparing the importance of the chevron depths.

For the chevron depth of 30 microns, like the chevron depth of 90 microns, $D_{x\text{-velocity}}$ (Table 54) for the maximum velocity (~30%) is ~50% greater than the $D_{x\text{-velocity}}$ for the minimum velocity (~20%). However, the magnitude of the x-velocity with the narrower chevron is significantly reduced to ~30% and ~-20% from ~50% and ~-30% for the chevron depth of 90 microns (Table 14). The reduction in the magnitude of the x-velocity which represents velocity toward and away from the binding surface is expected for the narrower chevron as the fluid does not fill as deep of a chevron microstructure. The value of $D_{y\text{-velocity}}$ (Table 54) for the maximum velocity is ~155% which is a reduction compared to ~160% for the chevron depth of 90 microns (Table 14). Given the numerical errors in the model, this difference does not conclusively indicate a major alteration in the maximum y-velocity occurred due to the altered geometry. The $D_{z\text{-velocity}}$ for the minimum and maximum are comparable for the 90 micron chevron (~+/-32%) versus the

30 micron chevron (~+/-27%). Therefore, the minimum and maximum values in that dimensions are not significantly altered by the change of chevron depth.

Table 54. D values. Normalized value of the maximum and minimum velocities in each dimension for the chevron microchannel. Model results. Depth of chevron is 30 microns (h=30 microns).

Chevron, h= 30 microns	5 nL/s		25 nL/s		50 nL/s	
	Max	Min	Max	Min	Max	Min
$D_{x\text{-velocity}}$	29	-20	28	-20	32	-20
$D_{y\text{-velocity}}$	154	-1	154	-1	156	-2
$D_{z\text{-velocity}}$	25	-27	25	-27	29	-27
$D_{velocity\ field}$	155	0	155	0	156	0

The fraction of the kinetic energy (Table 55) due to fluid velocity in the x-dimension for the narrower chevron (30 microns) is ~35% of the fraction of kinetic energy for the standard chevron depth (90 microns) (Table 15). The fraction of the kinetic energy (Table 55) in the z-dimension for the narrower chevron (30 microns) is ~40% of the fraction of kinetic energy due to the fluid velocity in the z-dimension for the standard chevron depth (90 microns) (Table 15). These results indicate that transverse flow and flow to and from the surface are reduced. Again this result is expected, as the narrower the chevron the more similar the geometry is to the straight microchannel, which has uni-directional flow. Furthermore, the chevron depth is 33% of the original depth which correlates well with the percentage of the original fraction of the energy ,due to the fluid velocity in the z- and x- dimensions for the narrower chevron microchannel.

Table 55. F values. Fraction of energy due to the velocity in each dimension. Model Results. Chevron microchannel with a depth of 30 microns (h=30 microns).

Chevron, h= 30 microns	5 nL/s	25 nL/s	50 nL/s
$F_{x\text{-dimension}}$	2.9E-03	2.9E-03	2.9E-03
$F_{y\text{-dimension}}$	9.9E-01	9.9E-01	9.9E-01
$F_{z\text{-dimension}}$	4.7E-03	4.7E-03	4.8E-03

For the deeper chevron depth (120 microns), the values of *D* (Table 56) are very similar to the values calculated for the standard chevron depth (90 microns) (Table 14). This

result indicates that the maximum and minimum velocity values are comparable for both geometries.

Table 56. D values. Normalized value of the maximum and minimum velocities in each dimension for the chevron microchannel. Model results. Depth of chevron is 120 microns (h=120 microns).

Chevron, h=120 microns	5 nL/s		25 nL/s		50 nL/s	
	max	Min	Max	Min	Max	Min
$D_{x\text{-velocity}}$	49	-32	47	-31	49	-32
$D_{y\text{-velocity}}$	158	0	158	-2	158	-1.9
$D_{z\text{-velocity}}$	30	-30	29	-29	29	-30
$D_{\text{velocity field}}$	160	0	160	0	160	0

The microchannel with the deeper chevron depth (120 microns) may not alter the maximum and minimum velocity, but the total kinetic energy contributed in each velocity dimension is altered. There is an increase in the total energy contributed in the x-dimension and the z-dimension. The fraction of the kinetic energy (Table 57) due to fluid velocity in the x-dimension for the narrower chevron (120 microns) is ~145% of the fraction of kinetic energy for the standard chevron depth (90 microns) (Table 15). The fraction of the kinetic energy (Table 57) in the z-dimension for the deeper chevron (120 microns) is ~135% of the fraction of kinetic energy, due to the fluid velocity in the z-dimension for the standard chevron depth (90 microns) (Table 15). These results indicate that transverse flow and flow to and from the surface are increased. Once again, the chevron depth is 133% of the original depth, which correlates well with the percentage of the original fraction of the energy due to the fluid velocity in the z- and x-dimensions for the deeper chevron microchannel.

Table 57. F values. Fraction of energy due to the velocity in each dimension. Model Results. Chevron microchannel with a depth of 120 microns (h=120 microns).

Chevron, h= 120 microns	5 nL/s	25 nL/s	50 nL/s
$F_{x\text{-dimension}}$	1.2E-02	1.2E-02	1.2E-02
$F_{y\text{-dimension}}$	9.7E-01	9.7E-01	9.7E-01
$F_{z\text{-dimension}}$	1.6E-02	1.6E-02	1.6E-02

F.2 Surface binding profiles of streptavidin in chevron microchannels

The model results (Figure 137) qualitatively indicate that the deeper the chevron depth, (h=30 microns versus h=120 microns) the more pronounced the pattern of the streptavidin surface binding profile. The deeper the chevron, the more distinct the reduction of the binding of streptavidin that occurs in the midline of the channel and the more significant the increase in binding due to the narrowing of the microchannel (indicated by black arrows along the microchannel in Figure 137).

However, even when the chevron depth is reduced to 30 microns (Figure 137A), the influence of the chevron on the binding profile is still apparent in the reduction in the binding at the midline of the channel and in a moderate increase in binding in the narrower region of the microchannel. Therefore, experimental results (where h=56 microns and the base microchannel is 90 microns) should still exhibit a similar binding profile to the model results.

The model results (Figure 138A and B) do not indicate that one chevron depth is more efficient at increasing the total amount of streptavidin bound to the surface at flow rate of either 5 nL/s or 50 nL/s over time.

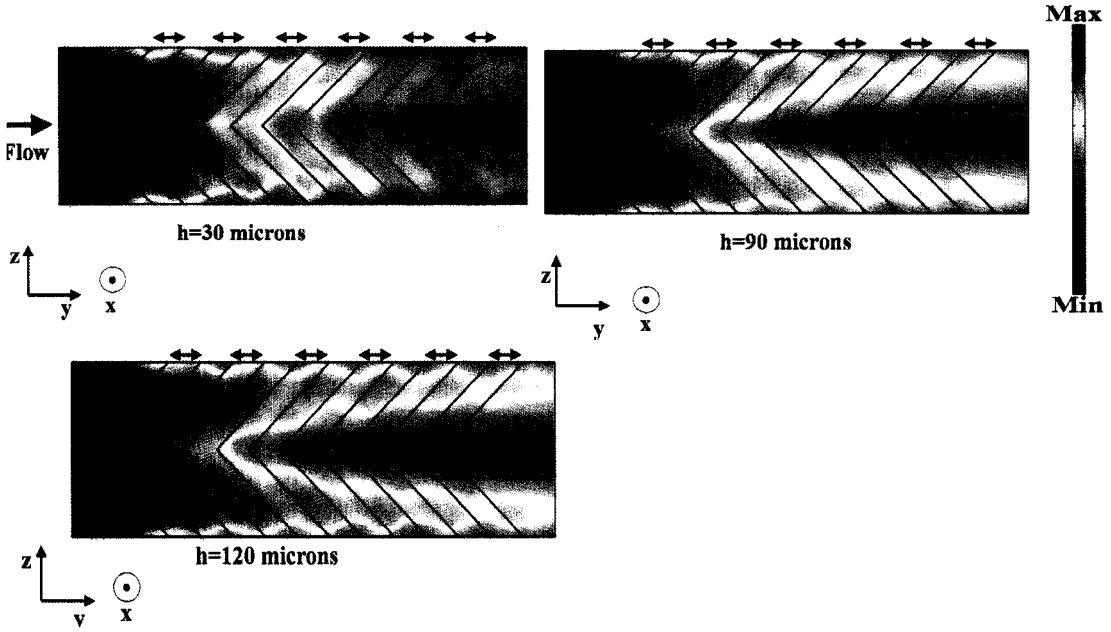

Figure 137. Binding profile of streptavidin to biotinylated surface (moles/m^2) for chevron microchannel with different chevron depths (h): 30 microns, 90 microns and 120 microns respectively. Model results. The streptavidin concentration introduced to the microchannel is 20 nM. Re= 0.01. Pe=135.1 Q=5nL/s. Time=700 seconds. The arrows indicate the deepest portion of the channel where the chevron structure is present. The maximum surface concentration is 3.99×10^{-8} moles/m^2. The minimum surface concentration is 0 moles/m^2.

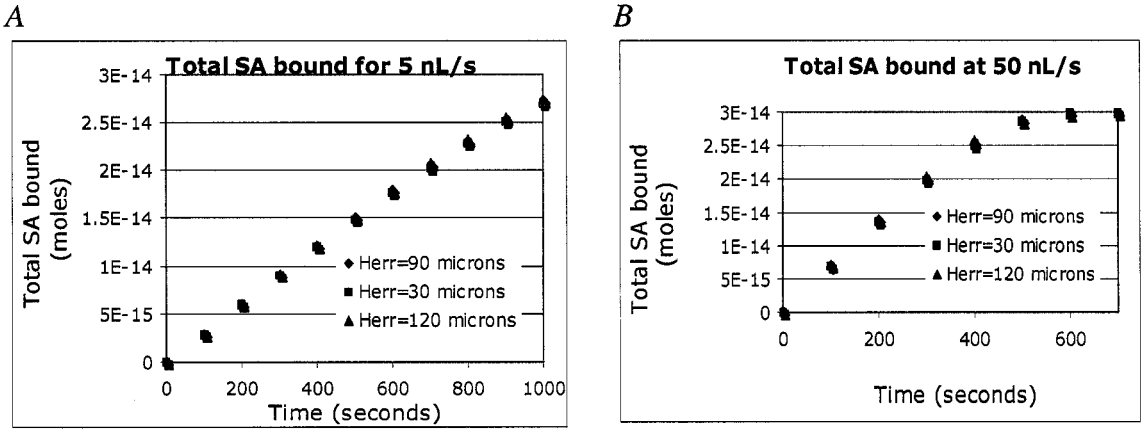

Figure 138. Model results. Total streptavidin bound to the surface for the chevron microchannel with a range of chevron depths (h) at (A) a flow rate of 5 nL/s and (B) a flow rate of 50 nL/s. The streptavidin concentration introduced to the microchannel is 20 nM. The theoretical maximum for total SA binding to the surface is 3×10^{-14} moles.

Appendix G: Surface binding profile in a square microchannel.

The chevron microchannel differs from a straight microchannel in two ways:

(1) the addition of equally spaced chevrons on top of the base microchannel

(2) the chevrons are at a 45 degree angle to the direction of flow

In Chapter 8, the surface binding profile of streptavidin in a chevron microchannel is compared to the binding profile in a straight microchannel. To computationally explore the influence of simply introducing ducts perpendicular to flow on top of a straight microchannel, the velocity and binding profiles of a different microchannel, the square microchannel (Figure 139), were modeled with COMSOL.

The purpose of this model was to explore the influence of the widening and narrowing of the channel depth (x-dimension) on the streptavidin surface binding profile, independent of any angled geometric features. Given the geometry, there should be velocity components in only two – not three – dimensions: the x-dimension (toward and away from the binding surface) and the y-dimension (down the length of the channel).

COMSOL models were completed as described in the Appendix and Chapters 5 and 8, with a streptavidin solution introduced to the microchannel and a BAT/PEG thiol functionalized gold surface. When solving the Navier-Stokes mode, the mesh consisted of 8,988 elements and had 91,171 degrees of freedom. When solving the convection-diffusion and surface binding modes, the mesh consisted of 60,817 elements and had 435,322 degrees of freedom.

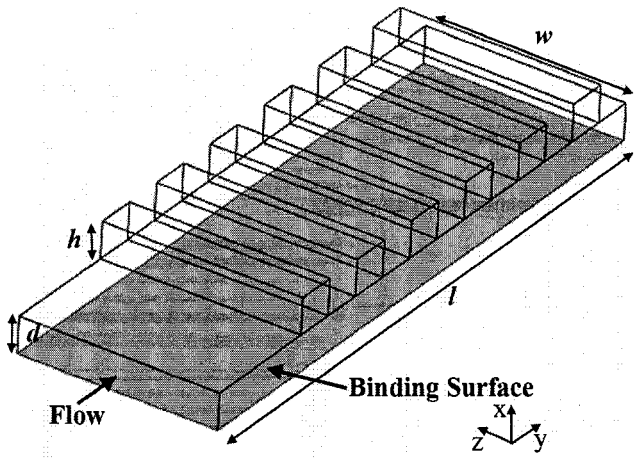

Figure 139. Square microchannel model geometry where d=90 microns, h= 90 microns, w=500 microns, and l=1.5 mm. The binding surface is indicated.

G1. Velocity profiles in the square microchannel.

The widening and narrowing of the square microchannel (x-dimension) alters the local fluid velocity (Figure 140). In the narrow regions (just the base microchannel), the average velocity is highest where the duct is not present whereas it lowest where a duct is present. It is important to note that the change in the fluid velocity is not a step function but gradually changes over the length (y-dimension) of the duct. Furthermore, the velocities within the ducts approach zero and are significantly lower than the velocity in the base microchannel.

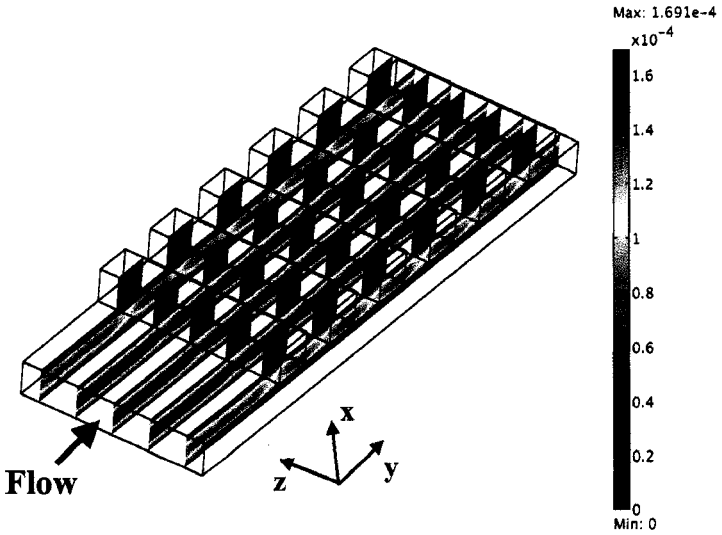

Figure 140. Velocity profile (m/s) in the square microchannel. Model results. The flow rate is 5 nL/s. Reynolds number = 0.01. Q=5 nL/s.

When the fluid approaches a duct, there will be an x-velocity component away from the binding surface (x-dimension) (Figure 141A) as the fluid travels to fill the duct. A positive velocity, indicated in the color red, indicates a velocity component away from the binding surface. The largest magnitude of the x-velocity occurs near the midline of the channel. At the end of a duct, the fluid must travel out of the duct and there is an x-velocity component toward the surface (x-dimension) (Figure 141A). In Figure 141, a negative velocity, indicated by the color blue, represents a velocity component directed towards the binding surface. Near the binding surface (x=30 microns Figure 141B) the x-velocity is still present (~9×10^{-6} m/s) but not nearly as large near the midline (~2×10^{-5} m/s at x=100 microns Figure 141C). At the top of the duct (x=150 microns Figure 141D), the x-velocity profile is altered, with the fluid being directed toward the surface at the beginning of the duct and away from the surface at the end of the duct. This suggests that there is a recirculation zone present at the top of the duct. However, given the magnitude of the x-velocity at x=100 microns (~2×10^{-6} m/s) compared to the magnitude of the x-velocity at the midline (~2×10^{-5} m/s) and the location of the recirculation region (150 microns away from the binding surface), the influence of the recirculation zone on the binding profile will not be significant.

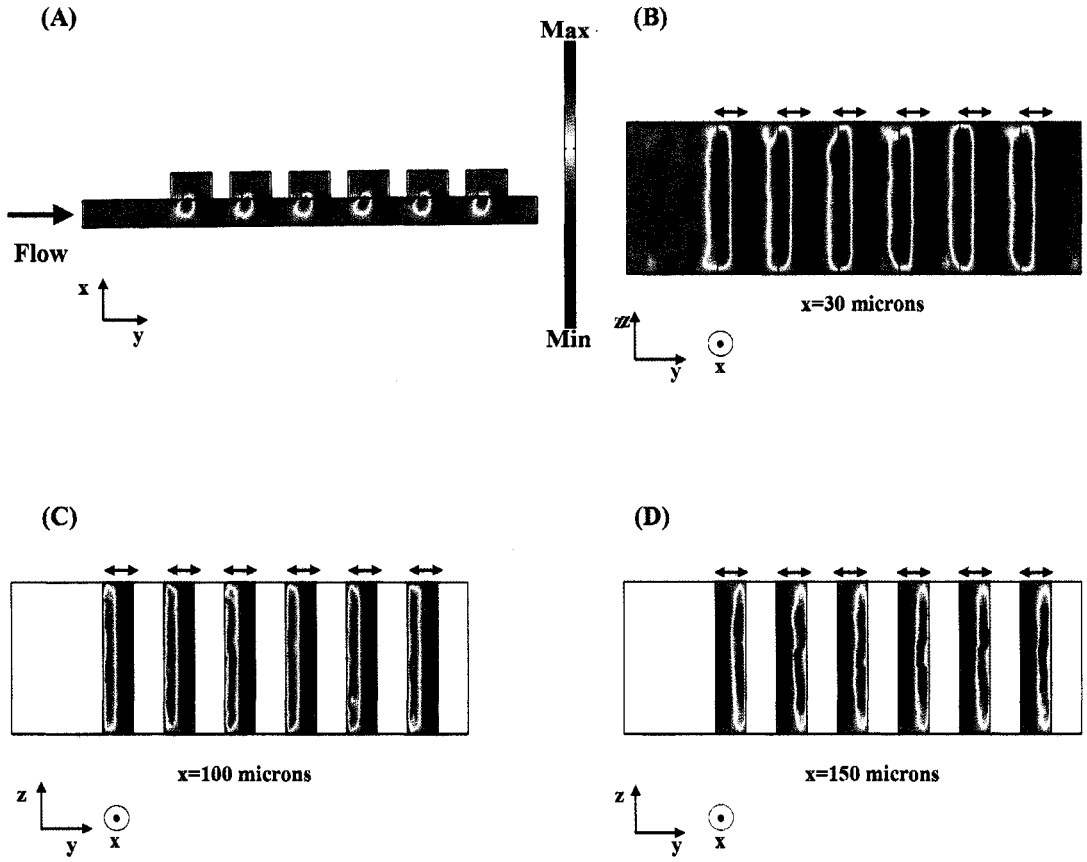

Figure 141. X-velocity profile (m/s) in the square microchannel. Model results. The flow rate is 5 nL/s. Reynolds number = 0.01. Q=5 nL/s. The arrows indicate the deepest portion of the channel where the rectangular structure is positioned above the base microchannel. The maximum velocity and minimum velocity are 3.66×10^{-5} m/s and -3.74×10^{-5} m/s in (A). The maximum velocity and minimum velocity are 9.54×10^{-6} m/s and -9.41×10^{-6} m/s at x= 30 microns. The maximum velocity and minimum velocity are 2.00×10^{-5} m/s and -1.8×10^{-5} m/s at x= 100 microns. The maximum velocity and minimum velocity are 2.66×10^{-6} m/s and -2.74×10^{-6} m/s at x= 150 microns.

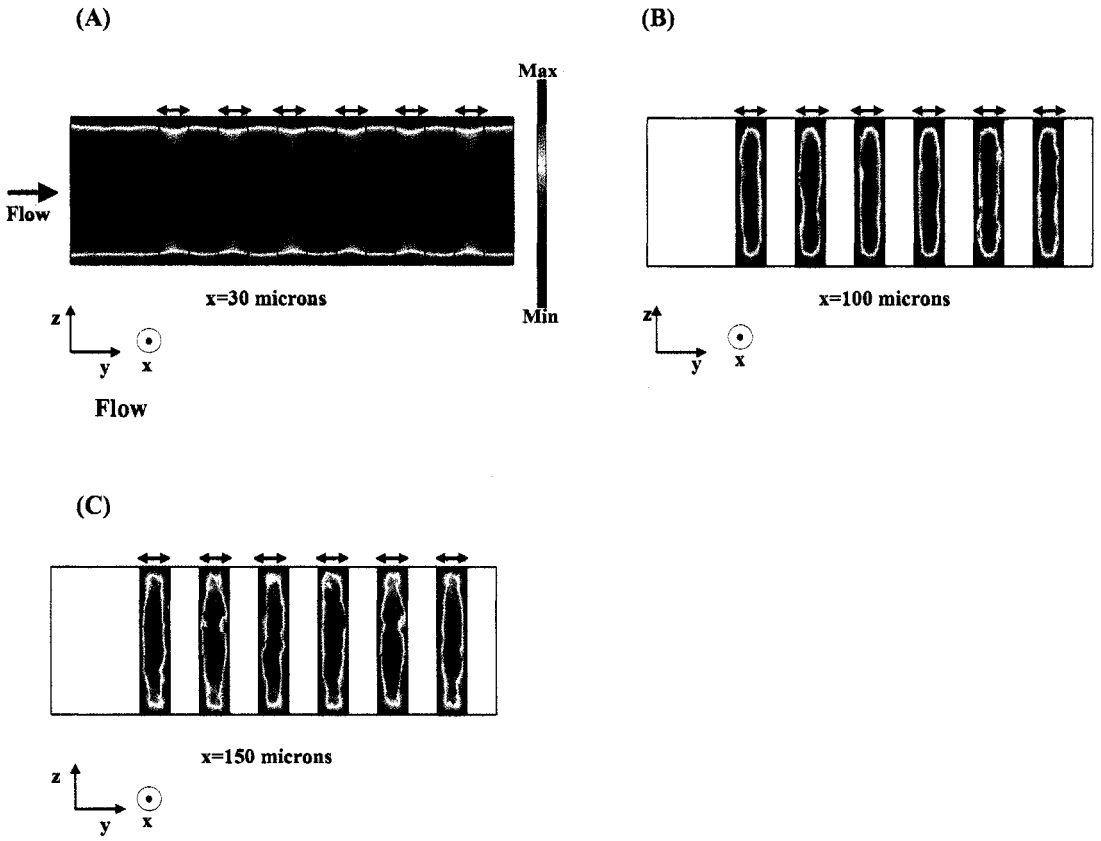

Figure 142. Y-velocity profile (m/s) for the square microchannel. Model results. The flow rate is 5 nL/s. Reynolds number = 0.01. Q=5 nL/s. The arrows indicate the deepest portion of the channel where the rectangular structure is positioned above the base microchannel. The maximum velocity and minimum velocity are 1.50×10^{-4} m/s and -4.73×10^{-19} m/s at x= 30 microns. The maximum velocity and minimum velocity are 4.14×10^{-5} m/s and -9.15×10^{-6} m/s at x= 100 microns. The maximum velocity and minimum velocity are 0 m/s and -1.45×10^{-6} m/s at x= 150 microns.

The y-velocity (Figure 142) shows the most significant change in its magnitude near the surface (x=30 microns) as a result of the widening and narrowing of the microchannel (Figure 142A) with an increase in the maximum y-velocity in the narrow regions ($\sim1.5\times10^{-4}$ m/s indicated by the black arrows at the side of the microchannel) and a reduction in maximum y-velocity ($\sim1.1\times10^{-4}$ m/s) in the wide regions (x-dimension). Near the midline of the microchannel and within the duct of the microchannel (x=100 microns Figure 142B), the magnitude of the maximum y-velocity is reduced ($\sim4\times10^{-5}$ m/s). The y-velocity profile at x=100 microns also suggests that the fluid has traveled into the duct, is then pushed through the duct (y-dimension), and is subsequently pushed down towards the base microchannel. Near the top of the duct (x=150 microns), the y-

velocity (Figure 142C) shows some interesting behavior. The maximum velocity, indicated in red and located at the walls, is ~0 and fulfills the no slip condition at the microchannel wall. However, the minimum velocity (-3×10^{-6} m/s) is located at the middle of the microchannel suggesting the fluid is traveling backwards. This combined with the inverted x-velocity profile (Figure 141D) once again is indicative of a small recirculation zone at the top of the duct. A recirculation zone has been identified in another computational model of a similar channel geometry.[244]

$$D_{n-velocity} = \frac{velocity_{\max or \min} square}{velocity_{average} straight} * 100 \qquad \text{Equation 48}$$

As discussed in Chapter 8, when assessing the influence of each velocity component (x- and y-) on the overall velocity, it is important to compare the maximum and minimum of each velocity component, as well as the total contribution of each velocity component to the overall velocity field, to a common standard. Once again, the values *D* and *F* will be used.

To normalize the maximum and minimum velocities in each dimension(x-, y- and z-dimensions), they were divided by the average velocity in a straight microchannel and multiplied by 100 yielding a value termed "*D*" (Equation 48 and Table 58). The values of *D* remain constant over a large range of flow rates, which can be expected under laminar flow conditions. The data suggests that the maximum magnitude of the $D_{\text{x-velocity}}$ is significant – ~25% of the average velocity of a straight microchannel. Furthermore, unlike the x-velocity in the chevron microchannel, the minimum and maximum velocities are equal in magnitude, indicative of a symmetric system in which the fluid travels toward and away from the surface with the same magnitude of velocity. The $D_{\text{y-velocity}}$ for the maximum velocity is 152%, which is expected since the maximum velocity occurs in the narrow regions of the microchannel which has the same dimension as the straight microchannel standard and it is well-known the maximum velocity in a straight channel is 1.5 times greater than the average velocity. The two percent error is within the error of the numerical simulation. The negative value (-8%) for the $D_{\text{y-velocity}}$ minimum could possibly arise from the backward flow (-y dimension) occurring in the top of the duct and previously shown at x=150 microns (Figure 142C). The fact that there is $D_{\text{z-velocity}}$

suggests that there are numerical artifacts and that this component of the velocity (data not shown) occurs in only a small fraction of the microchannel, particularly near the walls and the outlet.

Table 58. D values. Normalized value of the maximum and minimum velocities in each dimension for the square microchannel. Model results.

Square	5 nL/s		50 nL/s	
	max	min	Max	min
$D_{x\text{-velocity}}$	25	-25	25	-25
$D_{y\text{-velocity}}$	152	-8	152	-8
$D_{z\text{-velocity}}$	6	-5	6	-5
$D_{velocity\ field}$	157	0	152	0

Square	100 nL/s		250 nL/s		500 nL/s	
	max	min	Max	min	max	min
$D_{x\text{-velocity}}$	25	-25	25	-25	25	-25
$D_{y\text{-velocity}}$	152	-8	152	-8	152	-8
$D_{z\text{-velocity}}$	6	-5	6	-5	6	-5
$D_{velocity\ field}$	152	0	152	0	152	0

Table 59. F values. Fraction of energy due to the velocity in each dimension. Model Results. Square microchannel.

Square	5 nL/s	50 nL/s	100 nL/s	250 nL/s	500 nL/s
$F_{x\text{-dimension}}$	9.1E-03	3.9E-03	3.9E-03	3.9E-03	3.9E-03
$F_{y\text{-dimension}}$	9.9E-01	1.0E+00	1.0E+00	1.0E+00	1.0E+00
$F_{z\text{-dimension}}$	5.7E-05	5.3E-05	5.3E-05	5.3E-05	5.4E-05

F is the fraction of total kinetic energy contributed by the velocity in the x-, y-, or z-dimensions. The value of *D* gives an understanding of the relative influence of the maximum or minimum value of a velocity component. However, it does not give any insight into how significant to the overall velocity field that velocity component is, as the maximum or minimum velocities could occur in a large or small fraction of the microchannel volume. Calculating the fraction of overall kinetic energy each velocity component contributes, gives a sense of the relative significance each velocity component over the entire channel volume.

The results (Table 59) indicate that the most significant velocity component is in the y-dimension, with nearly 100% of the kinetic energy being directed in that dimension

(please note the values were rounded to two significant digits). The x-dimension's energy contribution is less than 1% suggesting it does not have a significant role in overall fluid velocity. This corroborates the qualitative results presented in the image of the velocity profile (Figure 140), in which the x-velocity equals zero in most of the microchannel. The value of $F_{z\text{-dimension}}$ is two orders of magnitude smaller than $F_{x\text{-dimension}}$ further suggest that it can be attributed to numerical errors.

G2. Surface binding profiles of streptavidin in the square microchannel.

The surface binding profile over time of streptavidin to the biotin-functionalized surface (Figure 143) indicates that there is a variation in the binding profile in the narrow and wide portions of the microchannel (x-dimension). The narrower portions, where the fluid is moving faster, show increased binding. Other than the variation in the binding pattern that mirrors the channel depth (x-dimension), the binding profile shows strong similarity to the straight microchannel.

Experimentally – given the SPR propagation length and the magnification of the instrument – these subtle features were not apparent. However, the model serves to give insight into the influence of the channel depth on the binding profile.

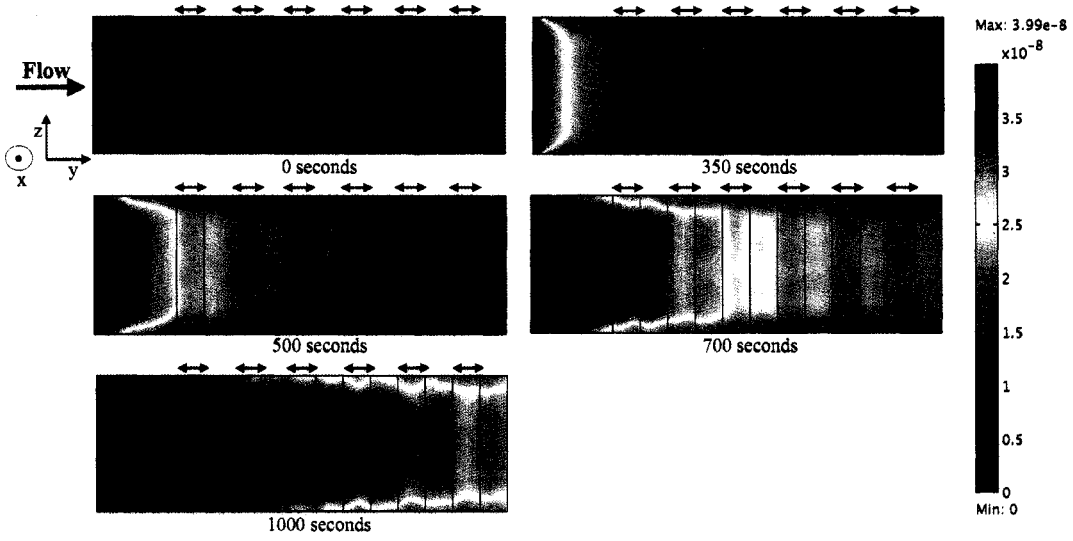

Figure 143. Surface concentration profile of bound streptavidin (moles/m^2) in the square microchannel. Model results. Streptavidin inlet concentration = 20 nM = 2×10^{-5} moles/m^3. Time = 350 seconds. Re= 0.01. Pe=135.1. Q=5 nL/s. The arrows indicate the deepest portion of the channel where the rectangular structure is positioned above the base microchannel. The theoretical maximum surface binding concentration is 3.99 $\times10^{-8}$ moles/m^2.

The bulk concentration profile of streptavidin in the microchannel (Figure 144) also shows strong similarity to the concentration profile within a straight microchannel. Near the binding surface there is a significant depletion zone, and the depth of the depletion zone becomes slightly larger further downstream. The location within the microchannel where the ducts occur (the deeper portion of the channel (x-dimension)) and the velocity is reduced has a slightly larger depletion zone (Figure 144B).

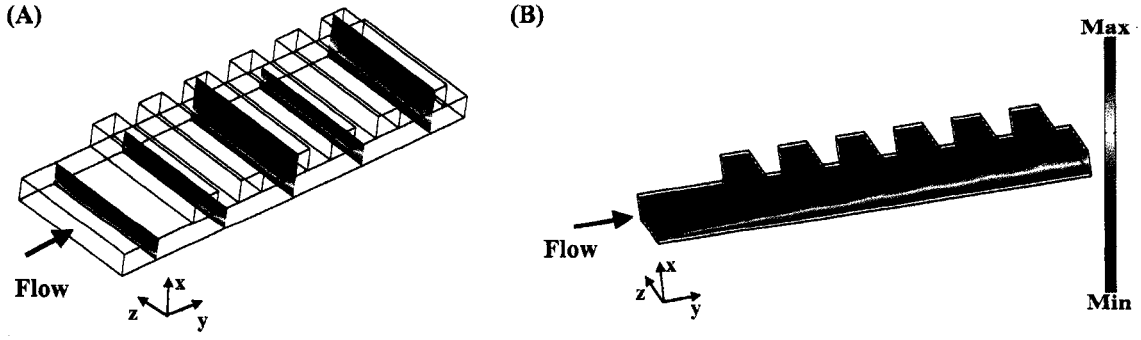

Figure 144. Concentration profile of streptavidin in the square microchannel channel (moles/m^3). Model results. The maximum concentration is 2.01 $\times10^{-5}$ moles/m^3 and 0 moles/m^3. Streptavidin inlet concentration = 20 nM = 2×10^{-5} moles/m^3. Time = 350 seconds. Re= 0.01. Pe=135.1. Q=5 nL/s. The arrows indicate the deepest portion of the channel where the chevron structure is present.

The variation in the bulk concentration profile of streptavidin as a function of the channel depth is illustrated in Figure 145. Flow is from left to right. Near the surface (x=1 micron), the concentration of streptavidin is quickly depleted as the protein binds to the surface, and the concentration approaches zero. Further away from the surface, the concentration of streptavidin increases. The concentration is greatest at all depths on the left (toward the inlet of the device), as the solution has yet to be depleted of streptavidin. In particular, at x=30 microns, the concentration of streptavidin mirrors the geometry, with an increase in concentration in the narrower portion of the channel. This result mirrors the surface binding profile in which more protein binds in the shallow (x-dimension) portion of the channel.

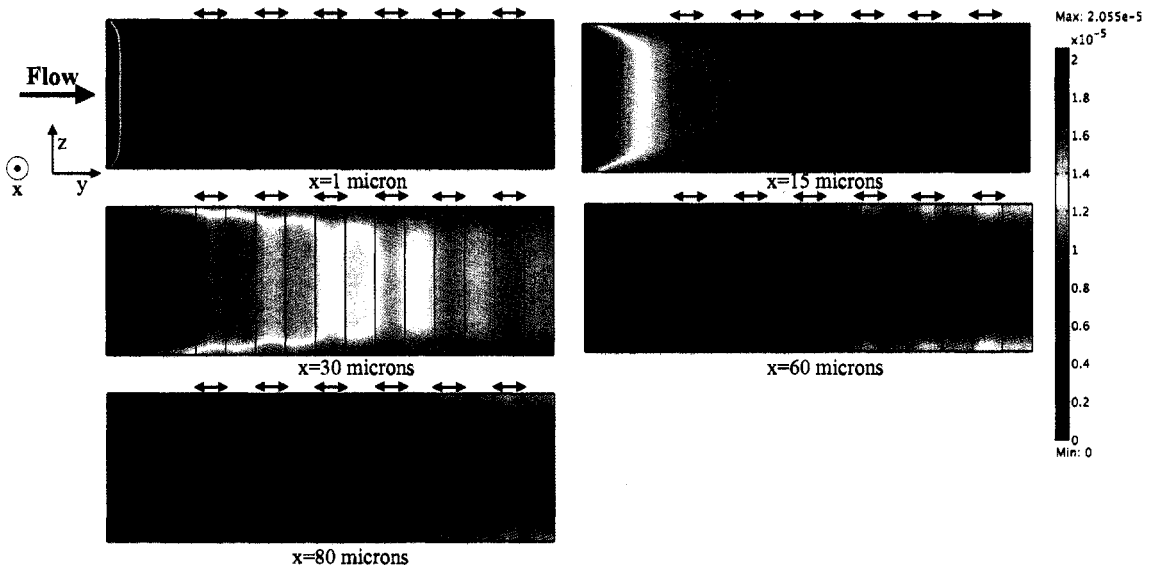

Figure 145. Concentration profile of streptavidin in the square microchannel (moles/m^3) as a function of distance from the binding surface (x-dimension). Model results. Streptavidin inlet concentration = 20 nM = 2×10^{-5} moles/m^3. Time = 350 seconds. Re= 0.01. Pe=135.1. Q=5 nL/s. The arrows indicate the deepest portion of the channel where the rectangular structure is positioned above the base microchannel.

At higher flow rates (50 nL/s versus 5 nL/s), the model results indicate that the depth of the depletion zone is reduced and more streptavidin is bound to the surface at time=350 seconds (Figure 146) than at the lower flow rate. These results are expected as (1) more protein has been introduced to the microchannel and (2) the velocity profile is altered so that the influence of diffusional and convective transport near the surface is altered, such that the depletion zone depth is reduced. Given the higher Peclet number, once again, the

model results exhibit more numerical noise. However, the general binding pattern in which more binding occurs in the narrow regions remains unchanged (Figure 146B).

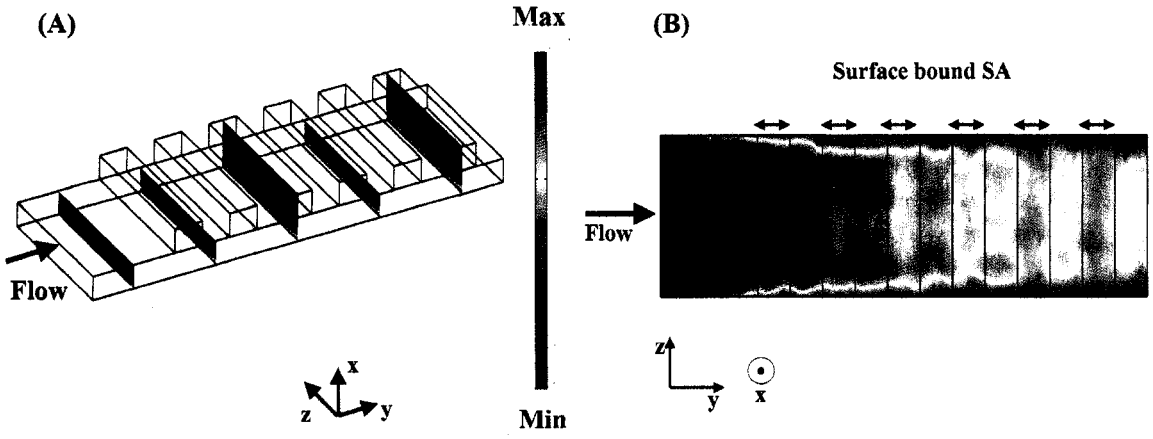

Figure 146. Influence of velocity on binding in the square microchannel. Model results. Q=50 nL/s. (A) Concentration of streptavidin in the microchannel (moles/m^3). The maximum concentration is 2.02 $\times 10^{-5}$ moles/m^3 and 0 moles/m^3. (B) Binding profile of streptavidin to biotinylated surface (moles/m^2). The maximum SA surface binding concentration is 3.99 $\times 10^{-8}$ moles/m^2. The minimum SA surface binding concentration is 0 moles/m^2.The streptavidin concentration introduced to the microchannel is 20 nM. Time = 350 seconds. Re= 0.1. Pe=1351. Q=50nL/s. The arrows indicate the deepest portion of the channel where the rectangular structure is positioned above the base microchannel.

G3. Comparison of the streptavidin surface binding profile and the velocity profiles in the square microchannel.

To make direct correlations between the velocity profile and the surface binding profile of streptavidin, line profiles of the velocity profile at x=30 microns and the surface concentration profile of bound streptavidin down the center of the microchannel were compared.

The x-velocity profile (blue line in Figure 147B) and the surface concentration profile of streptavidin (pink line in Figure 147B) show a strong correlation (Figure 147). When the x-velocity pushes fluid towards the surface (negative velocity in Figure 147B and colored blue in Figure 147A), there is an increase in the surface binding of streptavidin as more streptavidin molecules are brought closer to the surface. When the x-velocity component pulls fluid away from the surface (positive velocity in Figure 147B and colored red in Figure 147A), there is a reduction in the surface binding of streptavidin. Once again due

to the fact that the fresh streptavidin solution is introduced on the left and a depletion zone exists, there is a reduction in the total amount of bound streptavidin from left to right.

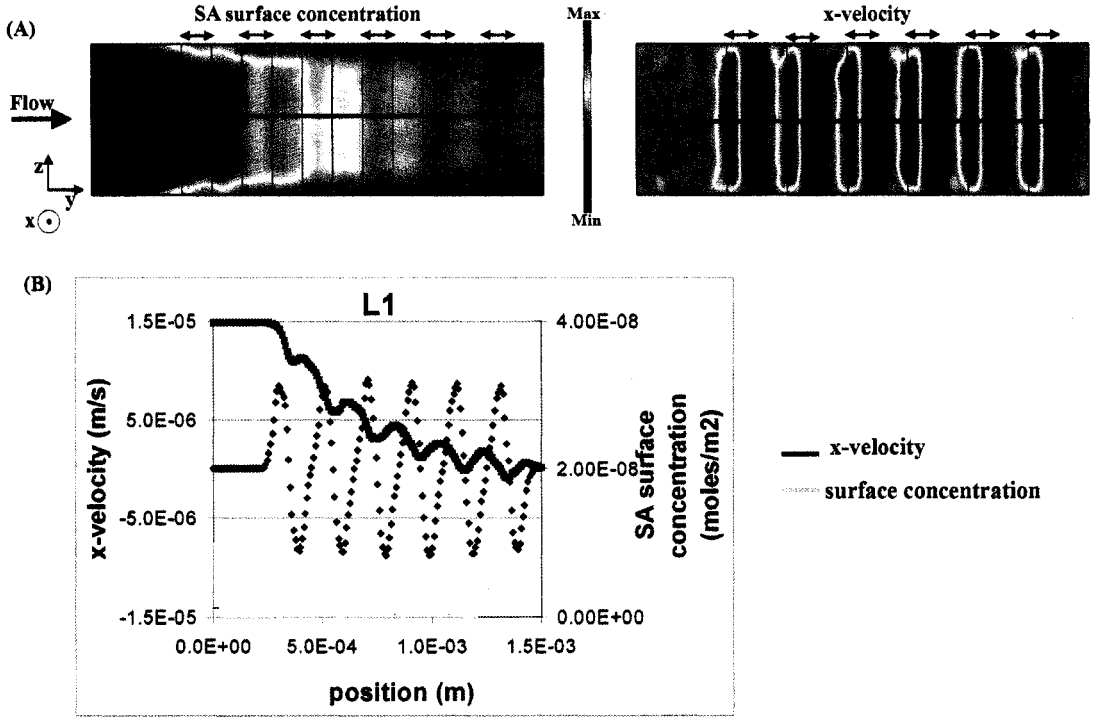

Figure 147. Comparison of the x-velocity profile and the binding profile in the chevron microchannel. Model results. (A) Surface concentration profile of bound streptavidin (moles/m^2). The maximum SA surface binding concentration is 3.99 $\times 10^{-8}$ moles/m^2. The minimum SA surface binding concentration is 0 moles/m^2. Velocity profile (m/s) in x-dimension. The maximum velocity and minimum velocity are 9.54 $\times 10^{-6}$ m/s and -9.41 $\times 10^{-6}$ m/s. (B) Line profile comparing the surface concentration profile and the velocity in the x-dimension. The location of the line profile (L1) is indicated in (A) and located at z=250 microns and y[0 to 1.5 mm]. Streptavidin inlet concentration = 20 nM = 2×10^{-5} moles/m^3. Time = 700 seconds. Re= 0.01. Pe=135.1. Q=5 nL/s. The arrows indicate the deepest portion of the channel where the chevron structure is present. The theoretical maximum surface binding concentration is 3.99 $\times 10^{-8}$ moles/m^2. The x-dimension is x=30 microns in (B).

The y-velocity profile (blue line in Figure 148B) strongly correlates with the surface binding profile of streptavidin (pink line Figure 148B). This result is expected since the y-velocity component has the most significant contribution to the overall kinetic energy in the fluidic system (Table 59). In regions of higher y-velocities, more streptavidin binds as convective rather diffusive transport is more dominant and the surface area of streptavidin binding region to volume of protein solution above it is increased by a factor of two. On the other hand, at lower y-velocities, less streptavidin binds to the surface as

the diffusive transport becomes more significant and the surface area of streptavidin binding region to volume (which includes the duct) is reduced.

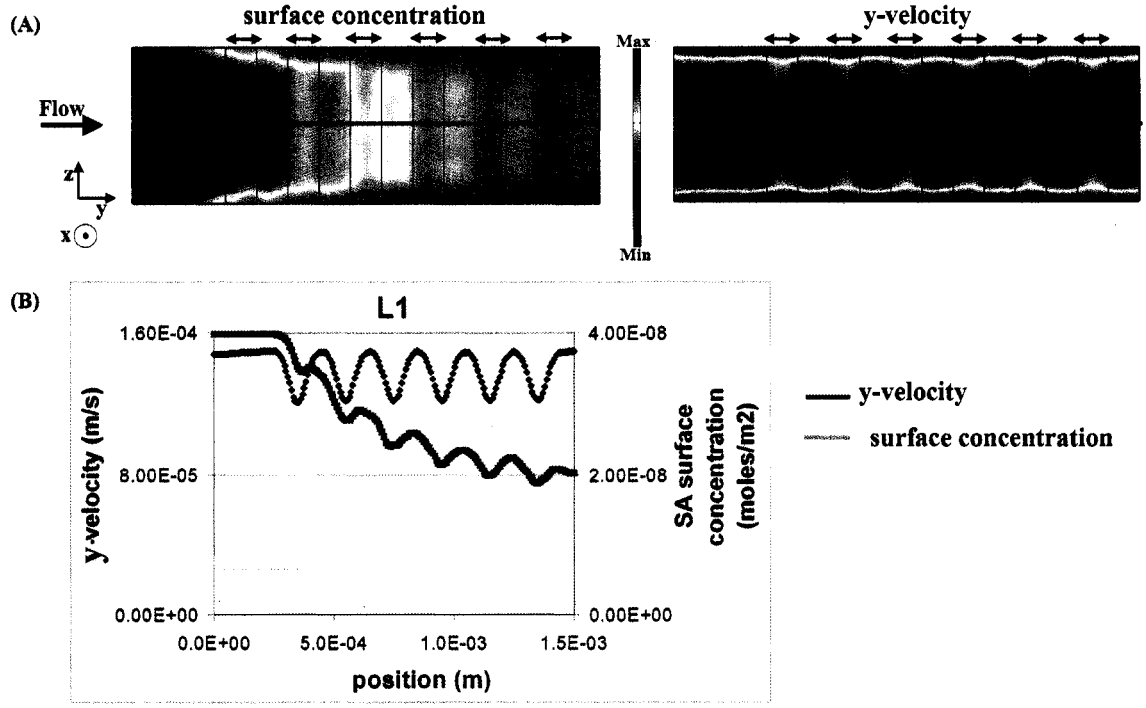

Figure 148. Comparison of the y-velocity profile and the binding profile in the square microchannel. Model results. (A) Surface concentration profile of bound streptavidin (moles/m^2). The maximum SA surface binding concentration is 3.99 $\times 10^{-8}$ moles/m^2. The minimum SA surface binding concentration is 0 moles/m^2. Velocity profile (m/s) in the y-dimension at x=30 microns. The maximum velocity and minimum velocity are 1.50 $\times 10^{-4}$ m/s and -4.73 $\times 10^{-19}$ m/s. (B) Line profiles comparing surface concentration profile and velocity in the y-dimension. The location of the line profile, L1, is indicated in (A) and located at z=250 microns and y[0 to 1.5 mm]. Streptavidin inlet concentration = 20 nM = 2×10^{-5} moles/m^3. Time = 700 seconds. Re= 0.01. Pe=135.1. Q=5 nL/s. The arrows indicate the deepest portion of the channel where the chevron structure is present. The theoretical maximum surface binding concentration is 3.99 $\times 10^{-8}$ moles/m^2.

Appendix H: Dispersion in microchannels

In most microfluidic assays conducted in the Yager lab, discrete volumes of biological samples are introduced to a device primed with a buffer solution. Due to the parabolic velocity profile of the fluid in the microchannel, the transport of the molecules into the microchannel is not uniform but reflects the parabolic velocity profile and the diffusion coefficient of the species. This phenomena – known as dispersion – was described by Taylor and has since become known as Taylor dispersion.[52]

The purpose of this appendix is to give the reader a qualitative sense of the influence of dispersion on the concentration profile of a protein molecule – streptavidin – introduced to a straight microchannel and a chevron microchannel filled with a buffer solution. Typically several hundred microliters of fluid are introduced to the device, and in this research, only the leading boundary between the buffer and the sample is significant for experimental results.

H.1 Straight microchannel

In this microchannel, streptavidin is introduced to a device that contains only buffer at time=0. A 20 nM solution of streptavidin is introduced to the microchannel. Unlike previous models, the protein does not bind to any of the channel walls. The dimensions of the microchannel are the same as those described in Chapter 5 (Figure 55).

The model results (Figure 149) clearly illustrate that at early time points, the concentration profile of streptavidin reflects the parabolic velocity profile. The fastest moving fluid is located in the center of the channel where the streptavidin concentration is the highest, as the protein is quickly convectively transported into the microchannel in those locations. The velocity at the walls is zero, and protein must be transported from the channel center to the wall by diffusion. Therefore, the sidewalls are the last locations to which the protein is transported. As a result, dispersion is very significant for surface

detection methods – such as SPR imaging – since the protein is transported to the surface regions last. At the front of the streptavidin solution, the protein diffuses down a sharp concentration gradient (arising from the interface between buffer and a concentrated protein solution). As a result, the protein solution becomes diluted at this interface.

In general, the dispersion profile will depend on the flow rate, the diffusion coefficient of the species, and the concentration of the species. At high flow rates (i.e., high Peclet numbers) there is a steeper velocity gradient. The species will be convected very quickly down the center of the channel, while the concentration at the walls will remain nearly zero. In these situations, the variation in concentration across the channel at early time points will be even more pronounced over a greater distance than in Figure 149 (assuming a similar diffusion coefficient as the streptavidin molecule). At very low flow rates (i.e., Peclet number ~1), the relative importance of diffusive and convective transport will be similar. In these situations, the variation in concentration across the channel will not be very significant due to the fact that the species will diffuse towards the walls on a similar time scale as it is convected down the channel. However, dilution due to the concentration gradient at the interface of the buffer and protein solution will still occur.

The diffusive transport is directly related to the diffusion coefficient as well as the local concentration gradient. When the species diffuses quickly, the solution concentration near the walls will increase much more rapidly as the species will diffuse from the center of the microchannel toward the walls. How quickly this occurs will depend on the local Peclet number. When the concentration of the species is high the concentration gradient between the center of the microchannel, where the concentration is much higher due to convective transport, and the walls, where no protein is present, is very high. Therefore, the higher the concentration of the species, the more quickly the species will be diffusively transported to the microchannel wall.

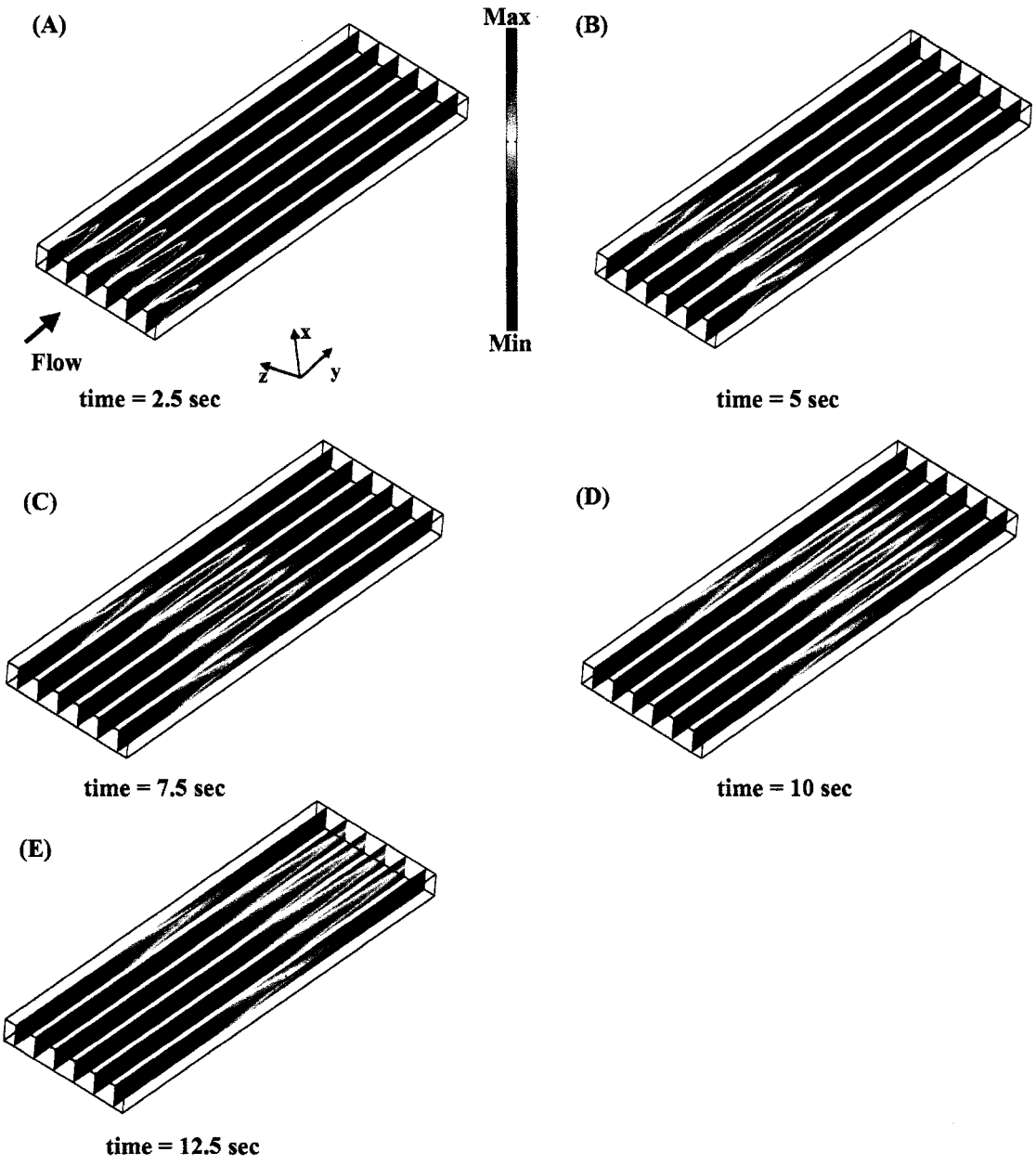

Figure 149. Dispersion in a straight microchannel (z-slices). Concentration profile of streptavidin in the channel (moles/m^3) over time. The maximum concentration is 2.1 $\times 10^{-5}$ moles/m^3 and -8.2 $\times 10^{-7}$ moles/m^3. Initial streptavidin concentration in the microchannel = 0 nM. Streptavidin concentration at inlet = 20 nM = 2×10^{-5} moles/m^3. Re= 0.01. Pe=135.1. Q=5 nL/s.

H.2 Comparison of straight and chevron microchannels

To qualitatively explore the dispersion profile for a straight microchannel and a chevron microchannel under the same conditions, simulations were completed for a straight microchannel and a chevron microchannel with a 20 nM solution of streptavidin introduced to a buffer filled microchannel at time= 0. The channel geometries were the same dimensions as described in Chapters 5 and 8 (Figure 55 and Figure 88). The purpose of the research was to gain a qualitative understanding of the potential influence of dispersion on the binding profile for a straight microchannel versus a chevron microchannel.

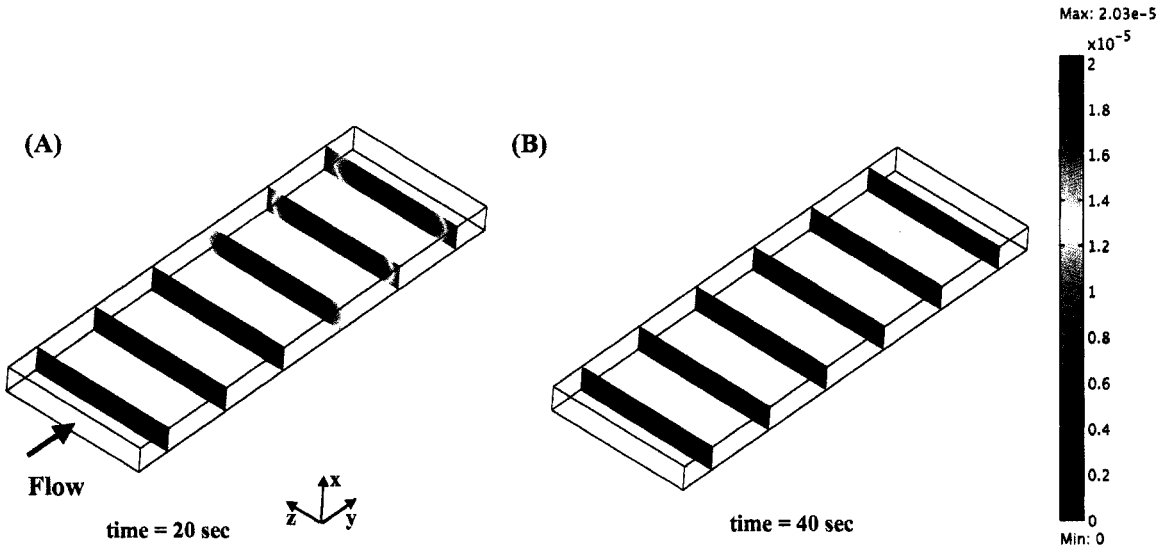

Figure 150. Dispersion in a straight microchannel (y-slices). Concentration profile of streptavidin in the channel (moles/m^3) over time. Streptavidin initial concentration in the microchannel = 0 nM. Streptavidin concentration at inlet = 20 nM = 2×10^{-5} moles/m^3. Re= 0.01. Pe=135.1. Q=5 nL/s.

The straight channel results (Figure 150) indicate that at 20 seconds the concentration of streptavidin within the microchannel is nearly uniform except at the sidewalls where the transport is more diffusion-limited than at the centerline of the channel. By 40 seconds the concentration of streptavidin within the modeled microchannel is approximately uniform. Dispersion in the chevron microchannel is not as simple. In the chevron microchannel, the velocity profile has components in three- not one-dimensions. The

chevron microchannel also is larger in volume than the straight microchannel as it incorporates the straight microchannel as the base microchannel plus the chevron microstructures. As a result, it requires over 60 seconds (as opposed to 40 seconds for the straight channel) for over 98% of the microchannel to reach a concentration of 20 nM.

To best illustrate the complex nature of the dispersion profile, several different slices of the concentration profile of streptavidin are presented (Figure 151, Figure 152, and Figure 153).

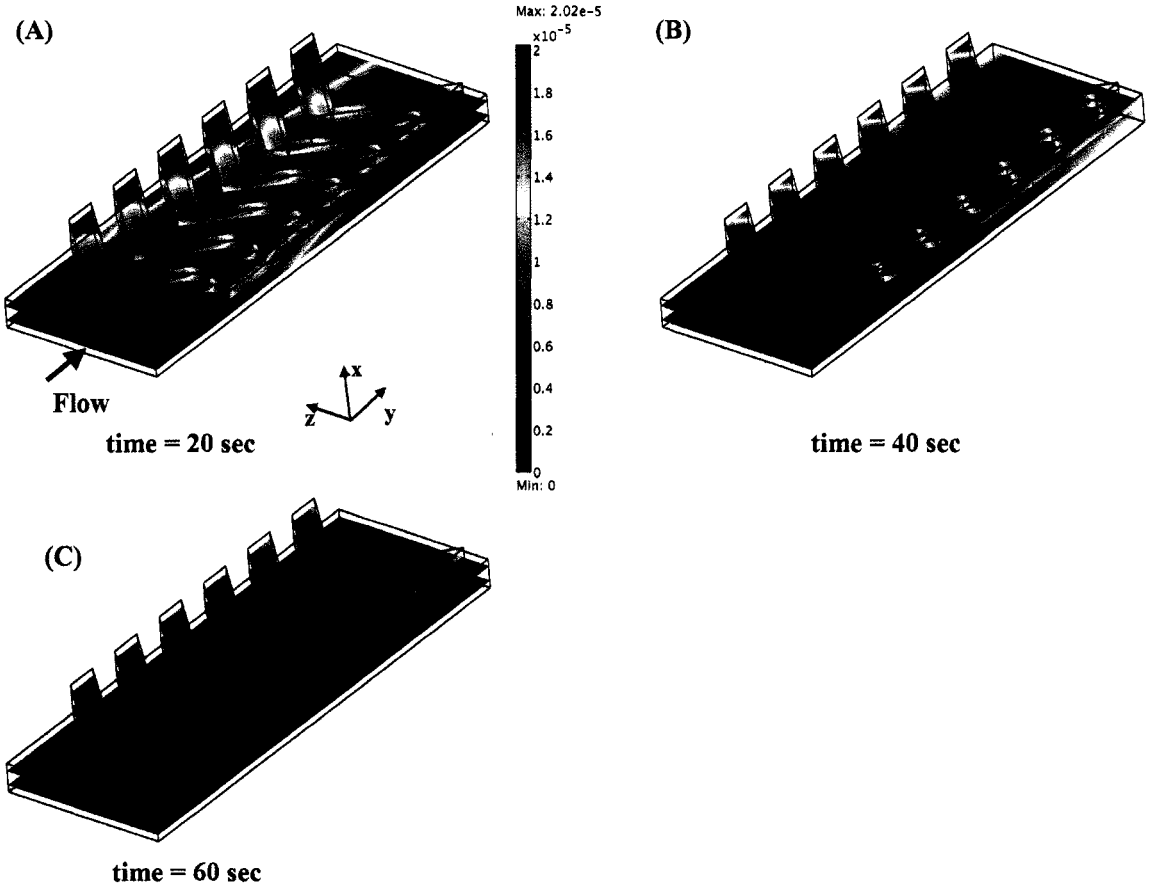

Figure 151. Dispersion in a chevron microchannel (x-slices). Model results. (A)–(C) Concentration profile of streptavidin in the channel (moles/m^3) over time. Streptavidin initial concentration in the microchannel = 0 nM. Streptavidin concentration at inlet = 20 nM = 2×10^{-5} moles/m^3. Re= 0.01. Pe=135.1. Q=5 nL/s.

The x-slice (Figure 151) of the concentration profile illustrates that the concentration in the chevrons, particularly near the sidewalls, is the last to reach the maximum concentration.

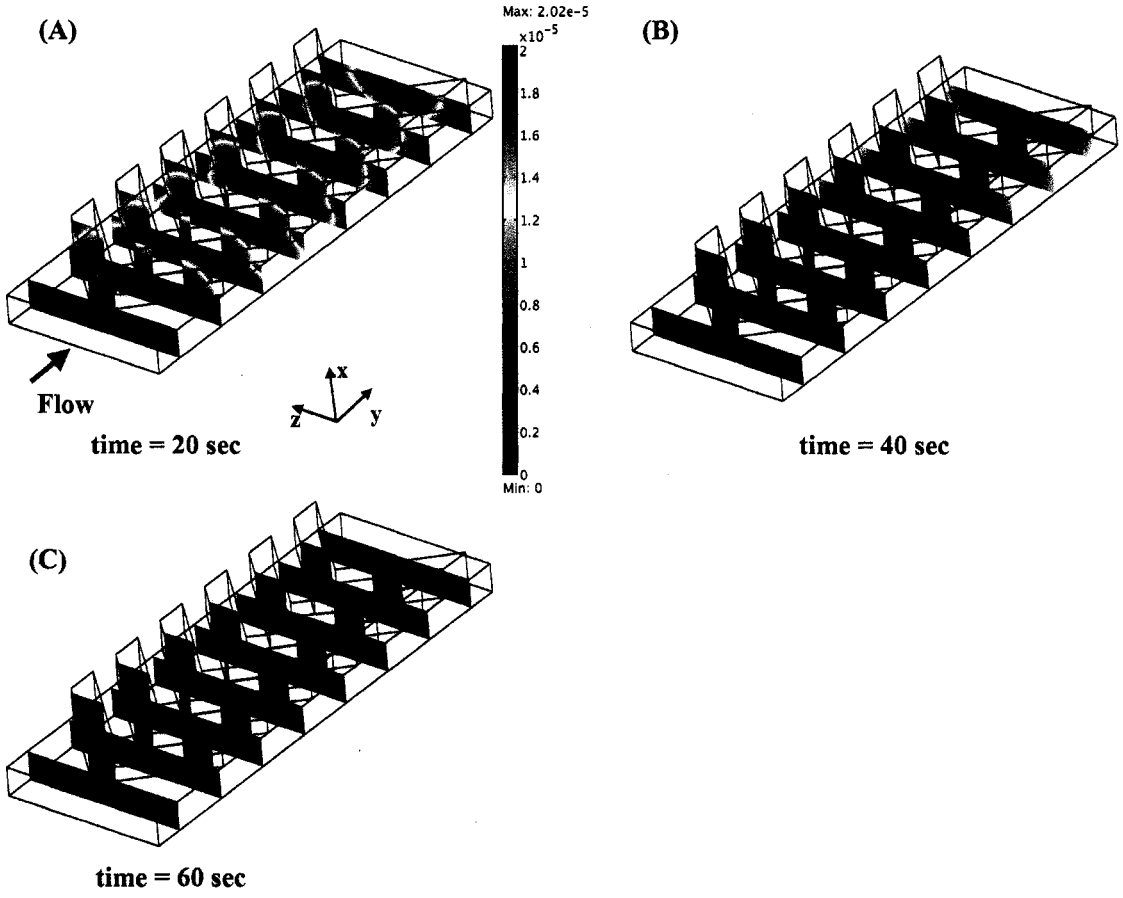

Figure 152. Dispersion in a chevron microchannel (y-slices). Model results. Concentration profile of streptavidin in the channel (moles/m^3) over time. Streptavidin initial concentration in the microchannel = 0 nM. Streptavidin inlet concentration = 20 nM = 2×10^{-5} moles/m^3. Re= 0.01. Pe=135.1. Q=5 nL/s.

The y-slices of the streptavidin concentration profile (Figure 152) illustrate that particularly at early time points the majority of the convective transport – as is the case for the straight microchannel – occurs down the center of the microchannel, where the velocity is the highest. Over time, the protein must diffuse down the concentration gradient towards the sidewalls.

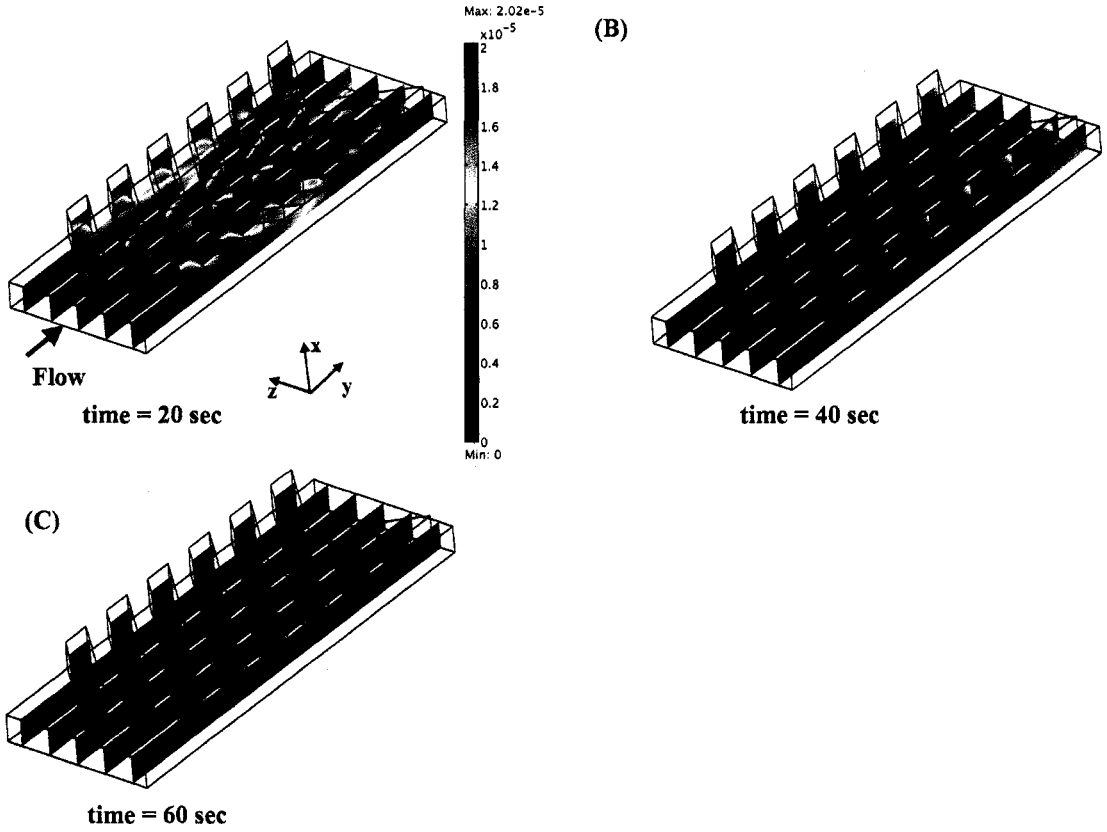

Figure 153. Dispersion in a chevron microchannel (z-slices). Concentration profile of streptavidin in the channel (moles/m^3) over time. Model results. Streptavidin initial concentration in the microchannel = 0 nM. Streptavidin inlet concentration = 20 nM = 2×10^{-5} moles/m^3. Re= 0.01. Pe=135.1. Q=5 nL/s.

The z-slices of the concentration profile (Figure 153) illustrate the complexity in the dispersion profile at early time points (20 seconds) arising from the mixing behavior that a chevron microchannel introduces to a fluid. The results indicate that at some locations downstream, the concentration of protein within the chevron (time= 20 seconds) is greater than the concentration of the fluid immediately below it, possibly due to the transverse flow (z-dimension) imparted by the microchannel.

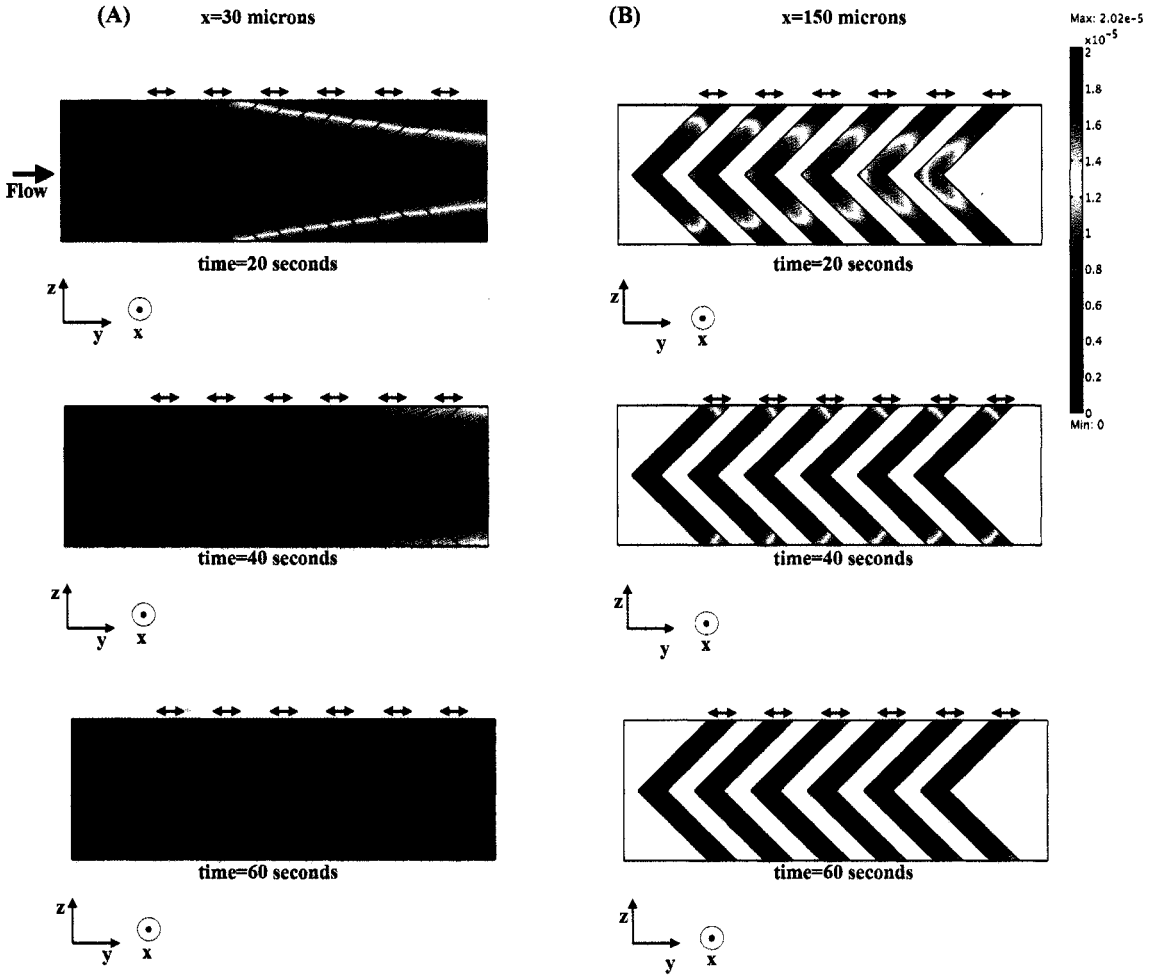

Figure 154. Dispersion in a chevron microchannel over time at two distances from the surface (x-dimension). Model results. Concentration profile of streptavidin in the channel (moles/m^3) over time. Streptavidin initial concentration in the microchannel = 0 nM. Streptavidin concentration at the inlet= 20 nM = 2×10^{-5} moles/m^3. Re= 0.01. Pe=135.1. Q=5 nL/s.

To better understand the concentration profile during dispersion in locations parallel to the SPR-imaging surface, concentration slices near the imaging surface (x=30 microns) and within the chevron (x=150 microns) are shown over time (Figure 154). In SPR-imaging, the surface concentration near the surface is what contributes to the signal. The results qualitatively suggest that like the straight microchannel that during dispersion, the concentration of protein in the center of the channel is the first to reach a maximum and gradually over time the concentration near the sidewall reaches the concentration of the

protein solution. The sidewalls and back edges of the chevron in which the local velocity is low remain the last location to which protein is transported.

Appendix I: Unprocessed XPS and XPS imaging data.

Survey scans for the XPS data. Images were copied from the data analysis software XVision. The materials and methods, analysis, and discussion of this data are located in Chapter 3. Any data sets that appear to be duplicates are replicates. Some of the data sets present the line profiles generated during the analysis.

XPS

Microcontact printing was completed using flat PDMS stamps which covered the entire gold coated slide substrate. The ink was either a solution of IgG or just buffer.

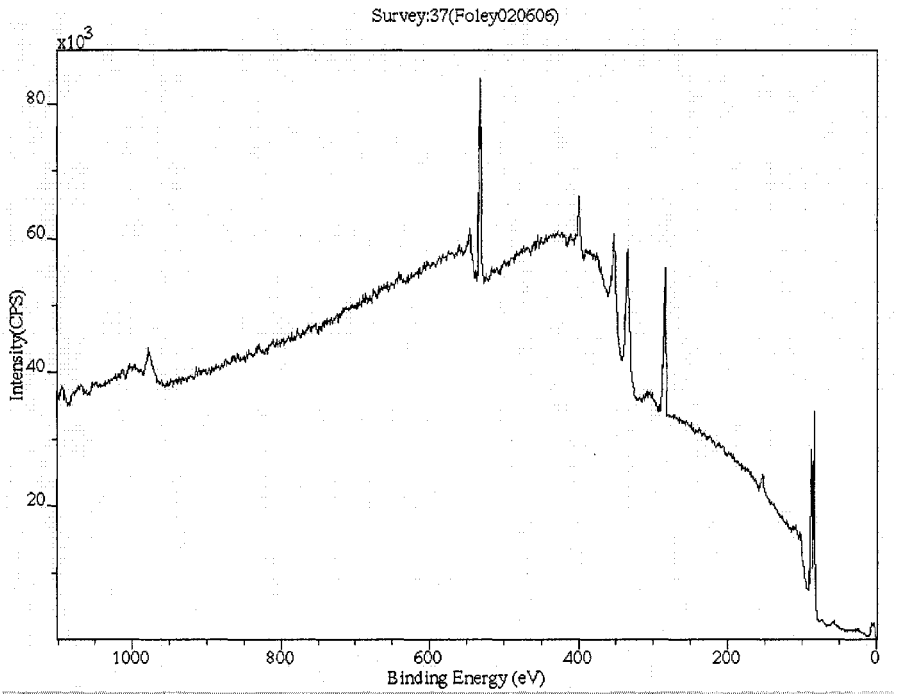

Figure 155. XPS data for microcontact printed IgG on a gold surface.

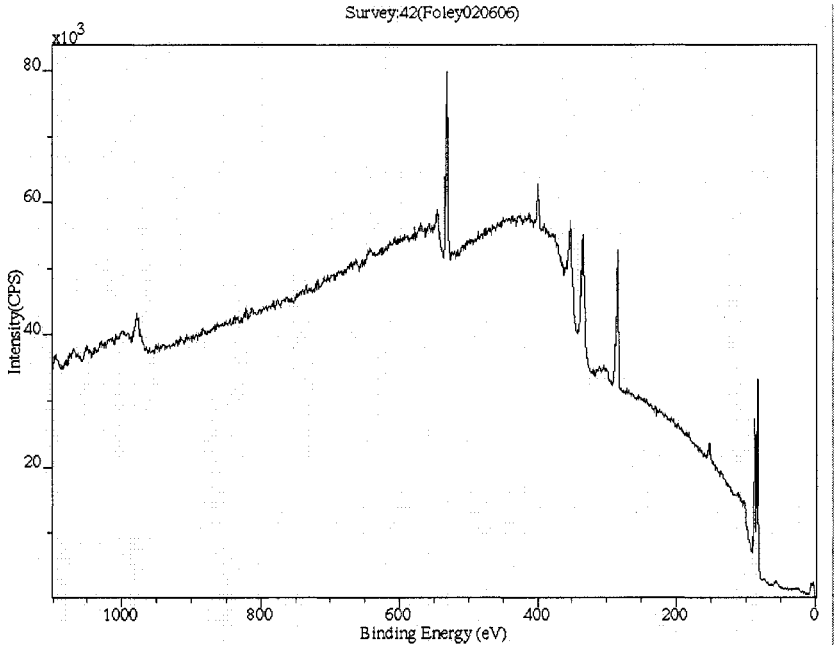

Figure 156. XPS data for microcontact printed IgG on a gold surface.

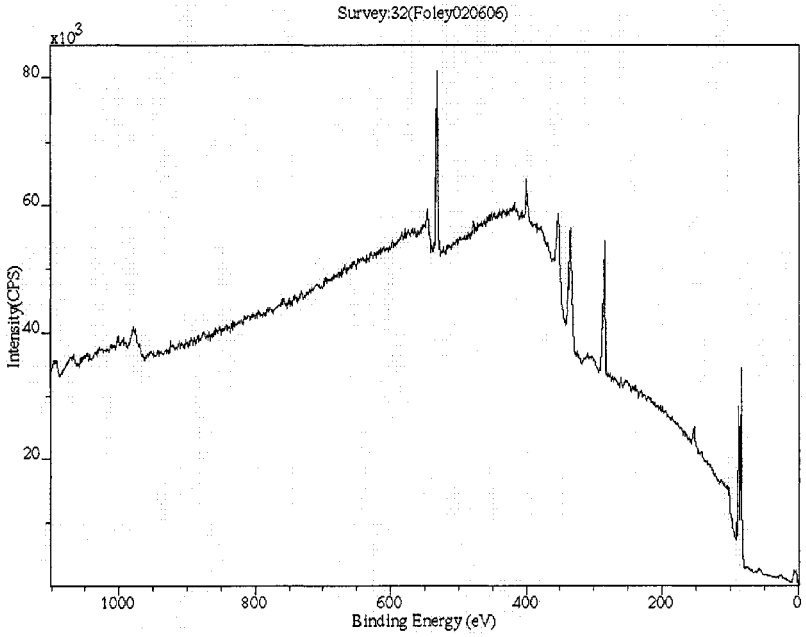

Figure 157. XPS data for microcontact printed IgG on a gold surface.

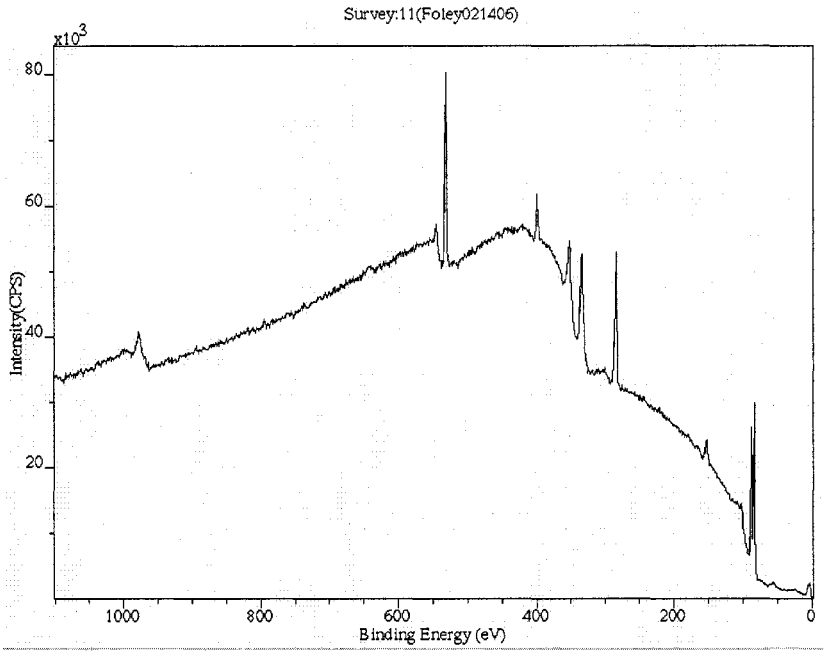

Figure 158. XPS data for microcontact printed IgG on a gold surface.

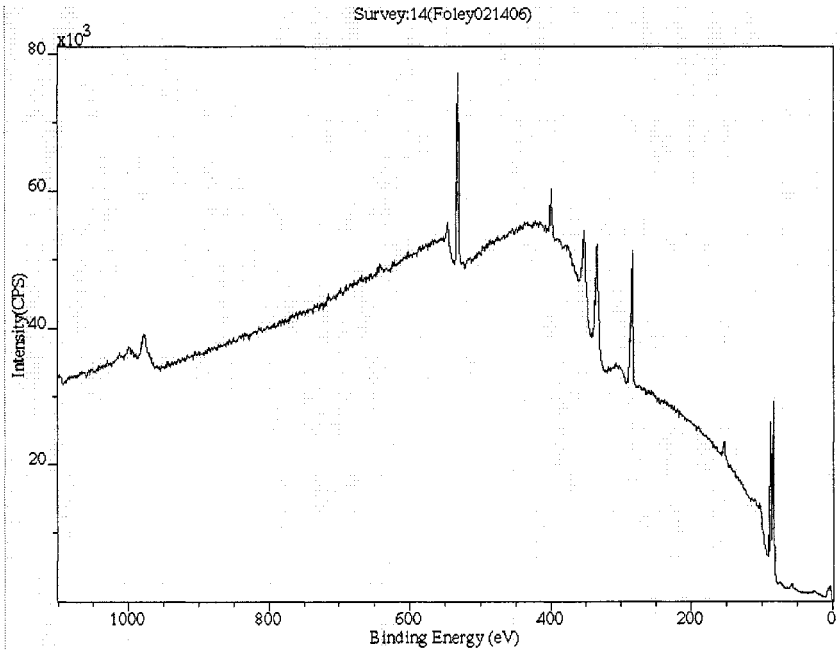

Figure 159. XPS data for microcontact printed IgG on a gold surface.

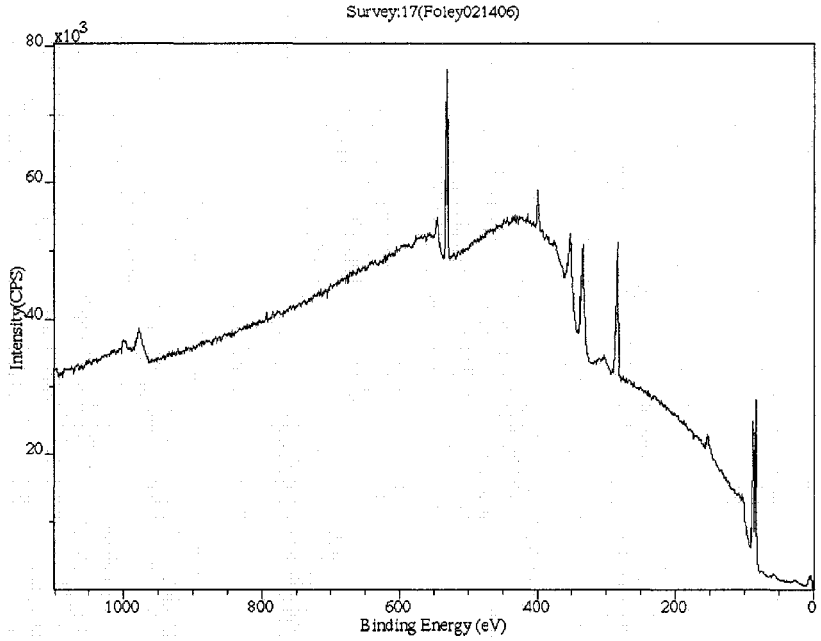

Figure 160. XPS data for microcontact printed IgG on a gold surface.

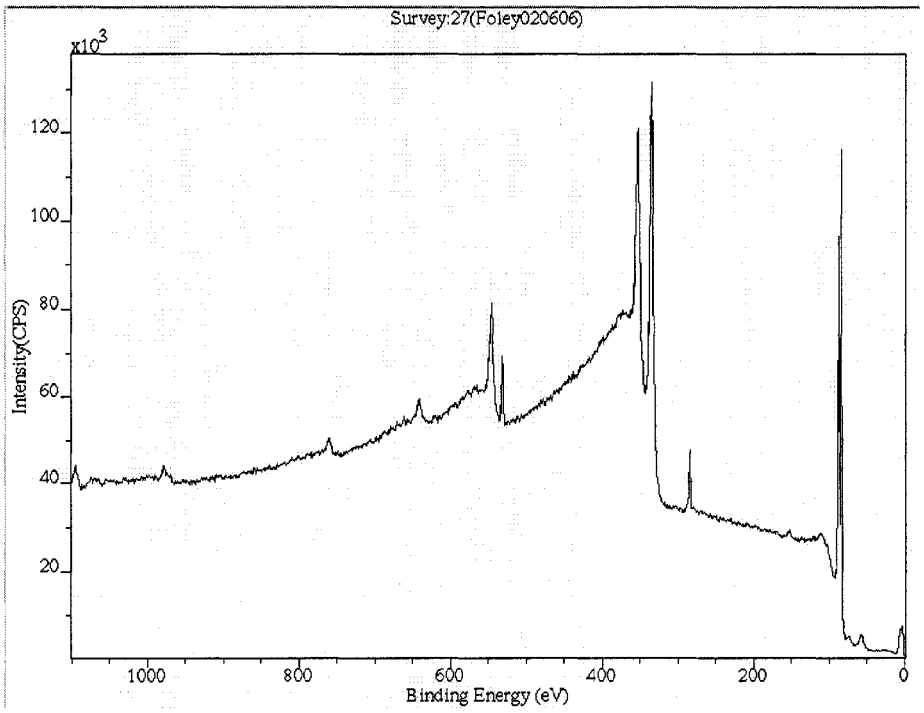

Figure 161.XPS data for microcontact printed buffer on a gold surface.

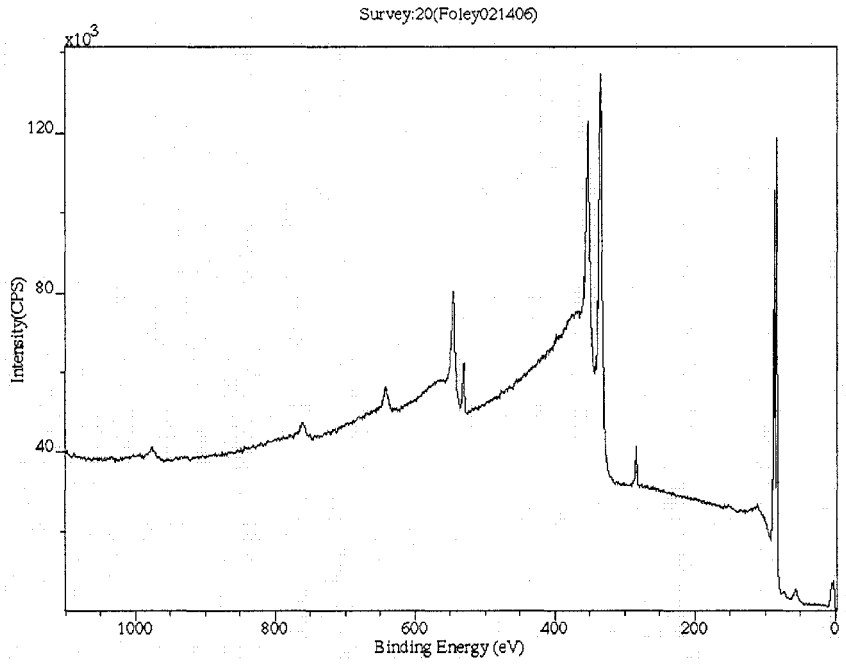

Figure 162. XPS data for microcontact printed buffer on a gold surface.

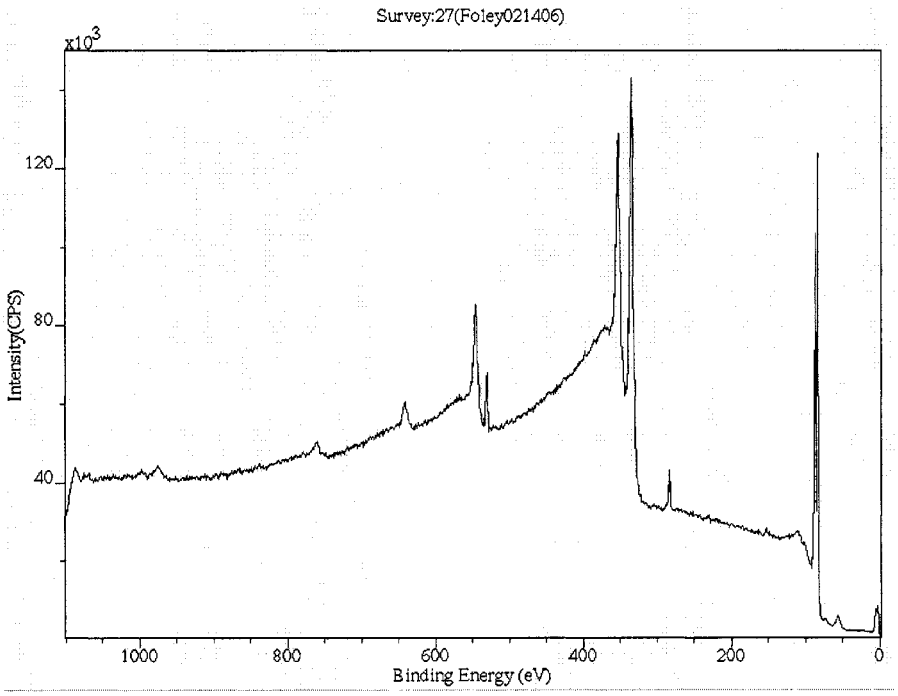

Figure 163. XPS data for microcontact printed buffer on a gold surface.

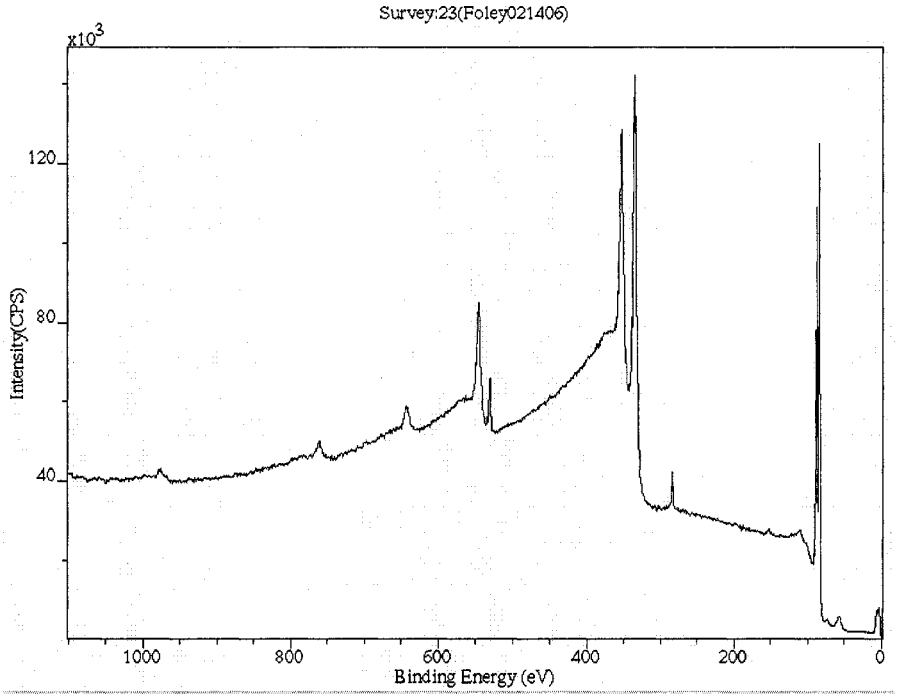

Figure 164. XPS data for microcontact printed buffer on a gold surface.

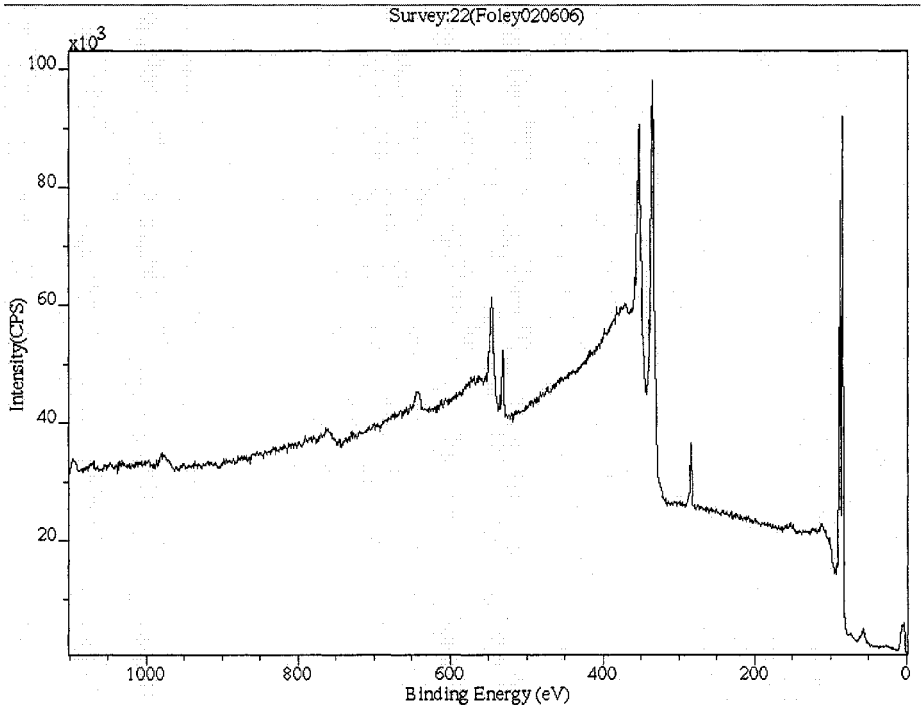

Figure 165. XPS data for microcontact printed buffer on a gold surface.

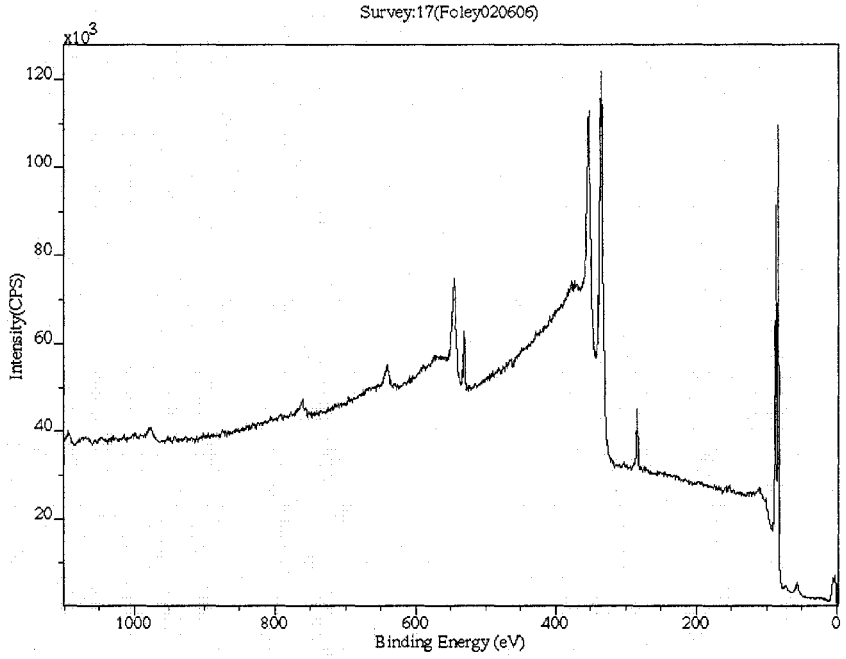

Figure 166. XPS data for microcontact printed buffer on a gold surface.

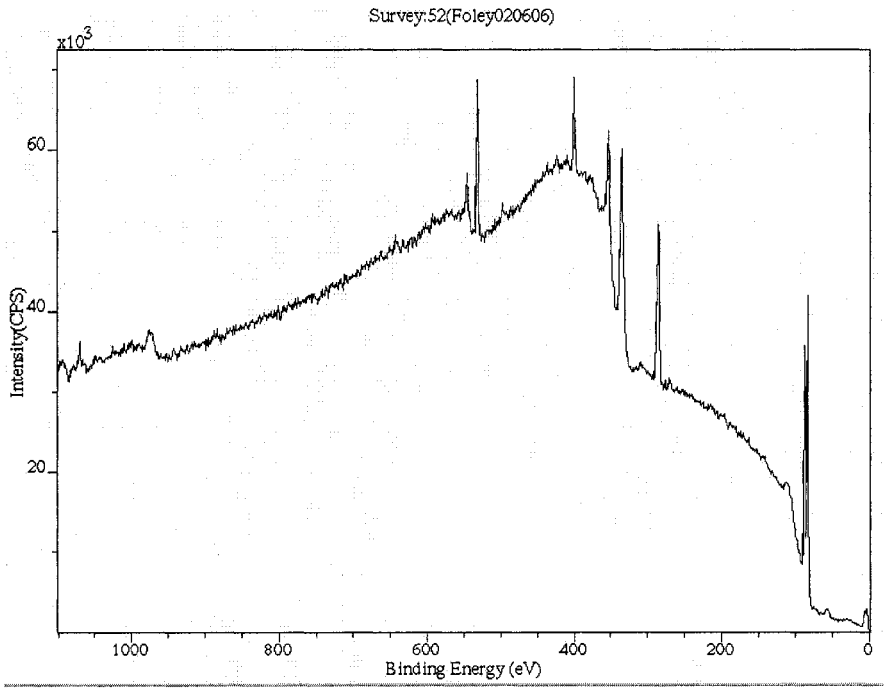

Figure 167. XPS data for physically adsorbed IgG on a gold surface.

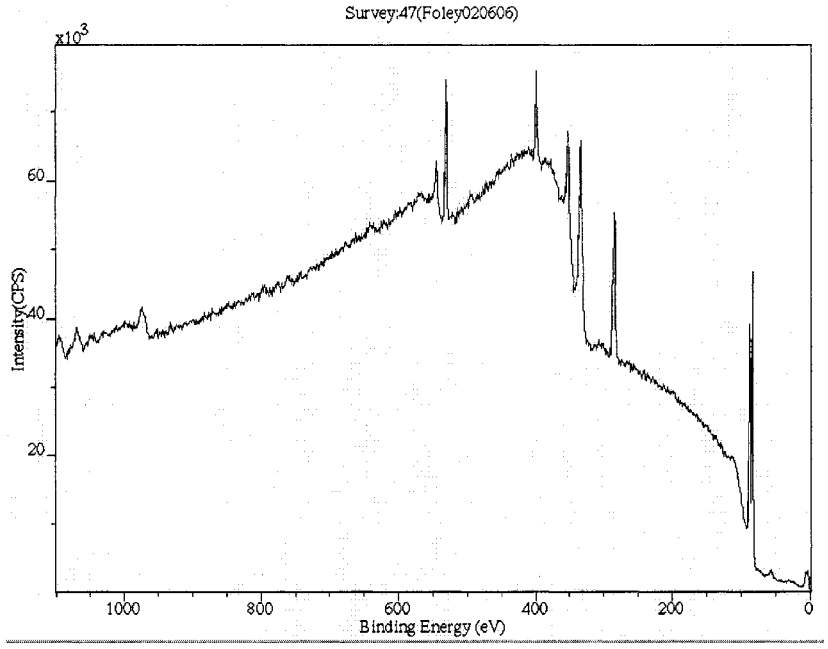

Figure 168. XPS data for physically adsorbed IgG on a gold surface.

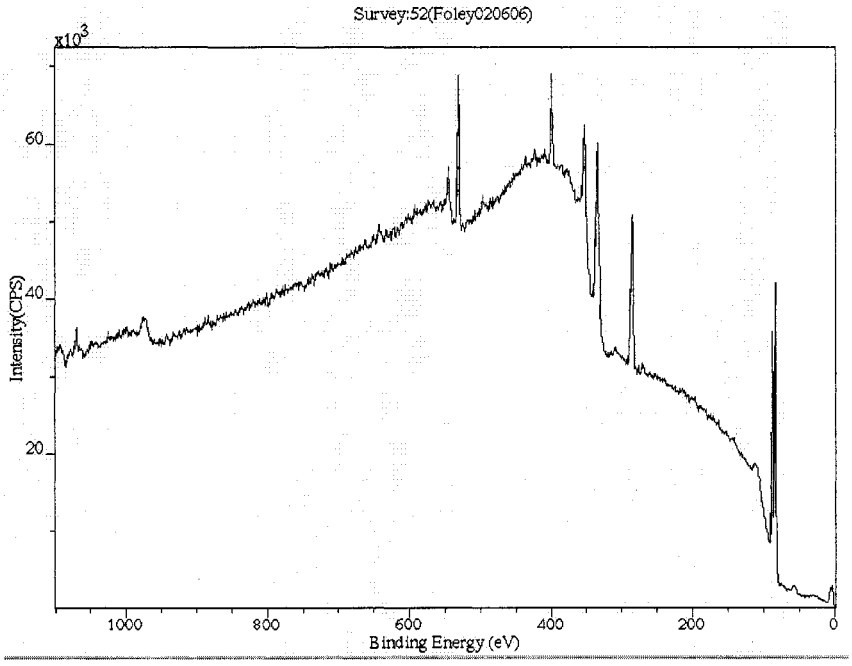

Figure 169. XPS data for physically adsorbed IgG on a gold surface.

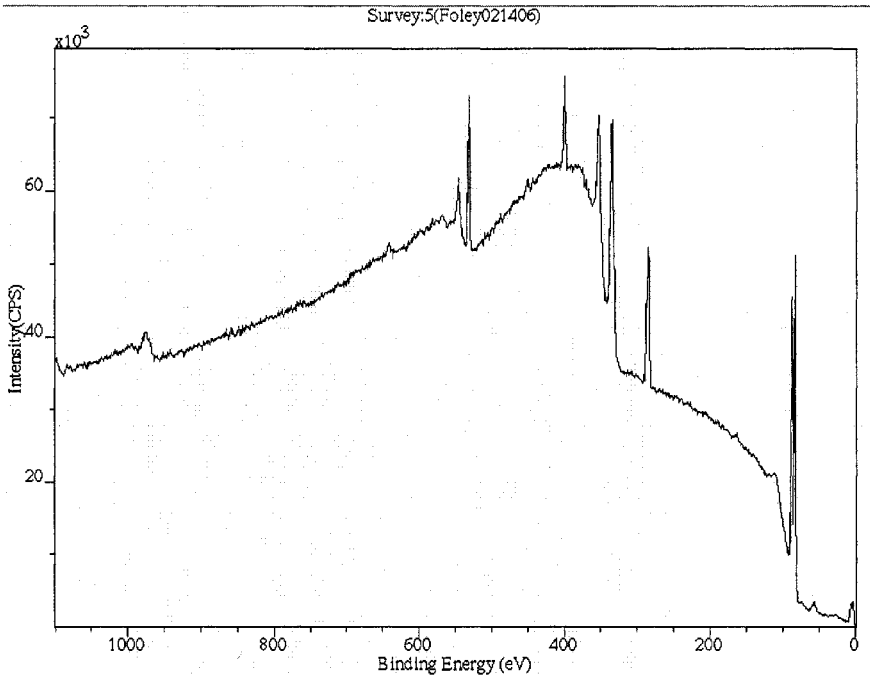

Figure 170. XPS data for physically adsorbed IgG on a gold surface.

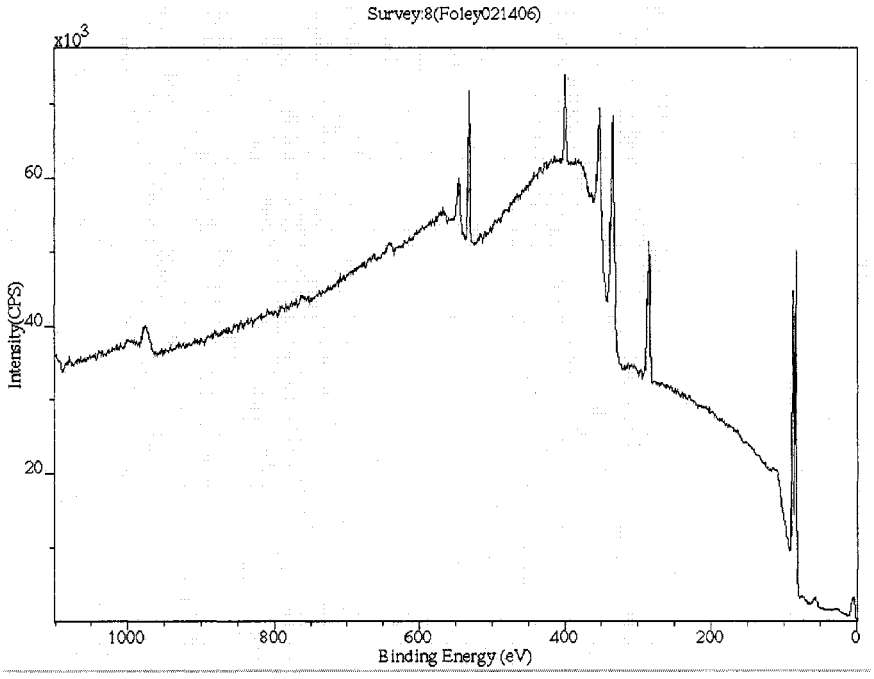

Figure 171. XPS data for physically adsorbed IgG on a gold surface.

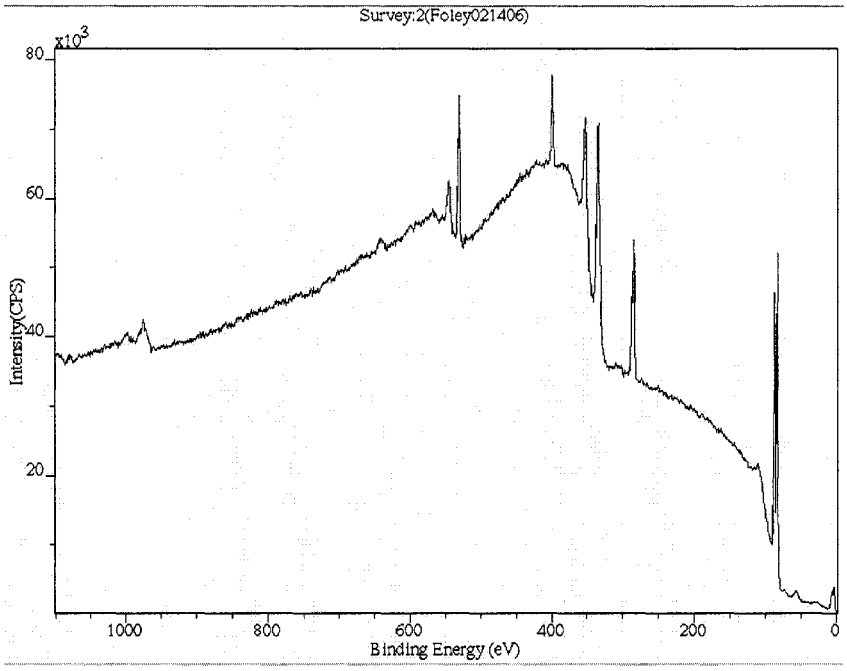

Figure 172. XPS data for physically adsorbed IgG on a gold surface.

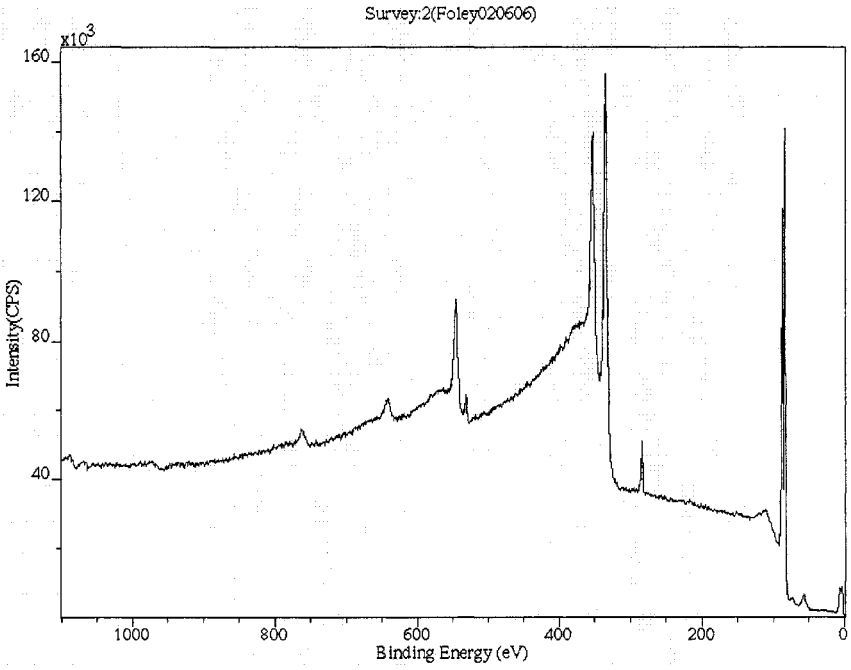

Figure 173. XPS data for a gold surface.

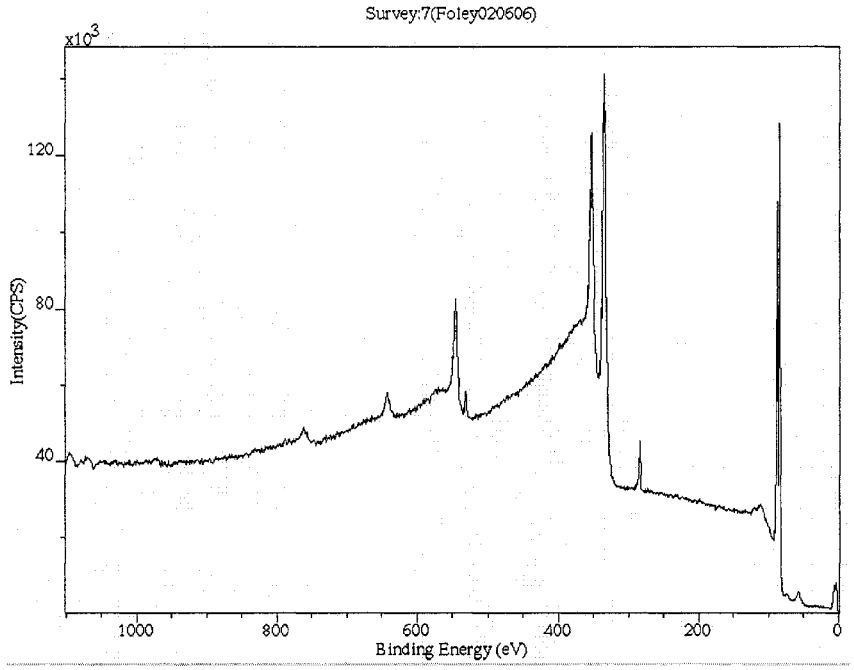

Figure 174. XPS data for a gold surface.

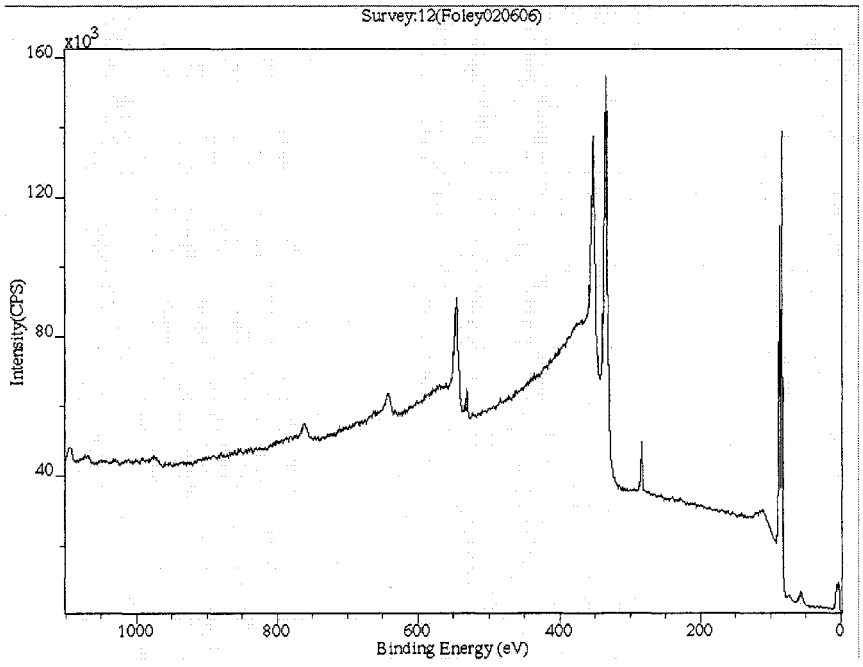

Figure 175. XPS data for a gold surface.

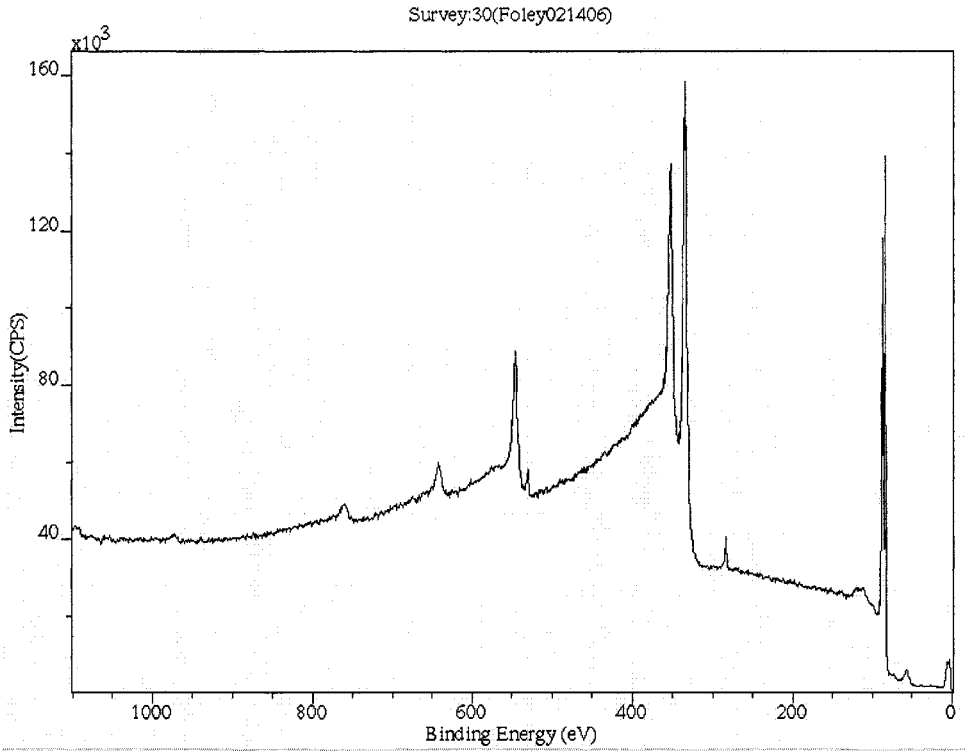

Figure 176. XPS data for a gold surface.

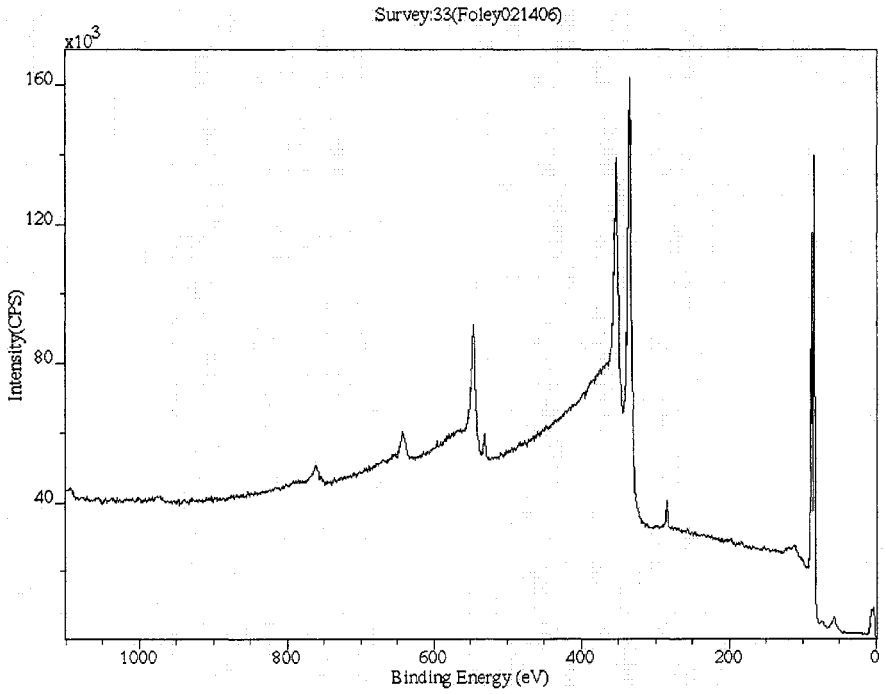

Figure 177. XPS data for a gold surface.

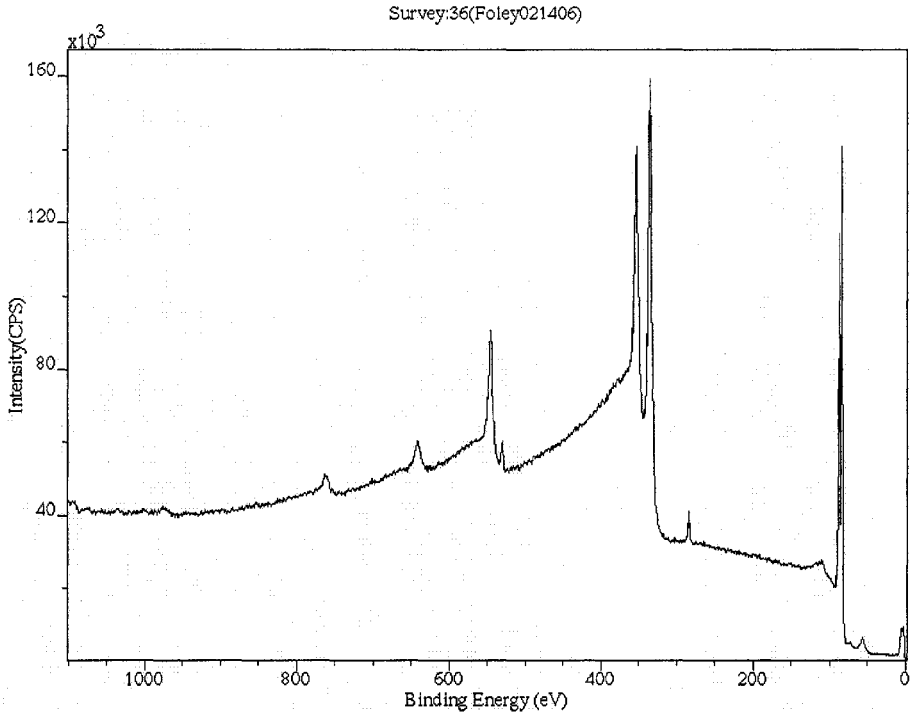

Figure 178. XPS data for a gold surface.

XPS imaging data

A 200 micron x 200 micron PDMS stamp inked with an IgG contacted a gold surface. High resolution scans of nitrogen, oxygen, carbon, silicon, and gold were completed in regions where the PDMS stamp contacted the gold coated slide surface and where the PDMS stamp did not contact the gold coated slide surface.

Region patterned with the IgG inked PDMS stamp.

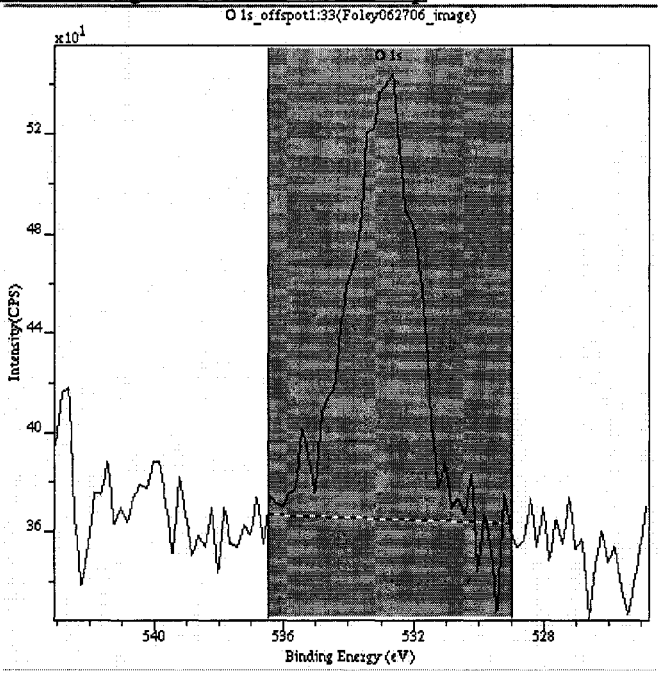

Figure 179. XPS high resolution scan for oxygen (1s) in an area contacted with a PDMS stamp inked with an IgG. XPS-imaging data.

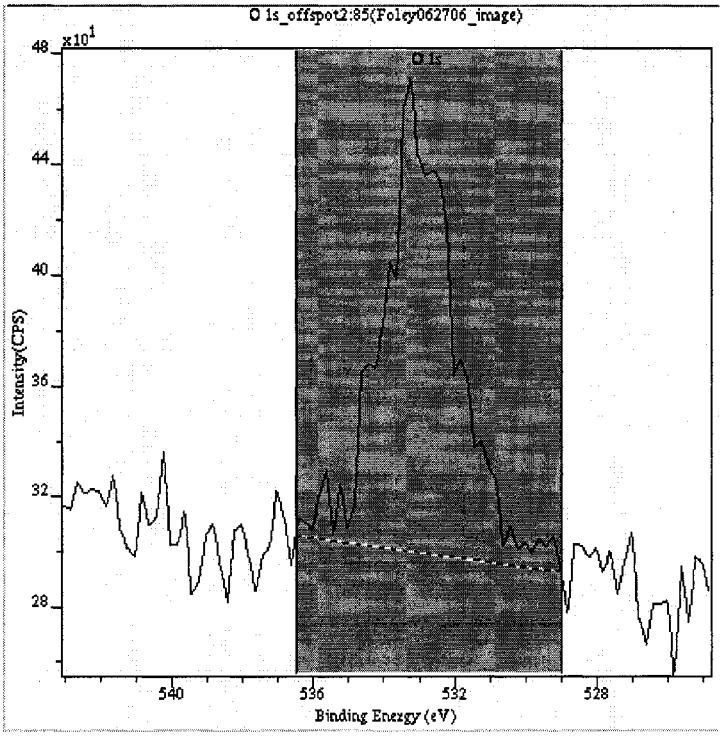

Figure 180. XPS high resolution scan for oxygen (1s) in an area contacted with a PDMS stamp inked with an IgG. XPS-imaging data.

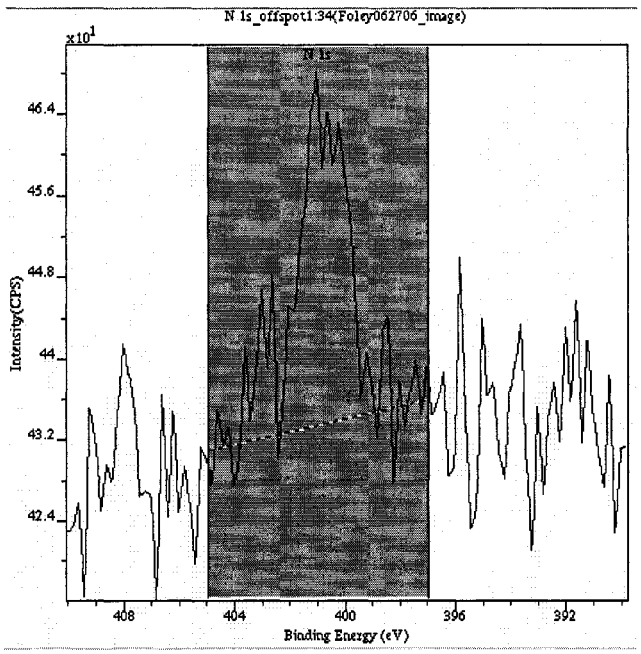

Figure 181. XPS high resolution scan for nitrogen (1s) in an area contacted with a PDMS stamp inked with an IgG. XPS-imaging data.

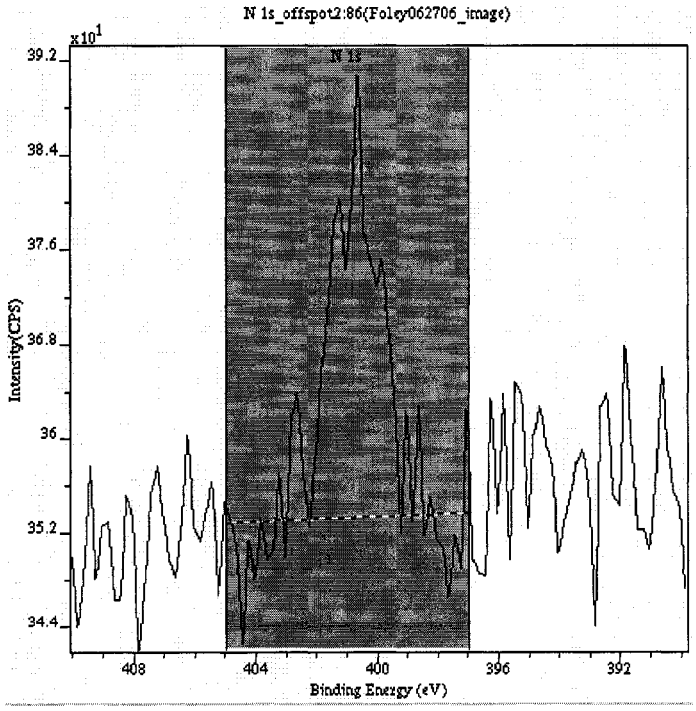

Figure 182. XPS high resolution scan for nitrogen (1s) in an area contacted with a PDMS stamp inked with an IgG. XPS-imaging data.

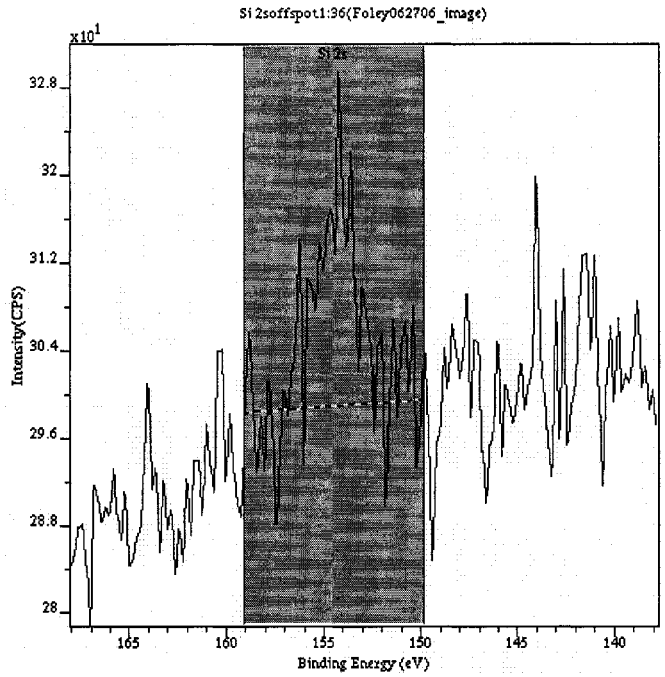

Figure 183. XPS high resolution scan for silicon (2s) in an area contacted with a PDMS stamp inked with an IgG. XPS-imaging data.

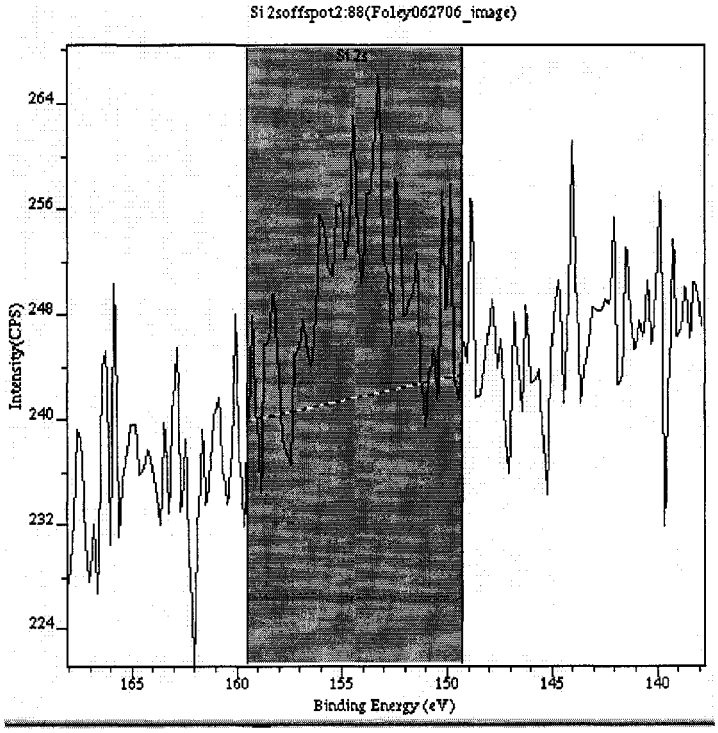

Figure 184. XPS high resolution scan for silicon (2s) in an area contacted with a PDMS stamp inked with an IgG. XPS-imaging data.

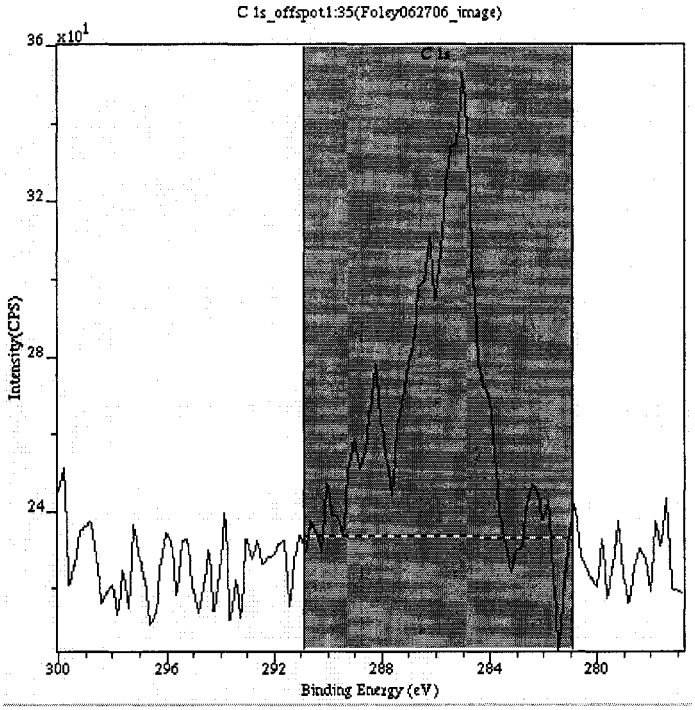

Figure 185. XPS high resolution scan for carbon (1s) in an area contacted with a PDMS stamp inked with an IgG. XPS-imaging data.

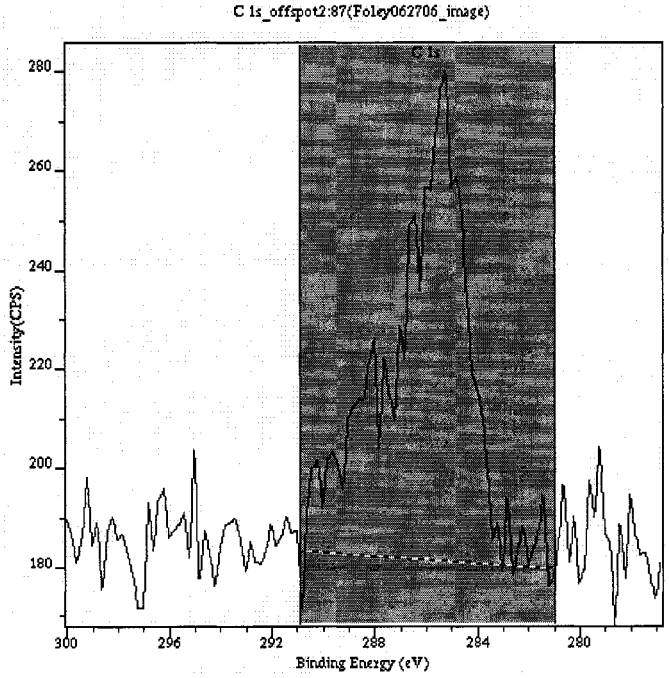

Figure 186. XPS high resolution scan for carbon (1s) in an area contacted with a PDMS stamp inked with an IgG. XPS-imaging data.

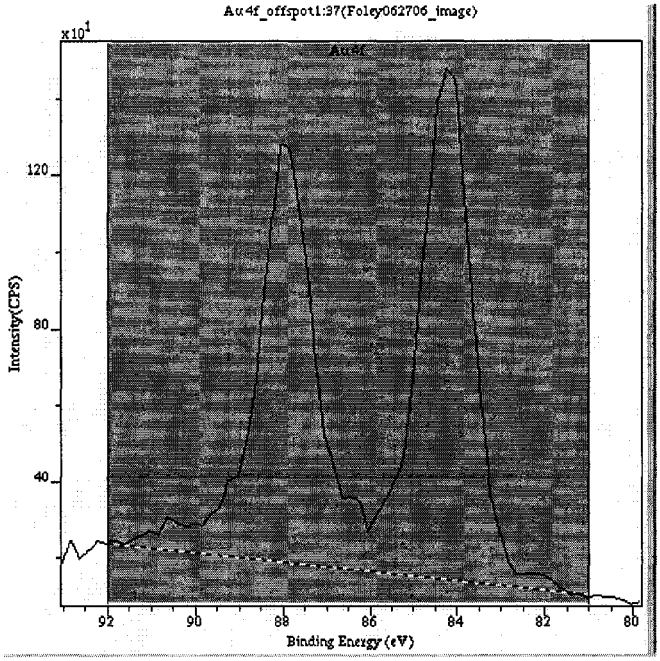

Figure 187. XPS high resolution scan for gold (4f) in an area contacted with a PDMS stamp inked with an IgG. XPS-imaging data.

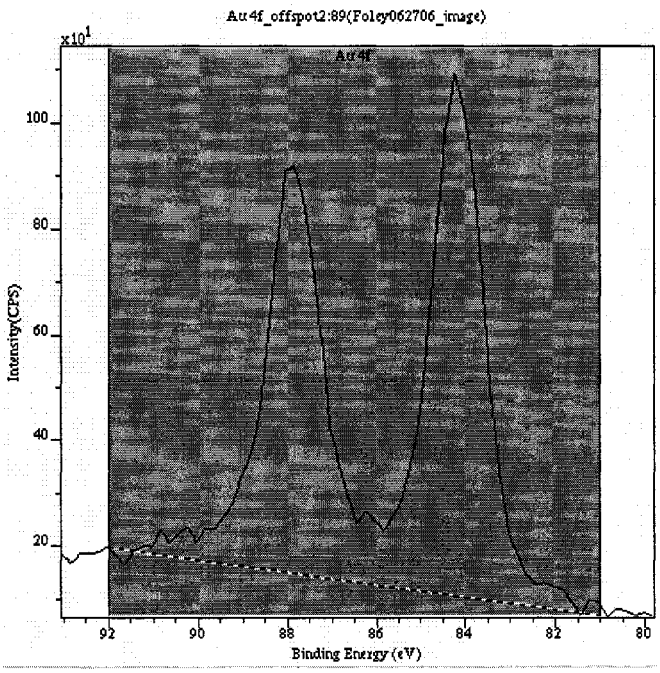

Figure 188. XPS high resolution scan for gold (4f) in an area contacted with a PDMS stamp inked with an IgG. XPS-imaging data.

Region patterned with the PDMS stamp inked with IgG.

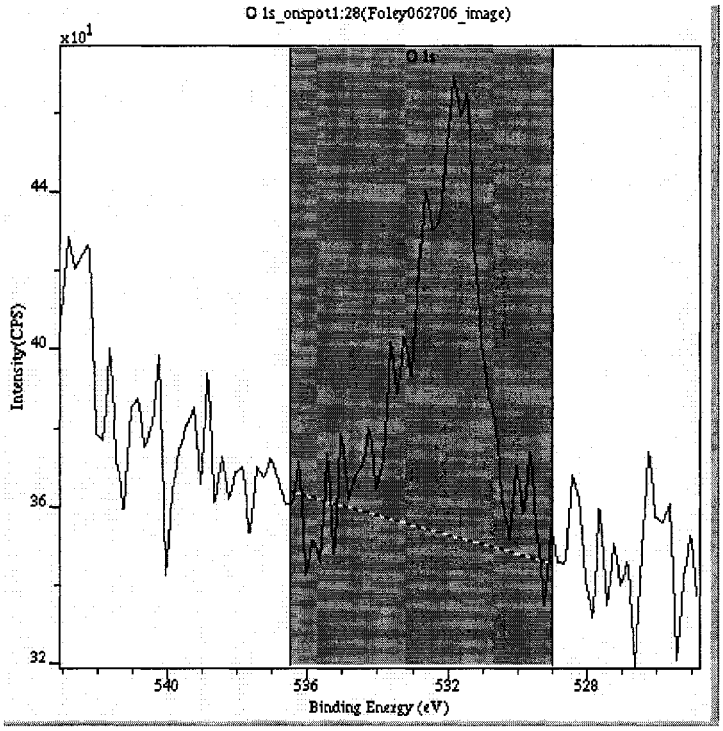

Figure 189. XPS high resolution scan for oxygen (1s) in an area *not* contacted with a PDMS stamp inked with an IgG. XPS-imaging data.

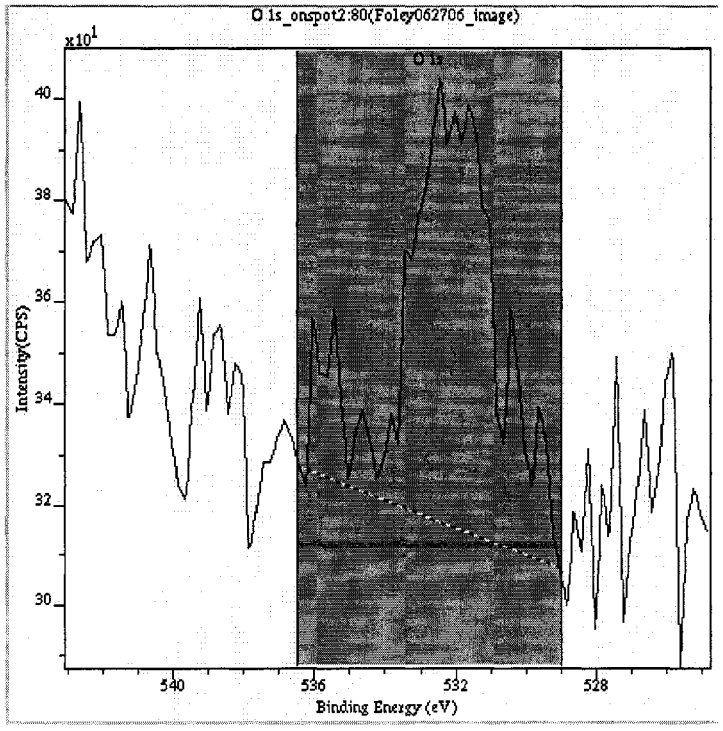

Figure 190. XPS high resolution scan for oxygen (1s) in an area *not* contacted with a PDMS stamp inked with an IgG. XPS-imaging data.

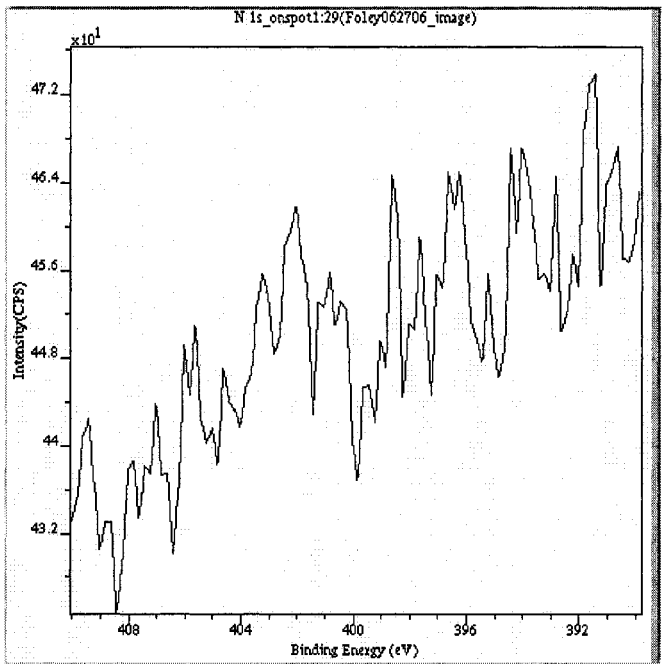

Figure 191. XPS high resolution scan for nitrogen (1s) in an area *not* contacted with a PDMS stamp inked with an IgG. XPS-imaging data.

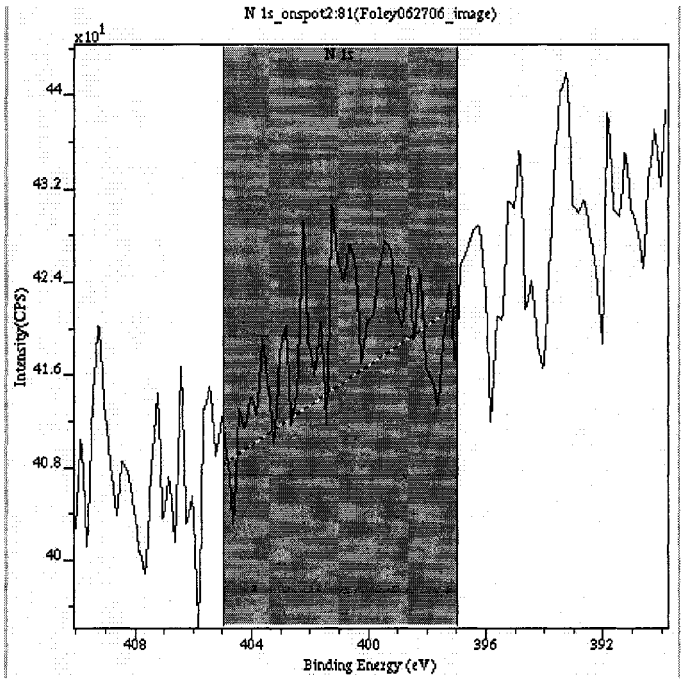

Figure 192. XPS high resolution scan for nitrogen (1s) in an area *not* contacted with a PDMS stamp inked with an IgG. XPS-imaging data.

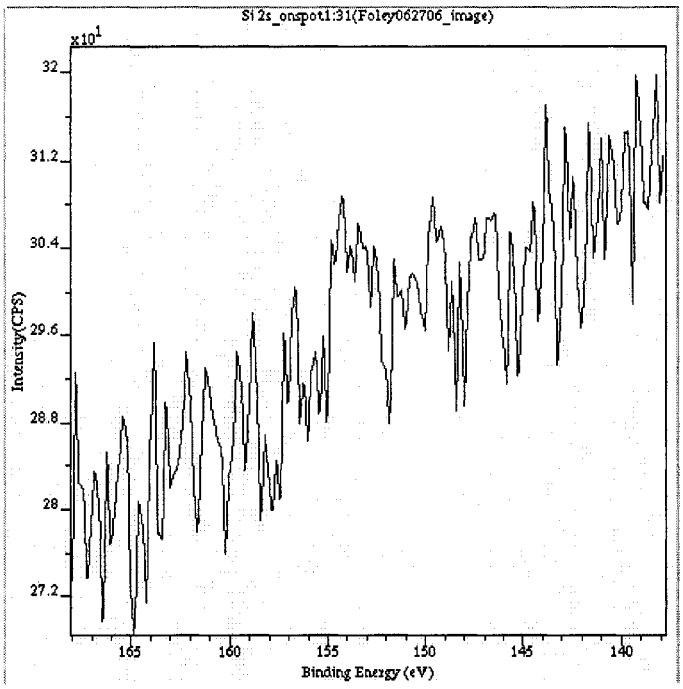

Figure 193. XPS high resolution scan for silicon (2s) in an area *not* contacted with a PDMS stamp inked with an IgG. XPS-imaging data.

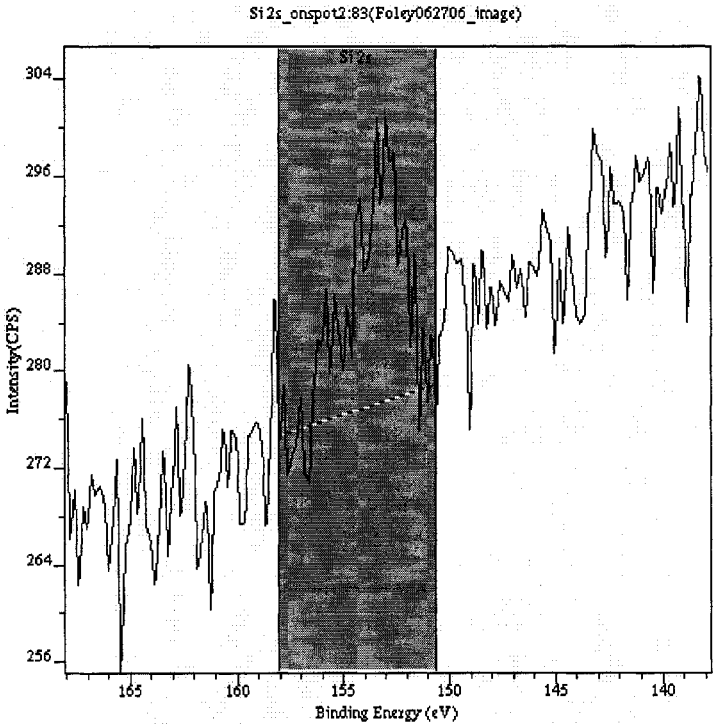

Figure 194. XPS high resolution scan for silicon (2s) in an area *not* contacted with a PDMS stamp inked with an IgG. XPS-imaging data.

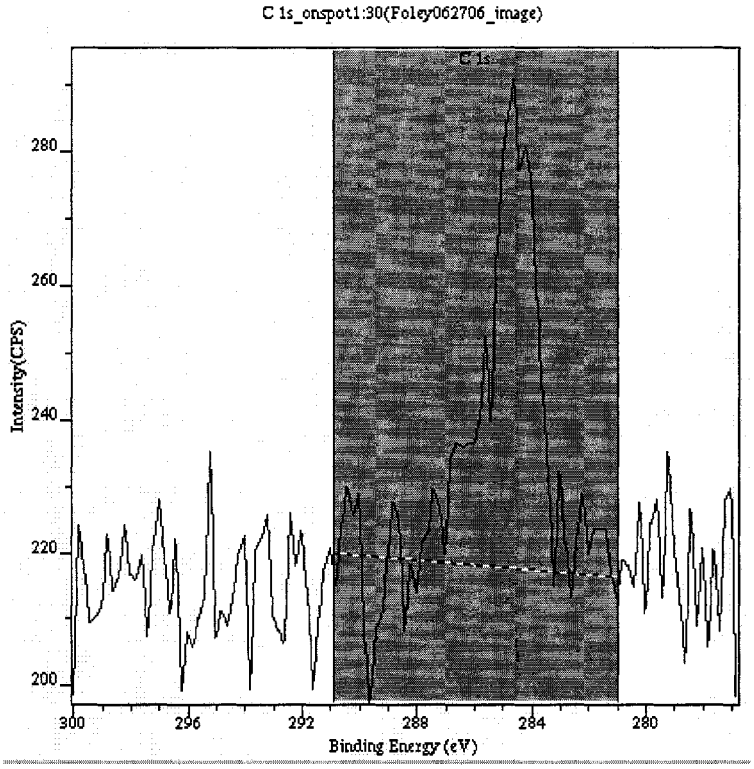

Figure 195. XPS high resolution scan for carbon (1s) in an area *not* contacted with a PDMS stamp inked with an IgG. XPS-imaging data.

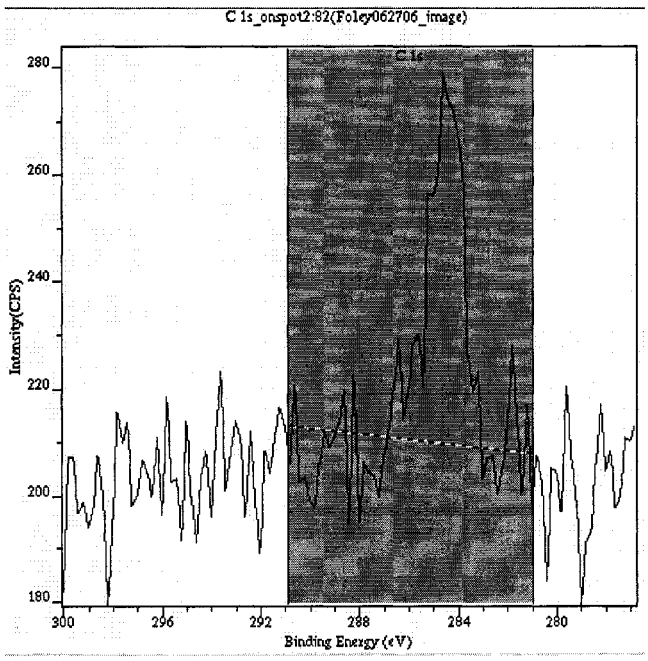

Figure 196. XPS high resolution scan for carbon (1s) in an area *not* contacted with a PDMS stamp inked with an IgG. XPS-imaging data

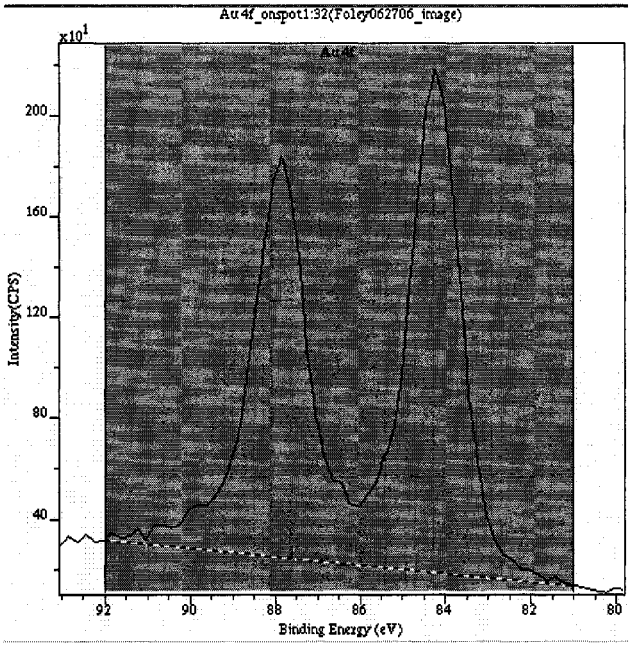

Figure 197. XPS high resolution scan for gold (4f) in an area *not* contacted with a PDMS stamp inked with an IgG. XPS-imaging data

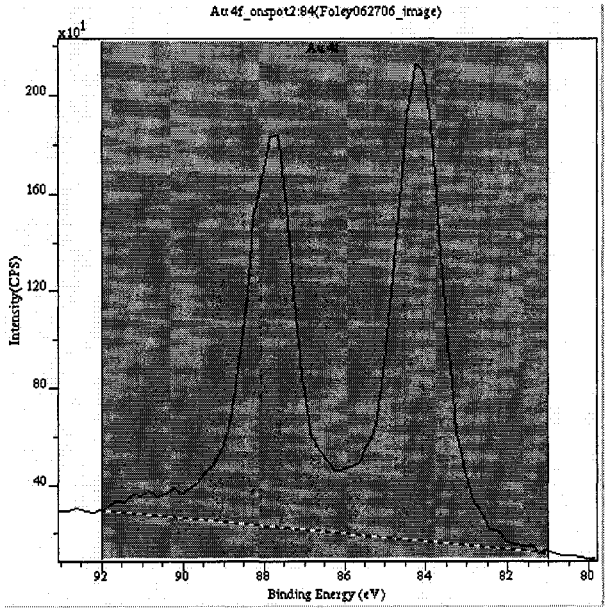

Figure 198. XPS high resolution scan for gold (4f) in an area *not* contacted with a PDMS stamp inked with an IgG. XPS-imaging data.

Curriculum Vita

Jennifer Foley

Education

University of Washington, Fall 2001 – Spring 2007
Ph.D. in Bioengineering
Thesis: Design and development of surface plasmon resonance imaging microfluidic assays
Advisor: Professor Paul Yager

Princeton University, Fall 1997 – Spring 2001
A.B. in Molecular Biology; *cum laude*

Grants

Engineered Biomaterials Training Grant (EBTP) Fall 2003- Fall 2006

Research Experience

Microfluidics Lab University of Washington; Winter 2002 – Spring 2007
Development of a salivary diagnostic under Professor Paul Yager. Worked on the development of a point-of-care salivary diagnostic that used surface plasmon resonance (SPR) microscopy as the detection method. The primary research focus was on surface chemistry development, computational modeling of microfluidic immunoassays, exploration into methods for signal amplification, and some assistance with instrument characterization.

Microprocessing Lab IBM Research Labs, Rueshlikon; Switzerland, Winter 2005
Development of a microcontact printing techniques under Dr. Emmanuel Delamarche. Learned microcontact printing – a method to micropattern proteins on surfaces. Developed a technique to use this method to pattern inside three-dimensional microstructures. The primary application of this printing method was to develop a patterning technique to be used in microfluidic medical diagnostics.

Biochemistry Lab Princeton University; Spring 2000-Spring 2001
Analysis of de novo designed proteins under Professor Michael Hecht. For senior thesis and junior independent work, analyzed alpha helical designed proteins that were found to bind heme. Characterization methods included electron paramagnetic resonance and the determination of redox potentials.

Biophysics Lab Rush Presbyterian Medical Center, Chicago, Illinois; Summer 1999
Studied ionic channels under Dr. Robert Eisenberg. Worked with a group that specialized in measuring ionic current through porin (a bacterial membrane channel).

Allergy and Asthma Drug Research Clinic Princeton, New Jersey; 1998-1999
Intern for Dr. Loren Southern. Observed research techniques for assessing impact of new drugs on asthma and allergy patients.

Molecular Biology Lab Lewis Thomas Laboratories, Princeton University; 1997-1998
Lab assistant for Professor Gerry Waters. Involved in reordering and transforming a bacterial plasmid library.

Publications

Moffet, D.A., Foley, J., and Hecht, M.H. (2003). "Midpoint reduction potentials and heme binding stoichiometries of de novo proteins from designed combinatorial libraries." *Biophysical Chemistry*. **105**, 231.

Fu, E., Foley, J., and Yager, P. (2003). "Wavelength-tunable surface plasmon resonance microscope." *Review of Scientific Instruments*. **74**, 3182.

Fu, E., Chinowsky, T., Foley, J., Weinstein, J. and P. Yager. (2004). "Characterization of a wavelength-tunable surface plasmon resonance microscope." *Review of Scientific Instruments*. **75**, 2300.

Foley, J. Schmid, H., Stutz, R. and E. Delamarche. "Microcontact printing of proteins inside microstructures." *Langmuir*. **21**, 11296.

Foley, J., Nelson, K., Mashadi-Hossein, A., Finlayson, B. and P. Yager. (2007). "Concentration Gradient Immunoassay II: Computational modeling for analysis and optimization." *Analytical Chemistry*. (in press).

Nelson, K., Foley, J. and P. Yager. (2007). "Concentration Gradient Immunoassay (CGIA): A rapid competitive immunoassay based on interdiffusion and surface binding in a microchannel." *Analytical Chemistry*. (in press).

Proceedings (Presenting author is underlined.)

Foley, J., Fu, E., and Yager, P. "T-sensor generated refractive index gradients: calibration of a SPR microscope." Microtas 2003 Proceedings, Oct. 5-9, 2003. Squaw Valley, CA.

Foley, J., Finlayson, B. and P. Yager. "Spatial and temporal variations in antigen binding to immobilized antibodies for determining diffusion coefficients." Chips to Hits Conference. September 20-23, 2004. Boston, MA.

Foley, J. Schmid, H., Stutz, R. and E. Delamarche. "Engineering microfluidic chips with integrated binding sites for ultraminiaturized immunoassays." Microtas 2005 Proceedings, Oct. 9-12, 2005. Boston, MA.

Fu, E. Foley, J. Chen, J., Wiley, B., Xia, Y., and P. Yager. "Wavelength-dependent signal amplification potential of gold nanocage tags for surface plasmon resonance imaging." Microtas 2005 Proceedings, Oct. 9-12, 2005. Boston, MA.